

A Search for Anti-electron-neutrinos from the Sun
at Super-Kamiokande

Ph.D. Thesis

Yoshihito Gando

*Graduate School of Science, Tohoku University
Sendai 980-8578, Japan*

February 2004

Abstract

Results of a search for anti-electron-neutrinos from the sun are presented based on 1496 live-days of Super-Kamiokande-I data taken from May 31 1996 to July 2001. No significant excess of events have been observed and we set an upper limit for the conversion probability to $\bar{\nu}_e$ of the ^8B solar neutrino. This conversion limit is 0.8% (90% confidence level) of the standard solar model for total energy 8 MeV - 20 MeV. We also set a flux limit for monochromatic $\bar{\nu}_e$ for $E_{\bar{\nu}_e} = 10 \text{ MeV} - 17 \text{ MeV}$.

We have also measured the ^8B solar neutrino flux. The ratio of the measured ^8B solar neutrino flux to the standard solar model BPB2001 prediction is $0.465 \pm 0.005(\text{stat.})^{+0.016}_{-0.015}(\text{sys.})$.

Global analysis of solar neutrino results, SK zenith angle spectra and KamLAND results have been performed for a two neutrino oscillation hypothesis and for a RSFP+MSW hybrid model. The LMA1 solution is singled out at 99% confidence level for the oscillation hypothesis. An upper limit of $\mu_\nu B_{\text{sun}}$ is obtained by combining the RSFP+MSW global analysis and $\bar{\nu}_e$ flux limit. And it turned out that the subdominant RSFP effect cannot exceed a few % level in the solar neutrino deficits.

Acknowledgements

First of all, I would like to express my great appreciation to my advisor, Professor. Kunio Inoue. He introduced me to experimental physics, and always found the time to help and the discussions. Without his excellent guidance and encouragement in many occasions, this thesis would never have been completed.

I would like to thank Prof. A. Suzuki, the leader of RC ν S (Research Center for Neutrino Science, Tohoku University). He gave me many valuable advice about physical interpretation.

I would like to be thankful to Prof. Y. Suzuki, the spokesman of the Super-Kamiokande. For most of my time on SK, he was the convener of solar neutrino analysis group, and he gave me various advice for solar neutrino analysis.

I am grateful to Prof. Y. Totsuka, who is the former spokesman and a father of the Super-Kamiokande, for his leadership.

Special appreciation goes to Prof. M. Nakahata, the convener of the solar neutrino analysis group. He was my advisor at Kamioka. He always found the time to help and the discussions about calibration, data analysis, neutrino physics, etc.. I learned various things from him.

I would like to thank all members of the solar neutrino analysis group. Prof. Y. Fukuda taught me about the reduction and trigger simulation. Dr. Y. Takeuchi gave me many suggestions about data analysis and taught me about time-weighted simulation. Dr. Y. Koshio taught me about oscillation analysis, M.C. simulation and the treatment about off-line calibration data. Dr. K. Ishihara taught me physics, experiment and calibration methods from the basics. Dr. Gene Guillian gave me many useful suggestions about $\bar{\nu}_e$ analysis. I would like to thank the other members, Prof. R. Svoboda, Dr. M. R. Vagins, Dr. M. Smy, Dr. K. Martens, Dr. N. Sakurai, Dr. T. Namba, Dr. M. Malek, Dr. D. Turcan, Dr. J. Yoo, Mr. D. Liu, Mr. M. Morii, Mr. Y. Ichikawa, Mr. R. Nambu, Mr. P. Cravens, Ms. J. Ishii, and special thanks go to Mr. C. Mitsuda.

I am grateful to all the Super-Kamiokande collaboration for very useful suggestions. Especially, Prof. K. Nakamura, Prof. K. Nishikawa, Prof. T. Kajita, Prof. M. Takita, Prof. K. Kaneyuki, Prof. Y. Itow, Prof. T. Nakaya, Dr. M. Miura. Dr. M. Shiozawa, Dr. Y. Hayato, Dr. Y. Obayashi, Dr. A. Ichikawa, Dr. T. Toshito, Dr. M. Yoshida, Dr. J. Kameda, Dr. K. Kobayashi and Dr. A. Kibayashi. Special thanks go to Dr. C. Mauger who read and checked this thesis. My great appreciation also goes to Prof. S.

Moriyama, who is the leader of calibration group at SK-II. He taught me about various experiments and calibration methods.

I would like to thank Dr. S. Yamada, Dr. S. Nakayama, Dr. C. Saji, Dr. K. Nitta, Mr. M. Ishitsuka, Mr. S. Fukuda, Mr. Y. Imori, Ms. Y. Kajiyama, Mr. I. Kato, Ms. H. Yokoyama, Mr. H. Maesaka, Mr. M. Hasegawa, Mr. S. Yamamoto, Mr. T. Kato, Ms. Y. Nakajima, Ms. M. Sekiguchi, Mr. Y. Ashie, Mr. A. Minamino, and all the SK and K2K graduate students. We had discussions about physics and unrelated to physics, and they gave me advise and friendship.

My appreciation goes to Prof. A. Yamaguchi, Prof. H. Yamamoto, Prof. J. Shirai, Prof. F. Suekane, Prof. T. Hayashino, Dr. T. Nagamine, Dr. T. Hasegawa, Dr. M. Koga, Ms. K. Tamae, Dr. T. Mitsui, Dr. K. Nakamura, Dr. M. Motoki, Dr. Y. Kishimoto, Dr. T. Iwamoto, Dr. H. Ogawa, Dr. O. Tajima, Mr. S. Enomoto, Mr. H. Watanabe, and other RC ν S members.

I also thank to my fellows, Mr. H. Ikeda, Mr. I. Higuchi, Mr. H. Handa, Mr. T. Kawaguchi, Ms. K. Watanabe, Mr. T. Yoshida, Mr. H. Kinoshita, Mr. T. Muroho, and Ms. K. Tsuchiya.

I would like to express my gratitude to Mr. T. Shibatsuka. His serious attitude toward physics and astronomy had big influence on me when I was an undergraduate student.

I gratefully acknowledge the cooperation of the Kamioka Mining and Smelting Company. The Super-Kamiokande has been built and operated from funding by the Japanese Ministry of Education, Culture, Sports, Science and Technology, the U.S. Department of Energy, and the U.S. National Science Foundation. I would like to thank for the financial support of Japan Society for the Promotion of Science.

Finally, my deepest appreciation goes to my parents, Masahiko and Akiko Gando, sister, Sachiko Gando, and brother, Toshiyuki Gando for unfailing support in my study and life.

Feb 2004
Yoshihito Gando

Contents

Abstract

Acknowledgements

| | | |
|----------|--|-----------|
| 1 | Introduction | 1 |
| 2 | Neutrinos and the Solar Neutrino Problem | 2 |
| 2.1 | The neutrino | 2 |
| 2.1.1 | Limits for neutrino mass | 2 |
| 2.1.2 | Limits on neutrino magnetic moment | 3 |
| 2.2 | Solar neutrinos | 6 |
| 2.2.1 | The sun and Standard Solar Model (SSM) | 6 |
| 2.2.2 | ^8B spectrum | 10 |
| 2.2.3 | Results of solar neutrino experiments | 10 |
| 2.3 | Neutrino oscillation and Resonant Spin Flavor Precession (RSFP) | 15 |
| 2.3.1 | Vacuum oscillation | 15 |
| 2.3.2 | Neutrino oscillation in matter (MSW effect) | 16 |
| 2.3.3 | The neutrino oscillation solution for solar neutrino problem and KamLAND result | 17 |
| 2.3.4 | RSFP+MSW model | 20 |
| 3 | The Super-Kamiokande Detector | 22 |
| 3.1 | Overview of the Super-Kamiokande detector | 22 |
| 3.2 | Neutrino interaction of neutrinos in Super-Kamiokande | 23 |
| 3.2.1 | Dominant neutrino interactions in the energy region of solar neu- trinos | 23 |
| 3.2.2 | Neutrino-electron elastic scattering | 25 |
| 3.2.3 | Inverse beta decay process for $\bar{\nu}_e$ detection | 27 |
| 3.2.4 | Cherenkov radiation | 29 |
| 3.3 | The water tank | 30 |
| 3.3.1 | The inner detector | 31 |
| 3.3.2 | The outer detector | 31 |

| | | |
|----------|---|-----------|
| 3.4 | 50 cm diameter photo-multiplier tube (ID PMT) | 33 |
| 3.5 | 20 cm diameter photo-multiplier tube (OD PMT) | 33 |
| 3.6 | Water purification system | 36 |
| 3.7 | Air purification system | 37 |
| 3.8 | Electronics and data acquisition system | 38 |
| | 3.8.1 Inner detector electronics | 38 |
| | 3.8.2 Outer detector electronics | 39 |
| 3.9 | Triggers | 41 |
| 3.10 | Online and offline system | 42 |
| 3.11 | Detector simulation | 43 |
| 4 | Event Reconstruction | 46 |
| 4.1 | Reconstruction of low energy events | 46 |
| | 4.1.1 Vertex reconstruction | 46 |
| | 4.1.2 Direction reconstruction | 50 |
| | 4.1.3 Energy reconstruction | 51 |
| 4.2 | Track reconstruction of cosmic ray muons | 54 |
| | 4.2.1 μ track | 54 |
| 5 | Calibration | 61 |
| 5.1 | Xe calibration | 61 |
| 5.2 | Ni-Cf calibration | 63 |
| 5.3 | TQ map | 66 |
| 5.4 | Water transparency | 68 |
| | 5.4.1 Direct measurement by laser and CCD camera | 68 |
| | 5.4.2 Time variation of water transparency by using decay electrons | 70 |
| 5.5 | Automatic calibration systems | 72 |
| | 5.5.1 Gain | 73 |
| | 5.5.2 Timing | 73 |
| | 5.5.3 water transparency | 73 |
| 5.6 | LINAC | 74 |
| 5.7 | DT calibration | 77 |
| 5.8 | Time variation of energy | 77 |
| 5.9 | Trigger efficiency | 82 |
| 6 | Data Reduction | 85 |
| 6.1 | Data sets and run | 86 |
| 6.2 | Online reduction | 86 |
| | 6.2.1 Total charge cut | 86 |
| | 6.2.2 Pedestal and periodic trigger cut | 86 |
| 6.3 | First reduction | 87 |

| | | |
|----------|--|------------|
| 6.3.1 | Fiducial volume cut | 87 |
| 6.3.2 | DT \geq 50 μ sec cut | 87 |
| 6.3.3 | OD triggered event cut | 89 |
| 6.3.4 | Noise (NSratio) cut | 89 |
| 6.3.5 | Cluster-ATM-hits-event cut | 89 |
| 6.3.6 | Flasher cut | 90 |
| 6.3.7 | Goodness cut | 90 |
| 6.3.8 | External flasher cut | 92 |
| 6.4 | Spallation cut | 94 |
| 6.5 | Second reduction | 96 |
| 6.5.1 | Goodness stability test | 97 |
| 6.5.2 | Vertex test after noise hit rejection | 98 |
| 6.5.3 | Cherenkov ring image test | 98 |
| 6.6 | External γ -ray cut | 99 |
| 6.7 | Reduction summary | 100 |
| 7 | Data Analysis and Results | 106 |
| 7.1 | Extraction of elastic scattering events | 106 |
| 7.2 | Results on the ^8B solar neutrino flux | 109 |
| 7.2.1 | ^8B solar neutrino flux | 109 |
| 7.2.2 | Day/Night flux asymmetry | 110 |
| 7.2.3 | Energy spectrum for recoil electrons | 110 |
| 7.3 | Systematic errors | 110 |
| 7.3.1 | Correlated errors | 111 |
| 7.3.2 | Uncorrelated errors | 114 |
| 7.4 | Search for $\bar{\nu}_e$ from the sun | 117 |
| 7.4.1 | Statistical subtraction of spallation backgrounds | 117 |
| 7.4.2 | ^8B spectrum dependent limit | 120 |
| 7.4.3 | Angular distribution analysis | 121 |
| 7.4.4 | ^8B spectrum independent limit | 124 |
| 8 | Discussions | 129 |
| 8.1 | Oscillation study | 129 |
| 8.2 | RSFP+MSW study | 131 |
| 8.2.1 | Magnetic field in the sun | 131 |
| 8.2.2 | Constraints on neutrino magnetic moment from flux measurements and zenith angle spectra | 135 |
| 8.2.3 | Constraint on neutrino magnetic moment from the $\bar{\nu}_e$ flux limit | 144 |
| 8.2.4 | Flux bias and spectrum distortion from RSFP | 147 |
| 9 | Conclusion | 153 |

| | | |
|----------|--|------------|
| A | Definition of spallation likelihood | 154 |
| A.1 | Likelihood for ΔL | 154 |
| A.2 | Likelihood for ΔT | 155 |
| A.3 | Likelihood for Q_{res} | 157 |
| B | Numerical calculation of neutrino propagation | 160 |
| C | Spectrum distortion from neutrino magnetic moment | 164 |
| | Bibliography | 166 |

List of Figures

| | | |
|------|---|----|
| 2.1 | Radiative correction giving rise to a magnetic moment of Dirac neutrino within standard Weinberg-Salam theory | 4 |
| 2.2 | Radiative correction giving rise to a magnetic moment in the left-right symmetric model | 4 |
| 2.3 | Radiative correction giving rise to a magnetic moment in a model with a charged scalar particle η | 5 |
| 2.4 | The pp-chain | 7 |
| 2.5 | The CNO cycle | 7 |
| 2.6 | Energy spectra of solar neutrinos | 8 |
| 2.7 | Production points of neutrinos as a function of the solar radius | 9 |
| 2.8 | Electron and neutron density in the Sun | 9 |
| 2.9 | Energy levels of decay chains of ${}^8\text{B}(\beta^+){}^8\text{Be}(2\alpha)$ | 10 |
| 2.10 | Time variation of ${}^{37}\text{Ar}$ production rate and sunspot number | 14 |
| 2.11 | The time variation of the observed solar neutrino flux in Kamiokande | 14 |
| 2.12 | The allowed region for neutrino oscillation parameters by solar neutrino measurements | 18 |
| 2.13 | KamLAND energy spectrum and allowed region | 19 |
| 3.1 | Location of Super-Kamiokande in Japan | 23 |
| 3.2 | Cosmic ray muon flux | 24 |
| 3.3 | The total cross-section as a function of neutrino energy | 27 |
| 3.4 | The average $\cos\theta$ distribution of positron for inverse beta-decay process | 29 |
| 3.5 | Definition of the Cherenkov angle $\theta_{\text{Cherenkov}}$ | 30 |
| 3.6 | The schematic view of the Super-Kamiokande detector | 31 |
| 3.7 | A schematic view of support structures for the inner detector | 32 |
| 3.8 | 50 cm photo-multiplier tube | 34 |
| 3.9 | Single photo-electron distribution of the 50 cm diameter PMT | 34 |
| 3.10 | The quantum efficiency of the PMTs as a function of light wavelength | 34 |
| 3.11 | The time variation of the number of dead ID PMTs | 35 |
| 3.12 | A schematic view of the 20 cm PMT with wavelength shifter | 35 |
| 3.13 | The time variation of the number of dead OD PMTs | 36 |
| 3.14 | A schematic view of the water purification system after improvements | 38 |

| | | |
|------|---|----|
| 3.15 | A schematic view of the Rn free air purification system | 39 |
| 3.16 | A schematic view of the ID data acquisition system | 40 |
| 3.17 | A schematic view of the OD data acquisition system | 41 |
| 3.18 | A schematic view of the online and offline data flow | 43 |
| 3.19 | Light reflection from black sheet and PMT | 44 |
| 3.20 | TDC resolution and timing shift | 45 |
| 4.1 | Event display of a typical low energy event | 47 |
| 4.2 | Timing distribution of the event in Figure 4.1 | 48 |
| 4.3 | The initial grid points for the vertex reconstruction | 48 |
| 4.4 | A typical <i>goodness</i> distribution of LINAC calibration data | 49 |
| 4.5 | Definition of Θ_i and θ_i | 50 |
| 4.6 | The distribution of the angle between charged particle direction and the vector from the reconstructed vertex to the hit PMT position | 51 |
| 4.7 | The effective photo cathode area $R_{cover}/S(\theta_i, \phi_i)$ | 53 |
| 4.8 | The correlation between N_{eff} and total energy | 54 |
| 4.9 | Flow chart of the muon reconstruction | 55 |
| 4.10 | The definition of parameters used in $goodness_\mu$ | 57 |
| 4.11 | The track resolution of the muon fitter | 58 |
| 4.12 | Charge distribution of cosmic μ events | 59 |
| 4.13 | Reconstructed zenith angle distribution of cosmic muons | 59 |
| 4.14 | Reconstructed azimuth angle distribution of cosmic muons | 60 |
| 5.1 | A schematic view of Xe calibration system | 62 |
| 5.2 | The relative acceptance function of PMT | 63 |
| 5.3 | Distribution of the corrected charge of all inner PMTs. | 64 |
| 5.4 | Time variation of sigma for charge spread | 64 |
| 5.5 | A schematic view of Ni-Cf calibration system. | 65 |
| 5.6 | The charge distribution of typical PMT after a single photo-electron hit | 65 |
| 5.7 | A schematic view of timing measurement system | 66 |
| 5.8 | The TQ map of a typical PMT | 67 |
| 5.9 | Timing resolution as a function of the pulse height | 67 |
| 5.10 | A schematic view of the direct measurement of the water transparency. | 68 |
| 5.11 | Results of the CCD camera direct measurement for 420 nm case | 69 |
| 5.12 | Water transparency as a function of wavelength | 69 |
| 5.13 | Definition of the PMTs which are used for water transparency calculation. | 71 |
| 5.14 | Time $\log(q(r))$ distribution as function of r | 71 |
| 5.15 | Time variation of water transparency | 72 |
| 5.16 | A schematic view of the system for automatic water parameter measurement | 74 |
| 5.17 | A schematic view of LINAC calibration system | 75 |
| 5.18 | Results of LINAC calibration | 76 |
| 5.19 | Schematic view of DT generator | 78 |

| | | |
|------|---|-----|
| 5.20 | An overview of DT calibration data taking | 78 |
| 5.21 | The energy distribution of a typical DT calibration | 79 |
| 5.22 | The position dependence of the energy scale from DT calibration | 79 |
| 5.23 | The angular dependence of energy scale from DT calibration | 80 |
| 5.24 | The energy spectrum of $\mu - e$ decay events in SK | 81 |
| 5.25 | The time variation of energy scale by decay electron events from cosmic-ray muons | 81 |
| 5.26 | The energy spectrum for spallation events | 82 |
| 5.27 | The time variation of the energy scale by spallation events | 83 |
| 5.28 | The LE trigger efficiency as a function of energy | 84 |
| 5.29 | The SLE trigger efficiency as a function of energy | 84 |
| 6.1 | The total charge distribution of typical data sample | 87 |
| 6.2 | Fiducial volume cut to a typical data sample | 88 |
| 6.3 | The distribution of the time difference from a typical data sample | 88 |
| 6.4 | The distribution of the noise ratio from a typical data sample | 89 |
| 6.5 | The distribution of the ATM ratio from a typical data sample | 90 |
| 6.6 | A vertex distribution for flasher events | 91 |
| 6.7 | Scatter plots of Q_{max} and max24 | 91 |
| 6.8 | The <i>goodness</i> distribution from a typical data sample | 92 |
| 6.9 | An example of the directional test | 93 |
| 6.10 | A distribution of the Dir_{ks} | 94 |
| 6.11 | Distributions of the spallation likelihood | 96 |
| 6.12 | Dead time distribution from spallation cut for each position | 97 |
| 6.13 | Distributions of $\Delta goodnes$ v.s. distance from reconstructed vertex | 98 |
| 6.14 | Examples of likelihood functions for the ring image test for vertices | 99 |
| 6.15 | The distribution of the average log likelihood for the ring image test | 100 |
| 6.16 | The definition of the effective distance from the wall | 101 |
| 6.17 | Distributions of effective distances | 101 |
| 6.18 | The Vertex distribution before and after the gamma cut | 102 |
| 6.19 | The directional distributions before and after the gamma cut | 102 |
| 6.20 | The Vertex distribution before and after the gamma cut | 103 |
| 6.21 | The direction distributions before and after the gamma cut | 103 |
| 6.22 | Energy spectra after each reduction step | 105 |
| 7.1 | Definition of $\cos \theta_{sun}$ | 107 |
| 7.2 | The $\cos \theta_{sun}$ distribution for 5.0 - 20.0 MeV | 108 |
| 7.3 | The probability density function for elastic scattering signals, P_{sig} | 108 |
| 7.4 | The probability density function for the background shape P_{sig} | 109 |
| 7.5 | The Day/Night dependence of the solar neutrino flux | 111 |
| 7.6 | The recoil electron energy spectra for the observed and expected solar neutrino events. | 112 |

| | | |
|------|--|-----|
| 7.7 | The definition of the zenith angle division | 112 |
| 7.8 | The zenith angle spectra | 113 |
| 7.9 | The fully correlated 1σ deformation of the energy spectrum from uncertainties | 115 |
| 7.10 | The $\cos \theta_{\text{sun}}$ distribution and $\bar{\nu}_e$ candidate region | 117 |
| 7.11 | Delta-T distribution of muons before low-energy events | 119 |
| 7.12 | Spallation contamination in each energy bins | 121 |
| 7.13 | The expected energy spectrum of $\bar{\nu}_e$ events | 122 |
| 7.14 | Energy spectrum of the observed data. | 122 |
| 7.15 | Summary of $\bar{\nu}_e$ limits that assuming ${}^8\text{B}$ spectrum is kept | 123 |
| 7.16 | Positron angular distributions for each visible energy | 125 |
| 7.17 | Typical Probability distribution of the shape analysis for visible energy 5 - 6 MeV | 125 |
| 7.18 | Energy spectra of observed and M.C. data | 127 |
| 7.19 | 90% C.L. upper limits of the $\bar{\nu}_e$ flux for each monochromatic $\bar{\nu}_e$ energy. | 128 |
| 8.1 | The zenith angle spectra with expected spectra | 132 |
| 8.2 | The allowed region of Δm^2 and $\sin^2 2\theta$ from a global analysis of the solar neutrino results. | 133 |
| 8.3 | The allowed region of Δm^2 and $\sin^2 2\theta$ from a global analysis of all solar neutrino results and KamLAND result | 133 |
| 8.4 | The assumed magnetic field profiles in the sun as a function of radius. | 135 |
| 8.5 | Probabilities to be each neutrino states as a function of radial position | 136 |
| 8.6 | neutrino spectrum for each magnetic field profiles | 137 |
| 8.7 | 95% C.L. allowed region for each $\mu_\nu B_{\text{sun}}$ in a case of profile1 | 138 |
| 8.8 | 95% C.L. allowed region for each $\mu_\nu B_{\text{sun}}$ in a case of profile2 | 139 |
| 8.9 | 95% C.L. allowed region for each $\mu_\nu B_{\text{sun}}$ in a case of profile3 | 140 |
| 8.10 | 95% C.L. solar global + KamLAND allowed region for each $\mu_\nu B_{\text{sun}}$ in case of profile1 | 141 |
| 8.11 | 95% C.L. solar global + KamLAND allowed region for each $\mu_\nu B_{\text{sun}}$ in case of profile2 | 142 |
| 8.12 | 95% C.L. solar global + KamLAND allowed region for each $\mu_\nu B_{\text{sun}}$ in case of profile3 | 143 |
| 8.13 | Expected $\bar{\nu}_e/\text{SSM}$ for each parameter region | 145 |
| 8.14 | Excluded region of oscillation parameters from the $\bar{\nu}_e$ flux limit | 146 |
| 8.15 | 90% C.L. allowed region from the solar + KamLAND global fit and 90% C.L. excluded region from the $\bar{\nu}_e$ limit for profile1 | 148 |
| 8.16 | 90% C.L. allowed region from the solar + KamLAND global fit and 90% C.L. excluded region from the $\bar{\nu}_e$ limit for profile2 | 149 |
| 8.17 | 90% C.L. allowed region from the solar + KamLAND global fit and 90% C.L. excluded region from the $\bar{\nu}_e$ limit for profile3 | 150 |

| | | |
|------|--|-----|
| 8.18 | Spectrum distortions from only MSW effect and MSW with RSFP | 151 |
| 8.19 | flux difference between MSW and MSW with RSFP at SK | 152 |
| A.1 | ΔL distribution for each Q_{res} range | 156 |
| A.2 | The distribution of the likelihood function for ΔL | 156 |
| A.3 | ΔT distribution for each time bins | 157 |
| A.4 | Q_{res} distribution for the spallation candidate (non-candidate) event . . . | 159 |
| A.5 | The distribution of the likelihood function for Q_{res} | 159 |
| B.1 | Direction of the neutrino propagation | 161 |
| B.2 | Electron density in the earth | 163 |
| C.1 | Expected energy spectrum of recoil electrons with and without electro- magnetic interaction | 165 |

List of Tables

| | | |
|-----|---|-----|
| 2.1 | Expected neutrino flux at 1 AU from BPB2001 | 8 |
| 2.2 | Expected solar neutrino event rate at Homestake experiment from the SSM | 11 |
| 2.3 | Expected flux at Ga experiments from SSM prediction | 12 |
| 2.4 | The relation between the electron density and the mixing angle in matter | 17 |
| 3.1 | History of the SLE trigger | 42 |
| 4.1 | Summary of muon fitter efficiency | 57 |
| 5.1 | Injection position of LINAC beam | 75 |
| 6.1 | Summary of possible spallation products | 95 |
| 6.2 | Summary of event reduction | 104 |
| 7.1 | Systematic errors for spallation background estimation | 120 |
| A.1 | The six ranges of Q_{res} and the parameters for the likelihood function $L_{spa}^{\Delta L}(\Delta L, Q_{res})$ for Q_{res} | 155 |
| A.2 | The parameters of the likelihood $L_{spa}^{\Delta T}(\Delta T)$ | 158 |
| B.1 | Parameters and step sizes for MSW+RSFP study | 161 |

Chapter 1

Introduction

Solar models tell that the sun shines by nuclear fusion reactions at its core. Although the sun is the nearest star, its inside cannot be seen optically. In order to confirm the model prediction called pp-chain, the first observation of the center of the sun was done by R. Davis and his collaborators [1] by detecting electron neutrinos from nuclear fusion reactions. They have observed solar neutrinos for about 30 years, but the observed neutrino flux was only one third of the prediction of standard solar models (SSMs). This is the so-called ‘Solar Neutrino Problem.’ The next solar neutrino experiments, Kamiokande, GALLEX/GNO, SAGE, Super-Kamiokande have also verified the deficit of solar neutrinos. From the improvement of theoretical discussions, the most likely reason for the deficit is considered to be neutrino properties like oscillations from mass and/or spin flip from magnetic moment instead of theoretical problems of SSMs.

Recent solar neutrino measurements from Super-Kamiokande [2] and SNO [3] established that the solar neutrino problem is explained by a transformation of electron neutrinos to the other active flavors of neutrinos, and the total flux of all neutrino types is conserved. Then, the ‘Solar Neutrino Problem’ as an astrophysical problem was already solved. But there is a question, ‘What is the reason of the neutrino transformation?’. Current solar neutrino data favor the Large Mixing Angle solution (LMA) under a neutrino oscillation hypothesis, and the first result of KamLAND favors the LMA solution [4]. The solution of the transformation has started to become clear in the last few years.

The next step of the solar neutrino experiments is research on neutrino properties by using one of the largest neutrino factories, the sun. In this thesis, we report the result of a search for $\bar{\nu}_e$ from the sun, examination of neutrino oscillations between two active neutrinos, and an investigation of a hybrid model of neutrino oscillation and neutrino spin flavor precession conversion from its transition magnetic moment.

Chapter 2

Neutrinos and the Solar Neutrino Problem

2.1 The neutrino

The neutrino was introduced to explain energy deficits in nuclear beta decay processes as a ‘neutron’ by W. Pauli [5] in 1930, and incorporated in a theory of beta decay by E. Fermi [6]. The existence of the neutrino was confirmed by F. Reines and C. L. Cowan in 1953 by using reactor neutrinos [7]. Now, we know the existence of different flavors, ν_μ [8], ν_τ [9], and the number of active light neutrino species is three [10]. Neutrinos are elementary particles in the standard model, and the elementary particles which have spin 1/2 organize phenomenologically in three generations by common features as follows,

$$\begin{pmatrix} e \\ \nu_e \end{pmatrix} \quad \begin{pmatrix} \mu \\ \nu_\mu \end{pmatrix} \quad \begin{pmatrix} \tau \\ \nu_\tau \end{pmatrix} \quad \text{Lepton} \quad (2.1)$$

$$\begin{pmatrix} u \\ d \end{pmatrix} \quad \begin{pmatrix} c \\ s \end{pmatrix} \quad \begin{pmatrix} t \\ b \end{pmatrix} \quad \text{Quark.} \quad (2.2)$$

In spite of having been used to explain physical phenomena for 70 years, our knowledge of the neutrino as an elementary particle is limited. In this section, the current limits for neutrinos are described.

2.1.1 Limits for neutrino mass

The Neutrino has traditionally been treated as massless, but nothing forbids a finite neutrino mass in the standard model and many models beyond the standard model require a finite mass. Therefore many experiments have tried to measure the neutrino mass directly. But, there is no direct evidence for finite mass and the upper limits on the masses have been obtained by several experiments as follows,

- ν_e :

The β -decay process of tritium, ${}^3\text{H} \rightarrow {}^3\text{He} + e^- + \bar{\nu}_e$ has a Q-value, 18.6 keV (Q-value is the energy difference between the two atoms), adequate for the search for neutrino mass. The limit from this direct measurement is [11] ;

$$m_{\nu_e} < 2.5 \text{ eV (95\% C.L.)} \quad (2.3)$$

- ν_μ :

From the momentum distributions of $\pi^+ \rightarrow \mu^+ + \nu_\mu$ decay [12] ;

$$m_{\nu_\mu} < 0.17 \text{ MeV (90\% C.L.)} \quad (2.4)$$

- ν_τ :

From the difference between fitting results of visible energy and invariant mass in $\tau^- \rightarrow 2\pi^- + \pi^+ + \nu_\tau$, and $\tau^- \rightarrow 3\pi^- + 2\pi^+ + (\pi^0) + \nu_\tau$ decay [13] ;

$$m_{\nu_\tau} < 18.2 \text{ MeV (95\%C.L.)} \quad (2.5)$$

- m_ν limit from cosmology ;

The massive neutrinos make cluster on very large scales during matter domination. Therefore this effect changes the shape of the matter power spectrum and suppresses the amplitude of fluctuations on the cosmic microwave background. Assuming there are three degenerate stable light neutrino species, the upper limit of neutrino mass is [14],

$$m_\nu < 0.23 \text{ eV (95\%C.L.)} \quad (2.6)$$

2.1.2 Limits on neutrino magnetic moment

In the standard Weinberg-Salam theory with minimal extension about ν_R and neutrino mass existence, the magnetic dipole moment for Dirac neutrino is induced by radiative corrections (Figure 2.1) and is calculated to be [15] ;

$$\mu_\nu = \frac{3eG_F}{8\sqrt{2}\pi^2} m_\nu = 3 \times 10^{-19} \mu_B \left(\frac{m_\nu}{1\text{eV}} \right), \quad (2.7)$$

where μ_B is the Bohr magneton ($= e/2m_e = 5.788 \times 10^{-9} \text{ eV/Gauss}$). Majorana neutrinos can not have a magnetic dipole moment because of CPT invariance [16]. The order of the magnetic dipole moment is not enough to be detected directly, however the off-diagonal transition moment may exist for Dirac and Majorana neutrinos. And beyond the standard model, neutrinos could have a larger magnetic moment than that of the standard model [17] (Figure 2.2) - as large as $\sim 10^{-11} \mu_B$ [18] (Figure 2.3). If we could measure a large magnetic moment exceeding that of equation 2.7, it would imply new physics. Many experiments have tried to measure the neutrino magnetic moment, but no evidence has been found so far. The upper limits are summarized as follows :

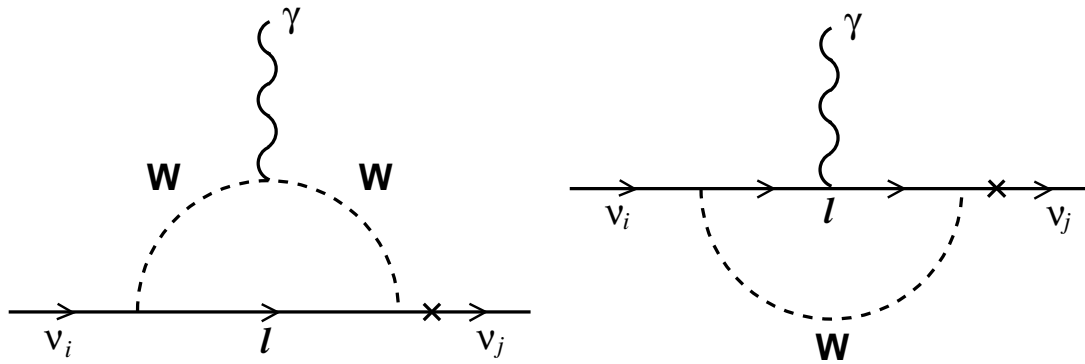


Figure 2.1: Radiative correction giving rise to a magnetic moment of Dirac neutrino within standard Weinberg-Salam theory.

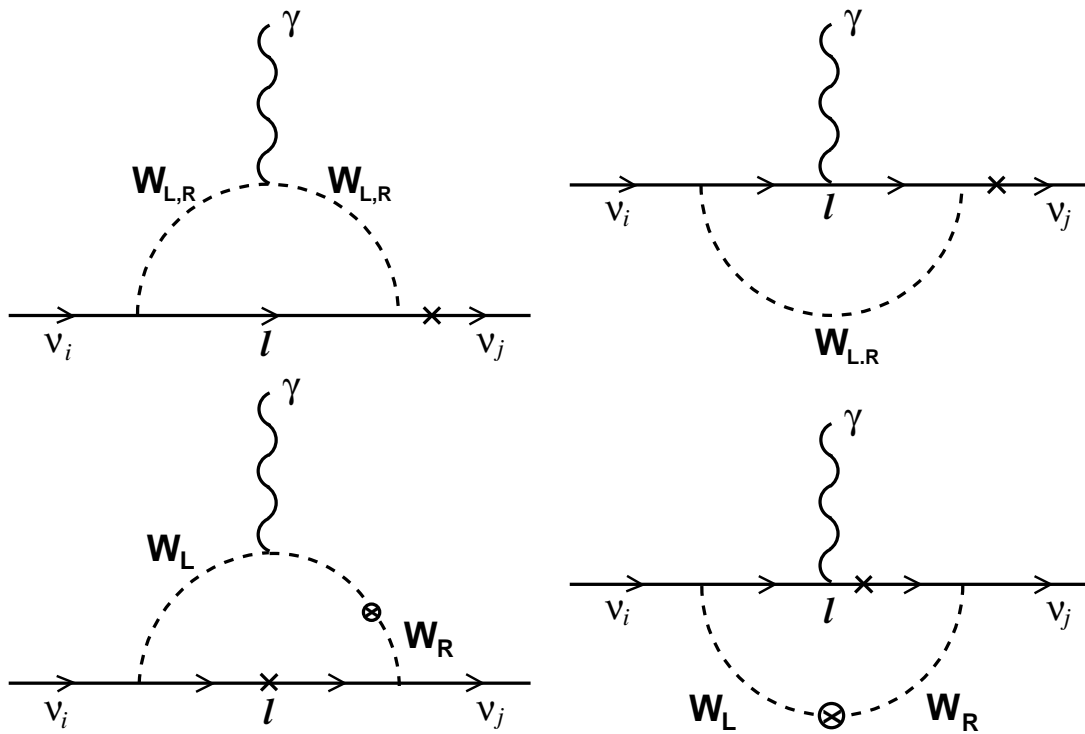


Figure 2.2: Radiative correction giving rise to a magnetic moment in the left-right symmetric model.

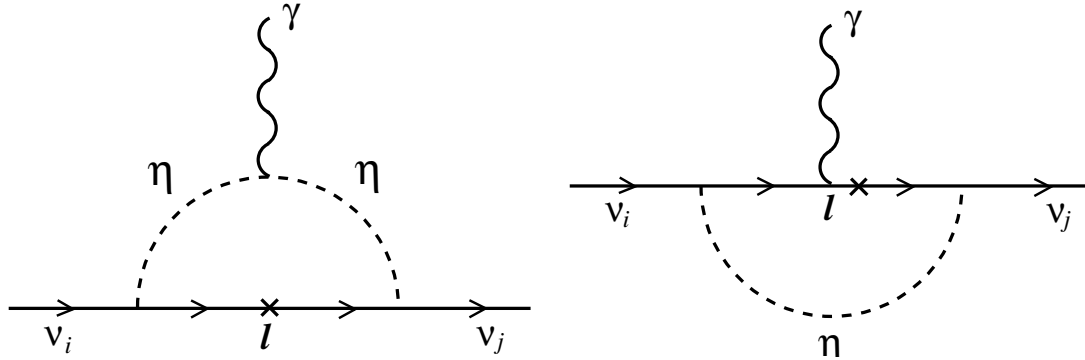


Figure 2.3: Radiative correction giving rise to a magnetic moment in a model with a charged scalar particle η .

- If neutrinos have a magnetic moment, the cross section of the neutrino-electron elastic scattering is modified by the following electro-magnetic term,

$$\left(\frac{d\sigma}{dT}\right)_{EM} = \mu_\nu^2 \frac{\pi\alpha^2}{m_e^2} \left(\frac{1}{T} - \frac{1}{E_\nu}\right), \quad (2.8)$$

where T is the kinetic energy of electron ; $E_e - m_e$ and E_ν is the neutrino energy. Looking for the distortion from this effect, the limits on $\mu_{\nu_e}, \mu_{\bar{\nu}_e}$ are obtained as follows [19, 20],

$$\mu_{\nu_e} < 1.5 \times 10^{-10} \mu_B \quad (90\% \text{ C.L.}), \quad (2.9)$$

$$\mu_{\bar{\nu}_e} < 1.0 \times 10^{-10} \mu_B \quad (90\% \text{ C.L.}). \quad (2.10)$$

- The accelerator-based experiments provided the following limit by using $\nu_{e,\mu,\tau} + e^- \rightarrow \nu_{e,\mu,\tau} + e^-$ scattering which are the same methods above [21, 22, 23],

$$\mu_{\nu_e} < 10.8 \times 10^{-10} \mu_B \quad (90\% \text{ C.L.}), \quad (2.11)$$

$$\mu_{\nu_\mu} < 6.8 \times 10^{-10} \mu_B \quad (90\% \text{ C.L.}), \quad (2.12)$$

$$\mu_{\nu_\tau} < 3.9 \times 10^{-7} \mu_B \quad (90\% \text{ C.L.}). \quad (2.13)$$

- The limits from astrophysics are much more restrictive.

If neutrinos have magnetic moment, the plasmon decay process $\gamma \rightarrow \nu + \bar{\nu}$ could be considered. From this process, the neutrinos take away the energy from the core of stars and slightly reduce the temperature. Then, neutrinos delay the ignition of helium for red giant stars. From the observation of the ratio between after and before the ‘helium flash’ in the globular clusters, an upper limit on the magnetic moment is obtained as follows [24],

$$\mu_\nu < 3 \times 10^{-12} \mu_B. \quad (2.14)$$

2.2 Solar neutrinos

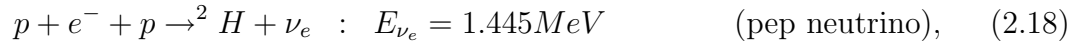
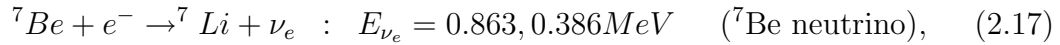
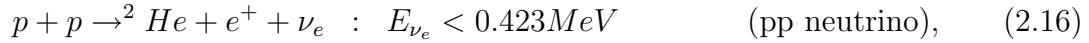
2.2.1 The sun and Standard Solar Model (SSM)

It is widely known that the sun has been generating energy for a long time by nuclear fusion reactions. The sun is a main-sequence star and is now in the stage in which it burns hydrogen stably in its core. 98.5% of the energy is generated by the reactions of the ‘pp-chain’ (proton-proton chain) and a small fraction of the energy is generated by the CNO-cycle (carbon-nitrogen-oxygen cycle) [25]. The overall reaction is written as follows,



This reaction generates 27 MeV of energy. A series of reactions in the pp-chain and CNO cycle are shown in Figure 2.4 and 2.5.

Reactions which generate neutrinos in pp-chain are listed below,



Reactions in the CNO cycle are as follows,



The Standard Solar Models (SSMs) have been improved by several authors, but we will use the solar neutrino fluxes and spectra (except ${}^8\text{B}$ spectrum, which is described in the next section) obtained by BPB2001 [26]. The neutrino energy spectrum produced by each set of reactions is shown in Figure 2.6. And the expected absolute fluxes at 1 AU distance from BPB2001 are summarized in Table 2.1.

The neutrino production points are different for each set of reactions because each rate of nuclear fusion reaction depends on composition of atoms, temperature and gravity. The neutrino production points are supplied by BPB2001 as shown in Figure 2.7. The electron density in the sun is also supplied by BPB2001 as shown in Figure 2.8. This information is important for neutrino propagation in the sun because the matter density along the neutrino trajectory affects neutrino oscillations via the matter effect.

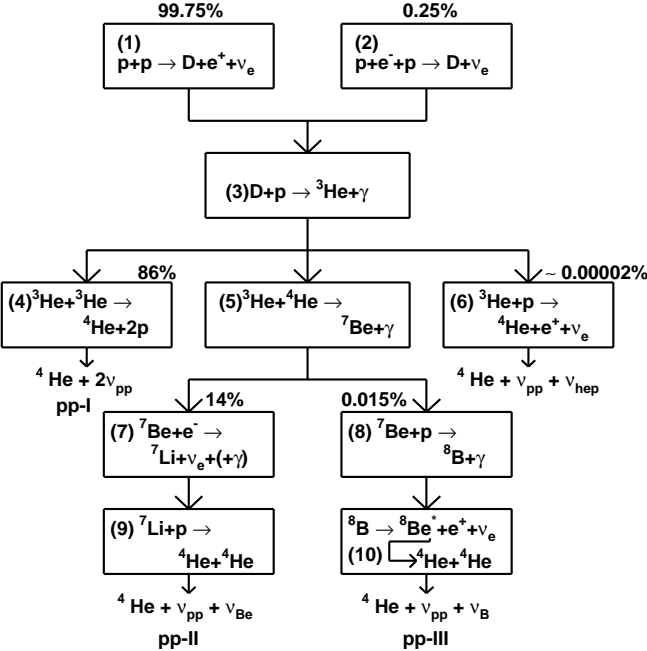


Figure 2.4: The pp-chain

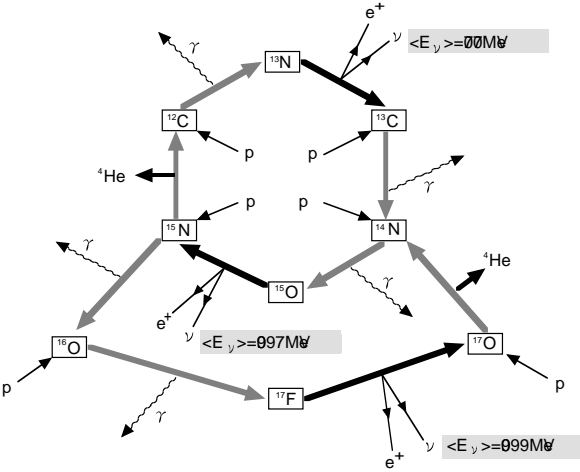


Figure 2.5: The CNO cycle

| source | flux(/cm ² /sec) | error |
|-----------------|-----------------------------|--------------------------|
| pp | 5.95×10^{10} | $1.00^{+0.01}_{-0.01}$ |
| ⁷ Be | 4.77×10^9 | $1.00^{+0.10}_{-0.10}$ |
| pep | 1.40×10^8 | $1.00^{+0.015}_{-0.015}$ |
| ⁸ B | 5.05×10^6 | $1.00^{+0.20}_{-0.16}$ |
| <i>hep</i> | 9.3×10^3 | $1.00^{+?}_{-?}$ |
| ¹³ N | 5.48×10^8 | $1.00^{+0.21}_{-0.17}$ |
| ¹⁵ O | 4.80×10^8 | $1.00^{+0.25}_{-0.19}$ |
| ¹⁷ F | 5.63×10^6 | $1.00^{+0.25}_{-0.25}$ |

Table 2.1: Expected neutrino flux at 1 AU from BPB2001. There is a large uncertainty for *hep* neutrinos, therefore only the central value is given by BPB2001.

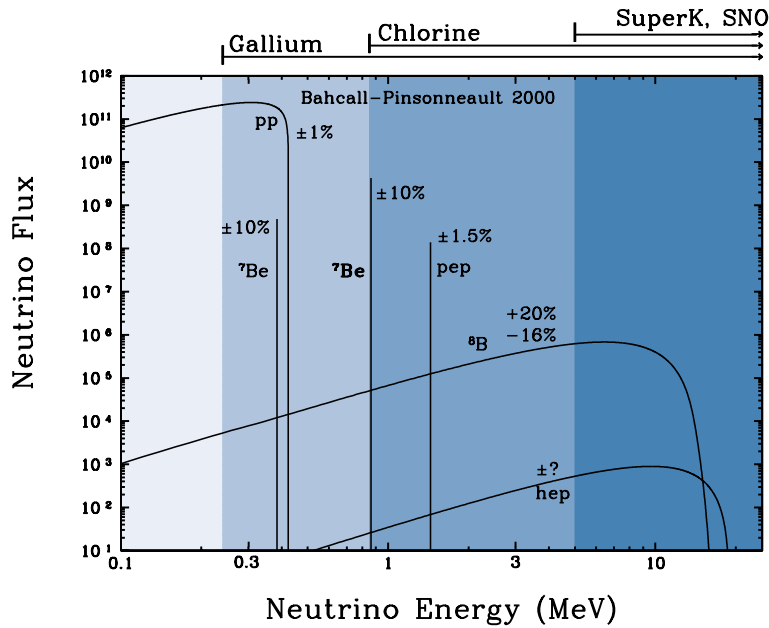


Figure 2.6: Energy spectra of solar neutrinos

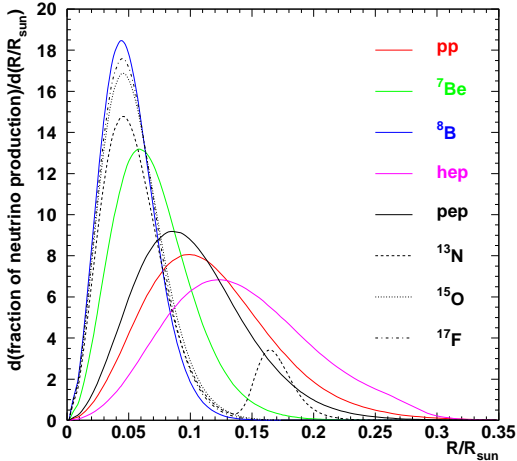


Figure 2.7: Production points of neutrinos as a function of the solar radius

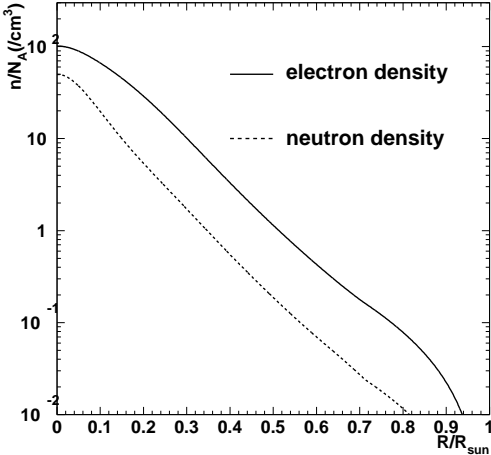


Figure 2.8: Electron and neutron density in the Sun. where N_A the Avogadro constant.

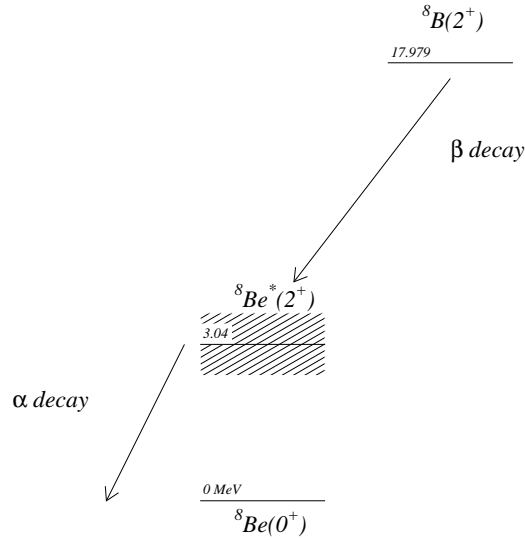


Figure 2.9: Energy levels of decay chains of ${}^8\text{B}(\beta^+){}^8\text{Be}(2\alpha)$

2.2.2 ${}^8\text{B}$ spectrum

The trigger threshold of SK is 3.5 MeV at the end of SK-I and the analysis threshold for solar neutrinos is 5.0 MeV, thus only ${}^8\text{B}$ and *hep* neutrinos are relevant. Although the *hep* neutrino flux has a large uncertainty, more than 99% of solar neutrino events in SK are from ${}^8\text{B}$ neutrinos. Therefore the ${}^8\text{B}$ neutrino spectrum is the primary contribution to the solar neutrino spectrum which SK measures. The ${}^8\text{B}$ neutrinos are generated via the β^+ decay of ${}^8\text{B}$. Its decay diagram is shown in Figure 2.9. The ${}^8\text{Be}^*$ produced by ${}^8\text{B}$ decay is unstable, and decays to 2α immediately. The energy of 2α is broad and affects neutrino energy spectrum. From the measurement of the broad 2α energy spectrum, the ${}^8\text{B}$ energy spectrum was obtained [27]. In this thesis, we use the absolute flux value from BPB2001 but use the ${}^8\text{B}$ spectrum shape from [27].

2.2.3 Results of solar neutrino experiments

Various experiments have measured solar neutrinos after the first observation by Davis and his collaborators [1]. In this section, the measured fluxes by solar neutrino experiments are described.

Homestake

The solar neutrino measurement from the Homestake experiment started in 1967. The detector was built 1500m underground (4100m water equivalent) in the Homestake Gold Mine at Lead, South Dakota, USA. The detector consists of a single horizontal steel tank

| neutrino source | expected rate (SNU) |
|-------------------|---------------------|
| pp | 0.0 |
| ${}^7\text{Be}$ | 1.15 |
| pep | 0.22 |
| ${}^8\text{B}$ | 5.76 |
| <i>hep</i> | 0.04 |
| ${}^{13}\text{N}$ | 0.09 |
| ${}^{15}\text{O}$ | 0.33 |
| ${}^{17}\text{F}$ | 0.0 |
| total | $7.6^{+1.3}_{-1.1}$ |

Table 2.2: Expected solar neutrino event rate at Homestake experiment from the SSM

containing 615 ton of pure liquid C_2Cl_4 . Its detection process is the following neutrino capture reaction,



and the energy threshold is 0.814 MeV. The expected event rate from BPB2001 is $7.6^{+1.3}_{-1.1}$ SNU as shown in Table 2.2, where SNU is the number of interactions / 10^{36} target-atoms/sec. The main contributions are ${}^7\text{Be}$ and ${}^8\text{B}$ neutrinos in this experiment.

The observed flux from this experiment is as follows [28],

$$R_{obs}^{Cl} = 2.56 \pm 0.16(\text{stat.}) \pm 0.16(\text{syst.}) \quad \text{SNU}. \quad (2.25)$$

The ratio of the observed neutrino flux to the SSM prediction is $0.34 \pm 0.021 \pm 0.021$.

Ga experiments (GALLEX/GNO and SAGE)

The gallium experiments use the following neutrino capture reaction,



and the energy threshold is 233 keV. Therefore Ga experiments can detect pp neutrinos.

The GALLEX experiment was started in 1991 and ended 1997, and the GNO experiment resumed in 1998 [29]. The detector is located in the Gran Sasso Underground Laboratory in Italy, and the depth is 3000m water equivalent. The target is 12-ton ${}^{71}\text{Ga}$ in the form of 100-ton GaCl_3 .

The SAGE experiment was started in 1990 [31]. The detector is stored in the Baksan Neutrino Observatory in the Northern Caucasus Mountains (the depth is 4800m water equivalent). The target is 30 tons (\sim July 1991) and 57 tons (August 1991 \sim) of metallic gallium (natural abundance of ${}^{71}\text{Ga}$ is \sim 40%).

| neutrino source | expected rate (SNU) |
|-------------------|---------------------|
| pp | 69.7 |
| ${}^7\text{Be}$ | 34.2 |
| pep | 2.8 |
| ${}^8\text{B}$ | 12.1 |
| <i>hep</i> | 0.1 |
| ${}^{13}\text{N}$ | 3.4 |
| ${}^{15}\text{O}$ | 5.5 |
| ${}^{17}\text{F}$ | 0.1 |
| total | 128^{+9}_{-7} |

Table 2.3: Expected flux at Ga experiments from SSM prediction

The expected flux from BPB2001 is 128^{+9}_{-7} SNU as shown in Table 2.3. The main contributions are pp and ${}^7\text{Be}$ neutrinos in these experiments.

The observed fluxes from Ga experiments are as follows [30, 32],

$$R_{obs}^{GALLEX/GNO} = 69.3 \pm 4.1(\text{stat.}) \pm 3.6(\text{syst.}) \quad \text{SNU} \quad (2.27)$$

$$R_{obs}^{SAGE} = 69.1 \quad {}^{+4.3}_{-4.2}(\text{stat.}) \quad {}^{+3.8}_{-3.4}(\text{syst.}) \quad \text{SNU}. \quad (2.28)$$

And the combined result for Ga experiments is,

$$R_{obs}^{Ga} = 69.2 \quad {}^{+4.0}_{-3.9} \quad (\text{total}) \quad \text{SNU}. \quad (2.29)$$

The ratio of the observed neutrino to the SSM prediction is $0.54 \quad {}^{+0.03}_{-0.03}$ SNU.

SNO

The Sudbury Neutrino Observatory (SNO) is a ring imaging water Cherenkov detector started in 1999. The detector is located 2070 m underground (6100m water equivalent) in the INCO's Creighton mine near Sudbury. For the target of neutrinos, 1000 tons of ultra-pure D_2O is used. The analysis energy threshold is around 5 MeV, therefore ${}^8\text{B}$ and *hep* neutrinos are detected. The detection processes are as follows,

$$\nu_e + d \rightarrow p + p + e^- \quad (\text{CC}) \quad (2.30)$$

$$\nu_x + e^- \rightarrow \nu_x + e^- \quad (\text{ES}) \quad (2.31)$$

$$\nu_x + d \rightarrow p + n + \nu_x \quad (\text{NC}) \quad (2.32)$$

SNO can statistically separate these three processes from their characteristic angular distributions and energy spectra. Fusion reactions in the sun generate only ν_e 's, and any excess of NC (or ES) over CC fluxes provides direct evidence for the flavor transformation of ν_e . Especially the neutral current reaction is equally sensitive to all types

of neutrinos, so SNO planned three steps of observations, pure-D₂O phase, salt-phase (using $n + {}^{35}\text{Cl} \rightarrow {}^{36}\text{Cl} + \gamma(8.6\text{MeV})$), and ${}^3\text{He}$ proportional counter phase in order to detect the neutral current events. The latest results are salt phase results with kinetic energy threshold 5.5 MeV. The obtained flux for each reaction type are as follows ($10^6/\text{cm}^2/\text{sec.}$) [33],

$$\phi_{CC}^{SNO} = 1.59_{-0.07}^{+0.08}(\text{stat.})_{-0.08}^{+0.06}(\text{syst.}) \quad (\text{CC}) \quad (2.33)$$

$$\phi_{ES}^{SNO} = 2.21_{-0.26}^{+0.31}(\text{stat.}) \pm 0.10(\text{syst.}) \quad (\text{ES}) \quad (2.34)$$

$$\phi_{NC}^{SNO} = 5.21 \pm 0.27(\text{stat.}) \pm 0.38(\text{syst.}) \quad (\text{NC}) \quad (2.35)$$

The ratio of the observed neutrino fluxes to the SSM predictions (${}^8\text{B}$ neutrino: $5.05 \times 10^6 / \text{cm}^2/\text{sec.}$) are as follows,

$$\phi_{CC}^{SNO} / \phi_{sB}^{SSM} = 0.315_{-0.014}^{+0.016}(\text{stat.})_{-0.016}^{+0.012}(\text{syst.}) \quad (\text{CC}) \quad (2.36)$$

$$\phi_{ES}^{SNO} / \phi_{sB}^{SSM} = 0.438_{-0.051}^{+0.061}(\text{stat.}) \pm 0.020(\text{syst.}) \quad (\text{ES}) \quad (2.37)$$

$$\phi_{NC}^{SNO} / \phi_{sB}^{SSM} = 1.03 \pm 0.053(\text{stat.}) \pm 0.075(\text{syst.}) \quad (\text{NC}) \quad (2.38)$$

The SNO result is the strongest evidence for the neutrino flavor conversion to the active neutrinos from electron neutrinos. And from the agreement between the observed NC flux and the SSM prediction, the solar neutrino problem as a astrophysical problem is solved.

Time variation of solar neutrino flux and correlation to the sunspot number

The Homestake experiment reported the anti-correlation between the neutrino flux and the sunspot numbers [34] as shown in Figure 2.10. The sunspot number has the time variation of 11 years periodicity. This argument implies a possibility of neutrino conversion with its neutrino magnetic moment. Because sunspots are the cross sections of strong magnetic fluxes and larger number of sunspots correspond to larger magnetic fields in the sun, the possibility of a spin precession solution from neutrino magnetic moment for the time variation and solar neutrino problem was proposed by several authors [35, 36]. However the Kamiokande 2079 days data, didn't show the correlation to the sunspot number within the errors [39].

Other possible time variations from neutrino magnetic moment are related to the revolution of the earth around the sun and an apparent rotation cycle of the sun, 27.3 days. The inclination of the earth's orbit relative to the solar equator by 7.25 degrees may cause half year modulation of the neutrino flux due to a gradient of the magnetic fields antisymmetric around the equator. This half year variation was also claimed in the chlorine data. Some authors claim that they found the 13.75 days periodicity (about a half of 27.3 days) at 98.9% C.L. and 99.9% C.L. [48, 49] by using SK 10 day bin's data [50]. From the SK collaboration's analysis by using correct time of each bins, and

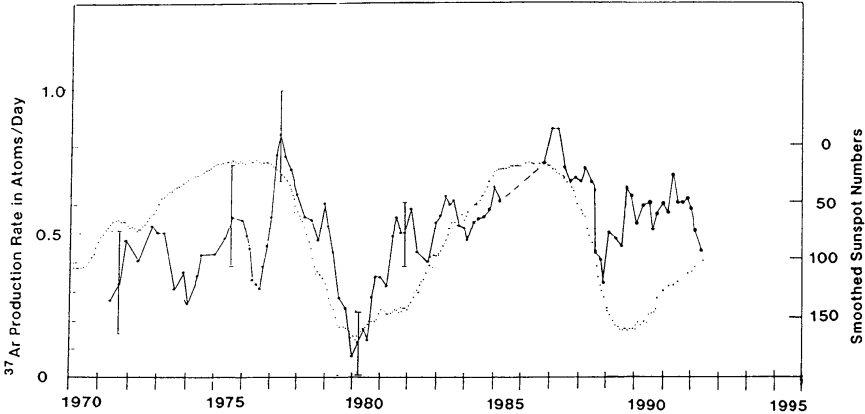


Figure 2.10: Time variation of ³⁷Ar production rate (solid line) and sunspot number (dotted line). The sunspot number is plotted inversely.

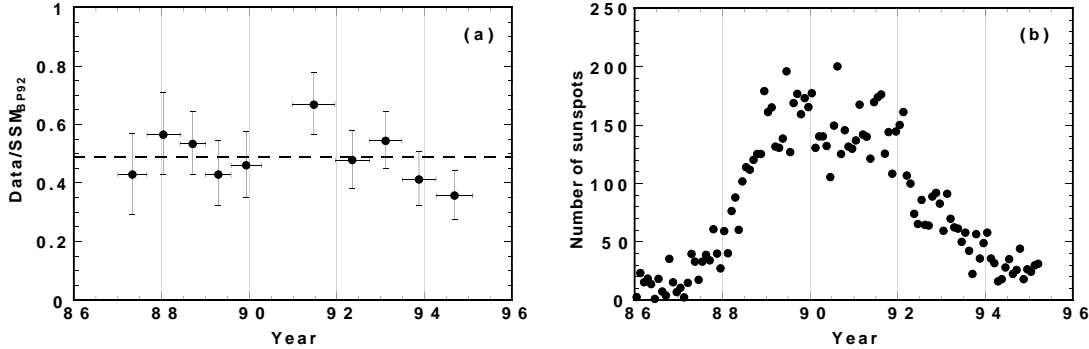


Figure 2.11: The time variation of the observed solar neutrino flux in Kamiokande during the solar cycle 22.

5 day bin's data, smaller confidence levels 81.70% and 63.09% are claimed [51]. And the SK statement is that there are no significant periodic variations. The time variation is disfavored by Kamiokande data, however, the magnetic moment solution for the solar neutrino problem has still been discussed [40]. And from the result of a search for $\bar{\nu}_e$ from the sun, some authors tried to set the limit on the neutrino magnetic moment.

In this section, the standard solar model and solar neutrino results are reviewed. The solar neutrino deficits are explained by flavor conversion. However the mechanism of this conversion is not clear yet. In the next section, possible solutions for this conversion, neutrino oscillations and spin flavor precession with the magnetic field are described.

2.3 Neutrino oscillation and Resonant Spin Flavor Precession (RSFP)

In this section, two types of flavor conversion mechanism, neutrino oscillations and spin conversions are described.

2.3.1 Vacuum oscillation

In the standard model, each charged lepton is paired with a neutrino and classified into generations. These generations are called flavor eigenstates. When the neutrinos have finite mass, the neutrinos have mass eigenstates ($|\nu_i\rangle$ ($i = 1, 2, 3$)) and these are not necessarily the same as the flavor eigenstates ($|\nu_x\rangle$ ($x = e, \mu, \tau$)). If the two eigenstates are not the same, these are connected by the mixing matrix U like the Kobayashi-Maskawa matrix in the quark sector,

$$|\nu_x\rangle = \sum_{i=1}^3 U_{xi} |\nu_i\rangle \quad (x = e, \mu, \tau). \quad (2.39)$$

In order to simplify the discussion, we will assume only two flavor oscillation $\nu_e \rightarrow \nu_x$. Then equation 2.39 is written as follows,

$$\begin{pmatrix} \nu_e \\ \nu_x \end{pmatrix} = \begin{pmatrix} \cos \theta & \sin \theta \\ -\sin \theta & \cos \theta \end{pmatrix} \begin{pmatrix} \nu_1 \\ \nu_2 \end{pmatrix}, \quad (2.40)$$

where θ is the mixing angle in vacuum. The propagation of the mass eigenstates of neutrinos in time is determined as,

$$i \frac{d}{dt} \begin{pmatrix} \nu_1(t) \\ \nu_2(t) \end{pmatrix} = \begin{pmatrix} E_1 & 0 \\ 0 & E_2 \end{pmatrix} \begin{pmatrix} \nu_1 \\ \nu_2 \end{pmatrix}. \quad (2.41)$$

where $E_{1,2}$ is the energy of $\nu_{1,2}$. From this equation 2.41, the wave function is written as follows,

$$\begin{pmatrix} \nu_1(t) \\ \nu_2(t) \end{pmatrix} = \begin{pmatrix} e^{-iE_1 t} & 0 \\ 0 & e^{-iE_2 t} \end{pmatrix} \begin{pmatrix} \nu_1(0) \\ \nu_2(0) \end{pmatrix}. \quad (2.42)$$

If ν_e is produced at $t=0$, the flavor survival probability $\nu_e \rightarrow \nu_e$ is,

$$\begin{aligned} P(\nu_e \rightarrow \nu_e) &= |\langle \nu_e(0) | \nu_e(t) \rangle|^2 \\ &= \left| (1, 0) \begin{pmatrix} \cos \theta & \sin \theta \\ -\sin \theta & \cos \theta \end{pmatrix} \begin{pmatrix} e^{-iE_1 t} & 0 \\ 0 & e^{-iE_2 t} \end{pmatrix} \begin{pmatrix} \cos \theta & -\sin \theta \\ \sin \theta & \cos \theta \end{pmatrix} \begin{pmatrix} 1 \\ 0 \end{pmatrix} \right|^2 \\ &= |e^{-iE_1 t} \cos^2 \theta + e^{-iE_2 t} \sin^2 \theta|^2. \end{aligned} \quad (2.43)$$

In the solar neutrino case, the neutrino energy is much larger than its mass, $E \gg m$. Therefore we can use the following approximation,

$$E_i = \sqrt{p^2 + m_i^2} \simeq p + \frac{m_i^2}{2p} (i = 1, 2), \simeq E + \frac{m_i^2}{2E} (i = 1, 2), \quad (2.44)$$

Therefore equation 2.43 becomes,

$$\begin{aligned} P(\nu_e \rightarrow \nu_e; L) &= 1 - \sin^2 2\theta \sin^2 \frac{m_1^2 - m_2^2}{4E} t \\ &= 1 - \sin^2 2\theta \sin^2 \left(1.27 \frac{\Delta m^2 (\text{eV}^2) L (m)}{E (\text{MeV})} \right), \end{aligned} \quad (2.45)$$

where $\Delta m^2 \equiv m_2^2 - m_1^2$, L is the distance traveled at the time t .

2.3.2 Neutrino oscillation in matter (MSW effect)

When neutrinos propagate through matter, they acquire the additional potential energy caused by interaction with matter. Especially, when we consider the ν_e and $\nu_x (x \neq e)$, both neutrinos can exchange a Z^0 boson with electrons but only the ν_e can exchange a W^\pm boson. The effect causes the different potential between ν_e and ν_x . This effect was pointed out by Wolfenstein [44] and was extended to the varying density of the sun by Mikheyev and Smirnov [45]. This resonant oscillation in matter is called the MSW effect. The propagation equation in matter is written as follows,

$$i \frac{d}{dt} \begin{pmatrix} \nu_e(t) \\ \nu_x(t) \end{pmatrix} = \left[U \begin{pmatrix} e^{-iE_1 t} & 0 \\ 0 & e^{-iE_2 t} \end{pmatrix} U^{-1} + \begin{pmatrix} V_e & 0 \\ 0 & 0 \end{pmatrix} \right] \begin{pmatrix} \nu_e(t) \\ \nu_x(t) \end{pmatrix}, \quad (2.46)$$

where V_e is an additional potential energy,

$$V_e = \sqrt{2} G_F N_e, \quad (2.47)$$

where G_F is the Fermi coupling constant, N_e is the electron number density. When we omit a common diagonal phase factor, equation 2.46 is written as follows,

$$i \frac{d}{dt} \begin{pmatrix} \nu_e(t) \\ \nu_x(t) \end{pmatrix} = \begin{pmatrix} -\frac{\Delta m^2}{4E} \cos 2\theta + V_e & \frac{\Delta m^2}{4E} \sin 2\theta \\ \frac{\Delta m^2}{4E} \sin 2\theta & \frac{\Delta m^2}{4E} \cos 2\theta \end{pmatrix} \begin{pmatrix} \nu_e(t) \\ \nu_x(t) \end{pmatrix}. \quad (2.48)$$

Here, assuming constant electron density, the above matrix in matter which is analogous to vacuum oscillations is written as follows,

$$\begin{pmatrix} \nu_e^m \\ \nu_x^m \end{pmatrix} = \begin{pmatrix} \cos \theta_m & \sin \theta_m \\ -\sin \theta_m & \cos \theta_m \end{pmatrix} \begin{pmatrix} \nu_1^m \\ \nu_2^m \end{pmatrix}, \quad (2.49)$$

where ν_1^m, ν_2^m are the effective mass eigenstates of neutrinos in matter and θ_m is the effective mixing angle which is as follows,

$$\tan 2\theta_m = \frac{\sin 2\theta \frac{\Delta m^2}{2E}}{\cos 2\theta \frac{\Delta m^2}{2E} - V_e}. \quad (2.50)$$

From the above equation, in the following case,

$$N_e^{resonance} = \frac{\Delta m^2}{2\sqrt{2}G_F E} \cos(2\theta), \quad (2.51)$$

neutrino mixing in matter(θ_m) can be enhanced. The relation between the electron number density and the mixing angle in matter is shown in Table 2.4.

| | | | | | |
|------------|----------|-----|-------------------|-----|----------|
| N_e | 0 | ... | $N_e^{resonance}$ | ... | ∞ |
| θ_m | θ | ... | $\pi/4$ | ... | $\pi/2$ |

Table 2.4: The relation between the electron density and the mixing angle in matter

2.3.3 The neutrino oscillation solution for solar neutrino problem and KamLAND result

By using the data from all solar neutrino measurements, global analyses under the two neutrino oscillation hypothesis have been done by various authors. An example of the allowed Δm^2 and $\tan^2(\theta)$ oscillation parameter region is shown in Figure 2.12. Only the LMA region is favored at the 95% C.L. in these analyses.

A terrestrial experiment was also performed to verify the LMA solution using artificial neutrinos. KamLAND is a long baseline reactor neutrino experiment. The target consists of 1000 ton of liquid scintillator and the detector is placed in the Kamioka mine in Gifu

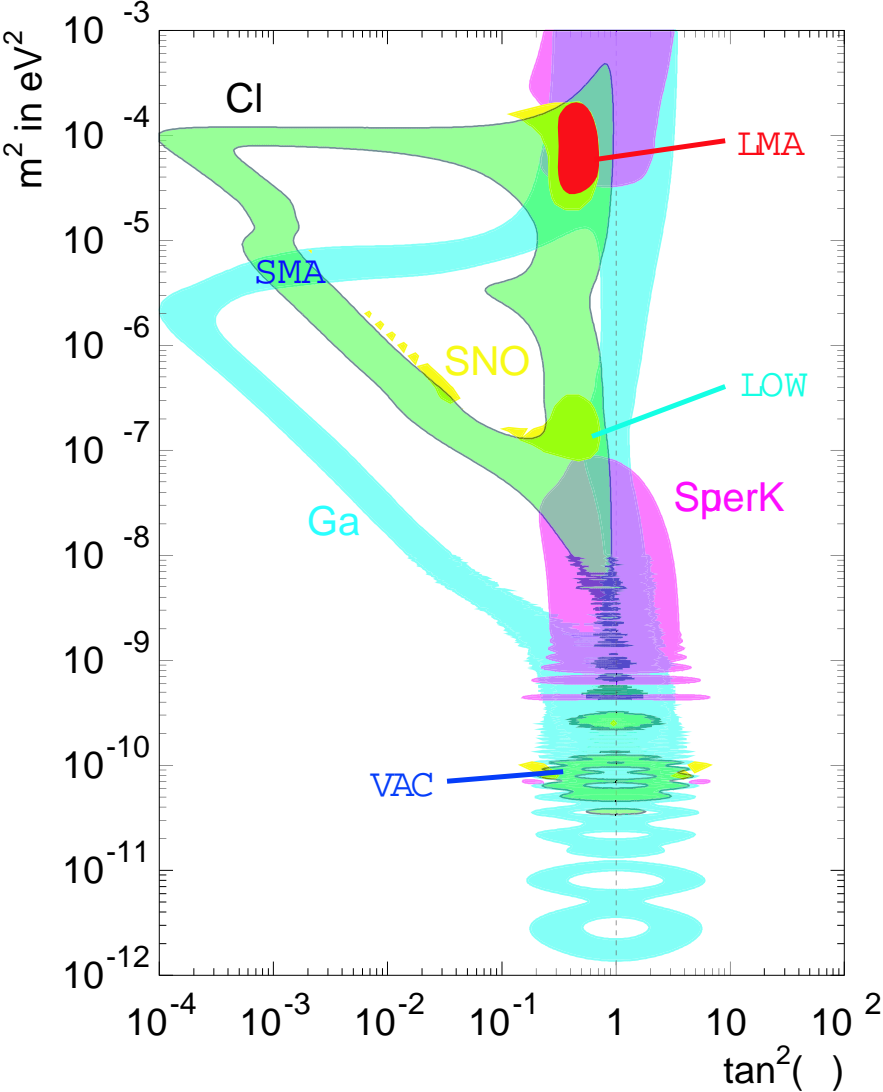


Figure 2.12: The allowed region for neutrino oscillation parameters by solar neutrino measurements [46]

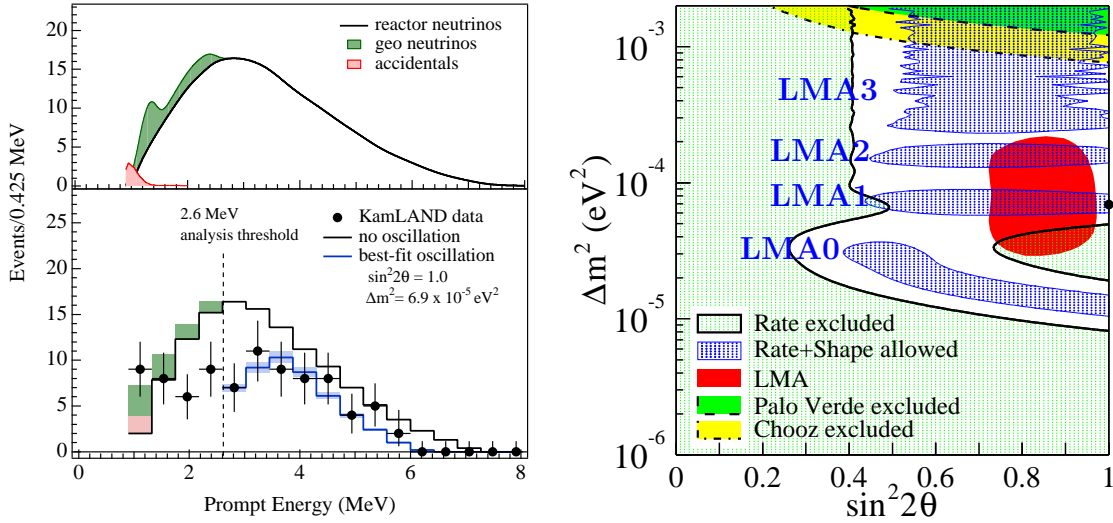


Figure 2.13: KamLAND energy spectrum and allowed region

prefecture, Japan. The neutrino sources are nuclear power reactors and the typical distance from the detector is 180 km. The detection process is the following successive reactions,

$$\bar{\nu}_e + p \rightarrow e^+ + n \quad (2.52)$$

$$n + p \rightarrow d + \gamma(2.2 \text{ MeV}). \quad (2.53)$$

In order to identify the $\bar{\nu}_e$ events, the time correlation between the prompt event (equation 2.52) and the delayed coincidence event (equation 2.53) with a lifetime $\sim 210 \mu$ seconds.

In 2002, KamLAND collaboration released the first data using 145.1 live days, and they reported the evidence for reactor $\bar{\nu}_e$ disappearance [4]. The ratio of the number of observed events to the expected is as follows,

$$\frac{N_{\text{observed}}}{N_{\text{expected}}} = 0.611 \pm 0.085(\text{stat}) \pm 0.041(\text{syst.}), \quad (2.54)$$

and the energy spectrum is shown at the left panel in Figure 2.13. If deficit is caused by a oscillation, the oscillation parameter is favored at the LMA region as shown in right panel of Figure 2.13, and all the other parameter regions are disfavored. This good agreement favors the neutrino oscillation as a solution for the solar neutrino problem. However subdominant flavor conversion is not still ruled out. In the next section, another possible flavor conversion, Spin Flavor Precession is described.

2.3.4 RSFP+MSW model

As described in the previous section, the solution for the solar neutrino problem should be an oscillation with matter effect, or dominant process is MSW effect. In 1988, another possibility was proposed [37, 38]. If neutrinos have magnetic moment, it can causes a resonant transition of neutrino helicity like MSW effect in matter. This effect is called Resonant Spin Flavor Precession (RSFP). This effect still can be a subdominant process of the solar neutrino deficit.

A simple propagation function in magnetic field is written as follows,

$$i \frac{d}{dt} \begin{pmatrix} \nu_L \\ \nu_R \end{pmatrix} = \begin{pmatrix} 0 & \mu B \\ \mu B & 0 \end{pmatrix} \begin{pmatrix} \nu_L \\ \nu_R \end{pmatrix}, \quad (2.55)$$

where μ is neutrino magnetic moment and B is magnetic field.

In matter, we have to consider the effective potential for each neutrinos. For the left-handed electron neutrino (ν_{eL}) case, the effective potential is the same as MSW case,

$$\begin{aligned} V_{\nu_e} &= V(\nu_e e \rightarrow \nu_e e)N_e + V(\nu_e p \rightarrow \nu_e p)N_p + V(\nu_e n \rightarrow \nu_e n)N_n \\ &= \frac{G_F}{\sqrt{2}}(1 + 4 \sin^2 \theta_W)N_e + \frac{G_F}{\sqrt{2}}(1 - 4 \sin^2 \theta_W)N_p - \frac{G_F}{\sqrt{2}}N_n \\ &= \frac{G_F}{\sqrt{2}}(2N_e - N_n), \end{aligned} \quad (2.56)$$

where θ_W is the Weinberg angle, G_F is the Fermi coupling constant, N_e, N_n, N_p is the number density for electron, neutron and proton, respectively. In the equation, we used $N_e = N_p$. For $\nu_x (x \neq e)$, effective potential is,

$$V_{\nu_x} = -\frac{G_F}{2}N_n, \quad (2.57)$$

and for right-handed Dirac neutrinos, $V_{\bar{\nu}} = 0$. On the other hand, Majorana neutrino case, $\nu_R = \bar{\nu}_L$. Therefore effective potentials are follows,

$$V_{\bar{\nu}_e} = -\frac{G_F}{\sqrt{2}}(2N_e - N_n), \quad (2.58)$$

$$V_{\bar{\nu}_x} = \frac{G_F}{\sqrt{2}}N_n. \quad (2.59)$$

Considering the effective potential above, the propagation function in matter for Dirac neutrinos is as follows,

$$i \frac{d}{dt} \begin{pmatrix} \nu_{eL} \\ \nu_{xL} \\ \bar{\nu}_{eR} \\ \bar{\nu}_{xR} \end{pmatrix} = \begin{pmatrix} \frac{G_F}{\sqrt{2}}(2N_e - N_n) & \frac{\Delta m^2}{4E} \sin 2\theta & \mu_{ee} & \mu_{ex}B \\ \frac{\Delta m^2}{4E} \sin 2\theta & -\frac{G_F}{\sqrt{2}}N_n + \frac{\Delta m^2}{2E} \cos 2\theta & \mu_{xe}B & \mu_{xx}B \\ \mu_{ee} & \mu_{ex}B & 0 & 0 \\ \mu_{xe}B & \mu_{xx} & 0 & \frac{\Delta m^2}{2E} \cos 2\theta \end{pmatrix} \begin{pmatrix} \nu_{eL} \\ \nu_{xL} \\ \bar{\nu}_{eR} \\ \bar{\nu}_{xR} \end{pmatrix}, \quad (2.60)$$

and for Majorana case, the propagation function is written as follows,

$$i \frac{d}{dt} \begin{pmatrix} \nu_e \\ \nu_x \\ \bar{\nu}_e \\ \bar{\nu}_x \end{pmatrix} = \begin{pmatrix} \frac{G_F}{\sqrt{2}}(2N_e - N_n) & \frac{\Delta m^2}{4E} \sin 2\theta & 0 & \mu B \\ \frac{\Delta m^2}{4E} \sin 2\theta & -\frac{G_F}{\sqrt{2}}N_n + \frac{\Delta m^2}{2E} \cos 2\theta & -\mu B & 0 \\ 0 & -\mu B & -\frac{G_F}{\sqrt{2}}(2N_e - N_n) & \frac{\Delta m^2}{4E} \sin 2\theta \\ \mu B & 0 & \frac{\Delta m^2}{4E} \sin 2\theta & \frac{G_F}{\sqrt{2}}N_n + \frac{\Delta m^2}{2E} \cos 2\theta \end{pmatrix} \begin{pmatrix} \nu_e \\ \nu_x \\ \bar{\nu}_e \\ \bar{\nu}_x \end{pmatrix}. \quad (2.61)$$

In the Majorana case, we should note that we can expect the solar $\bar{\nu}_e$ creation. The possible processes of $\bar{\nu}_e$ creation in the sun is as follows,

$$\nu_e \xrightarrow{\text{MSW}} \nu_\mu \xrightarrow{\text{RSFP}} \bar{\nu}_e, \quad (2.62)$$

$$\nu_e \xrightarrow{\text{RSFP}} \bar{\nu}_\mu \xrightarrow{\text{MSW}} \bar{\nu}_e. \quad (2.63)$$

If these conversions happen, Super-Kamiokande may be able to detect the solar $\bar{\nu}_e$. The current best upper limit of the solar $\bar{\nu}_e$ search is set by KamLAND experiment as follows [47],

$$\Phi_{\bar{\nu}_e} / \Phi_{SSM\nu_e} = 0.028\% \text{ (90\% C.L.)}. \quad (2.64)$$

In this thesis, we present the result of a $\bar{\nu}_e$ search in SK and study on the neutrino magnetic moment also considering effects of anti-neutrinos on elastic scattering events, and finally perform a global analysis under the RSFP+MSW hypothesis.

Chapter 3

The Super-Kamiokande Detector

3.1 Overview of the Super-Kamiokande detector

The Super-Kamiokande detector [52] is the world's largest water Cherenkov imaging detector and is located in the Kamioka mine in Gifu prefecture, Japan. Its geographic coordinates are $36^{\circ}25'32.6''\text{N}$, $137^{\circ}18'37.1''\text{E}$ (WGS-84, indicated by a black dot in Figure 3.1) and the detector lies 1000 m underground from the peak of Mt.Ikenoyama. The average rock overburden is 2,700 meters water equivalent (m.w.e.). The location was chosen for the following reasons.

- The Kamioka mine is one of the deepest mines in Japan. This depth can reduce the cosmic-ray muon flux to a non-obstructive level. Figure 3.1 shows the muon flux as a function of depth for past and current underground experiments. The muon flux at Super-Kamiokande is about 5 orders of magnitude smaller than that of ground level.
- A sufficient amount of clean natural water can be used.
- The rock is hard and stable enough for excavation of a large cavity.
- The temperature is stable($\sim 13^{\circ}\text{C}$).

These conditions enable high-statistics neutrino observation and low-background searches for nucleon decay.

This chapter describes the detection principle and the details of the Super-Kamiokande detector.



Figure 3.1: Location of Super-Kamiokande in Japan

3.2 Neutrino interaction of neutrinos in Super-Kamiokande

3.2.1 Dominant neutrino interactions in the energy region of solar neutrinos

The Super-Kamiokande detector holds 22.5 ktons of water in the fiducial volume, so the number of target particles are as follows ;

$$\begin{aligned}
 \text{electrons} & : 7.5 \times 10^{33} \\
 \text{free protons} & : 1.5 \times 10^{33} \\
 \text{oxygen nuclei} & : 7.5 \times 10^{32}
 \end{aligned}$$

In the energy region of solar neutrinos (below 20 MeV), neutrinos are detected through following processes ;

$$\nu_e + e^- \rightarrow \nu_e + e^- \quad (3.1)$$

$$\bar{\nu}_e + e^- \rightarrow \bar{\nu}_e + e^- \quad (3.2)$$

$$\nu_x + e^- \rightarrow \nu_x + e^- \quad (x = \mu, \tau) \quad (3.3)$$

$$\bar{\nu}_x + e^- \rightarrow \bar{\nu}_x + e^- \quad (x = \mu, \tau) \quad (3.4)$$

$$\bar{\nu}_e + p \rightarrow e^+ + n \quad (3.5)$$

$$\nu_e + {}^{18}\text{O} \rightarrow e^- + {}^{18}\text{F} \quad (3.6)$$

Equations 3.1 and 3.2 represent both charged and neutral current interactions, while equations 3.3 and 3.4 only occur via neutral current interactions and equations 3.5 and

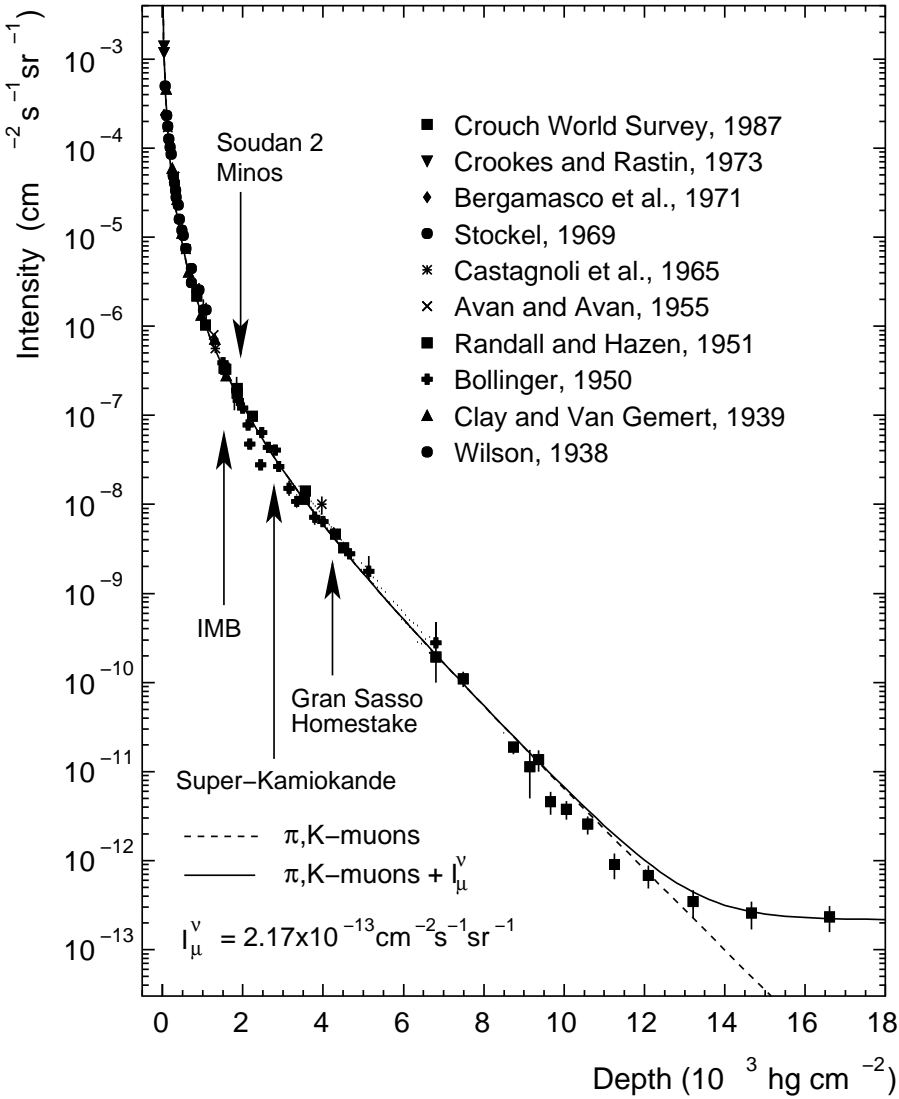


Figure 3.2: Cosmic ray muon flux

3.6 represent only charged current processes. Interactions with ^{16}O nuclei are negligible because the energies of the neutrinos are too low to excite the oxygen nucleus to make an observable signal [53].

3.2.2 Neutrino-electron elastic scattering

The differential cross-section including the radiative corrections of $\nu_{e,\mu}$ -e elastic scattering is given by [54] ;

$$\begin{aligned} \frac{d\sigma}{dT} = \frac{2G_F^2 m}{\pi} \quad \{ & g_L^2(T) \left[1 + \frac{\alpha}{\pi} f_-(Z) \right] \\ & + g_R^2(T) (1-z)^2 \left[1 + \frac{\alpha}{\pi} f_+(Z) \right] \\ & - g_R(T) g_L(T) \frac{m}{q} z \left[1 + \frac{\alpha}{\pi} f_{+-}(Z) \right] \}, \end{aligned} \quad (3.7)$$

where σ is the cross section, T the kinetic energy of the recoil electron, G_F ($=1.16639 \times 10^{-11} \text{ MeV}^{-2}$) the Fermi coupling constant, m the electron mass, α the fine structure constant, q the incident neutrino energy and z is T/q .

For ν_e , g_L and g_R in equation 3.7 are as follows ;

$$g_L^{(\nu_e,e)}(T) = \rho_{NC}^{(\nu,l)} \left[\frac{1}{2} - \hat{\kappa}^{(\nu_e,e)}(T) \sin^2 \hat{\theta}_W(m_Z) \right] - 1, \quad (3.8)$$

$$g_R^{(\nu_e,e)}(T) = -\rho_{NC}^{(\nu,l)} \hat{\kappa}^{(\nu_e,e)}(T) \sin^2 \hat{\theta}_W(m_Z), \quad (3.9)$$

where $\hat{\theta}_W(m_Z)$ ($\sin^2 \hat{\theta}_W(m_Z) = 0.2317$) is the Weinberg angle, $\rho_{NC}^{(\nu,l)} = 1.0126 \pm 0.0016$, and the function $\hat{\kappa}^{(\nu_e,e)}(T)$ is as follows :

$$\hat{\kappa}^{(\nu_e,e)}(T) = 0.9791 + 0.0097I(T) \pm 0.0025, \quad (3.10)$$

where

$$I(T) \equiv \frac{1}{6} \left\{ \frac{1}{3} + (3-x^2) \left[\frac{1}{2} x \ln \left(\frac{x+1}{x-1} \right) - 1 \right] \right\}, \quad (3.11)$$

and $x = \sqrt{1 + 2m/T}$.

For ν_μ ,

$$g_L^{(\nu_\mu,e)}(T) = \rho_{NC}^{(\nu,l)} \left[\frac{1}{2} - \hat{\kappa}^{(\nu_\mu,e)}(T) \sin^2 \hat{\theta}_W(m_Z) \right], \quad (3.12)$$

$$(3.13)$$

and

$$g_R^{(\nu_\mu,e)}(T) = -\rho_{NC}^{(\nu,l)} \hat{\kappa}^{(\nu_\mu,e)}(T) \sin^2 \hat{\theta}_W(m_Z). \quad (3.14)$$

Here,

$$\hat{\kappa}^{(\nu_e, e)}(T) = 0.9970 + 0.00037I(T) \pm 0.0025, \quad (3.15)$$

and $\rho_{NC}^{(\nu, l)}$ is the same as above. The functions $f_+(Z), f_-(Z), f_{+-}(Z)$ are QED effects and they are as follows,

$$\begin{aligned} f_-(Z) &= \left[\frac{E}{l} \ln \left(\frac{E+l}{m} \right) - 1 \right] \left[2 \ln \left(1 - z - \frac{m}{E+l} \right) - \ln(1-z) - \frac{1}{2} \ln z - \frac{5}{12} \right] \\ &+ \frac{1}{2} [L(x) - L(\beta)] - \frac{1}{2} \ln^2(1-z) - \left(\frac{11}{12} + \frac{z}{2} \right) \ln(1-z) \\ &+ z \left[\ln z + \frac{1}{2} \ln \left(\frac{2q}{m} \right) \right] - \left(\frac{31}{18} + \frac{1}{12} \ln z \right) \beta - \frac{11}{22} z + \frac{z^2}{24}, \end{aligned} \quad (3.16)$$

where $L(x)$ is the Spence function, $\int_0^x \ln |1-t| (dt/t)$, and $\beta = l/E$,

$$\begin{aligned} (1-z)^2 f_+(Z) &= \left[\frac{E}{l} \ln \left(\frac{E+l}{m} \right) - 1 \right] \\ &\left\{ (1-z)^2 \left[2 \ln \left(1 - z - \frac{m}{E+l} \right) - \ln(1-z) - \frac{\ln z}{2} - \frac{2}{3} \right] - \frac{z^2 \ln z + 1 - z}{2} \right\} \\ &- \frac{(1-z)^2}{2} \{ \ln^2(1-z) + \beta [L(1-z) - \ln z \ln(1-z)] \} \\ &+ \ln(1-z) \left[\frac{z^2}{2} \ln z + \frac{1-z}{3} \left(2z - \frac{1}{2} \right) \right] - \frac{z^2}{2} L(1-z) - \frac{z(1-2z)}{3} \ln z \\ &- \frac{z(1-z)}{6} - \frac{\beta}{12} \left[\ln z + (1-z) \left(\frac{115-109z}{6} \right) \right], \end{aligned} \quad (3.17)$$

$$f_{+-}(Z) = \left[\frac{E}{l} \ln \left(\frac{E+l}{m} \right) - 1 \right] 2 \ln \left(1 - z - \frac{m}{E+l} \right). \quad (3.18)$$

A detailed description is shown in [54].

The differential cross section of the $\bar{\nu}_{e,\mu}$ -e elastic scattering is given as follows [55] :

$$\frac{d\sigma}{dy} = \frac{2G_F^2 m}{\pi} \left\{ g_L^2 + g_R^2 (1-y)^2 + g_L g_R m_e \frac{y}{E_\nu} \right\}, \quad (3.19)$$

here $y = \frac{T}{E_\nu}$. For $\bar{\nu}_e$,

$$g_L = \sin^2 \theta_W, \quad (3.20)$$

and,

$$g_R = \sin^2 \theta_W + \frac{1}{2}. \quad (3.21)$$

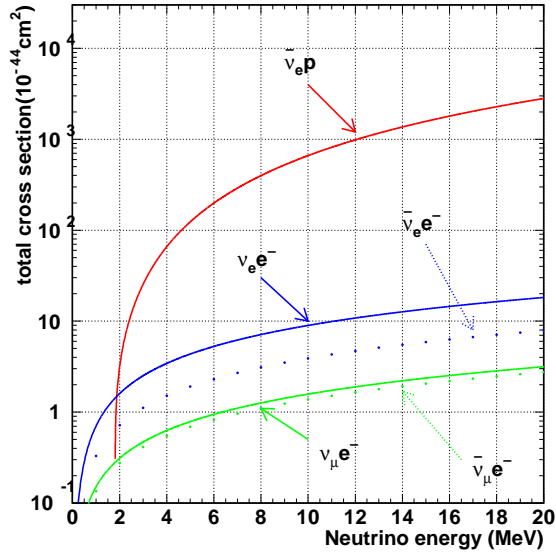


Figure 3.3: The total cross-section as a function of neutrino energy

For $\bar{\nu}_\mu$,

$$g_L = \sin^2 \theta_W, \quad (3.22)$$

and

$$g_R = \sin^2 \theta_W - \frac{1}{2}. \quad (3.23)$$

The total cross-sections as a function of neutrino energy are shown in Figure 3.3.

The scattering angle of the electron from the incident neutrino direction, θ , is kinetically determined as follows ;

$$\cos \theta = \frac{1 + m_e/E_\nu}{\sqrt{1 + 2m_e/Te}}. \quad (3.24)$$

Hence, the recoil electron keeps the information of the direction of the incident neutrino. The angular resolution which is limited by multiple scattering of the electron is about 26° for an electron energy of 10 MeV.

3.2.3 Inverse beta decay process for $\bar{\nu}_e$ detection

In SK, the dominant process of $\bar{\nu}_e$ interactions is the inverse beta-decay process because the total cross-section of $\bar{\nu}_e p$ is about 2 orders of magnitude greater than that of $\nu_e e$ elastic

scattering at 10 MeV, and the interaction rate is 20 times larger when the number of targets in water is taken into account.

The differential cross section of the $\bar{\nu}_e + p \rightarrow e^+ + n$ process is as follows [56] :

$$\left(\frac{d\sigma(E_{\bar{\nu}_e})}{d\cos\theta} \right)^{(1)} = \frac{\sigma_0}{2} [(f^2 + 3g^2) + (f^2 - g^2)v_e^{(1)} \cos\theta] E_e^{(1)} p_e^{(1)} - \frac{\sigma_0}{2} \left[\frac{\Gamma}{M} \right] E_e^{(0)} p_e^{(0)} \quad (3.25)$$

here, the positron energy to 1st order in $O(1/M)$ $E_e^{(1)}$ and 0th order $E_e^{(0)}$ are as follows :

$$E_e^{(1)} = E_e^{(0)} \left[1 - \frac{E_{\bar{\nu}_e}}{M} (1 - v_e^{(0)} \cos\theta) \right] \frac{y^2}{M} \quad (3.26)$$

$$E_e^{(0)} = E_{\bar{\nu}_e} - \Delta (\Delta = M_n - M_p) \quad (3.27)$$

$$\text{and,} \quad (3.28)$$

$$y^2 = \frac{\Delta^2 - m_e^2}{2} \quad (3.29)$$

$$p_e^{(i)} = \sqrt{(E_e^{(i)})^2 - m_e^2} (i = 0, 1) \quad (3.30)$$

$$v_e^{(i)} = p_e^{(i)} / E_e^{(i)} (i = 0, 1) \quad (3.31)$$

$$f = 1.0 (\text{vector coupling constant}) \quad (3.32)$$

$$g = 1.26 (\text{axial-vector coupling constant}) \quad (3.33)$$

$$\sigma_0 = \frac{G_F^2 \cos^2 \theta_c}{\pi} (1 + \delta_{inner}^{rad}) \quad (3.34)$$

$$\begin{aligned} \Gamma &= 2(f + f_2)g \left[(2E_e^{(0)} + \Delta)(1 - v_e^{(0)} \cos\theta) - \frac{m_e^2}{E_e^{(0)}} \right] \\ &+ (f^2 + g^2) \left[\Delta(1 + v_e^{(0)} \cos\theta) - \frac{m_e^2}{E_e^{(0)}} \right] \\ &+ (f^2 + 3g^2) \left[(E_e^{(0)} + \Delta) \left(1 - \frac{1}{v_e^{(0)}} \cos\theta \right) - \Delta \right] \\ &+ (f^2 - g^2) \left[(E_e^{(0)} + \Delta) \left(1 - \frac{1}{v_e^{(0)}} \cos\theta \right) - \Delta \right] v_e^{(0)} \cos\theta \end{aligned} \quad (3.35)$$

$\cos^2 \theta_c = 0.97$, δ_{inner}^{rad} is the inner radiative correction(=0.024), $f_2 = \mu_p - \mu_n$ (=3.706) and M is the average nucleon mass. The energy threshold for this reaction is,

$$E_{\bar{\nu}_e}^{thr} = \frac{(M_n + m_e)^2 - M_p^2}{2M_p} = 1.806 \text{ MeV.} \quad (3.36)$$

The total cross sections as a function of neutrino energy are shown in Figure 3.3. The output positron angular distribution relative to the incident $\bar{\nu}_e$ direction is nearly flat with

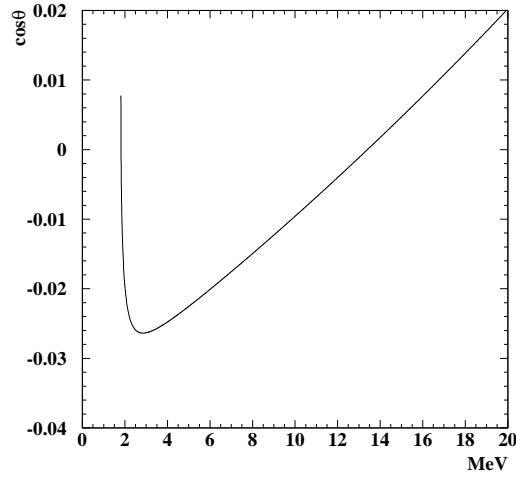


Figure 3.4: The average $\cos \theta$ distribution of positron for inverse beta-decay process

a small energy dependent slope, in contrast with the sharply peaked elastic scattering distribution. The average $\cos \theta$ of the output positron as a function of the neutrino energy, $\langle \cos \theta \rangle$ is shown in Figure 3.4.

3.2.4 Cherenkov radiation

The Super-Kamiokande detector is a ring imaging Cherenkov detector filled with 50 ktons of highly purified water. When a charged particle having a velocity of v traverses a medium which has an index of refraction n , Cherenkov photons are emitted if $v \geq c/n$, here c is the light speed in vacuum. The direction of the Cherenkov photons has an opening angle $\theta_{\text{Cherenkov}}$ from the direction of the charged particle (Figure 3.5) ;

$$\cos \theta_{\text{Cherenkov}} = \frac{1}{n(\lambda)\beta}, \quad (3.37)$$

here $n(\lambda)$, the index of refraction, depends on the wavelength λ and β is v/c . The index of refraction is about 1.34 in water, and the maximum $\theta_{\text{Cherenkov}}$ is 42° ($\beta \simeq 1$). The number of differential luminosity of Cherenkov photons is given as follows ;

$$\frac{d^2 N_{\text{photon}}}{dL d\lambda} = \frac{2\pi\alpha}{\lambda^2} \left(1 - \frac{1}{n^2\beta^2} \right), \quad (3.38)$$

here N_{photon} is the number of photons per track length (L) per unit unit wavelength ($d\lambda$) and α is the fine structure constant. The number of Cherenkov photons for $\lambda = 300$

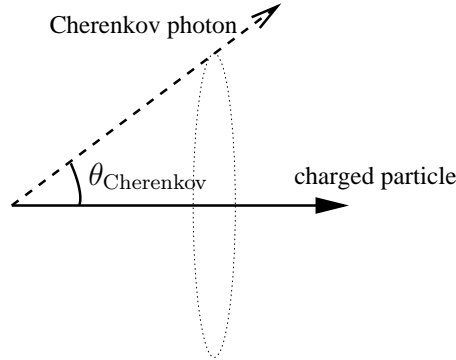


Figure 3.5: Definition of the Cherenkov angle $\theta_{\text{Cherenkov}}$

~ 600 nm (wavelengths where the 50cm PMTs are sensitive, see Figure 3.10) is about 340/1cm in water.

The threshold energy of Cherenkov photon emission is as follows ;

$$E_{\text{thr}} = \frac{n \times m}{\sqrt{n^2 - 1}}, \quad (3.39)$$

here m is mass of charged particle. For the case of an electron or positron ($m = 0.511$ MeV) in water, this threshold is 0.77 MeV in total energy.

The PMT hit timing, ring pattern and number of photons of Cherenkov radiation are useful to obtain the vertex, direction and energy of neutrino interactions. Real-time and directional observation of neutrinos become possible due to these features of Cherenkov radiation.

3.3 The water tank

The SK rock cavity is reinforced by a concrete wall. A cylindrical tank of 42m in height and 39.3 m in diameter is formed by stainless steel lining. The capacity of the tank is 50,000 cubic meters.

The inside of the tank is optically divided into an inner detector (ID) and an outer detector (OD). The ID collects neutrino events and the OD tags and/or absorbs backgrounds coming from outside, such as cosmic ray muons, γ -rays and neutrons from surrounding rock etc.. Separation of the ID and OD is done by a stainless steel structural grid, Tyvek and polyethylene black sheets, but water flow is not restricted between the ID and OD. The schematic view of the SK detector is shown in Figure 3.6.

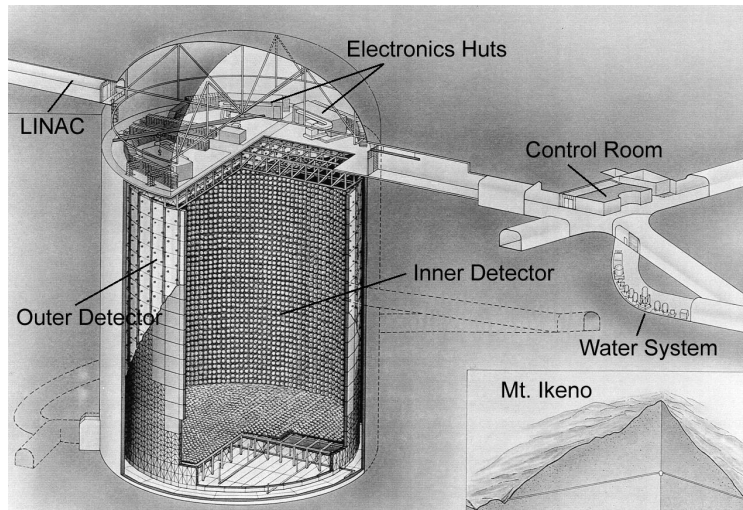


Figure 3.6: The schematic view of the Super-Kamiokande detector

3.3.1 The inner detector

The inner detector is a cylindrical form with a height 36.2m and a diameter 33.8m which contains 32 ktons of water and is viewed by 11,146 inward-facing 50 cm photo-multiplier tubes (PMTs, Hamamatsu R3600-05). The 50cm PMTs are mounted on a stainless steel frame. The basic unit is a stainless steel frame called a ‘supermodule’ holding ID PMTs in a 4×3 array. A schematic view of the supermodule is shown in Figure 3.7. The PMTs are mounted on a 70 cm grid. 7,650 PMTs are on the side wall (barrel), and 1,748 PMTs are on the top and bottom, respectively. The resulting photo-cathode coverage by all 11,146 PMTs is about 40% of the ID surface. Photo-insensitive areas are covered by black polyethylene sheets. This black sheet reduces reflected light on the surface which degrades timing information and forms an optical separation between the ID and OD.

3.3.2 The outer detector

The active region of the outer detector is between the stainless steel tank and the outer surface of the support structure. Its thickness is approximately 2 m. The active region is monitored by 1885 outward-facing 20 cm PMTs (Hamamatsu R1408) installed on the support structure. For an enhancement of the light collection efficiency, 60 cm square and 1.3 cm thick wavelength shifting plates are attached to each OD PMT. White Tyvek lining of the inner surface of the OD increases reflection light so that the muon tagging efficiency keeps high even if some PMTs stop functioning.

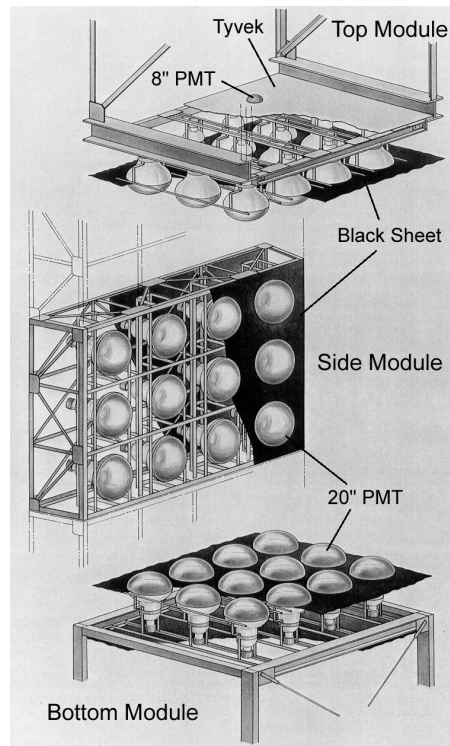


Figure 3.7: A schematic view of support structures for the inner detector

3.4 50 cm diameter photo-multiplier tube (ID PMT)

Figure 3.8 shows the schematic view of a 50 cm PMT used in the ID. The original 50 cm PMTs [57] were made by HAMAMATSU Photonics Company for the Kamiokande experiment, and later, its focusing grid, number of dynodes ratio of breeder resistances were further optimized for the Super-Kamiokande experiment [58]. After the modifications, the 1 photo-electron peak became clear as shown in Figure 3.9. The transit time spread at the 1 photo-electron level became narrower (5 sec \rightarrow 3 sec). Figure 3.10 shows the quantum efficiency of the 50 cm PMT, and the performance of the PMT is as follows ;

| | |
|------------------------|-----------------------------------|
| Photo-cathode area | : 50 cm in diameter |
| Shape | : Hemispherical |
| Window material | : Pyrex glass(4 ~ 5 mm) |
| Photo-cathode material | : Bi-alkali(Sb-K-Cs) |
| Dynodes | : 11 stage, Venetian blind |
| Pressure tolerance | : 6kg/cm ² water proof |
| Quantum efficiency | : 22% at $\lambda=390\text{nm}$ |
| Gain | : 10^7 at ~ 2000 volts |
| Dark current | : 200 nA at gain= 10^7 |
| Dark pulse rate | : 3kHz at gain= 10^7 |
| Cathode non-uniformity | : less than 10 % |
| Anode non-uniformity | : less than 40 % |
| Transit time spread | : $\sigma \sim 2.5$ nsec |

Water sealing of the breeder circuit has been also improved and the death rate became much smaller. The time-variation of the number of dead, high dark pulse rate and flasher PMTs is shown in Figure 3.11. In the period of SK-I, the number of bad PMTs was less than 1.8%.

3.5 20 cm diameter photo-multiplier tube (OD PMT)

The OD uses 20 cm diameter PMTs originally from the IMB experiment. A wavelength shifting plate attached to each PMT (as shown in Figure 3.12) increases the light collection efficiency by 50 % with a trade-off of slight degradation of the timing resolution from 5.5 nsec to 7.5 nsec. The time-variation of the number of dead PMTs is shown in Figure 3.13. In the period of SK-I, the number of bad OD PMTs was less than 16%.

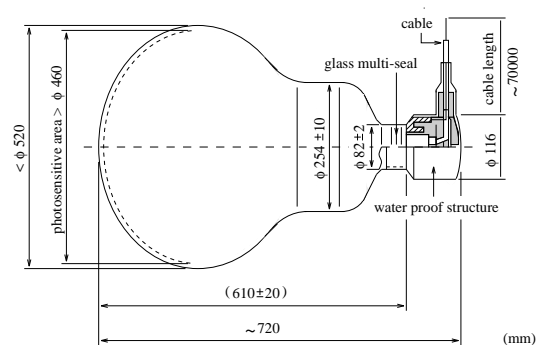


Figure 3.8: 50 cm photo-multiplier tube

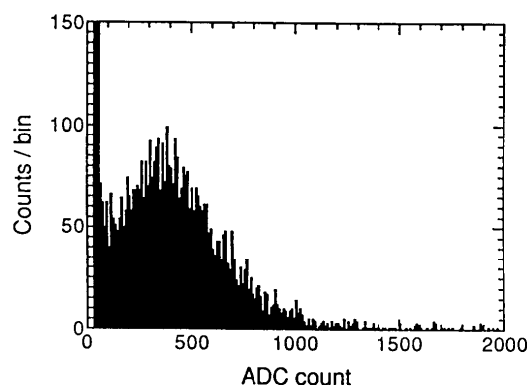


Figure 3.9: Single photo-electron distribution of the 50 cm diameter PMT

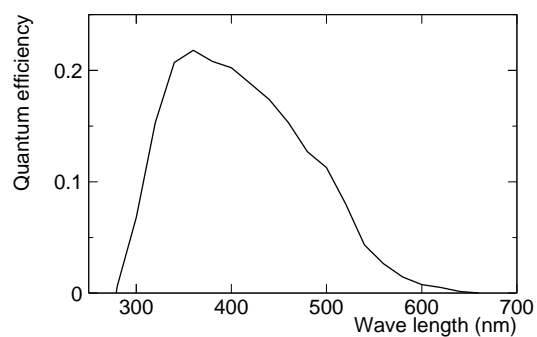


Figure 3.10: The quantum efficiency of the PMTs as a function of light wavelength

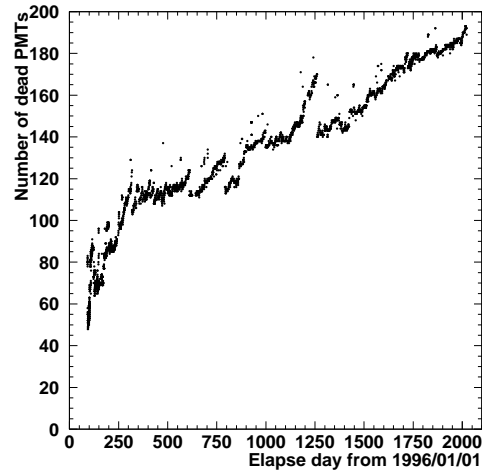


Figure 3.11: The time variation of the number of dead ID PMTs

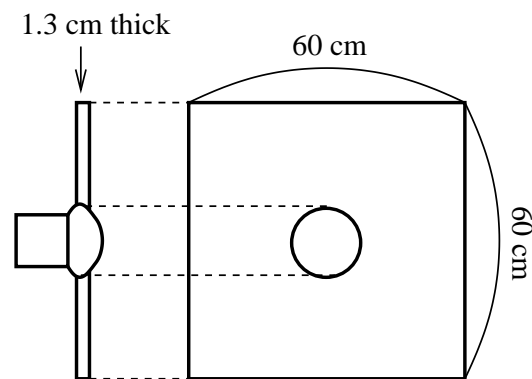


Figure 3.12: A schematic view of the 20 cm PMT with wavelength shifter

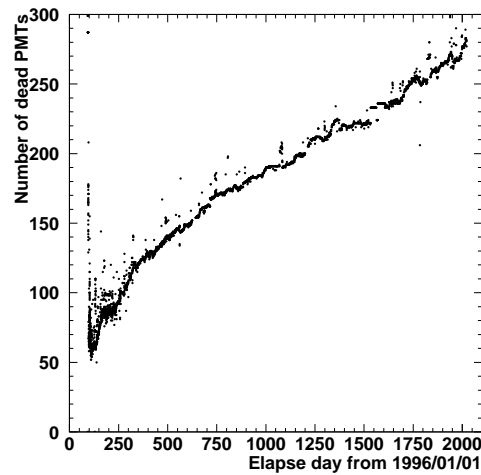


Figure 3.13: The time variation of the number of dead OD PMTs

3.6 Water purification system

A clean and large amount of natural water flow is available in the Kamioka mine. The water is used to fill the detector after thorough water purification. The purposes of water purification are as follows :

- To improve the transparency of water as much as possible.
Small dust, metal ions like Fe^{2+} , Ni^{2+} , Co^{2+} , and bacteria cause strong attenuation and scattering of Cherenkov light.
- To remove radioisotopes like ^{222}Rn and ^{226}Ra .
The mine water contains a large amount of radioactive elements and they cause serious backgrounds below 7 MeV.

A schematic view of the water purification system is shown in Figure 3.14 and the components are as follows :

- 1 μm water filter
To remove dust and to absorb ^{222}Rn
- Heat exchanger
To cool the water heated by water pumps and PMTs during filling and/or recirculation. Keeping the water temperature at 13 $^{\circ}\text{C}$, bacterial growth and convection of water are suppressed.

- Ion exchanger
To remove metal ions. $\text{Fe}^{2+}, \text{Ni}^{2+}, \text{Co}^{2+}$ are removed and Po(daughter nuclei of ^{222}Rn) which easily ionizes are also removed.
- Ultra-Violet sterilizer (UV)
To eliminate bacteria.
- Vacuum Degasifier system (VD)
To remove gas dissolved in water. About 99% of oxygen and 96% of radon are removed.
- Cartridge Polisher(CP)
To remove metal ions. It is a high performance ion exchanger.
- Ultra Filter
To remove small dust of a few nm size.
- Reverse osmosis filter(RO)
To remove small dust and organisms of the order of 100 molecular weight.

The usual water recirculation is bottom-supply and top-drain with a flow rate of 30 ~ 70 tons/hour. With this water system, ^{222}Rn concentration in the SK tank water is less than 5.7 mBq/m^3 [59].

For further reduction of ^{222}Rn , this water system was upgraded in 2000. From these improvements, the ^{222}Rn concentration in the supply water changed to less than 1 mBq/m^3 [60].

3.7 Air purification system

The ^{222}Rn concentration in the mine air is $50 \sim 2000 \text{ Bq/m}^3$ depending on the season. Therefore purified Rn free air is sent to the detector area from outside of the mine so that a tiny leak can be tolerable and human health can be kept. The schematic view of the water purification system is shown in Figure 3.15 and the components are as follows :

- Compressor
To take air from outside of the mine and compress it to $7.0 \sim 8.5 \text{ atm}$.
- $0.3 \mu\text{m}$ air filter
To remove dust in the air.
- Air drier
To remove moisture in the air. Humidity in the air lowers Rn removal efficiency of the carbon column below.

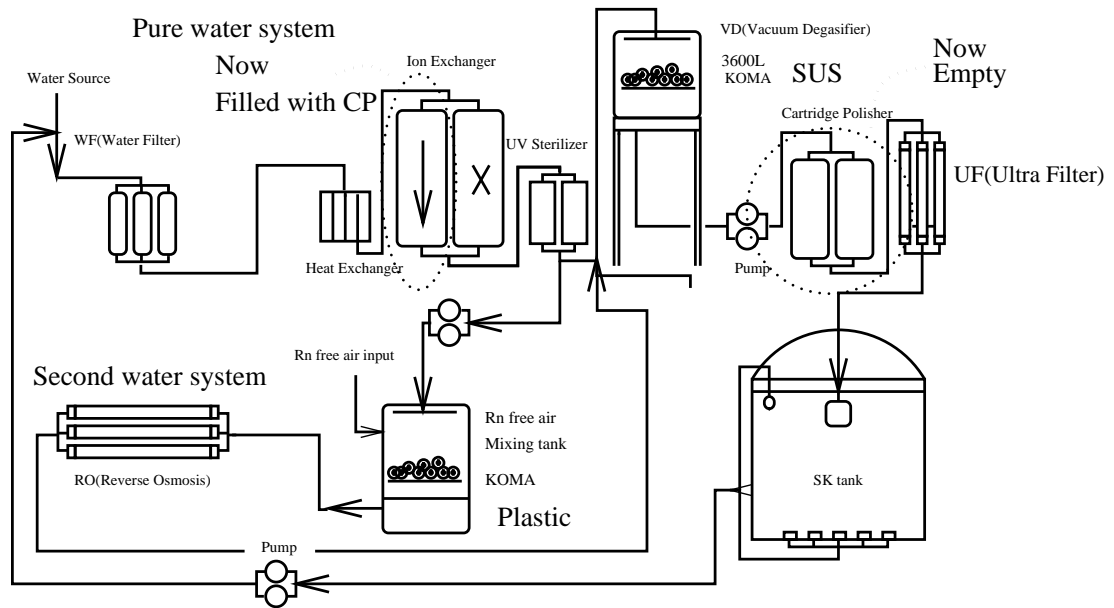


Figure 3.14: A schematic view of the water purification system after improvements

- Carbon column
To remove Rn.
- $0.1 \mu\text{m}$ and $0.01 \mu\text{m}$ air filter
To remove small dust in the air.
- Activated charcoal filters
To remove Rn. Activated charcoal is cooled at -40°C to enhance Rn adsorption efficiency.

Its air flow rate is $7 \text{ m}^3/\text{min}$. The ^{222}Rn rejection efficiency of this system is about 99.98% [61] and the concentration of ^{222}Rn in the air through this system is about a few mBq/m^3 .

3.8 Electronics and data acquisition system

3.8.1 Inner detector electronics

Figure 3.16 shows a schematic view of the ID data acquisition system. The signals from the PMTs are sent to an electronics module called ATM¹ [62] in each A TKO² crate.

¹Analog Timing Module

²Tristan-KEK-Online

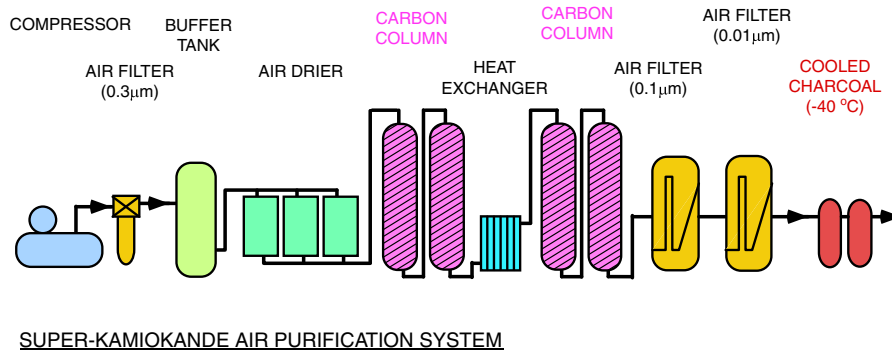


Figure 3.15: A schematic view of the Rn free air purification system

TKO crate holds GONG³, ATM and SCH⁴. The ATM module divides and digitizes signals from 12 PMTs. SCHs send digitized data from ATMs to SMPs⁵. SMPs buffer data for online computers, and GONG distributes global trigger information to each ATM.

When the divided PMT signal in ATM exceeds the threshold of 1/4 p.e., a rectangular signal with 200 nsec width and 11 mV height is generated for each PMT signal. These signals are analog summed as a HITSUM. A global trigger is issued when the HITSUM exceeds a threshold.

The other divided PMT signals are sent to the QAC⁶ and TAC⁷. QAC/TAC integrates and holds the signals within 1.3µsec. If a global trigger does not arrive, this information is abandoned. If a global trigger arrives, the voltages in QAC/TAC are digitized by ADC⁸/TDC⁹ and stored in a 1024 word FIFO memory¹⁰. Typically analog-digital conversion time is ~5.5µsec. And, one PMT channel has two QAC/TAC pairs to collect successive events like a stopping muon and its decay electron signals.

3.8.2 Outer detector electronics

The OD data acquisition system is independent of the ID system. Figure 3.17 shows a schematic view of the OD data acquisition system. Signals from a PMT are discriminated in a Charge to Time Converter (QTC) module. If the pulse height exceeds 25 mV (~0.25 p.e. level), QTC module generates a rectangular pulse whose edge expresses the hit

³GO and NoGo trigger distribution module

⁴Super Controller Header, bus-interface-module

⁵Super Memory Partner

⁶Charge to Analog Converter

⁷Timing to Analog Converter

⁸Analog to Digital Converter

⁹Time to Digital Converter

¹⁰First In/First Out

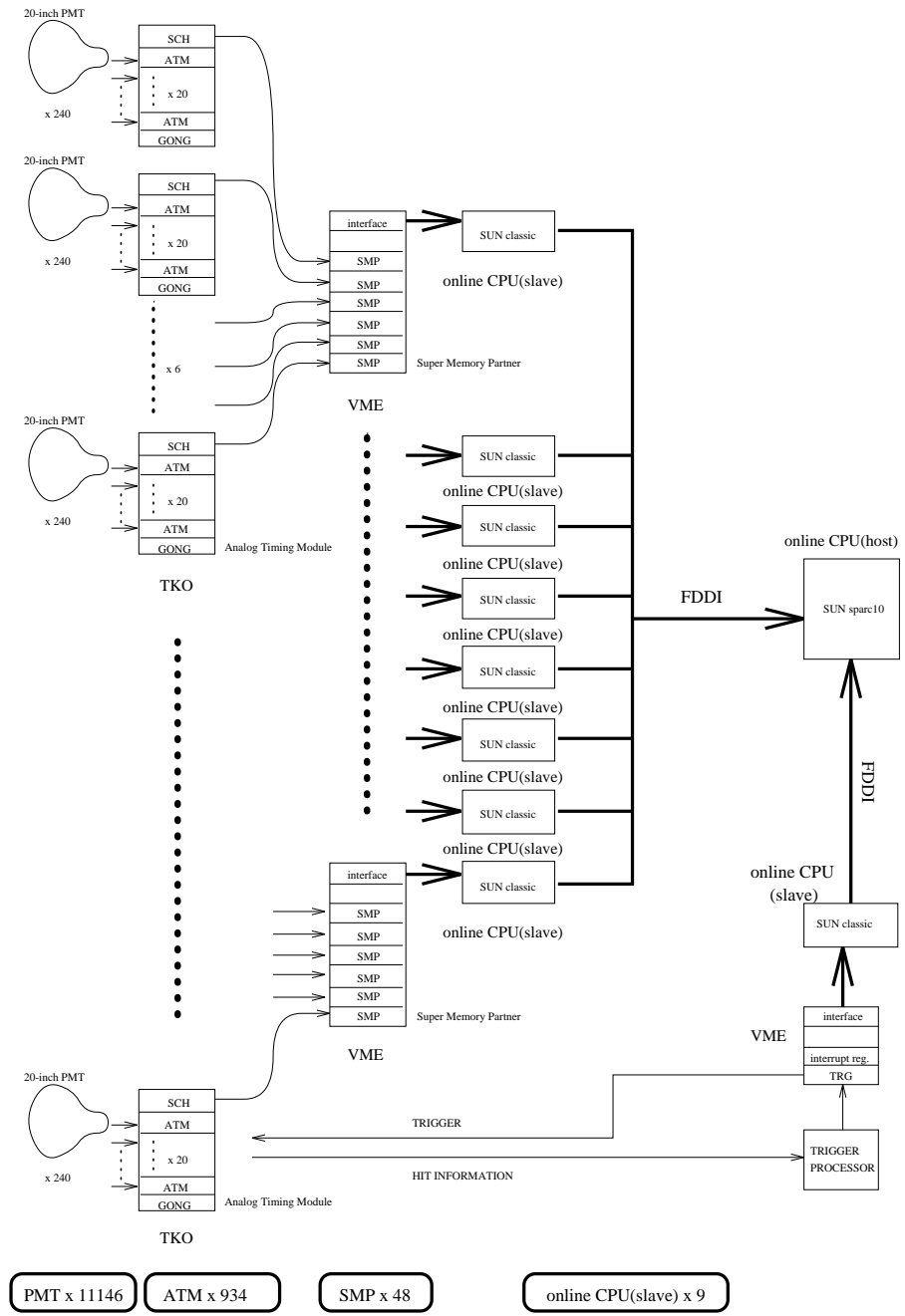


Figure 3.16: A schematic view of the ID data acquisition system

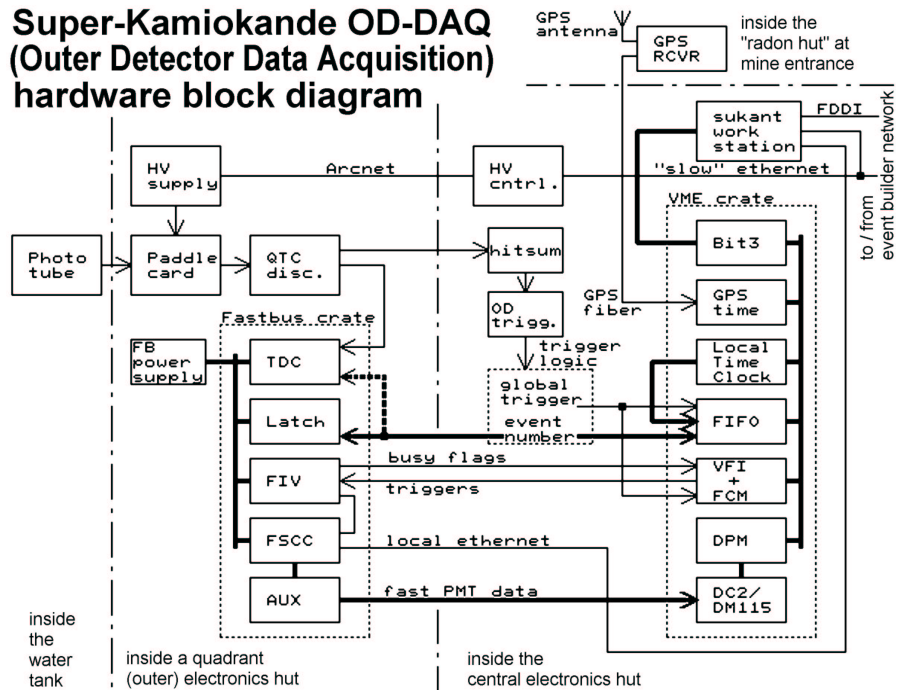


Figure 3.17: A schematic view of the OD data acquisition system

arrival timing and width represents the charge. This pulse is supplied to a LeCroy1887 multi-hit TDC¹¹ module and is digitized. The TDC module has 96 input channels and their resolution is ~ 0.5 nsec. The data acquisition timing window is $16\mu\text{sec}$ ($-10\mu\text{sec}$ to $+6\mu\text{sec}$ to the global trigger timing). The TDC is a Fastbus module and controlled by a Fastbus Smart Crate Controller (FSCC). The FSCC sends the digitized data to DPM¹² modules and these data are read by a workstation through the VME bus.

3.9 Triggers

The analog-sum of HITSUM signals from each ATM module generates an ID HITSUM signal. The low energy trigger (LE) threshold level of -320 mV. For High Energy trigger (HE), this threshold level is -340 mV. The LE trigger threshold level corresponds to 29 hits of ID PMTs within a 200 nsec time window. And an additional similar type trigger, the Super Low Energy trigger (SLE) was set in May, 1997. The SLE trigger threshold was changed several times in order to take lower energy data. But when the threshold is

¹¹Time to Digital Converters

¹²Dual Ported Memory

| start time | End date | Threshold | Trigger rate |
|-------------|-------------|---------------|--------------|
| 31 May 1996 | End of SK-I | -320 mV (LE) | ~11 Hz |
| 31 May 1997 | 14 May 1999 | -260 mV (SLE) | ~100 Hz |
| 14 May 1999 | 17 Sep 1999 | -250 mV (SLE) | ~170 Hz |
| 17 Sep 1999 | 20 Dec 1999 | -222 mV (SLE) | ~530 Hz |
| 20 Dec 1999 | 12 Jul 2000 | -212 mV (SLE) | ~540 Hz |
| 12 Jul 2000 | 31 Jul 2000 | -186 mV (SLE) | ~1.6kHz |
| 31 Jul 2000 | 27 Sep 2000 | -212 mV (SLE) | ~540 Hz |
| 27 Sep 2000 | End of SK-I | -186 mV (SLE) | ~1.6kHz |

Table 3.1: History of the SLE trigger

dropped, the rate of background events rises sharply and is hard to handle in the real time data processes. These very low energy background events are due to γ rays from the rock surrounding the detector, ID wall materials and radioactive decays in the PMT glass etc.. As a result, these vertices are distributed near the wall, thus the outside of the fiducial volume. In order to remove these backgrounds, a real-time fiducial volume cut is applied. If the reconstructed vertex is within 200cm from ID wall, the event is discarded. This software filtering procedure is called the intelligent trigger(IT). For this process, a parallel computing method was employed. And in 1999 and in 2000, the IT system was upgraded with additional CPUs. Table 3.1 summarizes each LE and SLE trigger threshold level and event rate.

3.10 Online and offline system

Figure 3.18 shows a schematic view of the online and offline system after the ID data acquisition system as shown in Figure 3.16. The digitized data are sent to 8 online workstations. These data are sent to a host workstation via FDDI¹³. The host workstation builds the event from these data, OD data and trigger data. The reconstructed data are sent to another workstation and reformatted into the ZEBRA format. Finally, ZEBRA format data are stored in the MTL¹⁴ and each analysis group process (Low-energy group; Solar neutrino, High-energy group; Atmospheric neutrino, Upward going muon group, Calibration group) selects the data and stores the data in the MTL and/or data disk system.

¹³high speed ring network with optical fiber cable

¹⁴Magnetic tape library

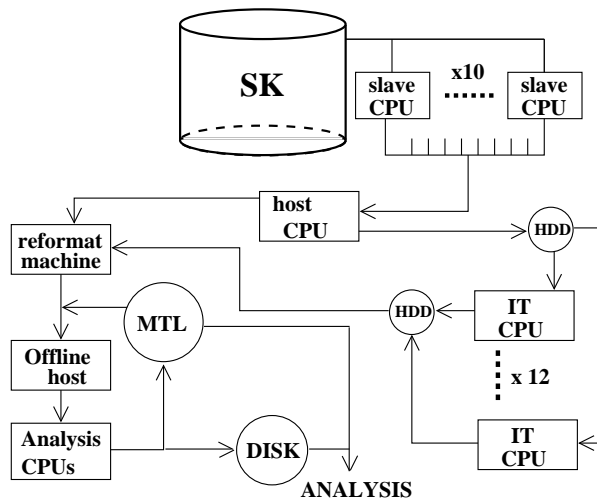


Figure 3.18: A schematic view of the online and offline data flow

3.11 Detector simulation

In order to simulate the response of the detector, a Monte Carlo simulation (M.C.) based on GEANT3.21 [63] is carried out. GEANT is developed at CERN for detector simulations of high energy experiments. This program package is able to simulate particle tracking and electromagnetic interactions such as ionization process, multiple scattering, bremsstrahlung, annihilation, Compton scattering, pair production etc. in an energy range of 10 keV to 10 TeV.

Cherenkov photon radiation is also treated in GEANT, but the tracking of Cherenkov photons which depends on the water parameters such as absorption and scattering is taken into account by custom user programs. For $\lambda \leq 400$ nm, Rayleigh scattering is dominant for light attenuation ($\propto 1/\lambda^4$), and for $\lambda \geq 400$ nm, absorption is dominant [66]. The magnitudes of these effects are tuned in the M.C.. These parameters are tuned so that the M.C. of the LINAC calibration reproduces real data. The attenuation length of light in pure water is measured as a function of wavelength by using a laser and a CCD camera (Sec.5.4.1). The magnitude of absorption in water strongly depends on the water quality. Therefore this relative time variation is traced by using muon-decay electrons (Sec.5.4.2) and considered in the simulation.

Cherenkov light could be reflected at the surfaces of the PMTs and black sheets. Normal reflections are calculable as shown in Figure 3.19 [67]. But diffused reflection is an issue of M.C. tuning.

In the SK detector simulation, the response of PMTs and electronics are also considered. The average PMT quantum efficiency as a function of photon wavelength measured at Hamamatsu photonics is shown in Figure 3.10.

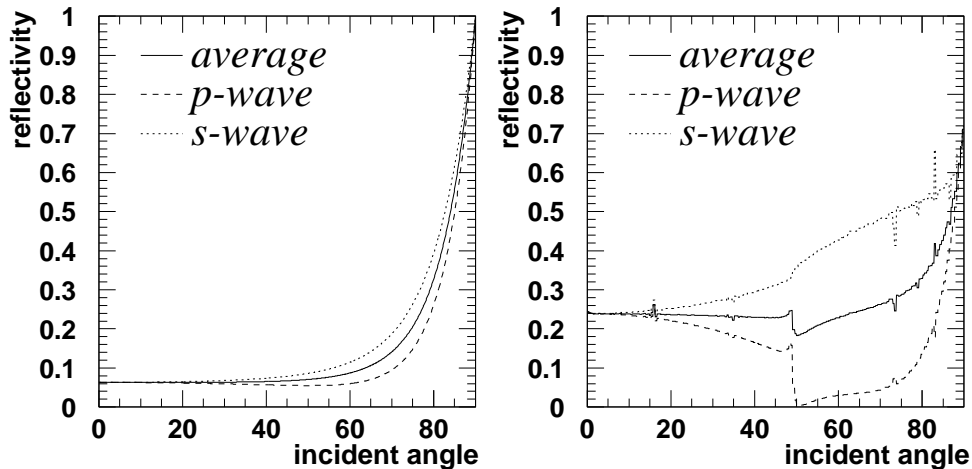


Figure 3.19: Light reflection from black sheet and PMT. The left figure shows the reflection probability of a PMT (left figure) and black sheet (right figure) as a function of incident angle. The photon polarization is considered.

The measured one photo-electron distribution is used to simulate dark noise and time variation of the dark noise rate is modeled using the average value of observed ID PMT dark rates. ID PMTs have after-pulses around 100 nsec after real signals. The reason of this after pulse is an electron elastically back scattered to the photo-cathode at the first dynode. This electron goes back to the dynode with a time lag. The probability of this after pulse is measured by LINAC and Ni-Cf calibrations, and observed 2 % is used in the simulation. Finally, resolutions of the ADCs and TDCs are taken into account. In the solar neutrino energy region, most PMTs detect only 1 p.e. The response of electronics at the 1 p.e. level is measured by Ni-Cf calibrations (Sec.5.2) and is considered in the M.C. simulation. The observable TDC count is dominated by the PMT transit time spread. The observable resolution is 2.90 nsec at 1 p.e. and the M.C. simulation uses overall timing resolution as a function of charge as shown in Figure 3.20. Fixed voltage discrimination causes a slewing effect in the TDC measurement at low charges. This effect is about 0.7 nsec at 1 p.e. and it is simulated as a function of charge as shown in Figure 3.20.

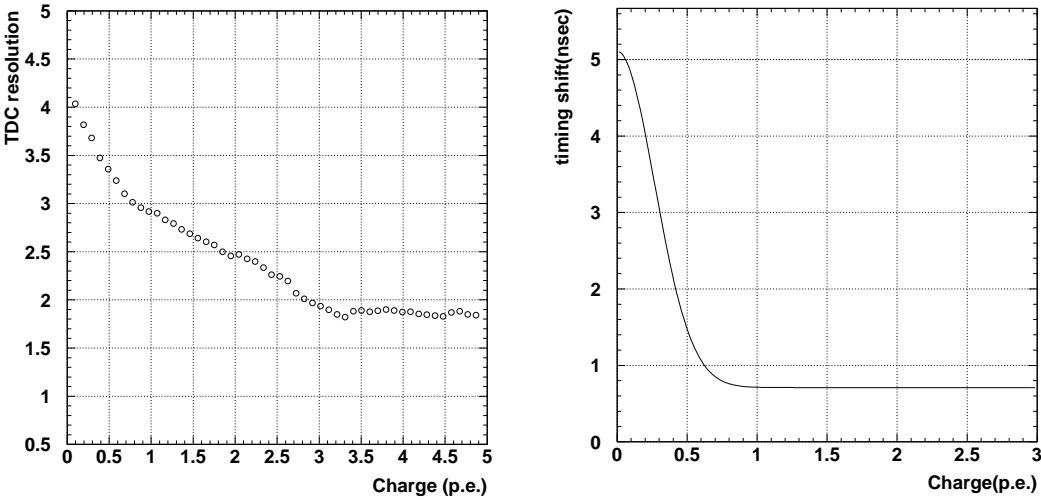


Figure 3.20: TDC resolution and timing shift. Left figure shows the TDC resolution as a function of charge used in the M.C. simulation. The right figure shows timing shift by slewing effect used in the M.C. simulation.

Chapter 4

Event Reconstruction

Super-Kamiokande is a ring imaging Cherenkov detector. Event vertices, directions and energies are reconstructed from timing, pattern and number of photo-electron information of Cherenkov ring images. In this chapter, vertex, direction and energy reconstruction of low energy events ($\lesssim 100$ MeV) and track reconstruction of muon events are described.

4.1 Reconstruction of low energy events

4.1.1 Vertex reconstruction

The vertex reconstruction uses timing information of hit PMTs. Low energy electrons relevant to solar neutrino observation travel only up to 10cm. That path length is much smaller than so far achieved vertex resolution (~ 75 cm at 10 MeV) thus we can suppose low energy events as point-like light sources for the moment.

The vertex reconstruction has 2 steps. The 1st step is a selection of on-timing hit PMTs to be used for the reconstruction. The 2nd step is a grid search for the best fit vertex.

1. Selection of hit PMTs

- The 200 nsec timing window which maximizes the number of hits (N_{200}) is obtained using a sliding window.
- The number of dark noise hits in the window is estimated event by event.

$$N_{noise} \equiv \frac{(t_3 - t_2)}{(t_2 - t_1) + (t_4 - t_3)} (N_{hit}(t_1 \sim t_2) + N_{hit}(t_3 \sim t_4)), \quad (4.1)$$

where $t_{1\sim 4}$ are defined in Figure 4.2.

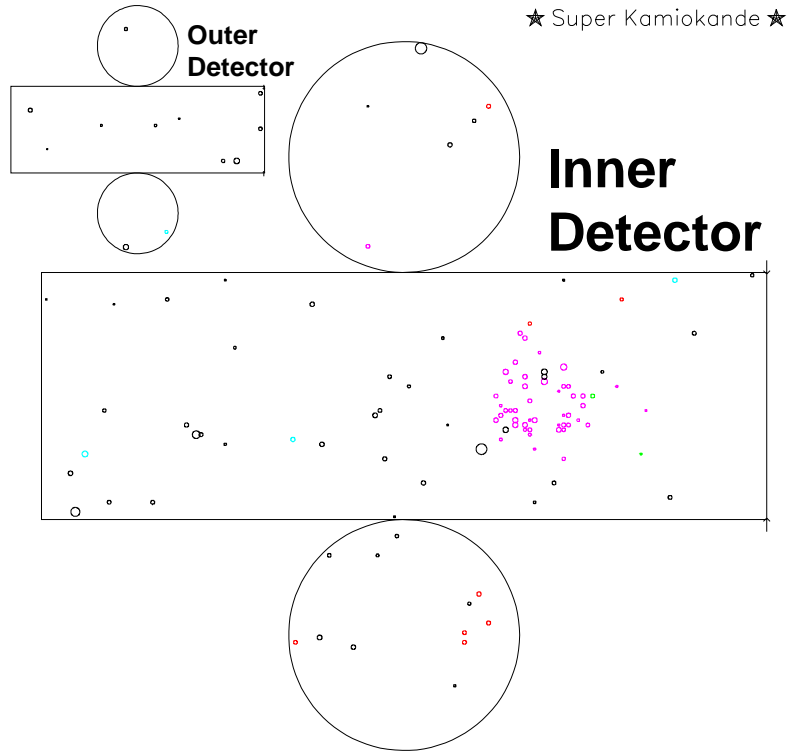


Figure 4.1: Event display of a typical low energy event

- The window is segmented into 11 bins and the significance S as defined below is calculated for each of the 11 bins,

$$S \equiv \frac{N_{200} - N_{noise}}{\sqrt{N_{noise}}}. \quad (4.2)$$

The time bin which gives the maximum Significance is selected and the hits included in the bin are used for the vertex grid search in the next step.

2. Grid search for a vertex

The ‘goodness’ of the vertex fit is defined by the following formula,

$$goodness(x, y, z) \equiv \frac{\sum_{i=1}^{N_{hit}} \frac{1}{\sigma^2} \exp\left(-\frac{\left(T_i(x, y, z) - \overline{T_i(x, y, z)}\right)^2}{2\sigma^2}\right)}{\sum_{i=1}^{N_{hit}} \frac{1}{\sigma^2}}, \quad (4.3)$$

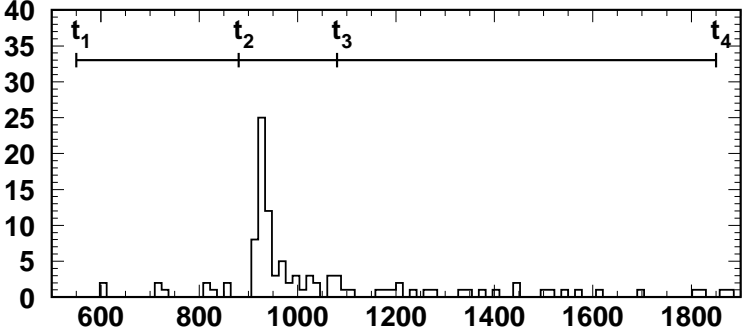


Figure 4.2: Timing distribution of the event in Figure 4.1

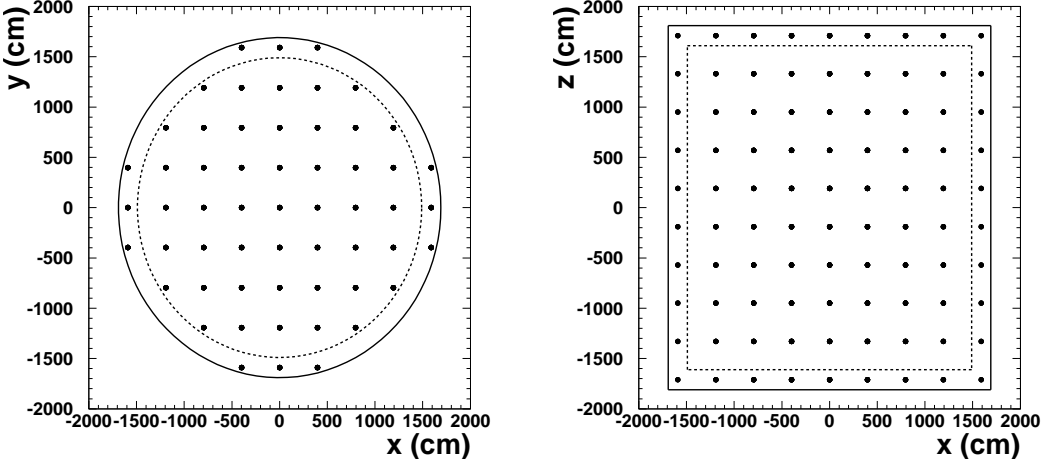


Figure 4.3: The initial grid points for the vertex reconstruction. Solid and dotted lines show the ID boundary and the 200 cm fiducial volume.

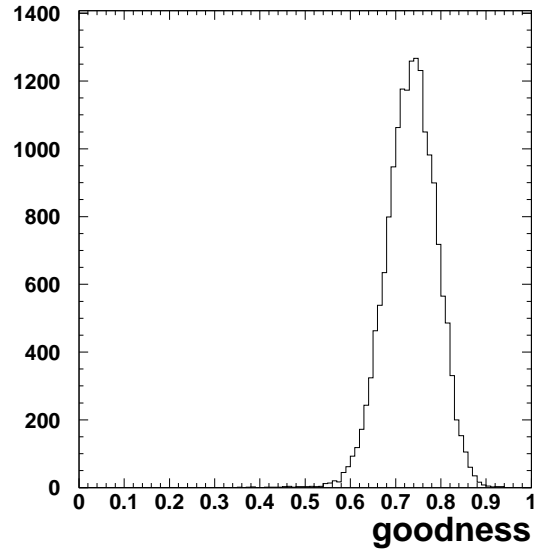


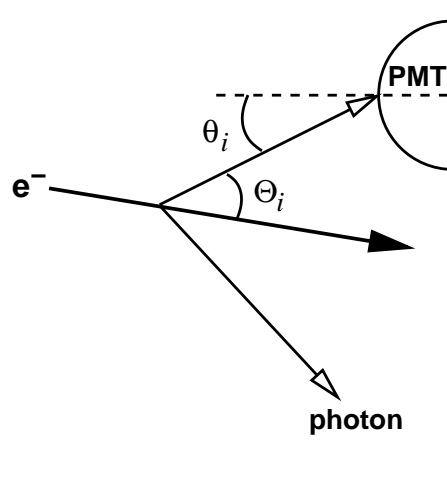
Figure 4.4: A typical *goodness* distribution of LINAC calibration data at the position $(x,y,z) = (-388.9\text{cm}, -70.7\text{cm}, +27\text{cm})$

here, (x,y,z) is an assumed vertex point, N_{hit} is the number of hit PMTs in the selected time window above, σ is the timing resolution of the PMTs and $T_i(x, y, z)$ is the hit timing of the i -th PMT after time of flight (TOF : propagation time of Cherenkov photon from the vertex to a hit PMT) subtraction. $T_i(x, y, z)$ is defined as follows,

$$T_i(x, y, z) \equiv t_i - \frac{n}{c} \sqrt{(x - x_i)^2 + (y - y_i)^2 + (z - z_i)^2}. \quad (4.4)$$

Here, t_i is the hit time of the i -th PMT, n is the refractive index of pure water, c is the light speed in vacuum and (x_i, y_i, z_i) is the position of the i -th hit PMT. The *goodness* indicates the quality of the vertex fit. In an ideal case, *goodness* becomes 1 because all $T_i(x, y, z)$ are equal. A grid search method is used to look for a position which gives the maximum *goodness* value. Initial grid points are chosen on intervals of 397.5 cm for X along the X and Y axes and those of 380.0 cm along the Z axis as sketched in Figure 4.3. In order to avoid a local minimum, *goodnesses* are calculated for these 570 initial points. From the best '*goodness*' points, finer grid searches with a 5 cm step are performed for the final vertex.

Figure 4.4 shows a typical *goodness* distribution of LINAC calibration data. Due to effects of light refraction, PMT resolution, dark noise etc. The actual '*goodness*' distribution peaks at ~ 0.75 . The vertex resolution measured by the LINAC calibration is, for example, ~ 75 cm at 10 MeV.

Figure 4.5: Definition of Θ_i and θ_i

4.1.2 Direction reconstruction

The direction reconstruction uses the opening angle distribution of the Cherenkov ring image with respect to the obtained vertex position. In an ideal case, the opening angle of Cherenkov radiation from the electron is 42° in water. A maximum likelihood method with the following likelihood function is used,

$$L(\mathbf{d}) = \sum_{i=1}^{N_{hit}} \log(P(\cos \Theta_i)) \times \frac{\cos \theta_i}{f(\theta_i)}. \quad (4.5)$$

Where, $P(\cos \Theta_i)$ is the probability function to have photons at the opening angle Θ_i (defined as Figure 4.5) from the particle direction as shown in Figure 4.6. $\cos \Theta_i$ is calculated for each hit PMT. The probability function contains the overall effects from multiple scattering, refraction and reflection etc. and is obtained from a M.C. simulation. θ_i is the incident angle of Cherenkov photon on the i -th PMT. $f(\theta_i)$ is the acceptance of a PMT depending on θ_i as defined in Figure 5.2. A grid search for the particle direction $\mathbf{d} = (d_x, d_y, d_z)$ is performed to obtain the direction yielding the maximum $L(\mathbf{d})$. Finer step size is progressively used for the grid search from 20° to 9° , 4° and 1.6° . The Cherenkov ring pattern diffuses due to various effects such as light scattering, refraction and multiple scattering of electron. The achieved direction resolution is $\sim 27^\circ$ at 10 MeV with a LINAC calibration.

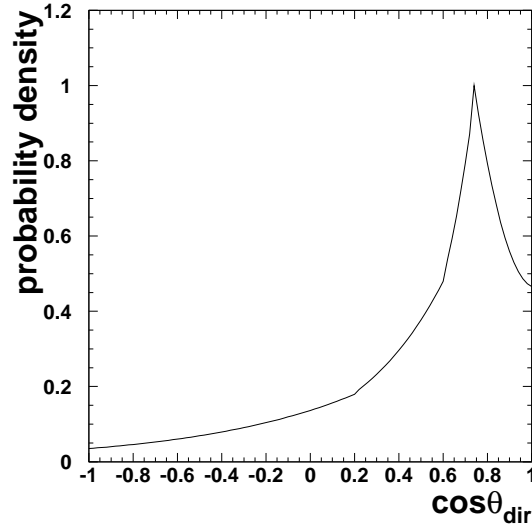


Figure 4.6: The distribution of the angle between charged particle direction and the vector from the reconstructed vertex to the hit PMT position

4.1.3 Energy reconstruction

The amount of Cherenkov radiation is approximately proportional to the energy of a charged particle, and the total number of photo-electrons is proportional to the number of Cherenkov photons. However, the energy reconstruction is based on the number of hit PMTs instead of total number of photo-electrons, because of the following reasons :

- Most PMTs receive only one photo-electron in low energy events, therefore, the total number of photo-electrons is almost equal to the number of hit PMTs.
- The charge resolution of the PMT is not good ($\sim 50\%$) at the single photo-electron level.
- One big noise such as a flasher can affect the total number of photo-electrons but its effect on the number of hits is only one noise hit.

In the energy reconstruction, only the number of hit PMTs within a 50 nsec timing window (N_{50}) is used. In order to obtain a uniform and stable energy scale, the effective number of hits with various corrections, N_{eff} , is introduced as follows :

$$N_{eff} = \frac{N_{total}}{N_{alive}} \times \sum_{i=1}^{N_{50}} (X_i + \epsilon_{tail} - \epsilon_{dark}) \times \frac{R_{cover}}{S(\theta_i, \phi_i)} \times \exp\left(\frac{r_i}{\lambda(run)}\right) \times K(i). \quad (4.6)$$

- N_{total}/N_{alive} : Correction for Dead PMT.
The number of dead PMTs has a time variation as shown in Figure 3.11. In order

to reduce the effect of dead PMTs, coverage decrease is corrected with this factor assuming a uniform distribution of dead PMTs. Here N_{total} is the total number of PMTs in the ID ($= 11146$), and N_{alive} is the number of available PMTs.

- X_i : Correction for multi photo-electron hit.

As energies go higher and/or distances to the wall become smaller, the Cherenkov photon flux at a PMT becomes larger and the probability to detect more than one photo-electron becomes larger. This multi-photon effect causes non-uniformity and non-linearity of the energy scale. The number of detected photo-electrons by a PMT can be estimated with an aid of the occupancy around the PMT. When the number of hit PMTs in surrounding eight PMTs is n_i and the number of alive PMTs in area is N_i , the mean number of photo-electrons at the central PMT is obtained as follows,

$$X_i = \frac{\ln\left(\frac{1}{1-\epsilon_i}\right)}{\epsilon_i}, \quad (4.7)$$

where,

$$\epsilon_i = \frac{n_i}{N_i}. \quad (4.8)$$

- ϵ_{tail} : Correction for reflected Cherenkov photons.

Cherenkov photons reflected by PMTs or black sheets are sometimes detected after the 50 nsec time window. In order to recover these photons, the correction factor ϵ_{tail} is multiplied. The correction factor is obtained as follows,

$$\epsilon_{tail} = \frac{N_{100} - N_{50}}{N_{50}}, \quad (4.9)$$

where N_{100} is similarly defined as N_{50} with a larger time window of 100 nsec.

- ϵ_{dark} : Correction for dark noise hits.

The mean dark noise rate of a PMT is about 3.3 kHz, and even a narrow 50 nsec timing window accidental dark noise hits can enter. The number of mean dark noise hits is obtained as follows,

$$\epsilon_{dark} = \frac{N_{alive} \times R_{dark} \times T_{window}}{N_{50}}, \quad (4.10)$$

where R_{dark} is the mean dark rate of PMTs in the run and T_{window} is the time window used for counting number of hit PMTs ($= 50$ nsec). This dark noise contribution is subtracted.

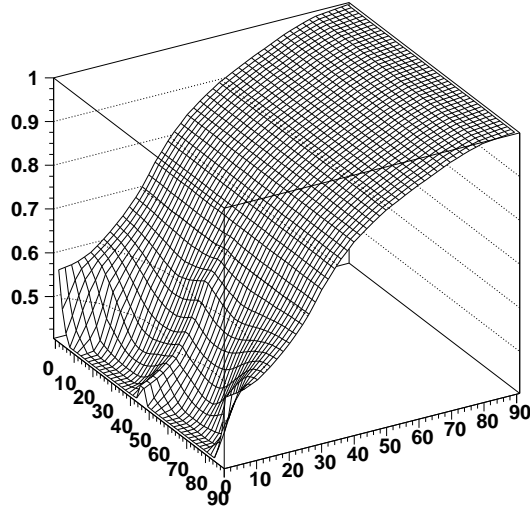


Figure 4.7: The effective photo cathode area $R_{cover}/S(\theta_i, \phi_i)$

- $R_{cover}/S(\theta_i, \phi_i)$: Correction for an effective photo coverage.
Effective photo coverage is different for each position. Therefore it is corrected in this term. R_{cover} is the average photo coverage ratio of the ID (=0.4041). $S(\theta_i, \phi_i)$ is the effective photo cathode area of the i -th PMT from the photon arrival direction (θ_i, ϕ_i) . Here θ_i is the incident angle to the i -th PMT and ϕ_i is the azimuth angle. The ϕ_i asymmetry is caused by the shadow of the neighboring PMTs. The $R_{cover}/S(\theta_i, \phi_i)$ ratio is shown in Figure 4.7.
- $\exp(r_i/\lambda(run))$: Correction for water transparency.
Cherenkov light is attenuated in water and the number of hits depends on the distance to the vertex position. r_i is the distance from the reconstructed vertex to the i -th PMT. $\lambda(run)$ is the attenuation length of Cherenkov light in water at the time. It is measured by decay electron events from cosmic ray muons for each period (it will be explained in Sec.5.4.2).
- $K(i)$: Correction for PMTs with high quantum efficiencies.
There are 375 PMTs with larger quantum efficiencies in the ID. These PMTs were produced at an earlier time than the rest of the PMTs. The average quantum efficiency of these PMTs relative to the others is measured by a Ni-Cf calibration (it will be explained in Sec.5.2) and the obtained correction factor is the following,

$$K(i) = \begin{cases} 0.833 & \text{for 375 PMTs with high quantum efficiencies} \\ 1.000 & \text{for the other PMTs} \end{cases} \quad (4.11)$$

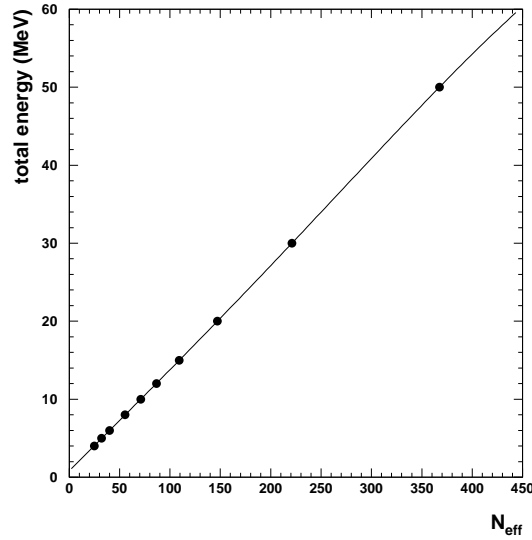


Figure 4.8: The correlation between N_{eff} and total energy. The line shows a 4-th order polynomial fit to the correlation between the peak value of N_{eff} and total energy of the electron

The uniformity of N_{eff} in the fiducial volume is calibrated to be within $\sim 1\%$ using LINAC calibration (Sec.5.6) and Ni-Cf calibration data. Finally, N_{eff} is converted to a total energy with the relation measured by a LINAC calibration as shown in Figure 4.8.

4.2 Track reconstruction of cosmic ray muons

The muon rate in SK is ~ 2 Hz. These muons sometimes break ^{16}O nuclei in water and make radio-isotopes called “spallation products”. When spallation products decay, e^{\pm} and/or γ are emitted and these events are one of the major backgrounds and are called “spallation events”. In order to reject these backgrounds, space and time correlations between muons and low energy events, and muon pulse height information are used as cut parameters. A muon track reconstruction is necessary to evaluate the space correlation. In this section, track reconstruction for penetrating cosmic muon events is described.

4.2.1 μ track

Penetrating muons have entrance and exit points. The entrance point is easily found by looking for the earliest PMT hit. The exit point can be found either by using Cherenkov ring pattern information or PMT hit timing information. A fast muon reconstruction using the pattern information and a TDC fit using timing information are developed.

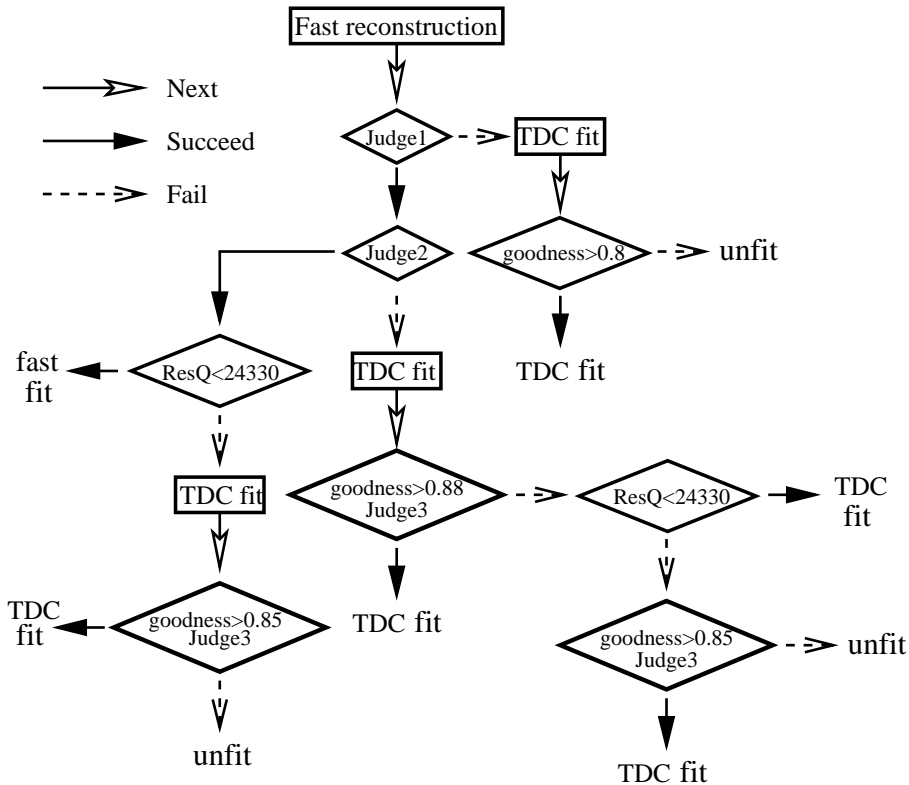


Figure 4.9: Flow chart of the muon reconstruction. ‘fit’ is for successful muon reconstruction and ‘unfit’ for mis-reconstruction.

Latter is more precise and stable but time consuming and it is applied only when the fast muon fit fails. The flow chart of the muon track reconstruction is shown Figure 4.9.

1. The fast reconstruction

entrance : The earliest hit PMT with more than 2 neighboring hit PMTs within 5 nsec is looked for. This requirement of a cluster avoids an accidental dark hit to be considered as the entrance.

exit : Saturation of ATM (and PMT) corresponds to 231 photo-electrons. It usually happens around the exit point. The weighted center of those saturated PMT positions is considered as the exit point.

quality check : If there is a saturated-PMT which has a distance of more than 300 cm to the entrance (Judge1) and less than 300 cm to the exit (Judge2), the reconstruction is classified as ‘succeeded’. This fast reconstruction doesn’t work well with stopping muons and muon bundles.

2. The TDC fit

entrance : It is common with the fast reconstruction.

exit : A grid search of the exit point is done with the $goodness_\mu$ defined as follows,

$$goodness_\mu \equiv \frac{\sum_{i=1}^{N_{hit}} \frac{1}{\sigma_i^2} \exp \left\{ -\frac{1}{2} \left(\frac{t_i - T}{1.5\sigma_i} \right)^2 \right\}}{\sum_{i=1}^{N_{hit}} \frac{1}{\sigma_i^2}} \quad (4.12)$$

here,

$$t_i = T_i - \frac{d_\mu^i(x_{exit})}{c} - \frac{d_{photon}^i(x_{exit})}{c/n} \quad (4.13)$$

σ_i = Time resolution of the i -th hit PMT
 T = Time when the muon enters the ID
 T_i = Time when the i -th PMT detects Cherenkov photon
 T_i = Time when the i -th PMT detects Cherenkov photon
 x_{exit} = Muon exit point
 $d_\mu^i(x_{exit})$ = Pass length of the muon before Cherenkov emission to i -th PMT
 $d_{photon}^i(x_{exit})$ = Flight length of the Cherenkov photon detected by i -th PMT
= Light velocity in vacuum
= Refractive index of water

Figure 4.10 shows the definition of parameters used in $goodness_\mu$.

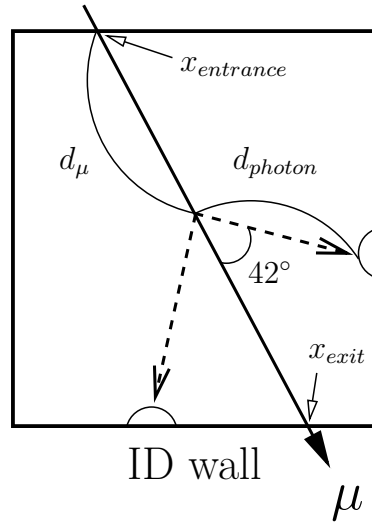
quality check : The $goodness_\mu$, Judge3 (if a saturated-PMT with distance less than 300 cm to the exit exists) and the value ResQ described below are used.

If the muon is very energetic, many PMTs saturate and Judgement1~3 are not relevant. The ResQ defined in the following formula discriminates such muons,

$$ResQ = Q_{total} - p \times L_\mu. \quad (4.14)$$

Here Q_{total} is the total photo-electrons in the event, L_μ is the track length of the muon and p is the average number of photo-electrons per unit track length for a minimum ionization muon (= 23p.e./cm). If $ResQ \geq 24330$ photo-electrons, the muon is flagged as ‘unfit’.

The efficiency of a good ‘fit’ with this combination of muon reconstructions was studied with manually scanned 1000 real muon events. Efficiencies for the following

Figure 4.10: The definition of parameters used in $goodness_\mu$

| μ type | number of events | number of unfitted events | efficiency |
|--------------|------------------|---------------------------|------------|
| clear | 835 | 5 | 99.4% |
| stopping | 10 | 8 | 20% |
| hard | 41 | 2 | 95.1% |
| edge clipper | 58 | 19 | 67.2% |
| multi | 56 | 28 | 50% |
| Total | 1000 | 62 | 93.8% |

Table 4.1: Summary of muon fitter efficiency for various types of muons

muon categories are obtained as shown in Table 4.1,

- clear : A through-going muon which has a clear single track
- stopping : A muon which stopped in the ID
- hard : A muon with $ResQ \geq 24331$ photo-electron
- edge clipper : A through-going muon with track length $\leq 5m$
- multi : A event which contains more than 1 muon track

The overall efficiency of the muon reconstruction is found to be approximately 94%.

The resolution of the muon track reconstruction is estimated by a muon M.C. simulation. Manually obtained entrance points ($P_{ent}(eye)$) and exit points ($P_{exit}(eye)$) are compared with entrance points ($P_{ent}(fit)$) and exit points ($P_{exit}(fit)$) from the muon track reconstruction. Difference($diff_\mu$) of them defined below was obtained as shown in

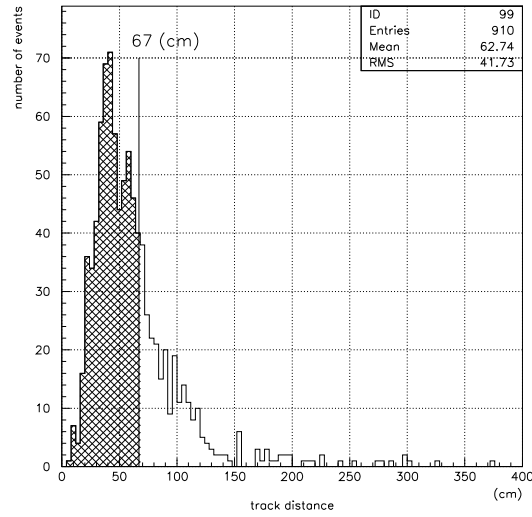


Figure 4.11: The track resolution of the muon fitter. The resolution is obtained as 67 cm.

Figure 4.11.

$$diff_{\mu} = \frac{|P_{ent}(eye) - P_{ent}(fit)| + |P_{exit}(eye) - P_{exit}(fit)|}{2}. \quad (4.15)$$

The 1σ track resolution defined by the $diff_{\mu}$ is found to be 67 cm.

Figure 4.12~ 4.14 show the charge distribution of cosmic-ray μ events, reconstructed zenith angle distribution and azimuth angle distribution of cosmic-ray muons. The azimuthal distribution is not uniform due to different thickness of Mt.Ikenoyama and neighboring mountains.

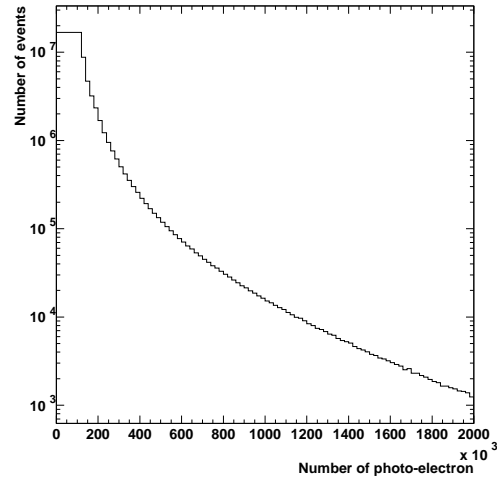
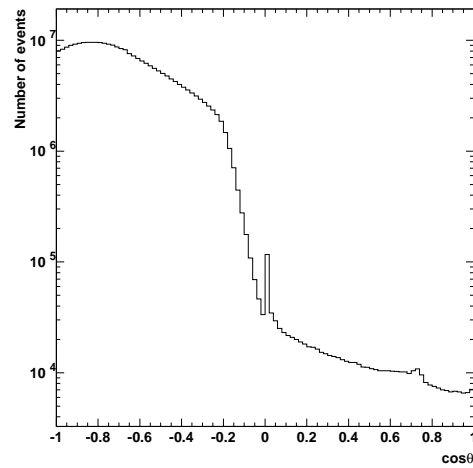
Figure 4.12: Charge distribution of cosmic μ events

Figure 4.13: Reconstructed zenith angle distribution of cosmic muons

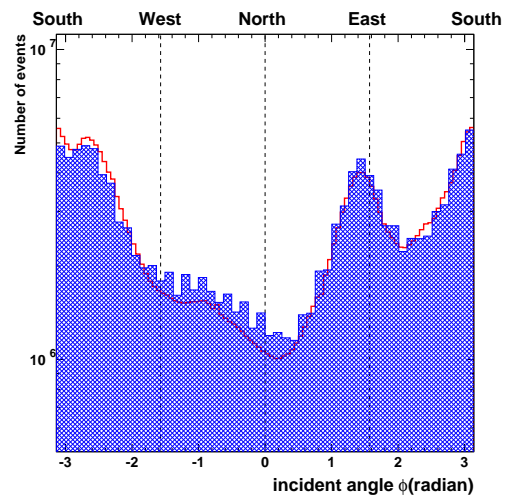


Figure 4.14: Reconstructed azimuth angle distribution of cosmic muons (red) and expected azimuthal angular distribution (blue hatched histogram) [64].

Chapter 5

Calibration

In order to check the detector performance, various calibrations have been done in Super-Kamiokande. In this chapter, calibration systems and results for relative and absolute PMT gain, timing, water transparency, energy and trigger efficiency are described.

5.1 Xe calibration

The relation between gain(G) and high voltage which is applied to the PMT(V) is expressed approximately as follows,

$$G = a \cdot V^b. \quad (5.1)$$

Here a and b are constants for each PMT and V is the high voltage(HV). At the first period of SK-I, relative gain for each PMT is adjusted by changing HV based on equation 5.1.

In order to calibrate the relative gain for inner PMTs [68] and to search for dead or broken channels, the Xe calibration is used. A schematic view of this calibration system is shown in Figure 5.1 and each components are as follows :

- Xenon flash lamp
A xenon flash lamp is used as a light source. The xenon flash lamp is a pulsed light source. Intensity fluctuations are less than 5%. After a few hours of operation, this change is less than 1%.
- Filters
The light generated by the Xe flash lamp passes through UV¹ filters and ND² filters. The scintillator ball absorbs UV light, so UV filters are used to select UV

¹Ultraviolet

²neutral density

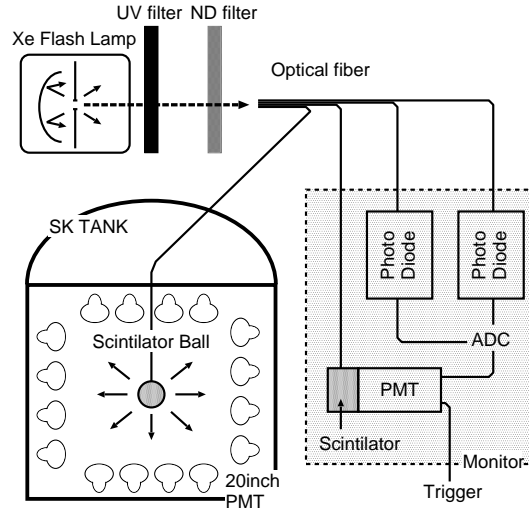


Figure 5.1: A schematic view of Xe calibration system

light and reject light of other wavelengths. ND filters are used to attenuate the light. The intensity of light from scintillator ball is controlled by using ND filters.

- Light transport and optical fiber
After passing the filters, the light is split to four lines. Three lines are connected to a photo-diode and a 2 inch PMT to monitor the light intensity and to be used as a trigger. The fourth line connected to an optical fiber which is inserted into the scintillator ball. The optical fiber has a pure quartz core so transmission losses are small in the UV region we use.
- Scintillator ball
The scintillator ball is made of acrylic plastic which contains 50 ppm³ BBOT and 500 ppm MgO. BBOT is used as a wavelength shifter. The typical wavelength of the light emitted from the scintillator ball is 440 nm, which is similar to Cherenkov light. MgO is used to diffuse light so the output light distribution is uniform.

In order to check the relative charge, water transparency, light diffusion, acceptance of PMT and ball asymmetry effects are corrected. The definition of the corrected charge (corrected Q) for each PMT is as follows,

$$\text{corrected Q} = \frac{Q \times r^2}{\exp(-r/L) f_{acc}(\theta_{PMT}) f_{ball}(\theta) f_{ball}(\phi)}, \quad (5.2)$$

³part per million

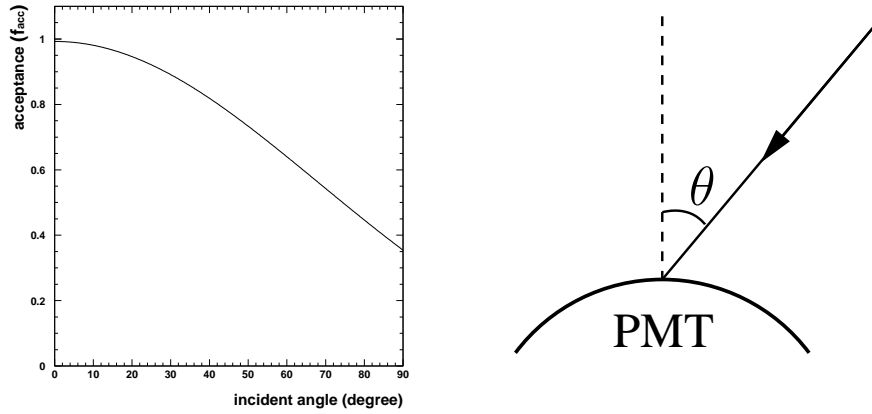


Figure 5.2: The relative acceptance function of PMT. Left figure shows the relative acceptance as a function of θ . Right Figure shows the definition of θ

where,

- Q : Charge of a PMT
- r : Distance from PMT to the scintillator ball
- L : Attenuation length of water
- f_{acc} : Acceptance correction of PMT(Figure 5.2)
- $f_{ball}(\theta)$: Correction function of scintillator ball asymmetry
(vertical direction angle)
- $f_{ball}(\phi)$: Correction function of scintillator ball asymmetry
(horizontal direction angle)

Figure 5.3 shows the corrected Q of all PMTs. The spread in relative gain is almost 7%. The time variation in the gain spread is found to be stable within 2% as shown in Figure 5.4.

5.2 Ni-Cf calibration

Ni-Cf calibration system is used to check the PMT gain at the single photo-electron level. A schematic view of the Ni-Cf calibration system is shown in Figure 5.5. In this calibration, gamma-rays from the $\text{Ni}(n,\gamma)\text{Ni}^*$ reaction are used. Here n is a thermalized neutron which is emitted from a spontaneous fission of ^{252}Cf located in the center. The energy range of this gamma-ray is $6 \sim 9$ MeV, and Compton electrons produced by the gamma-rays emit Cherenkov photons. Each PMT detects a signal at the one photo-electron level, therefore the peak value of the output charge is related to the absolute

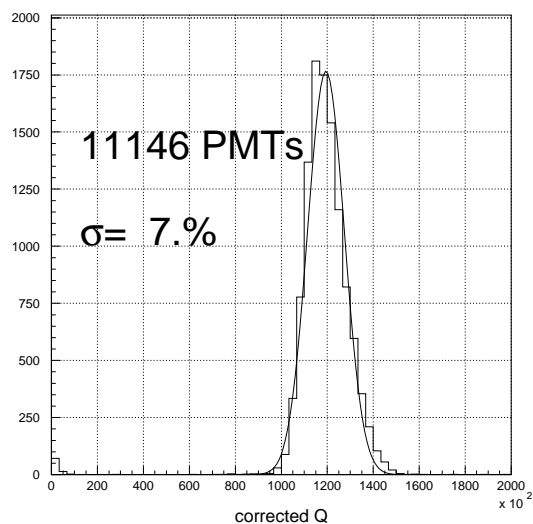


Figure 5.3: Distribution of the corrected charge of all inner PMTs.

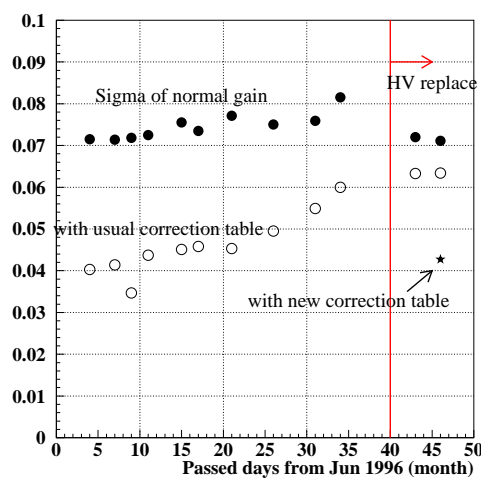


Figure 5.4: Time variation of sigma for charge spread. Black circles show the sigma of corrected Q. Blank circles show the corrected Q with the gain correction table [68] which is used in the atmospheric neutrino analysis. In July, 2000, all HV was fixed and the gain was slightly changed, so the correction table was made to cancel this effect. The black star shows corrected Q with the new correction table.

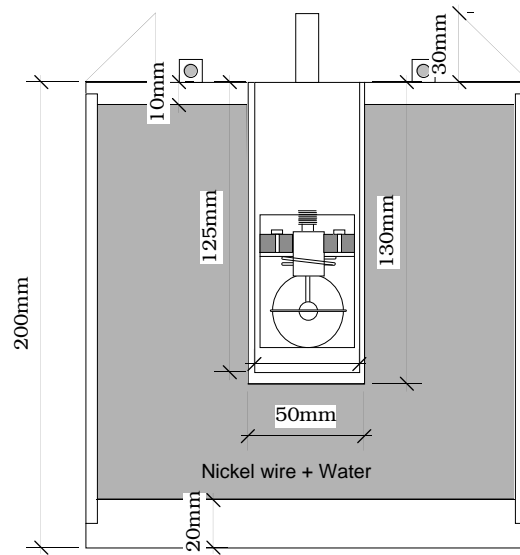


Figure 5.5: A schematic view of Ni-Cf calibration system.

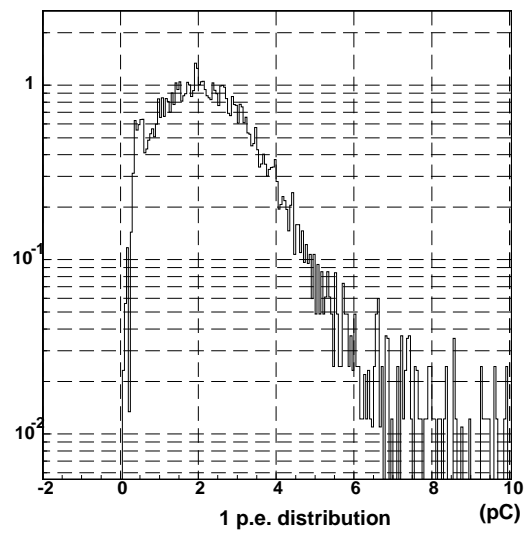


Figure 5.6: The charge distribution of typical PMT after a single photo-electron hit

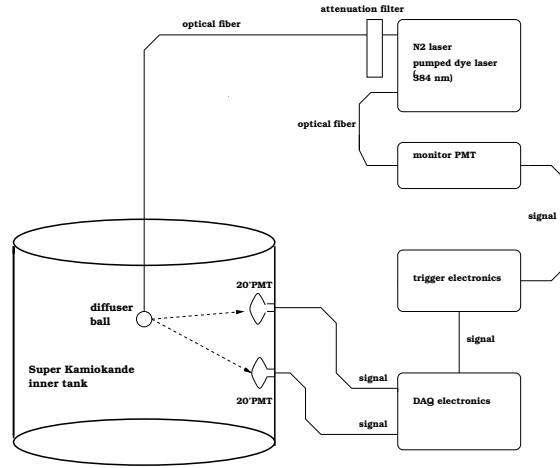


Figure 5.7: A schematic view of timing measurement system

gain. Figure 5.6 shows the typical output charge distribution for the 1 p.e. level. From the mean value of these distributions, the relation between output charge and p.e. is obtained as 1 p.e. = 2.055 pC.

5.3 TQ map

The timing information of each PMT is used for vertex and direction reconstruction, but the timing of each PMT is different by the length of cable, transit time in the PMT and the quantity of received photons. The time when a signal exceeds a threshold in the discriminator is defined as the time the light reached the PMT (T_0). In order to calibrate these timing differences, the laser calibration system is used. A schematic view of the laser calibration system is shown in Figure 5.7. A N_2 laser is used for the light source and generates 337 nm wavelength with a pulse width of about 3 nano seconds. Output light from the laser is fed to a dye laser and shifted to 384 nm. The laser light is split. One branch goes to a diffuser ball optical fiber, the other goes to a monitor PMT whose signal is used for monitoring and triggering. The diffuser ball consists of TiO_2 and LUDOX. LUDOX is a silica gel with 20 nm glass fragments. TiO_2 is attached to the tip of optical fiber. These provide effective diffusion without timing spread.

Figure 5.8 shows the timing response as a function of charge for a typical PMT. This figure is called ‘TQmap’. In order to get the correction function for timing, the following function is used for fitting to the TQmap,

$$T(Q) = a_0 + a_1Qi + a_2Q^2 + a_3Q^3 + a_4Q^4 + a_5Q^5 + a_6Q^6 + a_7Q^7. \quad (5.3)$$

The timing resolution is estimated from the $T(Q)$ distribution for each pulse height Q .

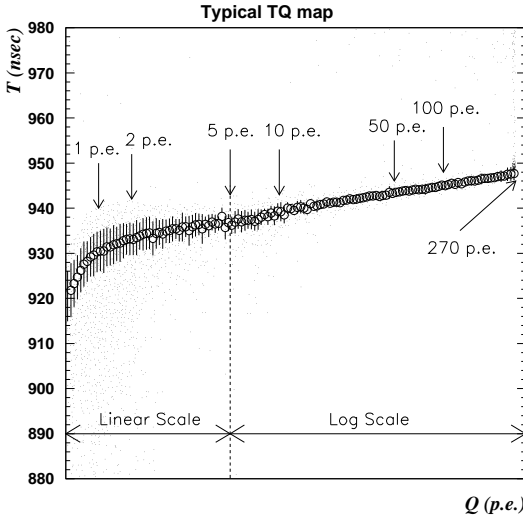


Figure 5.8: The TQ map of a typical PMT

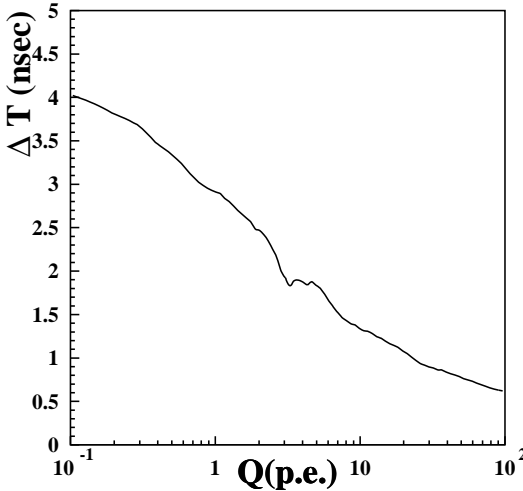


Figure 5.9: Timing resolution as a function of the pulse hight

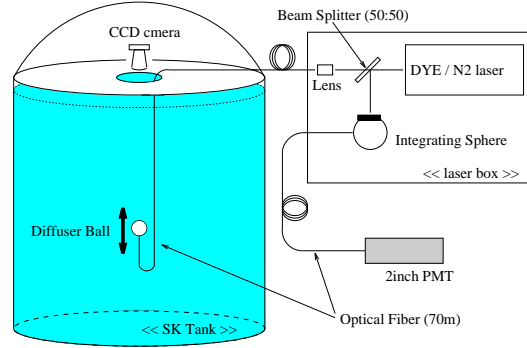


Figure 5.10: A schematic view of the direct measurement of the water transparency.

Figure 5.9 shows the timing resolution as a function of pulse height and this resolution at the 1 p.e. level is about 3 nsec.

5.4 Water transparency

Water transparency is important information for event reconstruction, because the number of photons which arrive at the PMTs depends on the water transparency. Water transparency is measured by two methods in SK. One is a direct measurement using a CCD camera and the other uses Michel electrons.

5.4.1 Direct measurement by laser and CCD camera

Figure 5.10 shows a schematic view of the direct water transparency measurement. A N_2 laser and DYE is the light source in this measurement. Light from the laser is split with half of the light used to monitor its intensity and half of the light used for the measurement. The light used for the measurement travels down an optical fiber to a diffuser ball placed in the SK tank. The diffuser ball is an acrylic ball with MgO and can be moved in the vertical direction. The light from diffuser ball is measured by a CCD camera at the top of the SK tank. The water transparency L is obtained from following function,

$$I(d) = \frac{I_0}{d^2} \exp\left(-\frac{d}{L}\right) \quad (5.4)$$

where I_0 is the intensity of the light source and $I(d)$ is the measured intensity at the distance of d . Figure 5.10 shows the result of measured light intensities as a function of the distance between the CCD camera and the diffuser ball for a wavelength of 420 nm. The fit result for this measurement is 97.9 ± 3.5 m. This measurement is performed for

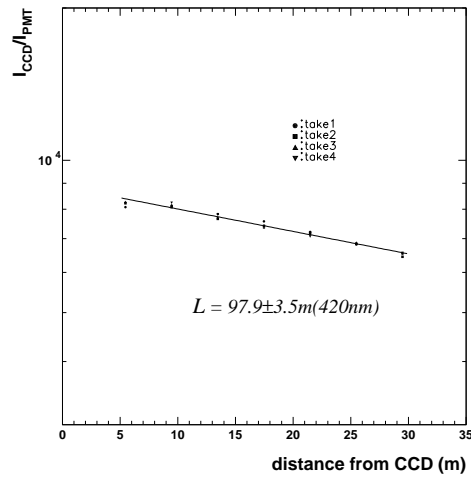


Figure 5.11: Results of the CCD camera direct measurement for 420 nm case

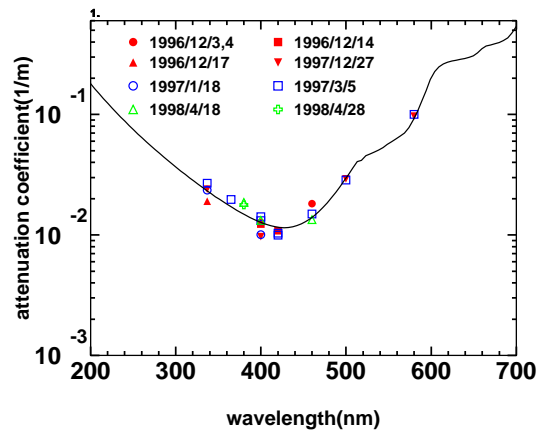


Figure 5.12: Water transparency as a function of wavelength

other wavelengths (337 nm \sim 580 nm) as well. Figure 5.12 shows the water transparency as a function of wavelength. The solid line in this figure shows the water transparency used in the detector simulation.

5.4.2 Time variation of water transparency by using decay electrons

The time variation of water transparency is monitored by using the decay electron from cosmic ray muons [69]. The selection criteria of decay electron events are as follows,

- In water, The life time of a stopped muon is 2.08 μ sec. Therefore, events where the time difference between a stopping muon and a low energy event is within 1.5 μ sec \sim 8 μ sec are selected.
- The low energy event is in the fiducial volume (distance between reconstructed vertex and wall is larger than 200cm)
- The number of effective PMT hits is larger than 70.

The number of decay electron events selected is about 1500 per day. For the transparency calculation, Cherenkov radiation from the decay electron is used. The relevant hit PMTs are selected as follows :

- Hit timing after TOF subtraction is within 50 nsec.
- PMT positions are within a cone of Cherenkov opening angle $32^\circ \sim 52^\circ$ (Figure 5.13).

Water transparency is calculated as follows :

$$Q = q(r) \exp\left(\frac{r}{\lambda}\right), \quad (5.5)$$

where r is the distance between the hit PMT and reconstructed PMT, λ is the water transparency and $q(r)$ is the charge of hit PMTs at distance r . From this equation, $\log(q(r))$ is obtained as follows,

$$\log(q(r)) = -\frac{r}{\lambda} + \log Q. \quad (5.6)$$

Figure 5.14 shows the typical distribution of $\log(q(r))$ as function of r . From a linear fit to this distribution, λ is obtained. Figure 5.15 shows the long term time variation of water transparency by this method. Water transparency varies according to water purification mode and improvements, but this variation is reflected in energy reconstruction and M.C. detector simulation.

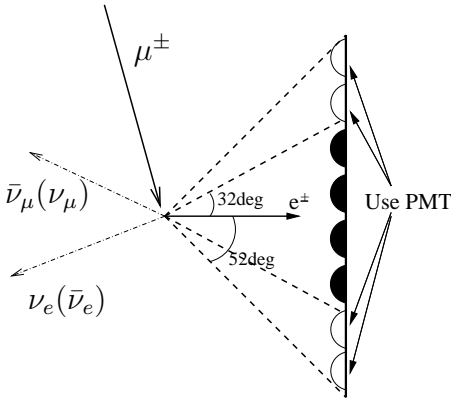


Figure 5.13: Definition of the PMTs which are used for water transparency calculation.

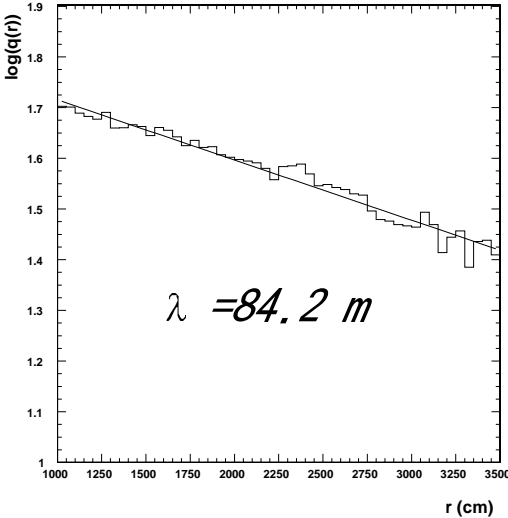


Figure 5.14: Time $\log(q(r))$ distribution as function of r

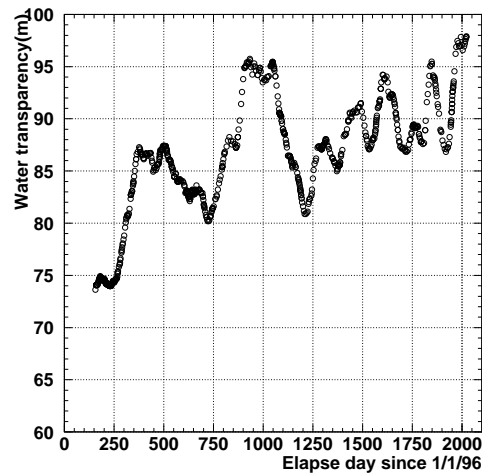


Figure 5.15: Time variation of water transparency

5.5 Automatic calibration systems

Automatic calibration systems were installed in October 1999. The purposes of this system are as follows :

- Conventional calibrations had been performed a few times per year and bad channels were selected using these calibrations, but we wanted to find bad channels immediately.
- For a failure or an improvement, exchange of hardware was often performed. The effect on the data should be studied and be corrected.
- We wanted to monitor the state of a detector continuously.
- We don't know when a supernova burst will happen, but conventional measurements required us to halt physics data-taking. Therefore we wanted to reduce the frequency of conventional calibration.

In order to satisfy these demands, relative gain and timing calibration were changed to automatic calibration. Also, water transparency calibration was added to this system.

Automatic calibrations are performed in physics run mode. To separate these calibration data from physical events, online processes make a 'periodic trigger' once every 6 seconds. This periodic trigger is supplied for each calibration system and one light source in the automatic calibration system is fired from this trigger. This trigger is 1 set by six kinds and assigned as follows, 'Timing, Xe, water 337 nm, water 371 nm, water 400 nm,

water 420 nm'. The calibration data is selected in the offline process. Each calibration data type is separated by using the event pattern information. Selected calibration data are stored in a data disk in order to re-analyze the calibration data.

5.5.1 Gain

A Xe Lamp system (Figure 5.1) is used in automatic Xe calibration. The scintillator ball for this calibration consists of a 50 mm diameter acrylic plastic ball which contains 25 ppm POPOP and 2000 ppm MgO. And 3 mm in diameter and 5 mm in height cylindrical diffuser tip with 10000 ppm of MgO which is placed at the center of this ball. The scintillator ball is placed at (+318.1, -70.7, 0.0) cm in the SK tank.

A Xe calibration trigger is assigned once every 36 seconds, but the Xe lamp flashes every 216 seconds. This event rate was calculated in order to be within 1% of statistical precision using one week of data acquisition.

Automatic gain calibration is used for selection of the dead, unstable gain and gain changed PMTs during real time process. Therefore if the measured charge of a PMT changes 10% from the standard value which is calculated from past value, this PMT is set as a bad PMT and e-mail with the bad PMT list is sent to the experts from the real time process. If Xe lamp is not flashing, e-mail is sent like above. When the experts receive this e-mail, they check the data and improve or get in touch with each hardware expert.

5.5.2 Timing

Laser calibration system (Figure 5.7) is used in automatic timing calibration. The diffuser ball for this calibration consists of a 50 mm diameter acrylic plastic ball which contains 1,500 ppm of MgO, and a 3 mm in diameter with 5 mm in height cylindrical diffuser tip with 10000 ppm of MgO placed at the center. The scintillator ball is placed at (-141.4, -70.7, 0.0) cm in the SK tank. The laser flashes every 360 seconds. Automatic gain calibration is used for the selection of bad timing PMTs which are caused by hardware replacement or trouble. A PMT whose T_0 is changed more than 1 nsec from the mean of all PMTs is labeled a bad channel and e-mail with the bad PMT list is sent to the experts from the real time process like automatic Xe calibration. When the experts receive this e-mail, they check the data and improve or get in touch with each hardware expert. If this change is caused by a hardware replacement, a new TQ-map is installed by this calibration data.

5.5.3 water transparency

Figure 5.16 shows the automatic water transparency calibration system and typical event pattern. 4 wavelengths are used in this calibration and are injected in SK tank via optical

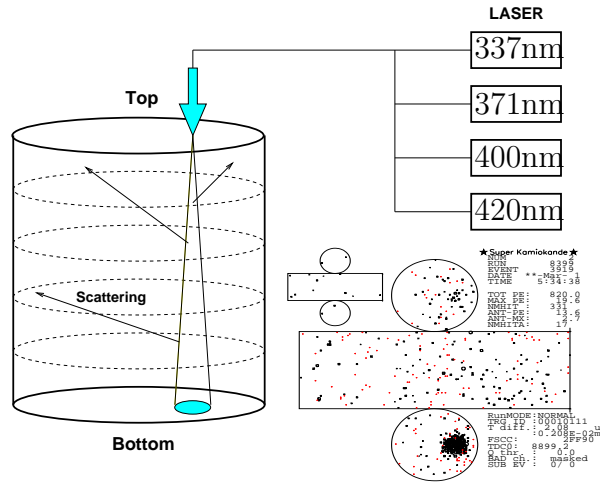


Figure 5.16: A schematic view of the system for automatic water parameter measurement

fibers. Each laser of a given wavelength flashes every 36 seconds. The injection point is (35.5, -777.7) cm. This calibration is used for measuring water parameters and their time variation. Water transparency consists from absorption, Rayleigh scattering, and Mie scattering. The M.C. simulation is used to tune these parameters.

5.6 LINAC

Precise knowledge of the absolute energy scale, energy resolution, vertex resolution and angular resolution for electrons are important for solar neutrino measurements. In order to satisfy these demands, an electron linear accelerator (LINAC) is used in SK [70]. Figure 5.17 shows a schematic view of LINAC calibration system. The electron energy from the LINAC can be changed from 5 ~ 16 MeV. The accelerated electrons are bent by D1 ~ D3 magnets and energy selected by magnets. The electron current is reduced by magnets and collimators near magnets. Almost 0.1 electrons per bunch are injected in the SK tank in order to ensure there is no more than one electron per bunch.

The beam energy is measured by a germanium detector. After data taking, the D3 magnet which bends the beam to the SK tank is removed and a germanium detector is set in the beam line. The germanium detector is calibrated by 1.33 MeV gamma-rays of ^{60}Co , 0.662 MeV gamma-rays of ^{137}Cs and 6.098 MeV ~ 9.000 MeV gamma-rays from the $\text{Ni}(n,\gamma)\text{Ni}^*$ reaction (Sec. 5.2).

Figure 5.18 shows a comparison of various parameters between observed LINAC data and M.C. simulation for each beam injection point (shown in Figure 5.17 and Table 5.1) The results of absolute energy scale, energy resolution, angular resolution, vertex resolution are shown in (a), (b), (c), (d), respectively.

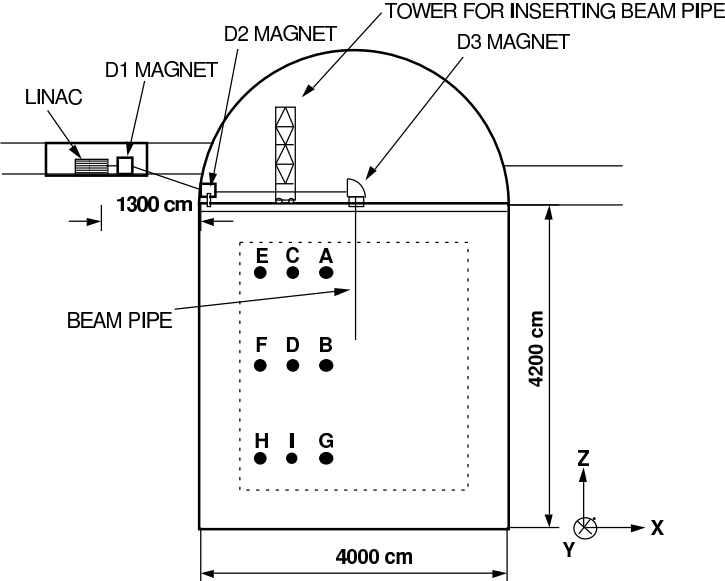


Figure 5.17: A schematic view of LINAC calibration system

| No. | X(cm) | Y(cm) | Z(cm) |
|-----|---------|-------|---------|
| A | -388.9 | -70.7 | 1228.0 |
| B | -388.9 | -70.7 | 27.0 |
| C | -813.1 | -70.7 | 1228.0 |
| D | -813.1 | -70.7 | 27.0 |
| E | -1237.0 | -70.7 | 1228.0 |
| F | -1237.0 | -70.7 | 27.0 |
| G | -388.9 | -70.7 | -1173.0 |
| H | -1237.0 | -70.7 | -1173.0 |
| I | -813.1 | -70.7 | -1173.0 |

Table 5.1: Injection position of LINAC beam

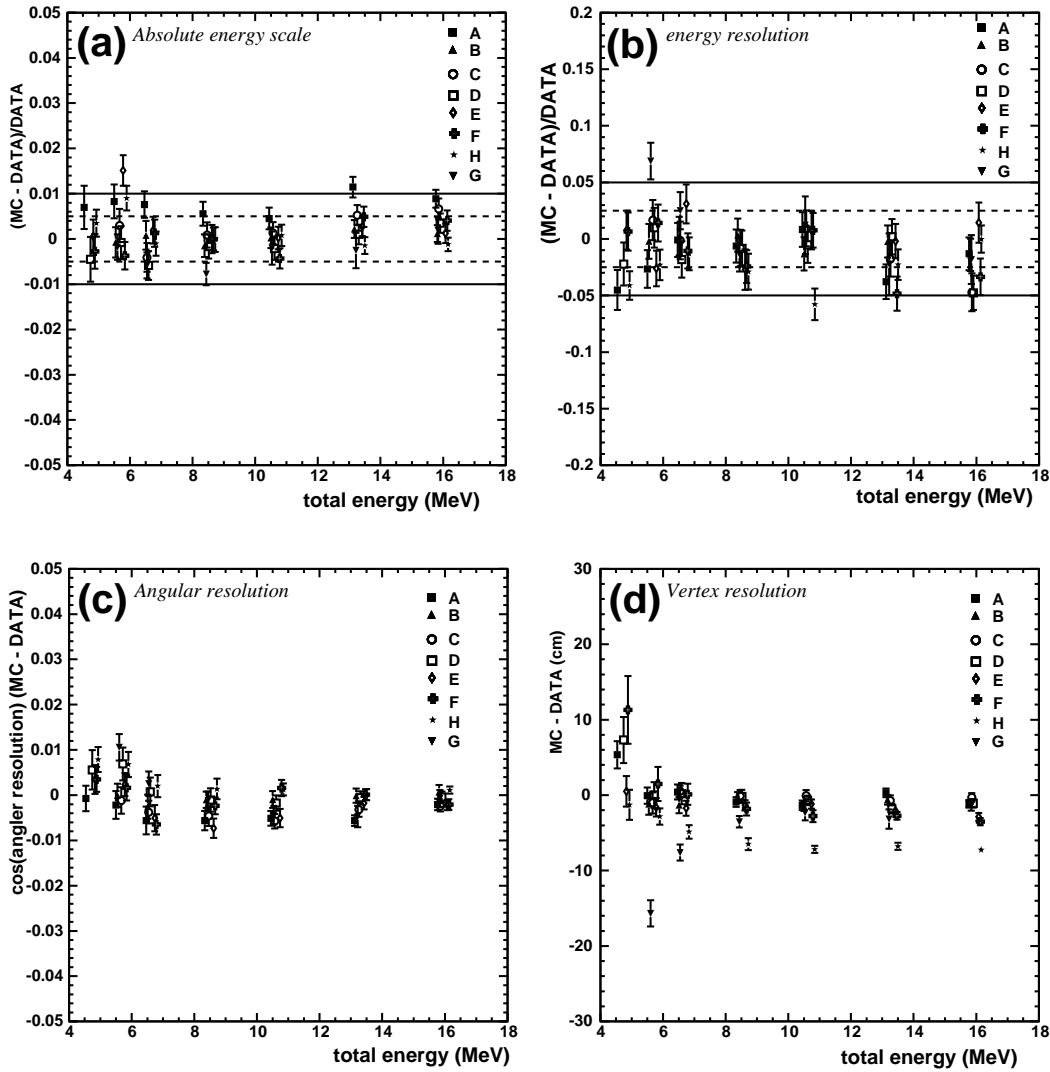


Figure 5.18: Results of LINAC calibration. These figures show comparison between observed data and M.C. simulation data for each beam injection point shown in Table 5.1. (a) : absolute energy scale, (b) : energy resolution, (c) : angular resolution and (d) : vertex resolution.

5.7 DT calibration

The electron and γ -ray from the decay of ^{16}N are used to cross check the LINAC calibration results, to check the directional dependence of the energy scale and to check the trigger efficiency. ^{16}N is produced by the following reaction,



The neutron is provided by a deuterium-tritium neutron generator (DTG) [71]. A schematic of the DTG is shown in Figure 5.19. The difference from the LINAC calibration is as follows,

- It is easy to set up the calibration equipment for each point.
- It is possible to carry out in a short time.
- The LINAC can check only downward-going events, but the DT calibration is isotropic.

The DTG produces neutrons by the following reaction,



The generated neutron by the DTG has 14.2 MeV and is enough to make ^{16}N by the (n,p) reaction on ^{16}O in the water of SK. The half-life of ^{16}N is 7.13 seconds. The ^{16}N decay with a Q-value of 10.4 MeV produces an electron with a 4.3 MeV maximum energy and a 6.1 MeV γ -ray. This electron and γ -ray is appropriate for the absolute energy scale calibration.

Figure 5.20 shows an overview of DT calibration data taking. First of all, the DTG is set to the position of data taking(a), and is fired in this position(b). After the DTG is fired, it is pulled up 2m(c) and data is collected. The DTG is pulled up to minimize reflection and shadowing.

Figure 5.22 and Figure 5.23 show the position dependent energy scale difference between observed data and M.C. data and the directional dependent one. The energy scale z-dependence is within $\pm 1\%$, the r-dependence within the fiducial volume is within $\pm 0.5\%$, and the azimuthal angle dependence is within $\pm 0.5\%$ and the zenith angle dependence is within $\pm 0.5\%$.

5.8 Time variation of energy

The energy scale is sensitive to water transparency and the transparency changes with time. The time variation effect of water transparency is corrected by decay electron events from cosmic-ray muons. However it is important to check the time variation of

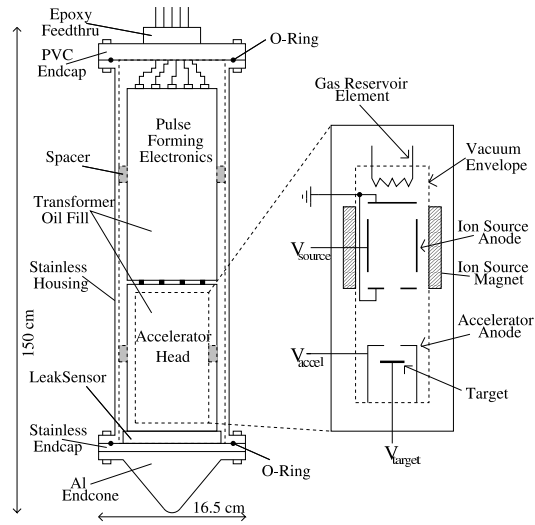


Figure 5.19: Schematic view of DT generator

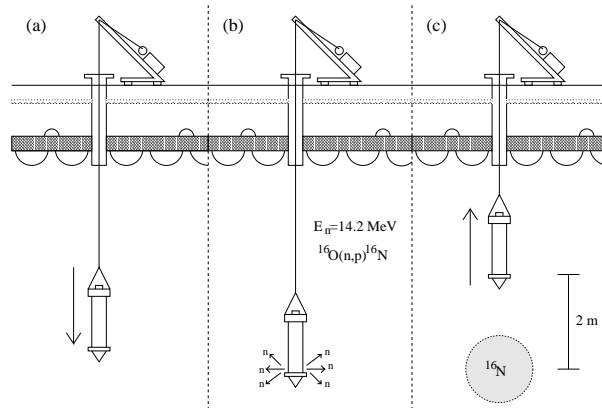


Figure 5.20: An overview of DT calibration data taking

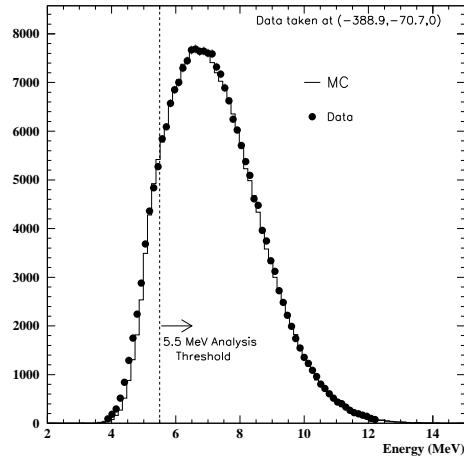


Figure 5.21: The energy distribution of a typical DT calibration

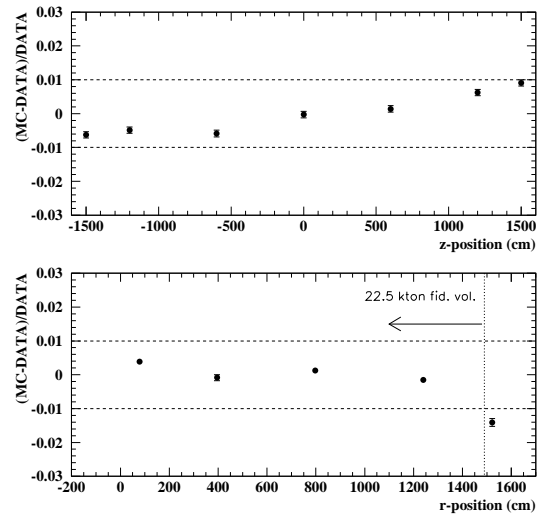


Figure 5.22: The position dependence of the energy scale from DT calibration

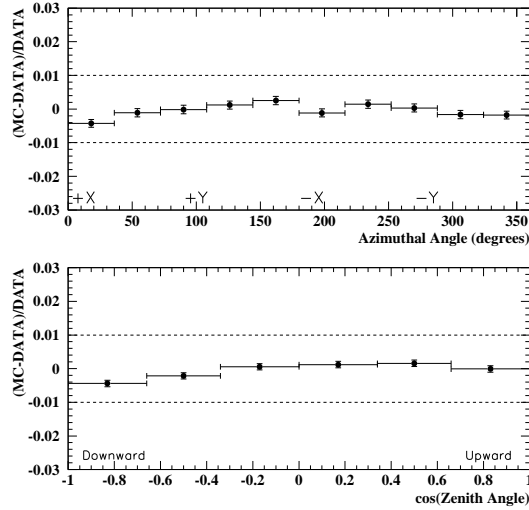


Figure 5.23: The angular dependence of energy scale from DT calibration

the energy scale. In order to check the time variation of energy scale, the decay electron events from the cosmic-ray muons and spallation events are used.

The energy spectrum of the decay electrons from stopping muons is called the Michel spectrum and is shown as following equation,

$$\frac{dN}{dE_e} = \frac{G_F^2}{12\pi^3} m_\mu^2 E_e^2 \left(3 - \frac{4E_e}{m_\mu} \right) \quad (E_e < \frac{m_\mu}{2}). \quad (5.9)$$

The average energy of these electrons (Figure 5.24) is almost 37 MeV and this energy region is much higher than solar the neutrino energy region. Therefore these events couldn't be used for the energy calibration. However they are useful to check for systematic differences of energy scale. Figure 5.25 shows the time variation of the mean N_{eff} value for decay electron events. This figure shows the energy scale is stable within $\pm 0.5\%$

The energy spectra of spallation events are also used to check for the time variation of the energy scale. Spallation events are caused by β and γ rays from radioactive nuclei produced by cosmic ray muon interactions in the water. Therefore, these spallation events are used to check the time variation of energy scale.

In order to use spallation events for this stability check, these criteria are applied for event selection.

- The time difference from a muon event to a low energy event is less than 0.1 seconds
- The distance between the reconstructed vertex of a low energy event with a reconstructed muon track is less than 300 cm

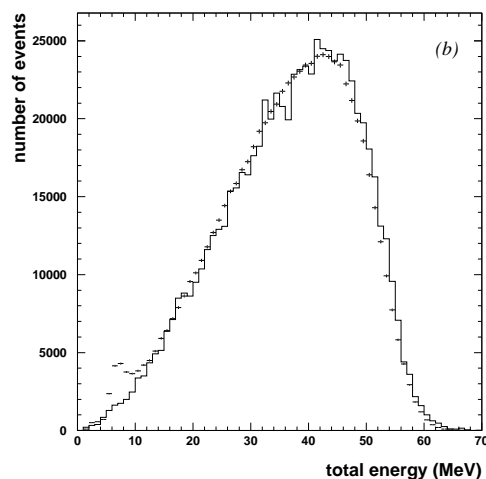


Figure 5.24: The energy spectrum of $\mu - e$ decay events in SK. The solid line shows M.C. events and the cross marks show observed data. The peak around 7 MeV is γ -ray events from ^{16}N which is made by the muon capture process, $\mu^- + ^{16}\text{O} \rightarrow \nu_\mu + ^{16}\text{N}$.

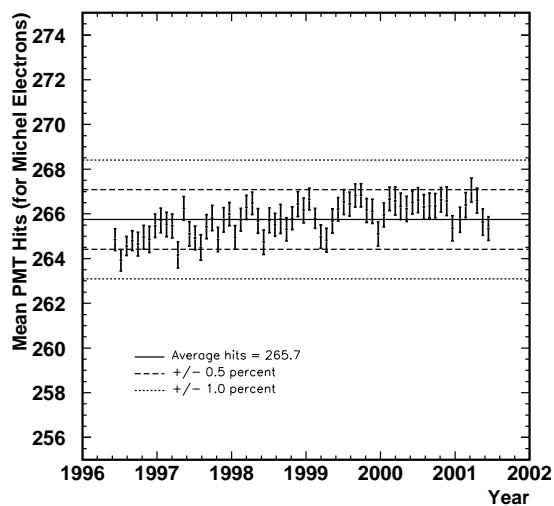


Figure 5.25: The time variation of energy scale by decay electron events from cosmic-ray muons. The dashed lines show $\pm 0.5\%$ deviation and the dotted lines show $\pm 1.0\%$ deviation.

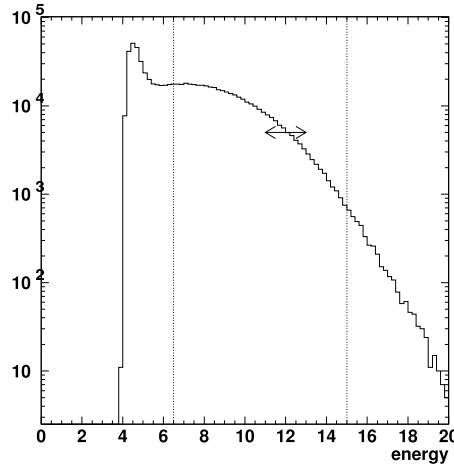


Figure 5.26: The energy spectrum for spallation events

- The spallation likelihood is larger than 0.98 (see Sec. 6.4 and Appendix. A)
- The vertex distance from inner wall is less than 200 cm(fiducial cut)
- $6.5 \text{ MeV} \leq E \leq 15.0 \text{ MeV}$
- The gamma cut (effective wall $\geq 450 \text{ cm}$)

Figure 5.26 shows the energy spectrum for spallation events. The energy spectrum for each period and all periods are used to check the energy scale difference. In order to compare the two spectra, the energy spectrum of each period and a scaled spectrum for all periods are prepared. By a χ^2 test for the two spectra, the relative time variation of the energy scale is calculated. Figure 5.27 shows the time variation of energy scale by using spallation events. The dashed line shows 0.5% and the dotted line shows 1.0 %. This figure shows that the energy scale is consistent within $\pm 1.0\%$ over the entire run time.

5.9 Trigger efficiency

As described in Sec. 3.9, LE and SLE triggers were used in the solar neutrino analysis. These two types of trigger had different thresholds, and the SLE threshold was changed several times in order to take lower energy data. Therefore it is important to measure this threshold when we want to use lower energy data and set an analysis threshold.

The trigger efficiency is measured by using the DT generator and the Ni-Cf source. When we take data for trigger threshold analysis, a special low energy trigger (DT trigger or Ni trigger) was set. These triggers have a lower threshold, -150 mV , than standard

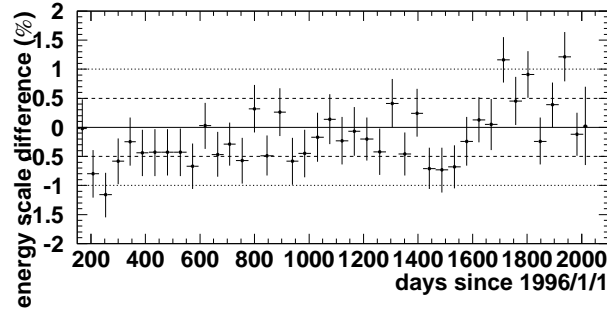


Figure 5.27: The time variation of the energy scale by spallation events

SLE data. The trigger threshold is analyzed from the ratio of the number of LE(SLE) events and special trigger events. The definition of trigger efficiency is as follows,

$$\text{Trigger efficiency} = \frac{N_{\text{LE(SLE) trigger}}}{N_{\text{DT(Ni) trigger}}}. \quad (5.10)$$

Here, $N_{\text{LE(SLE) trigger}}$ is the number of events which are identified by both the LE (or SLE) triggers and the special (DT or Ni) trigger. $N_{\text{DT(Ni) trigger}}$ is the number of events which are identified by the special trigger.

The trigger efficiency differences depend on the event vertex position, Cherenkov light direction and water transparency especially for lower energies because attenuation of light by the water transparency and electronics behavior for each electronics hut make asymmetries. In order to trace these asymmetries in the M.C. simulation, the trigger efficiency simulator is used. The trigger efficiency simulator makes flag information for each M.C. event by using the number of hit information after the application of an asymmetric correction. Therefore the trigger efficiency is obtained by this flag information similar to observed data.

Figure 5.28 shows the LE trigger efficiency as a function of energy for typical DT calibration data and M.C. data after the trigger simulation. The trigger efficiency of LE is almost 100% above 6.5 MeV and the difference between calibration data and M.C. data is used for the estimation of the systematic error.

SLE trigger threshold was changed at several times as described in Sec. 3.9. Figure 5.29 shows the latest SLE trigger efficiency, -186 mV case, as a function of energy. The trigger efficiency of latest SLE is almost 100% above 4.5 MeV. Trigger efficiencies were measured whenever the threshold was changed. For all periods after the SLE trigger was set, trigger efficiencies above 6.0 MeV are 100%. For below 6.0 MeV, efficiencies were not 100% for all periods, but these effects are traced by the M.C. and trigger simulation.

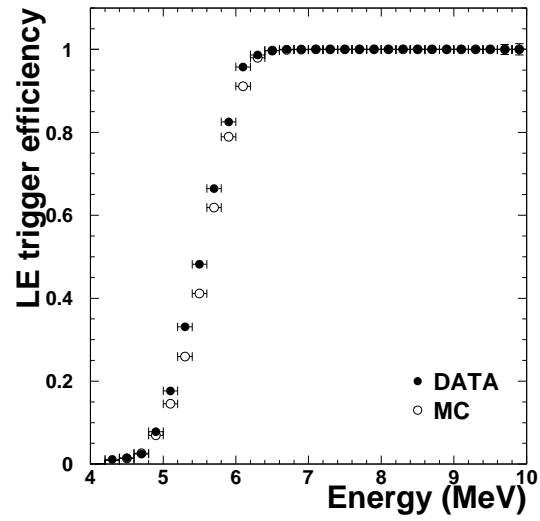


Figure 5.28: The LE trigger efficiency as a function of energy

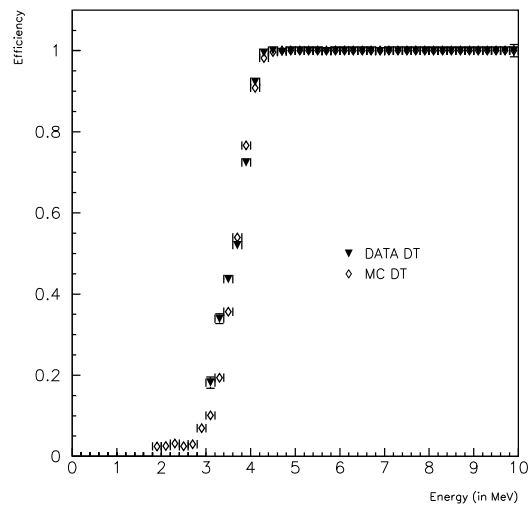


Figure 5.29: The SLE trigger efficiency as a function of energy

Chapter 6

Data Reduction

The data used for the solar neutrino measurement and the $\bar{\nu}_e$ search have been acquired in 1496 live days from May 31, 1996 to July 15, 2001. Dominant backgrounds in the solar neutrino data sample are as follows :

- electronics noise and flashing PMTs
- cosmic ray muons
- electrons from the decay of stopping muons
- muon-induced spallation products
- β from ^{214}Bi in Uranium chain (^{222}Rn background)
- external gamma rays from detector materials and surrounding rock

In order to reject these backgrounds and improve the S/N ratio, the following background reductions are performed step by step : first reduction, spallation cut, second reduction, and external γ -ray cut. The first reduction removes events from electronics noise and other non-physical sources, and events with poorly reconstructed vertices. The spallation cut removes events due to radio-isotopes (X) produced by cosmic ray muon interactions with water: $\mu + ^{16}\text{O} \rightarrow \mu + X + \dots$. These radio-isotopes are called “spallation products.” The spallation products emit beta and gamma rays and have lifetimes ranging from 0.001 to 14 sec. We cut these events using likelihood functions based on time, position, and muon pulse height. The time and position likelihood functions are measures of the proximity of a candidate event to a muon track, while the pulse height likelihood function measures the likelihood that a muon produced a shower. These three likelihood functions are used together to discriminate spallation events. The second reduction removes events with poor vertex fit quality and diffuse Cherenkov ring patterns, both characteristics of low-energy background events. The external γ -ray cut removes events due to γ -rays from the surrounding rock, PMTs, etc.. In this chapter, the data reductions are explained.

6.1 Data sets and run

The unit of the collected data is called ‘run’. The maximum run time is 24 hours and each run is divided into subruns whose times are about $60 \sim 600$ seconds, depending on the event rate. Bad runs (subruns) are rejected before to start the reduction with the following selection criteria,

- Run time is less than 5 minutes
These runs were stopped just after the start. It generally indicates that the DAQ system had some problems.
- Subrun time is less than 30 seconds.
It is difficult to check the data quality for such short subrun.
- Run has a hardware or software trouble
For example, high voltage, electronics troubles and lack of necessary information are serious problems for analysis.
- Calibration run or a calibration source is in the ID or on the tank
In order to study Rn effects, Rn water has once been put into the ID. In the case that a γ -ray source was on the tank before/after calibration run, the run is rejected.

6.2 Online reduction

Online reduction is performed to select the low energy events in real time with the following two cuts as described in Sec.3.10.

6.2.1 Total charge cut

The low energy analysis covers solar neutrino observation and the search for supernova neutrinos. The relevant energy region of the analysis is up to ~ 100 MeV. The total charge cut at 1000 p.e. corresponding to a recoil electron energy ~ 130 MeV removes muon events as shown in Figure 6.1.

6.2.2 Pedestal and periodic trigger cut

In the SK data acquisition system, pedestal data are taken once every 30 minutes (Sec.3.8.1) and auto calibration data are taken once every 6 seconds (Sec.5.5) during normal running. These unphysical events are tagged with special trigger flags (pedestal trigger or periodic trigger), and are rejected according to the flags.

Therefore the data which contain these special triggers are rejected.

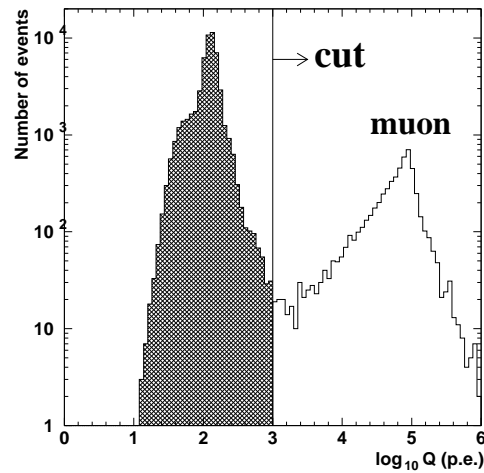


Figure 6.1: The total charge distribution of typical data. The total charge cut saves events below 1000 p.e.

6.3 First reduction

The purpose of the first reduction is to remove unphysical events such as electronic noise events, flash tube events, other non-physical sources and events with poorly reconstructed vertices. It also discards events near the wall for reducing the number of events to be supplied to later sophisticated but time-consuming selections. In this section, criteria for the first reduction are described.

6.3.1 Fiducial volume cut

Vertices of γ -ray events from the surrounding materials are close to the ID wall. In order to reject these events, the events which have a vertex position within 200 cm of the ID wall are removed. With this cut, the fiducial radius, the fiducial height, the fiducial volume for the solar neutrino analysis are defined to be 1490 cm, 3220 cm and 22.5 kton, respectively. Figure 6.2 shows vertex distributions before and after the fiducial volume cut to a typical data sample.

6.3.2 $DT \geq 50 \mu\text{sec}$ cut

In order to remove decay electrons from stopping muons and ‘ringing events’, events with a time difference from previous events of less than $50 \mu\text{sec}$ are removed. ‘Ringing event’ is a DAQ noise event appearing after a very large energy deposit. Figure 6.3 shows the time difference distribution before and after the cut.

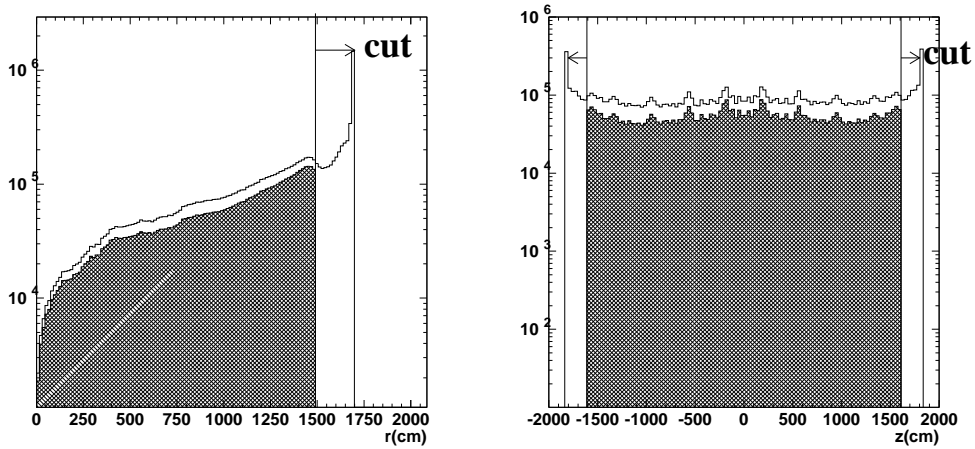


Figure 6.2: Vertex distributions before and after the fiducial volume cut to a typical data sample. The blank histograms show the distribution before the cut and the hatched histograms are after the cut. The left figure shows the distribution as a function of radial position ($r = \sqrt{x^2 + y^2}$). The right figure shows the distribution as a function of z position.

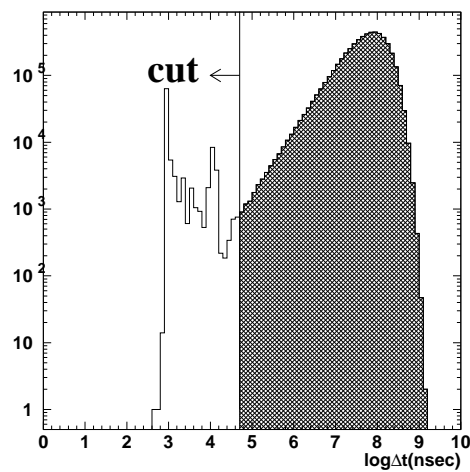


Figure 6.3: The distribution of the time difference from a typical data sample. The line shows the $50 \mu\text{sec}$ cut line and the hatched region shows the remaining events after the time different cut.

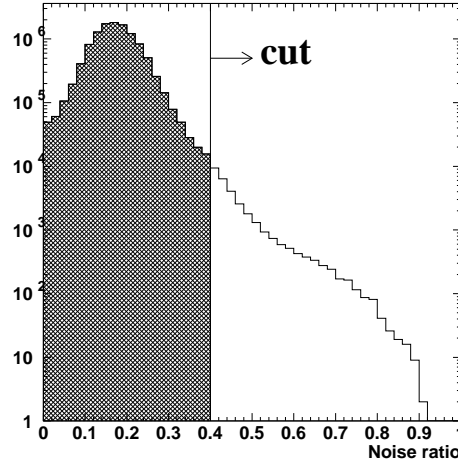


Figure 6.4: The distribution of the noise ratio from a typical data sample.

6.3.3 OD triggered event cut

In order to reject lower energy cosmic ray muons with total photo-electron less than 1000 p.e., events with an OD trigger (total OD-PMT-hits in a 200 nsec time window are larger than 19) are rejected.

6.3.4 Noise (NSratio) cut

When turning on a fluorescent light near the detector and/or from other electric actions, electronics noise events often appear. Most of the hit channels in those events have charges of less than 0.5 p.e. The following ‘noise ratio’ discriminates those noise events very well :

$$\text{noise ratio} = \frac{N_{\text{noise}}}{N_{\text{total}}}, \quad (6.1)$$

where N_{noise} is the number of hit PMTs with charges less than 0.5 p.e. and N_{total} is the total number of hit PMTs. Figure 6.4 shows the noise ratio distribution. If the noise ratio is larger than 0.4, the event is thrown away.

6.3.5 Cluster-ATM-hits-event cut

Some noises in a ATM board unit, make clustering noise hit PMTs in one ATM board. These events are removed with a measure ‘ATM ratio’ defined as follows,

$$\text{ATM ratio} = \frac{N_{\text{hit}}_{\text{max hit ATM}}}{N_{\text{hit}}_{\text{total}}}, \quad (6.2)$$

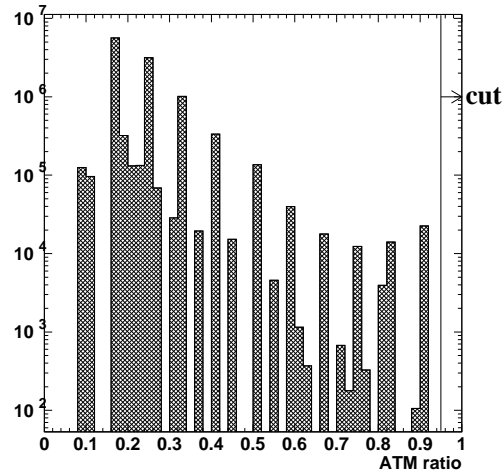


Figure 6.5: The distribution of the ATM ratio from a typical data sample.

here $N_{hit_{\max \text{ hit ATM}}}$ is the maximum number of hit PMTs in one ATM board and $N_{hit_{\text{total}}}$ is the total number of hit PMTs. Figure 6.5 shows the ATM ratio distribution. If the ATM ratio is larger than 0.95, the event is abandoned.

6.3.6 Flasher cut

The water leak of a PMT breeder circuit sometimes causes light emission from electric discharge of dynodes or strong spark noises. Such PMTs are called ‘flashers’ and those events are called ‘flasher events’. Figure 6.6 shows the vertex distribution from a typical data sample containing flasher events. In order to remove these events, two parameters, ‘ Q_{\max} ’ and ‘max24’ are used. The PMT which has the largest signal, Q_{\max} , in an event is considered as a possible flasher candidate. When a flasher event happens, the PMTs around the flasher will detect intense light from the flasher. Therefore 24 PMTs (5×5 PMTs – flasher) around the flasher are investigated, and the number of hit PMTs in the PMT group is defined as max24. Figure 6.7 shows scatter plots of Q_{\max} and max24 from a typical normal data sample and a typical data sample with flashers and the selection criteria of flasher events.

6.3.7 Goodness cut

The ‘goodness’ is used for the vertex search (as described in Sec.4.1.1) but also indicates how well the vertex is reconstructed. Normal physical events peak at $goodness \sim 0.6$. But unphysical events (noises, flashers, etc.), have $goodness$ less than 0.4 because they have

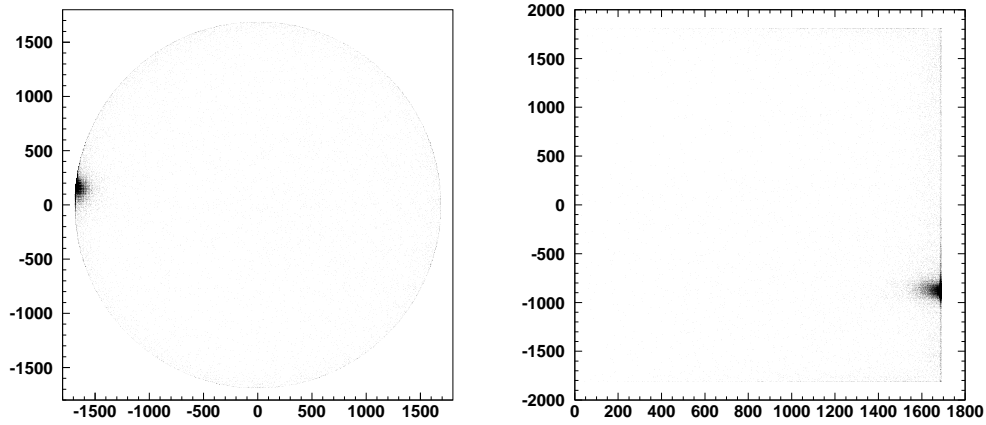


Figure 6.6: A vertex distribution from a typical data sample containing flasher events. The left figure shows a projection on the X-Y plane in SK geometry. The right figure shows a projection on the R-Z plane.

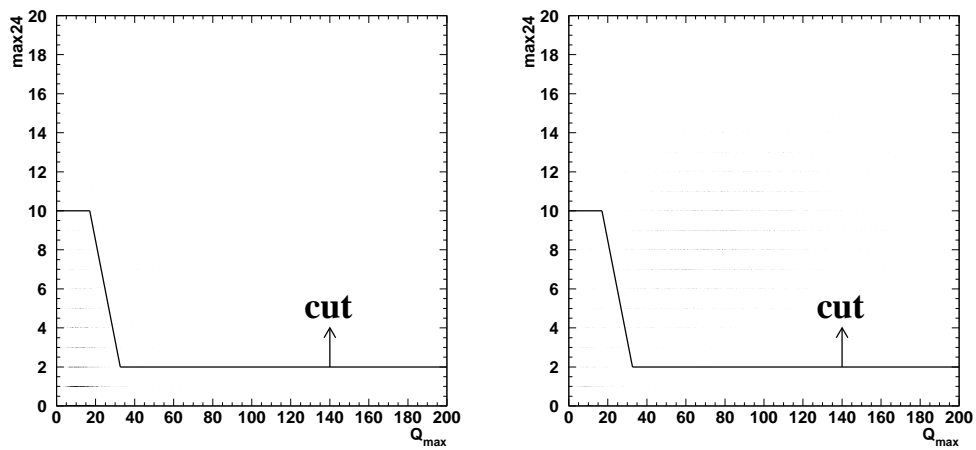


Figure 6.7: Scatter plots of Q_{max} and max24. The left figure shows a typical normal data sample. The right figure shows a typical data sample containing flasher events. Events above the 'cut' line are discarded flasher candidates.

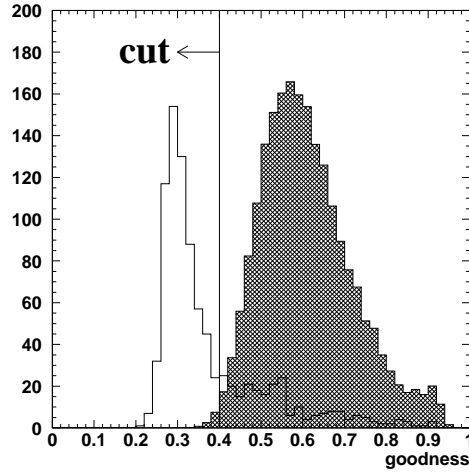


Figure 6.8: The *goodness* distribution. The hatched histogram is for a typical normal data sample and the blank for a flasher candidate event sample. The ‘cut’ line shows the discrimination value.

no clear vertices. Therefore events with *goodness* less than 0.4 are rejected. Figure 6.8 shows the *goodness* distribution for a typical normal data sample and the distribution for a flasher candidate data sample.

6.3.8 External flasher cut

The previous flasher cut may not be applicable to dim flasher events so a supplemental flasher cut is employed. Real physics events from Cherenkov photons will have a uniform PMT hit distribution around the reconstructed direction unlike flasher events. The difference is quantified by a Kolmogorov-Smirnov(KS)-like test.

Figure 6.9 shows an example of the test. Upper figures show a good event and lower a typical flasher event. The figures on the left show the hit pattern of each event and those on the right the KS test of them. The flasher event shows a cluster in the azimuthal distribution of on-time hit PMTs around the reconstructed direction. Selection is done with parameters, *goodness* and Dir_{ks} . Here, Dir_{ks} is defined as the full width (shown arrow in the right figures) divided by 360. Flasher events (lower right figure) have larger Dir_{ks} relative to normal events (upper right figure). Figure 6.10 shows a distribution of the Dir_{ks} from a typical data sample and M.C. sample. Events satisfying the following criteria are removed,

$$\begin{aligned} Dir_{ks} &\geq 0.25, \\ goodness &< 0.6. \end{aligned}$$

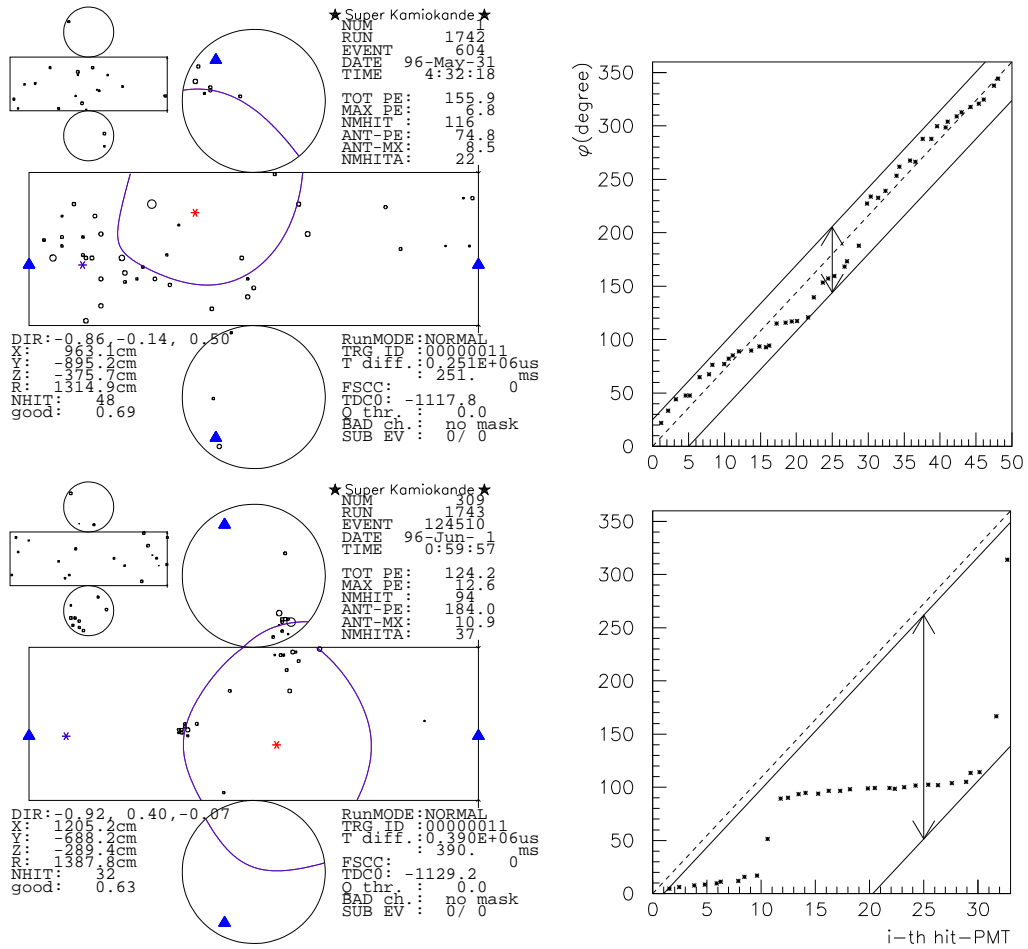


Figure 6.9: An example of the directional test

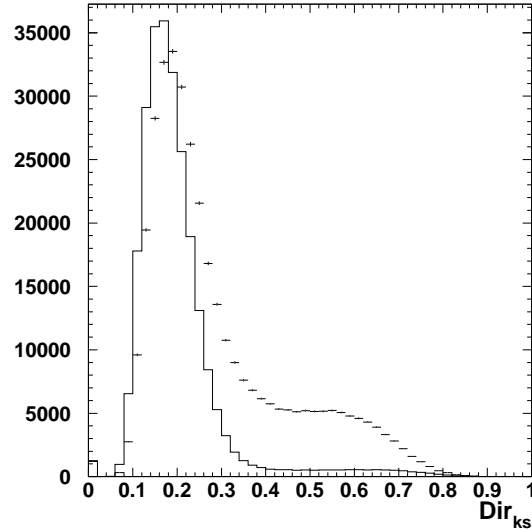
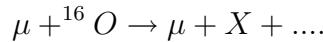


Figure 6.10: A distribution of the Dir_{ks} . The lines and error bars show the Dir_{ks} distribution from a typical data sample. The histogram shows the Dir_{ks} distribution from a M.C. sample.

6.4 Spallation cut

Cosmic ray muons sometimes interact with ^{16}O nuclei in the water and produce radioactive nuclei,



These radio-isotopes (X) are called “spallation products.” There are several long-lived (up to 14 sec) β and γ emitters in the products as listed in Table 6.1.

β and γ rays from spallation products are observed in SK and these events are called “spallation events”. These spallation events are one of the major backgrounds especially for energies above 6.5 MeV. Likelihood functions based on the following parameters are used to identify and remove these spallation events :

- ΔL : Distance from the low-energy event to the preceding muon track.
- ΔT : Time difference between the muon and the low-energy event.
- Q_{res} : Residual charge of the muon event ($= Q_{total} - Q_{unit} \times L_{\mu}$).

Here, Q_{total} is the total charge, Q_{unit} is the charge per unit length and L_{μ} is the reconstructed muon track length. By using these three parameters, the likelihood value is calculated for each possible muon and low-energy pair. When the muon track reconstruction doesn’t converge, only ΔT and Q_{res} are used. The definition and an explanation of the spallation likelihood function are described in Appendix A.

| Isotope | $\tau_{\frac{1}{2}}$ (sec) | Decay mode | Kinetic Energy(MeV) |
|----------------------|----------------------------|----------------------------------|---|
| ${}^8_2\text{He}$ | 0.122 | β^- $\beta^- \text{ n}$ | 10.66 + 0.99 (γ) (11 %) |
| ${}^8_3\text{Li}$ | 0.84 | β^- | 12.5 ~ 13 |
| ${}^8_5\text{B}$ | 0.77 | β^+ | 13.73 |
| ${}^9_3\text{Li}$ | 0.178 | β^- $\beta^- \text{ n}$ | 13.5 (75 %) 11.0 + 2.5 (γ) ~ 10 (35 %) |
| ${}^9_6\text{C}$ | 0.127 | $\beta^+ \text{ p}$ | 3 ~ 13 |
| ${}^{11}_3\text{Li}$ | 0.0085 | β^- $\beta^- \text{ n}$ | 20.77 (31 %) ~ 16 (61 %) |
| ${}^{11}_4\text{Be}$ | 13.8 | β^- | 11.48 (61 %) 9.32 + 2.1 (γ) (29 %) |
| ${}^{12}_4\text{Be}$ | 0.0114 | β^- | 11.66 |
| ${}^{12}_5\text{B}$ | 0.0204 | β^- | 13.37 |
| ${}^{12}_7\text{N}$ | 0.0110 | β^- | 16.38 |
| ${}^{13}_5\text{B}$ | 0.0173 | β^- | 13.42 |
| ${}^{13}_8\text{O}$ | 0.0090 | β^- | 8 ~ 14 |
| ${}^{14}_5\text{B}$ | 0.0161 | β^- | 14.07 + 6.09 (γ) |
| ${}^{15}_6\text{C}$ | 2.449 | β^- | 9.82 (32 %) 4.51 + 5.30 (γ) |
| ${}^{16}_6\text{C}$ | 0.7478 | β^- | ~ 4 |
| ${}^{16}_7\text{N}$ | 7.134 | β^- | 10.44 (26 %) 4.27 + 6.13 (γ) (68 %) |

Table 6.1: Summary of possible spallation products. Long lived β and γ emitters with $A \leq 16$ are listed.

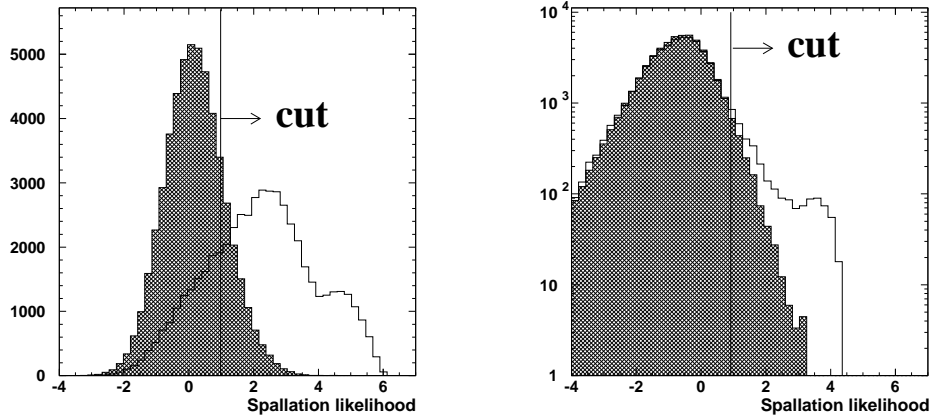


Figure 6.11: Distributions of the spallation likelihood. The blank histogram shows spallation candidate events and the hatched histogram shows non-spallation candidate events. The left figure shows the distribution for events where muon track reconstruction was successful and the right figure shows the distribution for events where muon track reconstruction failed.

For the spallation cut, the likelihood values are calculated for muons in the previous 100 seconds from each low energy event, and the muon which gives the maximum likelihood value (L_{max}) is selected as a pairing muon. The left figure in 6.11 shows the L_{max} distribution for events where the muon track reconstruction succeeded. Events with $L_{max} > 0.98$ are considered spallation events and are cut. The right figure in 6.11 shows L_{max} distribution for the case muon track reconstruction failed. Events with $L_{max} > 0.92$ are cut.

The dead time caused by the spallation cut is estimated to be 21.1%. This estimation is done using observed muon tracks and randomly chosen times and positions as expected for neutrino events. This dead time has a position dependence because of the SK tank geometry. Figure 6.12 shows the position dependence of the dead time as a function of distance from the barrel wall and the top wall.

6.5 Second reduction

The purpose of the second reduction is the elimination of remaining spallation events and events with broad goodness distributions. In this section, the criteria for the second reduction are described.

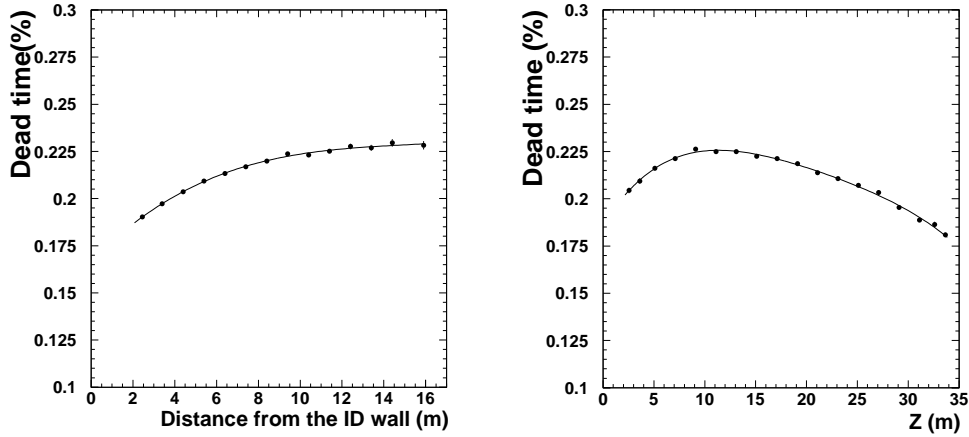


Figure 6.12: Dead time distribution from spallation cut for each position. The left figure shows a projection on the R and the right figure shows a projection on the Z.

6.5.1 Goodness stability test

The *goodness* cut can remove most events with many noise hits. Remaining noisy events have a broad *goodness* distribution around the reconstructed vertices due to noise hits whereas good events have very sharp *goodness* distribution. In order to remove these noisy events, *goodness* stability test for virtual vertices is done in the following steps :

1. The plane perpendicular to the reconstructed direction of the event which contains the reconstructed vertex is considered. Virtual vertices are selected on the plane (the minimum length from the reconstructed vertex is 1.6m and the maximum one is 16m).
2. The *goodness* for each virtual vertex is calculated.
3. The difference of the *goodness* to that of the reconstructed vertex is calculated ($\Delta goodnes$). Figure 6.13 shows the distributions for $\Delta goodnes$ v.s. distance from the reconstructed vertex for observed and M.C. data. From these distributions, the criteria are determined as red lines.
4. The number of points whose $\Delta goodnes$ is below the threshold is counted as N_{bad} .
5. The ratio of N_{bad} to the total number of points N_{total} are calculated.

If N_{bad}/N_{total} is larger than 0.08, the event is considered as noise-rich event and is removed.

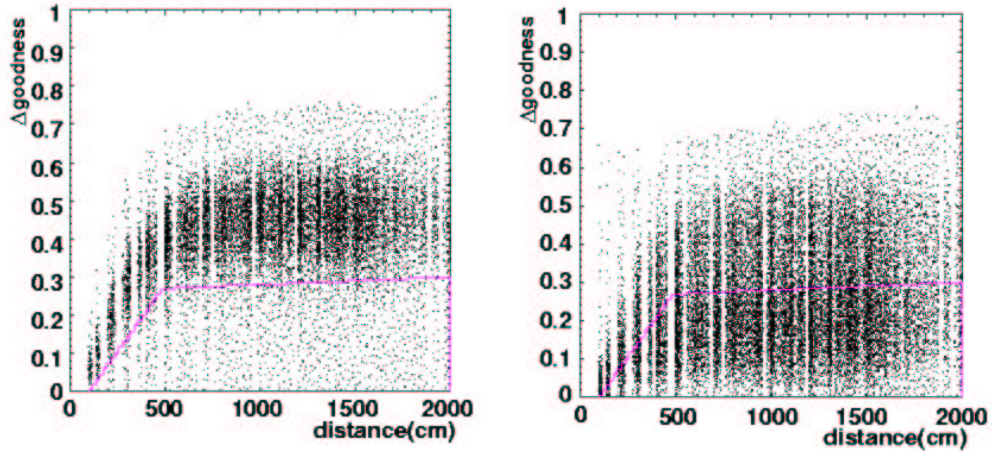


Figure 6.13: Distributions of $\Delta_{goodness}$ v.s. distance from the reconstructed vertex. The red lines in the figures show the threshold line for the N_{bad} calculation. The number of points below the red line is calculated as N_{bad} . The left figure shows a distribution for typical M.C. events, the right for typical observed events.

6.5.2 Vertex test after noise hit rejection

Reconstructed vertices may be affected by noise hits in an event. Therefore after the noise hit rejection, the vertex is reconstructed and a fiducial volume cut is applied once more.

In order to reject a noise hit, timing information is useful. In this cut, noise hits are rejected by the following criteria :

1. Hit PMTs with distances to the other hit PMTs larger than 1250 cm and with time differences to the other hit PMTs larger than 35 nsec are treated as noise hits.
2. The causality of each PMT hit is tested supposing Cherenkov light from a point source. When we define the time difference between the i -th hit PMT and the j -th hit PMT as ΔT_{ij} and the distance difference as ΔL_{ij} , this causality is $\Delta L_{ij}/c' > \Delta T_{ij}$, where c' is the light speed in water. The number of hit PMTs which satisfies the relation is calculated for each PMT. If the number is larger than 10, this PMT is treated as a real hit by Cherenkov light.

After the noise hit rejection, the vertex is re-reconstructed. Finally, if the re-reconstructed vertex is within 200 cm of the ID wall, the event is removed.

6.5.3 Cherenkov ring image test

One solar neutrino event consists of one Cherenkov ring or even with shower creation all rings have the same direction. But some spallation products and Rn daughters emit

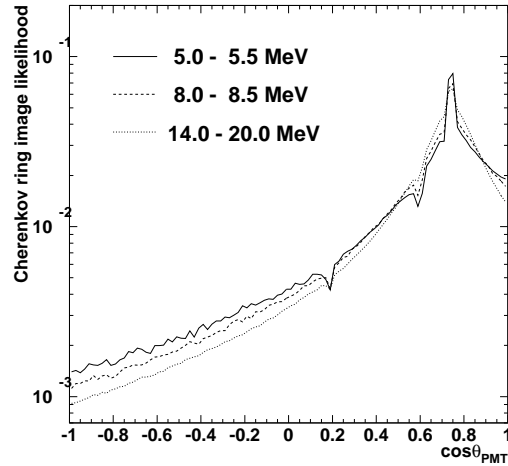


Figure 6.14: Examples of likelihood functions for the ring image test for vertices 1200 cm to 1700 cm from the ID wall.

two or more Cherenkov rings isotropically. If the events contain many noise hits, the distribution of directions for each hit-PMT is different from real neutrino events. In order to reject these events, a pattern test of the Cherenkov ring image is done by the following procedure :

1. Cherenkov-ring-likelihood-functions of angular distribution of hit PMTs ($\Delta angle$) with respect to the reconstructed direction are made by M.C. simulation. The likelihood is a function of energy, distance to the ID wall and the angle. Figure 6.14 shows examples of the likelihood function for three energy regions with the distance from 1200 cm to 1700 cm.
2. $\Delta angle$ and thus the likelihood are calculated for each hit in a 50 nsec time window. The average log-likelihood of the hits is used for the selection.
3. If the average log-likelihood value is less than threshold value, the event is rejected.

Figure 6.15 shows the average log-likelihood distribution. From this distribution, the threshold is determined to be -1.85.

6.6 External γ -ray cut

The external γ -ray reduction is used in order to cut gamma rays from the surrounding materials. These gamma rays are one of the major backgrounds especially in the lower

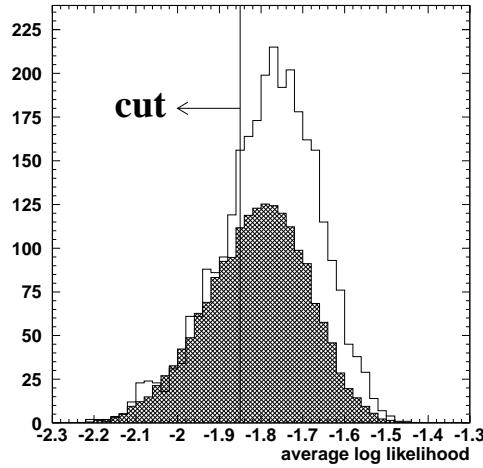


Figure 6.15: The distribution of the average log likelihood for the ring image test. The blank histogram shows the distribution for the $\cos \theta_{\text{sun}} \geq 0.8$ region. The hatched histogram shows the distribution for the $\cos \theta_{\text{sun}} \leq 0.8$ region. The line shows the cut line in this cut.

energy region. External gamma rays are characterized by their inward direction and vertices close to the wall. We use the effective distance back to the wall d_{eff} as defined in Figure 6.16 to remove these events as follows,

1. $d_{\text{eff}} \geq 450$ cm (for $E \geq 6.5$ MeV)
2. $d_{\text{eff}} \geq 800$ cm (for $5.0 \text{ MeV} \leq E < 6.5$ MeV)

Figure 6.17 shows the effective distance distributions of M.C. and observed data for different energy regions and selection thresholds are also shown.

Figure 6.18 shows the vertex distributions before and after the γ -ray cut for real data with $E \geq 6.5$ MeV. Figure 6.19 shows the direction distributions before and after the γ -ray cut for real data with $E \geq 6.5$ MeV.

6.7 Reduction summary

The number of events after each reduction step and efficiencies for M.C. events with energies between 5.0 MeV to 20.0 MeV are summarized in Table 6.2. Figure 6.22 shows the energy spectrum after each reduction step. After the application of all reductions, the number of solar neutrino candidates is 295,922. Possible remaining backgrounds are β from daughter nuclei of ^{222}Rn , γ -rays from detector materials and the surrounding

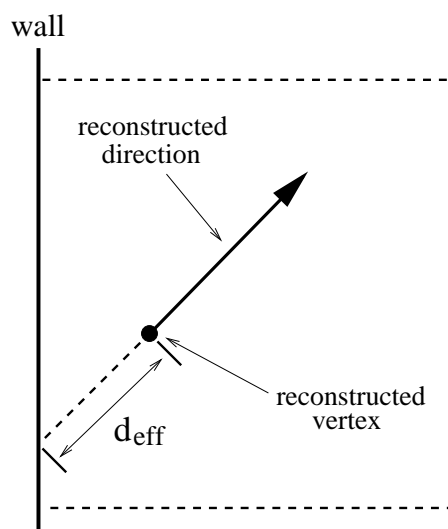
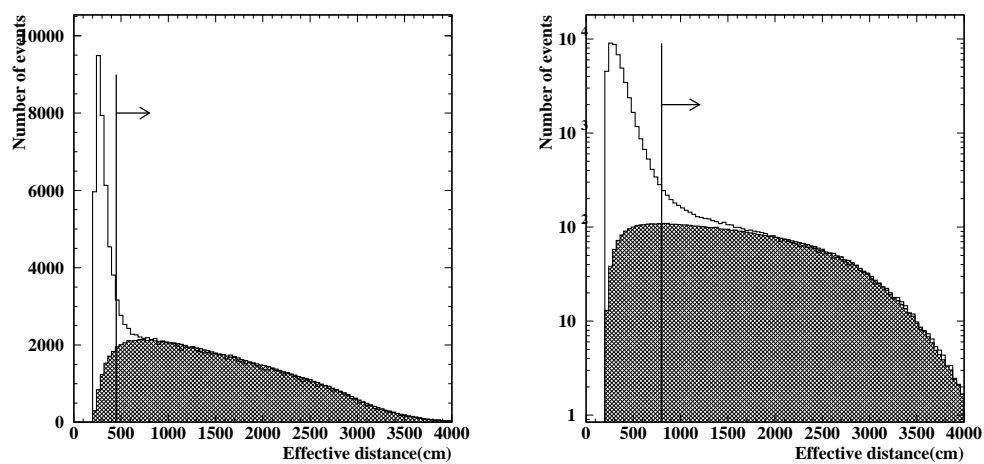


Figure 6.16: The definition of the effective distance from the wall

Figure 6.17: Distributions of effective distances. Blank histograms show real data and hatched areas show solar neutrino M.C. The left figure shows a distribution for $E \geq 6.5$ MeV. The right figure shows a distribution for $5.0 \text{ MeV} \leq E < 6.5 \text{ MeV}$.

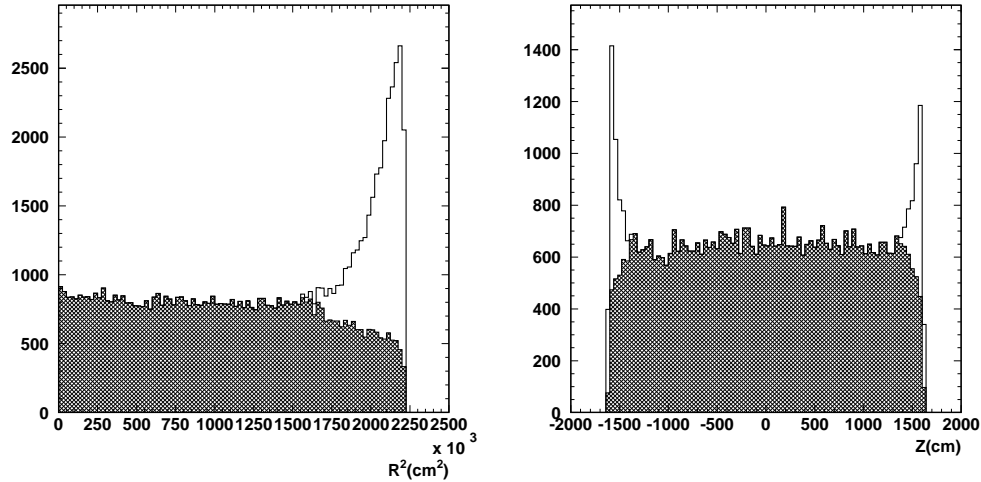


Figure 6.18: The Vertex distribution before and after the gamma cut. Blank histograms show the distribution before the cut and hatched histograms show that after the cut. The left figure shows the R^2 distribution for $E \geq 6.5$ MeV and $|Z| < 1000$ cm case. The right figure shows the Z distribution for $E \geq 6.5$ MeV and $|R| < 1000$ cm case.

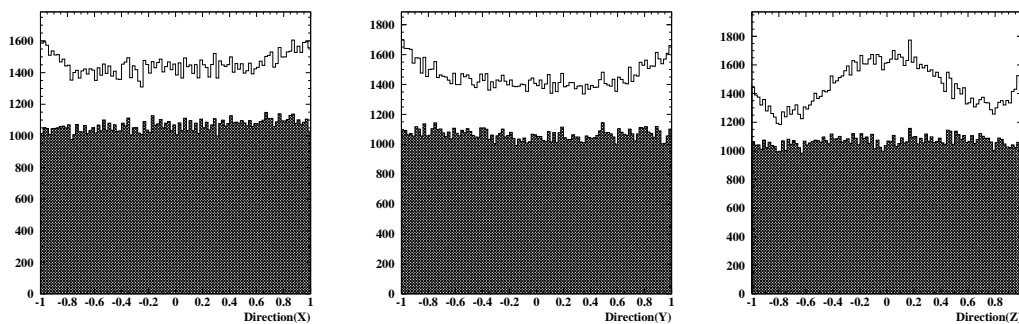


Figure 6.19: The directional distributions before (blank histogram) and after (hatched histogram) the gamma cut for $E \geq 6.5$ MeV. The left figure shows the projection on X. The center figure shows that on Y and the right figure on Z.

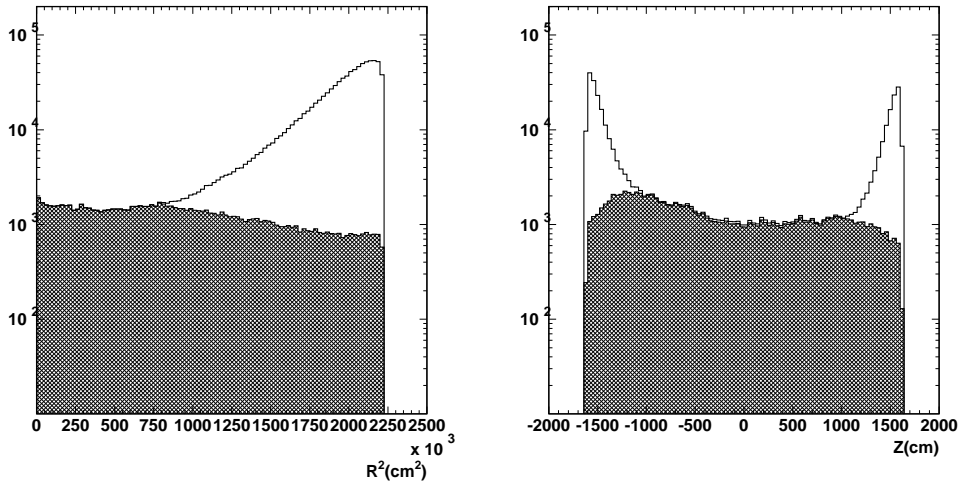


Figure 6.20: The Vertex distribution before and after the gamma cut. Blank histograms show the distribution before the cut and hatched histograms show the distribution after the cut. The left figure shows the R^2 distribution for $5.0 \text{ MeV} \leq E < 6.5 \text{ MeV}$ and $|Z| < 1000 \text{ cm}$ case. The right figure shows the Z distribution for $5.0 \text{ MeV} \leq E < 6.5 \text{ MeV}$ and $|R| < 1000 \text{ cm}$ case.

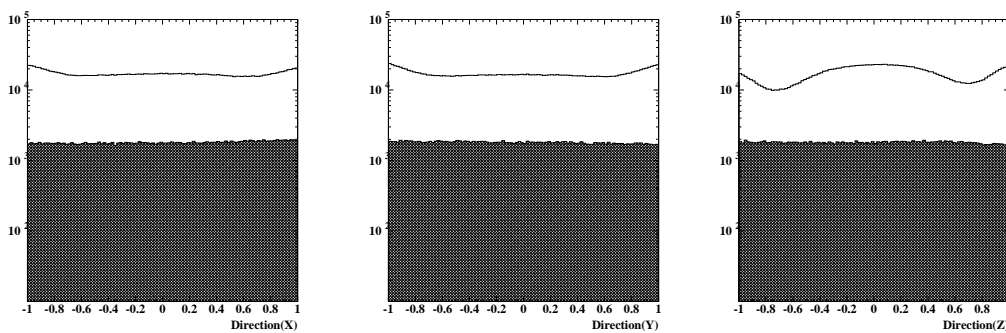


Figure 6.21: The direction distributions before (blank histogram) and after (hatched histogram) the gamma cut for $5.0 \text{ MeV} \leq E < 6.5 \text{ MeV}$. The left, center and right figures show projections on the X, Y and Z axis, respectively.

| Reduction step | Observed data | elastic scattering M.C. | $\bar{\nu}_e$ M.C. |
|---|---------------|-------------------------|--------------------|
| After on line reduction | 176906705 | 100 % | 100 % |
| First reduction | | | |
| Fiducial volume cut | 34301372 | 74% | 72% |
| DT \geq 50 μ sec cut | 26627697 | 100% | 100% |
| OD triggered event cut | 25068589 | 100% | 100% |
| Noise cut | 25014073 | 100% | 100% |
| Cluster-ATM-hits-event cut | 25004524 | \sim 100% | \sim 100% |
| Flasher cut | 24773119 | 99% | 99% |
| Goodness cut | 24398348 | \sim 100% | \sim 100% |
| External flasher cut | 18100641 | \sim 100% | \sim 100% |
| total | 18100641 | 73% | 71% |
| Spallation cut | | | |
| Spallation cut | 12868437 | 79% | 79% |
| total | 12868437 | 79% | 79% |
| Second reduction | | | |
| Goodness stability test | 3614781 | 88% | 89% |
| Cherenkov ring image test | 2724267 | 87% | 88% |
| Vertex test after noise hit rejection | 1856647 | 98% | 98% |
| total | 1856647 | 75% | 77% |
| External γ-ray cut | | | |
| External γ -ray cut | 295922 | 89% | 90% |
| total | 295922 | 89% | 90% |
| total | | | |
| total | 295922 | 38% | 39% |

Table 6.2: Summary of event reduction

rock, and long lived spallation events. These events look similar to solar neutrino events and it is difficult to identify them event by event. Therefore after all reductions, solar neutrino extraction and background estimation are done by statistical methods.

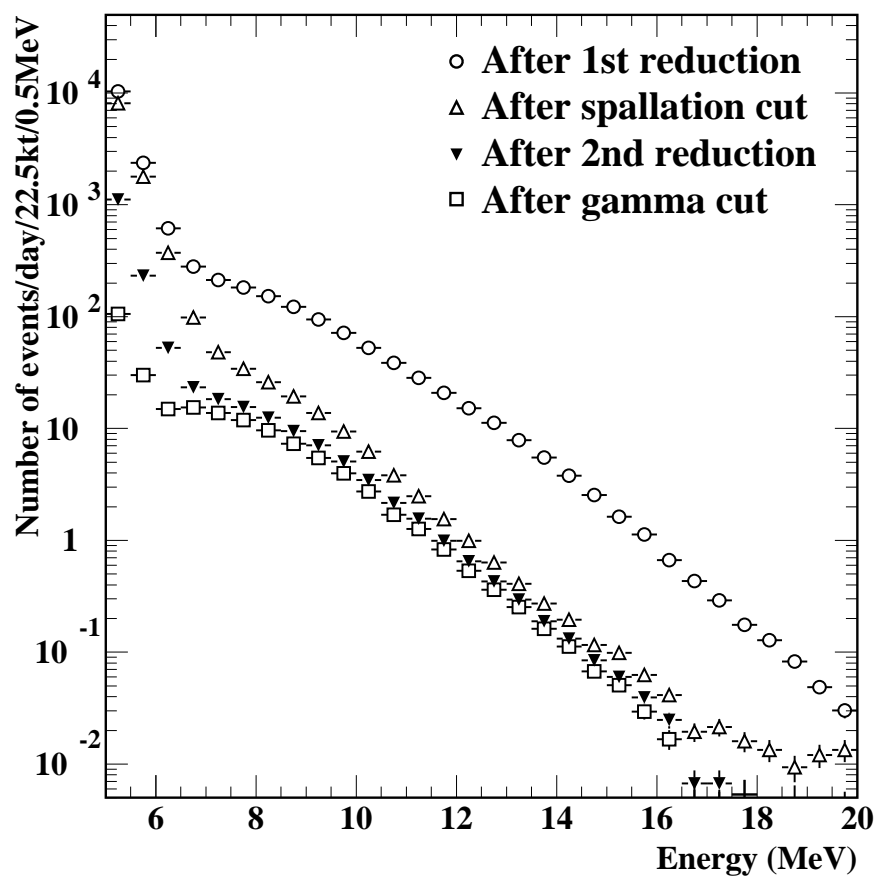


Figure 6.22: Energy spectra after each reduction step. The vertical axis shows the event rate and the horizontal axis shows the visible energy.

Chapter 7

Data Analysis and Results

7.1 Extraction of elastic scattering events

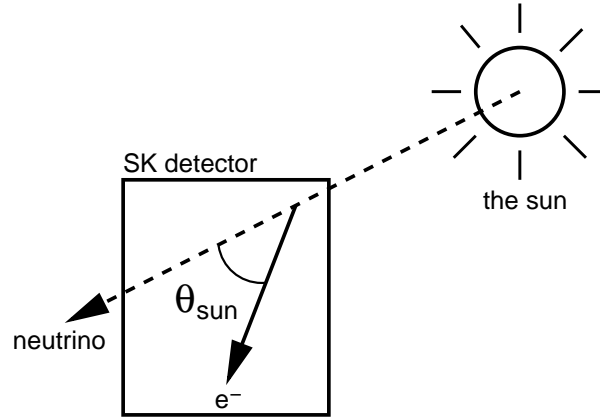
The solar neutrino data sample after all the reductions still contains many background events. The direction of the recoil electron has a strong correlation with the incident neutrino direction. Such directional neutrino signals are statistically extracted in the $\cos \theta_{\text{sun}}$ distribution of the observed data. Figure 7.1 shows the definition of θ_{sun} . Figure 7.2 shows the $\cos \theta_{\text{sun}}$ distribution of the observed data. The clear peak towards $\cos \theta_{\text{sun}} = 1$ is due to elastic scattering events of solar neutrinos and the flat component is from backgrounds independent of the solar direction.

In order to extract the solar neutrino signal, a maximum likelihood method is used. The probability function for the likelihood consists of signal and background terms,

$$P(\cos \theta_{\text{sun}}, E_e, \alpha) = \alpha \times P_{\text{sig}}(\cos \theta_{\text{sun}}, E_e) + (1 - \alpha) \times P_{\text{bg}}(\cos \theta_{\text{sun}}, E_e), \quad (7.1)$$

where E_e is the total energy of the recoil electron, α is the fraction of solar neutrino signals in the observed data. $P_{\text{sig}}(\cos \theta_{\text{sun}}, E_e)$ is the probability density function for elastic scattering signals obtained by a M.C. simulation. Figure 7.3 shows P_{sig} distributions for each energy. The background shape should be flat if it's angular distribution is spherically uniform. However γ -rays from the surrounding materials and the non-uniform ^{222}Rn distribution in the SK tank may slightly affect the background shape. In order to obtain the background shape in $\cos \theta_{\text{sun}}$ distribution, the non-uniform zenith angle distribution ($\cos \theta_z$) of the observed data is fit with an 8-th degree polynomial, and then is converted to the $\cos \theta_{\text{sun}}$ distribution (P_{bg}) assuming azimuthal symmetry. Figure 7.4 shows the P_{bg} distribution for each energy.

It should be noted that the α depends on the signal to noise ratio of each energy bin and thus differs bin to bin. If one constrains the solar neutrino spectrum to an expected

Figure 7.1: Definition of $\cos \theta_{\text{sun}}$

shape, the probability function and α for each bin can be derived as follows,

$$P(\cos \theta_{\text{sun}}, E_e, \alpha_i) = \alpha_i \times P_{\text{sig}}(\cos \theta_{\text{sun}}, E_e) + (1 - \alpha_i) \times P_{\text{bg}}(\cos \theta_{\text{sun}}, E_e), \quad (7.2)$$

$$\alpha_i = \alpha \times \frac{N_{\text{all}}^{\text{data}} N_i^{\text{MC}}}{N_i^{\text{data}} N_{\text{all}}^{\text{MC}}}, \quad (7.3)$$

where N_i^{data} is the number of events in the i -th energy bin, $N_{\text{all}}^{\text{data}}$ is the total number of observed events, N_i^{MC} , $N_{\text{all}}^{\text{MC}}$ are similarly defined but represent M.C. data, i is the index of energy bins. By using this probability function, the likelihood function is defined as follows,

$$L(\alpha) = \prod_{i=1}^{N_{\text{ene}}} \prod_{j=1}^{N_i^{\text{data}}} P_{ij}(\cos \theta_{\text{sun}}, E_e, \alpha_i), \quad (7.4)$$

where N_{ene} is the number of the energy bins.

The number of solar neutrino signals (N_{elastic}) is obtained from the α_{max} which maximizes $L(\alpha)$ as follows,

$$N_{\text{elastic}} = \alpha_{\text{max}} \times N_{\text{all}}^{\text{data}}, \quad (7.5)$$

The statistical error of N_{elastic} is obtained as the difference between α_{max} and α which gives $L(\alpha) = e^{-0.5} L(\alpha_{\text{max}})$.

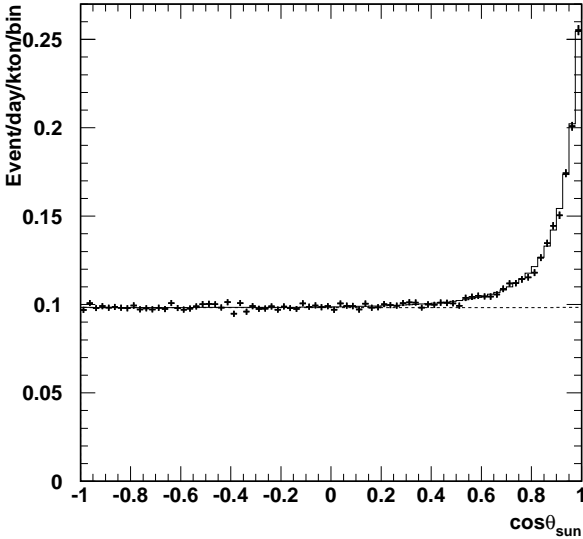


Figure 7.2: The $\cos\theta_{\text{sun}}$ distribution for 5.0 - 20.0 MeV. The crosses show data, the histogram shows the best fit distribution in the maximum likelihood method, and the dotted line shows the background shape.

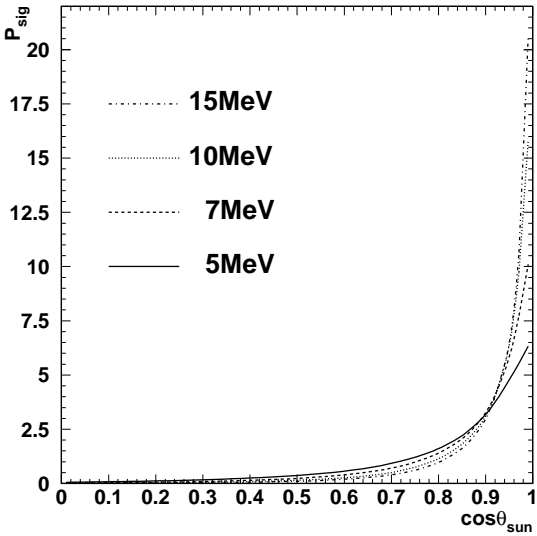


Figure 7.3: The probability density function for elastic scattering signals, P_{sig} .

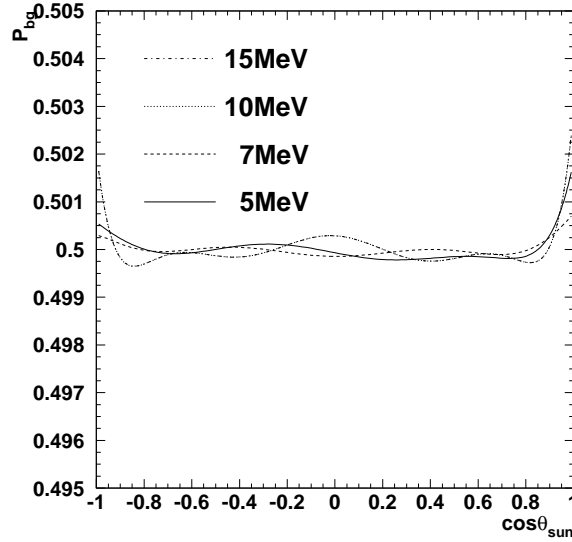


Figure 7.4: The probability density function for the background shape P_{sig}

7.2 Results on the ^8B solar neutrino flux

7.2.1 ^8B solar neutrino flux

The measured number of recoil electron events for the energy range 5 – 20 MeV and for the live time of 1496 days is,

$$N_{elastic} = 22404 \pm 226(\text{stat.})_{-717}^{+784}(\text{sys.}). \quad (7.6)$$

The expected number of events is obtained as follows,

$$N_{expect} = \sum_{i=1}^{N_{thr}} \frac{N_{MC\ aft,i}}{N_{MC\ bef,i}} \times T_{live,i} \times N_{SSM}, \quad (7.7)$$

where N_{thr} is the number of trigger threshold types. $N_{MC\ aft,i}$ is the number of M.C. events after the reduction, $N_{MC\ bef,i}$ before the reduction, thus $\frac{N_{MC\ aft,i}}{N_{MC\ bef,i}}$ means the efficiency of the data reduction. $T_{live,i}$ is the livetime of i -th threshold type, and N_{SSM} is the SSM prediction for the expected number of elastic scattering events in SK. The expected number of elastic scattering events for the BPB2001 SSM flux, 5.05×10^6 /cm²/sec, and the ^8B spectrum [27] is,

$$N_{expect} = 48173 \text{ events.} \quad (7.8)$$

The ratio of the observed number of events to the prediction is thus,

$$\frac{N_{elastic}}{N_{expect}} = 0.465 \pm 0.005(\text{stat.})_{-0.015}^{+0.016}(\text{sys.}). \quad (7.9)$$

In another words, the observed ${}^8\text{B}$ neutrino flux $\Phi_{8\text{B}}$ is,

$$\Phi_{8\text{B}} = 2.35 \pm 0.02(\text{stat.}) \pm 0.08(\text{sys.}) \times 10^6/\text{cm}^2/\text{sec}. \quad (7.10)$$

7.2.2 Day/Night flux asymmetry

One of the features of Super-Kamiokande is real-time observation. We can investigate time variations of the neutrino flux such as a daytime flux to nighttime flux. In the LMA region of neutrino oscillation parameters, the matter effect in the earth causes a day/night variation of the neutrino flux. The day/night flux difference is useful to determine neutrino oscillation parameters independently from the SSM flux prediction.

Figure 7.5 shows the zenith angle dependence of the solar neutrino flux. The daytime and night time flux are obtained as follows,

$$\Phi_{\nu}^{Day} = 2.32 \pm 0.03(\text{stat.})_{-0.07}^{+0.08}(\text{sys.}) \times 10^6/\text{cm}^2/\text{sec}, \quad (7.11)$$

$$\Phi_{\nu}^{Night} = 2.37 \pm 0.03(\text{stat.}) \pm 0.08(\text{sys.}) \times 10^6/\text{cm}^2/\text{sec}. \quad (7.12)$$

The difference of day/night flux is

$$\frac{\Phi_{\nu}^{Day} - \Phi_{\nu}^{Night}}{(\Phi_{\nu}^{Day} + \Phi_{\nu}^{Night})/2} = -0.021 \pm 0.020(\text{stat.})_{-0.012}^{+0.013}(\text{sys.}), \quad (7.13)$$

where the common systematic errors such as the cross section cancel by taking the ratio.

7.2.3 Energy spectrum for recoil electrons

The energy spectrum of recoil electrons is one of the important pieces of information, because distortion of it is a clear signature of neutrino physics such as neutrino oscillations and/or RSFP independent from the SSM uncertainties. The upper figure in 7.6 shows the observed and expected energy spectrum of recoil electrons, and lower figure shows the ratio of them. The energy spectra for various zenith angles (zenith angle spectra) are used to extract information on both the spectrum distortion and the time variation from the matter effect in the earth. Figure 7.7 shows the definition of the zenith angle division and Figure 7.8 shows the zenith angle spectra.

7.3 Systematic errors

Systematic errors in the solar neutrino analysis are categorized in two types. The first category is the energy dependent systematic errors called ‘correlated error’, and the second category is the non-dependent errors called ‘uncorrelated error’.

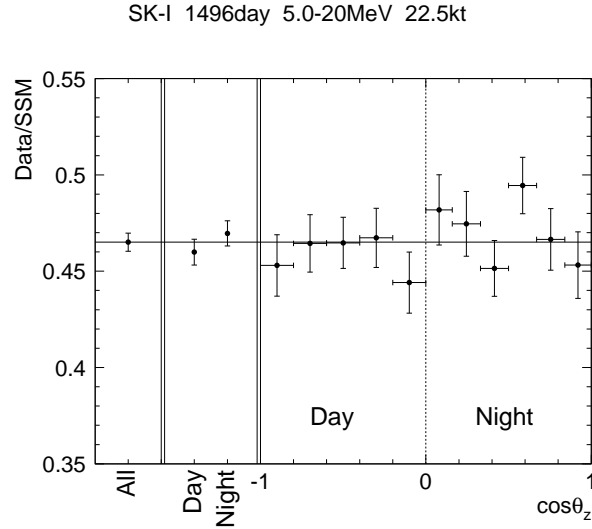


Figure 7.5: The Day/Night dependence of the solar neutrino flux. $\cos\theta_z$ denotes the zenith angle of the sun.

7.3.1 Correlated errors

Uncertainties of the absolute energy scale and the energy resolution make bin to bin correlated systematic errors. Their effects are reflected in the analysis taking in to account shape deformations in the following way,

$$F(E_{vis}) = \int_0^{\infty} F_0(E_e)R(E_{vis}, E_e)P(E_e)dE_e. \quad (7.14)$$

Where $F_0(E_e)$ is the expected spectrum, E_e is the total energy of recoil electrons, $R(E_{vis}, E_e)$ represents detector responses, E_{vis} is the visible energy in the SK detector, $P(E_e)$ is the detection efficiency, and $F(E_{vis})$ is the obtained shape deformation from each uncertainty to be used in a shape analysis. Uncertainties of the scale and the resolution come from the following facts :

- Position dependence
It is estimated by $(\text{Data} - \text{M.C.})/\text{M.C.}$ using LINAC calibrations at various positions and the measured systematic biases are as follows,
 $\pm 0.5\%$: energy scale
 $\pm 2.0\%$: energy resolution
- Energy dependence
Is is also estimated by the LINAC calibration with various energies to be the following,

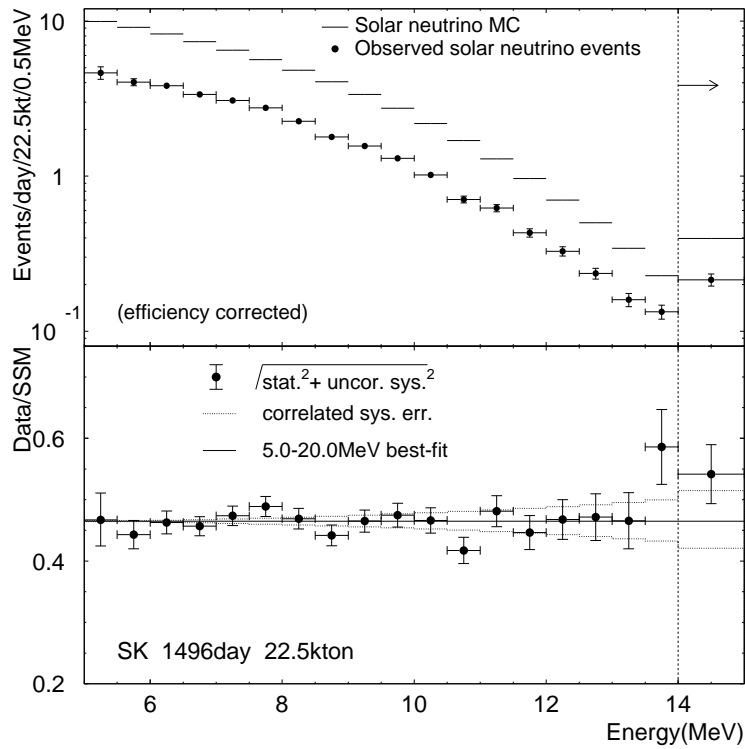


Figure 7.6: The recoil electron energy spectra for the observed and expected solar neutrino events. The solar neutrino M.C. denotes the SSM prediction.

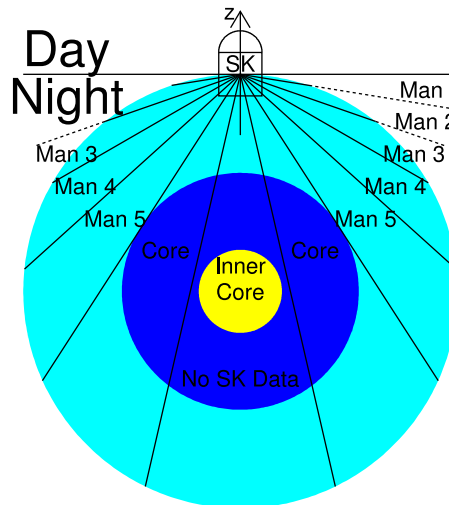


Figure 7.7: The definition of the zenith angle division

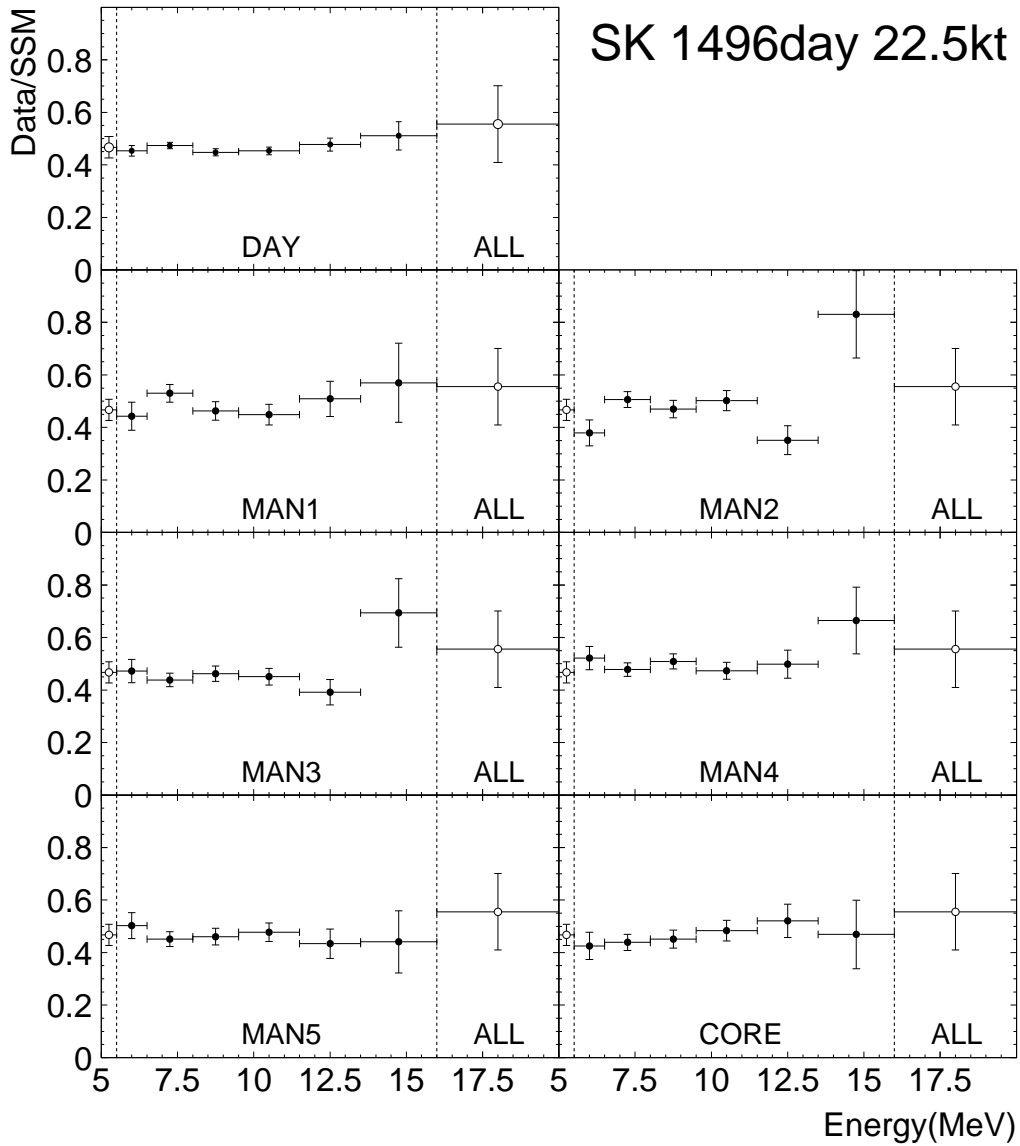


Figure 7.8: The ratios of the measured recoil electron energy spectra to the predicted spectra for each zenith angle bin. Due to statistical limitations, the 5.0 - 5.5 MeV and 16.0 - 20.0 MeV energy bins are combined for all zenith angles and all are identical.

- $\pm 0.5\%$: energy scale
- $\pm 2.0\%$: energy resolution

- Precision of the LINAC energy [70].
- Directional dependence of the energy scale
Energy spectra of spallation events toward various directions agree within $\pm 0.5\%$
- Stability of water transparency
The time variation of water transparency is monitored by decay electron data and spallation data within $\pm 0.22\%$ precision.

In addition to the correlated errors from the uncertainties of the energy scale and the energy resolution, the ambiguity of the ${}^8\text{B}$ neutrino spectrum is also treated in the same way. Figure 7.9 shows fully correlated 1σ spectrum deformation from energy scale, energy resolution, and ${}^8\text{B}$ neutrino energy spectrum uncertainties. The systematic uncertainties for the flux measurements are the integration of these deformations above the threshold and they are obtained as $\pm 1.9\%$ for the average flux and ${}^{+1.2\%}_{-1.1\%}$ for the day/night fluxes.

7.3.2 Uncorrelated errors

- Trigger efficiency
The trigger efficiency is almost 100% above 7.0 MeV with the LE trigger and above 6.0 MeV with the SLE trigger, and the systematic errors above these energies are negligible. Trigger efficiencies below these energies are calculated by the M.C. detector simulation and are calibrated by ${}^{16}\text{N}$ data from the DT neutron generator as described in Sec.5.9. The obtained systematic errors for each energy bins are ${}^{+2.2\%}_{-1.0\%}$ for 5.0 - 5.5 MeV bin, ${}^{+0.6\%}_{-0.3\%}$ for 5.5 - 6.0 MeV bin, ${}^{+0.2\%}_{-0.2\%}$ for 6.5 - 7.0 MeV bin, and ${}^{+0.3\%}_{-0.2\%}$ for 5.0 - 20.0 MeV integrated data.
The systematic errors from the IT online reduction are estimated in the same way. Since the IT online reduction is applied for the SLE trigger events, events with energy more than 6.5 MeV are not affected. The obtained systematic errors are $\pm 1.1\%$ for 5.0 - 5.5 MeV bin, $\pm 0.5\%$ for 5.5 - 6.0 MeV bin, and $\pm 0.1\%$ for 6.0 - 6.5 MeV bin.
- Reduction
The systematic errors from the 1st and the 2nd reduction are estimated by comparing their reduction efficiency on data to that on M.C. as $(\text{Data} - \text{M.C.})/\text{M.C.}$. Where ‘Data’ means the efficiency for well-tagged spallation events. DT calibration data, and Ni-Cf calibration data. The total systematic error for all reduction steps is estimated to be ${}^{+2.1\%}_{-1.6\%}$ for the flux measurement and $\pm 0.85\%$ for the spectrum shape analysis.

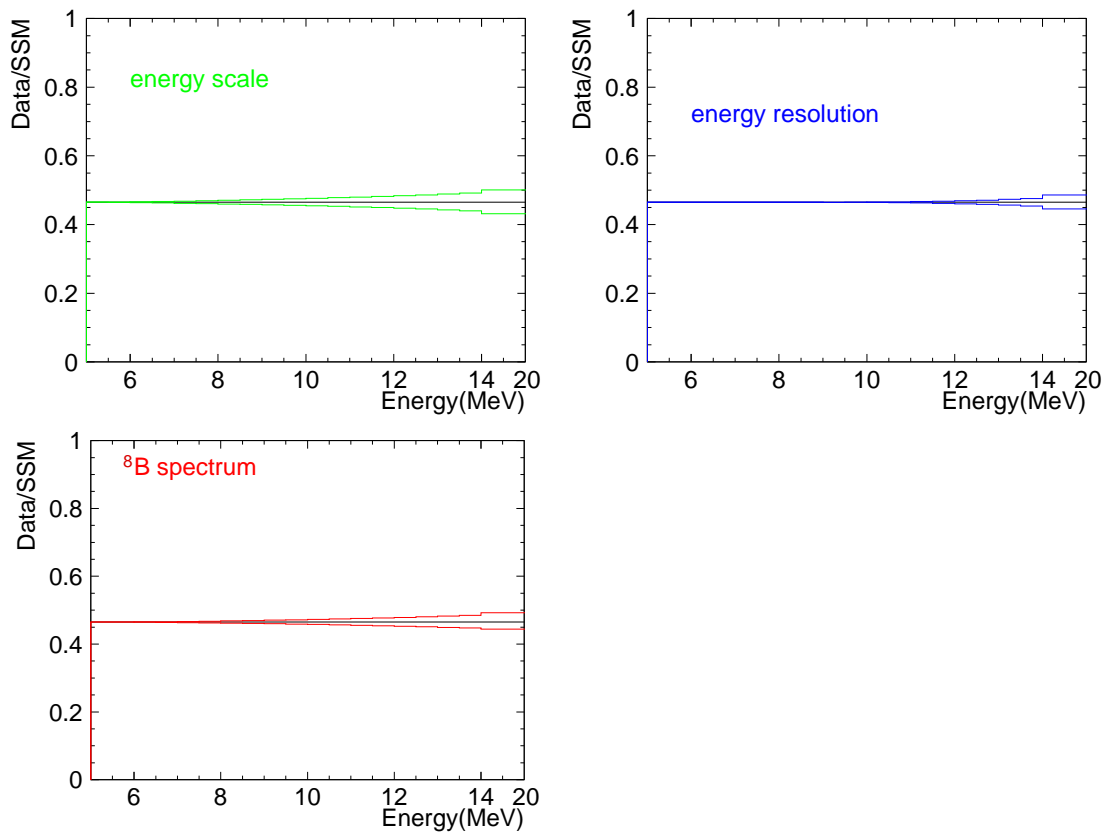


Figure 7.9: The fully correlated 1σ deformation of the energy spectrum from uncertainties of the energy scale, the energy resolution and ^8B neutrino spectrum.

- Spallation dead time
The absolute dead time is obtained at $\pm 0.2\%$ precision and the relative error for such as the Day/Night and seasonal analysis is $\pm 0.1\%$.
- Vertex shift
A possible vertex bias causes an error on the fiducial volume and it may be energy dependent. Using the Ni-Cf calibration at various positions close to the fiducial edges, the errors on the target fiducial volume are estimated to be $\pm 1.3\%$ for the flux measurement, and $\pm 0.2\%$ for the spectrum shape analysis.
- γ -ray cut
The effect of a vertex bias on the γ -cut efficiency is considered and the errors, $\pm 0.5\%$ for the flux and $\pm 0.1\%$ for the shape analysis, are assigned.
- Non-flat background
As described in Sec.7.1, a converted distribution of the data from $\cos\theta_z$ to the $\cos\theta_{\text{sun}}$ is used as a background shape. However a ϕ asymmetry of the data may also introduce non-flatness in the $\cos\theta_{\text{sun}}$ distribution. A study of the ϕ asymmetry requires lots of data and it is hard to trace a time variation of the effect. Differences of results between analyses with and without an assumption of ϕ symmetry are investigated for the total data and are considered as systematic errors. The estimated systematic errors are $\pm 0.1\%$ for the total flux measurement, $\pm 0.4\%$ for the Day/Night difference, $\pm 0.6\%$ for 5.0 - 5.5 MeV bin, $\pm 0.5\%$ for 5.5 - 6.0 MeV bin, and $\pm 0.1\%$ for the energy above 6.5 MeV bin.
- Angular resolution
The difference of angular resolutions obtained from LINAC calibration data and from M.C. data is taken as the systematic error. For the flux measurement, the systematic error is $\pm 1.2\%$. For the spectrum shape analysis, the systematic errors are estimated to be $\pm 2.3\%$ in the energy region 5.0 - 5.5 MeV, $\pm 1.0\%$ for above 5.5 MeV energy region.
- Cross section
The uncertainty of the neutrino-electron elastic scattering cross section is due to the uncertainty of the Weinberg angle θ_W . We use the systematic error 0.5% suggested in reference [54].
- Livetime
Differences in the livetime calculation from the raw data, the muon data, and the low energy data are studied. The systematic error is estimated to be $\pm 0.1\%$ for both the flux measurement and the Day/Night flux difference.

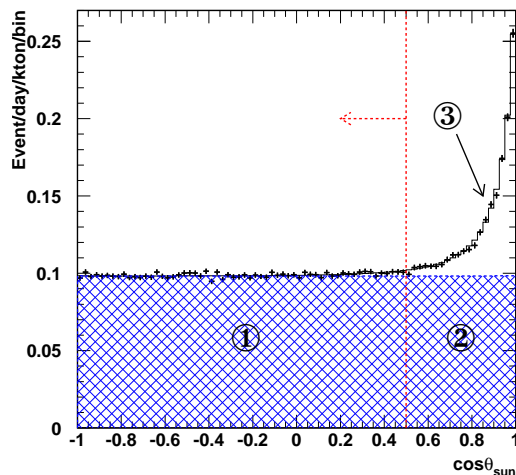


Figure 7.10: The $\cos \theta_{\text{sun}}$ distribution and $\bar{\nu}_e$ candidate region

7.4 Search for $\bar{\nu}_e$ from the sun

7.4.1 Statistical subtraction of spallation backgrounds

The dominant process of $\bar{\nu}_e$ detection in SK is the inverse β decay, $\bar{\nu}_e + p \rightarrow e^+ + n$. A neutron capture reaction, $n + p \rightarrow d + \gamma(2.2 \text{ MeV})$, takes place successively, but, 2.2 MeV is below the energy threshold and the γ -ray can not be used to tag the inverse β decay. Therefore, statistical methods are necessary to subtract the background. Figure 7.10 shows the $\cos \theta_{\text{sun}}$ distribution for 5.0 - 20.0 MeV. The positron angular distribution from $\bar{\nu}_e$ events is nearly flat on $\cos \theta_{\text{sun}}$, therefore the hatched region in Figure 7.10 is relevant for a $\bar{\nu}_e$ search. On the other hand, elastic scattering has sharp forward peak and it distributes in the region shown as ③ in Figure 7.10. If $\bar{\nu}_e$'s are coming from the sun, these events should be included in elastic scattering events. But $\bar{\nu}_e$ events can not be distinguished from other neutrino types and its event rate is much smaller than that through the inverse β decay process. Therefore elastic scattering events are not useful in this search. In order to reject the elastic scattering events, $\cos \theta_{\text{sun}} > 0.5$ region are rejected. And in this analysis, only region ① is used.

For $\cos \theta_{\text{sun}} \leq 0.5$ and the $E \leq 8 \text{ MeV}$ region, most of background events are due to radioactivities in the detector materials such as ^{222}Rn and these events have no correlation with the other events. In contrast, for $E \geq 8 \text{ MeV}$, most of background events are due to spallation products. The spallation cut (as described in Sec.6.4) efficiently removes spallation events. However event by event removal of long-lived spallation products such as $^{16}_7\text{N}$ ($\tau_{1/2} = 7.1 \text{ sec}$) and $^{11}_4\text{Be}$ ($\tau_{1/2} = 13.8 \text{ sec}$) is impractical with an acceptable dead time. Instead, spallation backgrounds are statistically estimated with the following

technique.

1. Make a timing distribution of muon events preceding each low-energy event by up to 200 seconds (Figure 7.11(A)). Since the average muon rate at SK is ~ 2.5 Hz, there are ~ 500 preceding muon events for each low-energy event. If a low-energy event is due to a long lived spallation product, its timing will be correlated with one of the ~ 500 preceding muon events. If this is not the case, then its event time will be uncorrelated with all of the muon events. Thus, the timing distribution of preceding muon events for the final sample shows a tiny correlation as expected for a little *correlated* μ in a large amount of *uncorrelated* μ as shown in Figure 7.11(A).
2. In order to estimate the number of *correlated* μ responsible for spallation events, we have to subtract the number of μ which did not make spallation events from the total number of μ . To perform this subtraction, we made a sample of simulated events distributed randomly in space and time. We applied the spallation cut to this sample as done for the actual data sample in order to account for biases introduced by this cut. The muon timing distribution for the random sample is shown in Figure 7.11(B). The dip near delta-T = 0 is due to the accidental loss of events by the spallation cut. This distribution shows the time distribution of *uncorrelated* μ .
3. The normalized distribution of Figure 7.11(B) is subtracted from the distribution in Figure 7.11(A). The residual of the subtraction is shown in Figure 7.11(C) (*correlated* μ distribution), where the normalization factor is calculated from the off timing region delta-T = 100 \sim 200 seconds. The contamination from muons which make such long-lived spallation products is negligible.
4. Finally, the number of spallation events is obtained as

$$N_{\text{spallation}} = N_{0-50\text{sec}}^{\text{observed}} - N_{0-50\text{sec}}^{\text{random}} \times \frac{N_{100-200\text{sec}}^{\text{observed}}}{N_{100-200\text{sec}}^{\text{random}}}. \quad (7.15)$$

Where, $N_{0-50\text{sec}}^{\text{observed}}$ is the number of muon events within 50 seconds preceding the observed events, $N_{0-50\text{sec}}^{\text{random}}$ are similarly defined but for random events, $N_{100-200\text{sec}}^{\text{observed}}$ and $N_{100-200\text{sec}}^{\text{random}}$ are the same definition with $N_{0-50\text{sec}}^{\text{observed}}$ and $N_{0-50\text{sec}}^{\text{random}}$ but the time window is 100 – 200 seconds.

For 8.0 – 20.0 MeV and $\cos \theta_{\text{sun}} \leq 0.5$, the number of spallation background events obtained by this method is $(2.77 \pm 0.20) \times 10^4$. The number of observed $\bar{\nu}_e$ candidate events is 29781, so the ratio of spallation events to observed events is $93\% \pm 7\%$.

We assumed the delta-T = 100 – 200 seconds region is flat in this analysis. But if this region is not flat, the number of spallation events is changed. Therefore we estimated the systematic error by dividing the normalization time region. In this estimation,

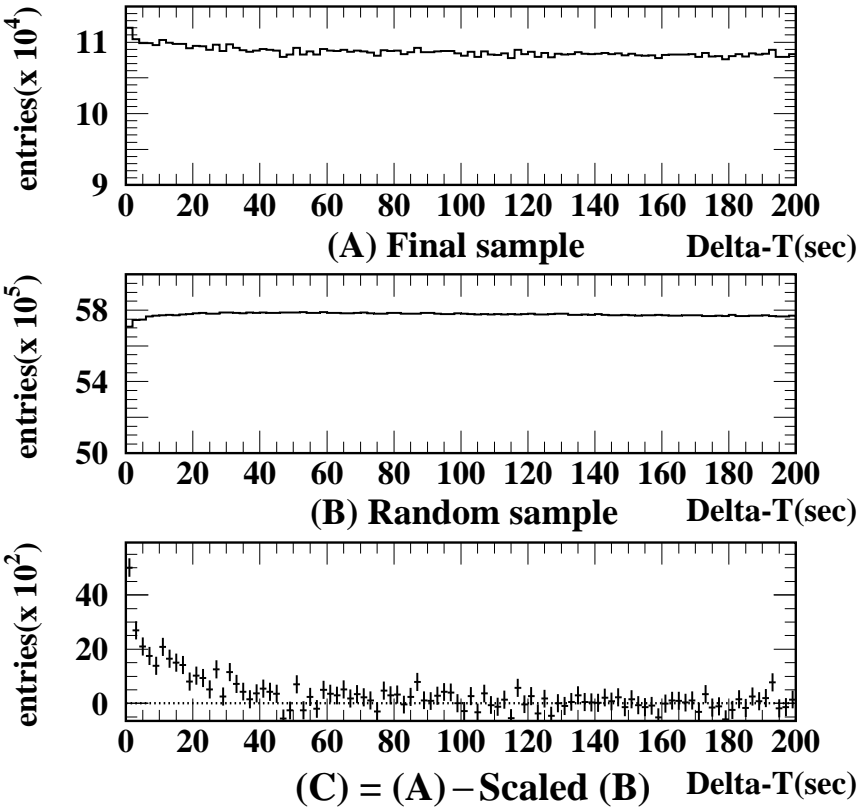


Figure 7.11: Delta-T distribution of muons before low-energy events. (A) shows distribution for observed events, (B) for random events, and (C) for events caused by spallation products obtained by $(A) - \alpha \times (B)$.

| Energy range (MeV) | Systematic error (%) |
|--------------------|----------------------|
| 8.0 – 9.0 | $\pm 0.6 \%$ |
| 9.0 – 10.0 | $\pm 1.4\%$ |
| 10.0 – 11.0 | +9.5% -9.4% |
| 11.0 – 12.0 | $\pm 15.0\%$ |
| 12.0 – 20.0 | $\pm 2.1\%$ |
| 8.0 – 20.0 | $\pm 1.1\%$ |

Table 7.1: Systematic errors for spallation background estimation

$N_{100-150\text{sec}}^{\text{observed}}/N_{100-150\text{sec}}^{\text{random}}$ and $N_{150-200\text{sec}}^{\text{observed}}/N_{150-200\text{sec}}^{\text{random}}$ were used as normalization factors instead of $N_{100-200\text{sec}}^{\text{observed}}/N_{100-200\text{sec}}^{\text{random}}$. $N_{\text{spallation}}$ differences from each result are considered as the systematic error. The obtained systematic error is $\pm 1.1\%$ for $E = 8.0 \text{ MeV} - 20.0 \text{ MeV}$. The systematic errors for each energy bin are shown in Table 7.1. The spallation contamination in each energy bin is shown in Figure 7.12.

7.4.2 ^8B spectrum dependent limit

As described in the previous section, the major component of the $\bar{\nu}_e$ candidate events is spallation backgrounds in the 8.0 – 20.0 MeV region. A statistical subtraction was performed. We set the flux upper limit conservatively assuming all the remaining events to be $\bar{\nu}_e$ events.

In this section, we use the standard solar model (SSM) BPB2001 [26] for the ^8B neutrino flux and assume converted $\bar{\nu}_e$ to keep the original ^8B spectrum [27]. The expected $\bar{\nu}_e$ spectrum after the reduction is obtained by a Monte Carlo simulation. The angular correlation of the inverse β decay reaction is also simulated, and the effect of this dependence on the reduction efficiency is taken into account (Sec.6.7). Figure 7.13 shows the energy spectrum of $\bar{\nu}_e$ M.C. after the application of all reductions and $\cos\theta_{\text{sun}} \leq 0.5$ cut. And Figure 7.14 shows the energy spectrum of the observed data. Comparing the observed data with the M.C. data, a $\bar{\nu}_e/\text{SSM}$ conversion limit is obtained.

The upper limit of $\bar{\nu}_e/\text{SSM}$, α , is defined by a 90% one-sided limit of a gaussian distribution,

$$F_{90} = 0.9 \times F_{\text{total}} \quad (7.16)$$

$$F_{90} = \frac{1}{\sqrt{2\pi}\sigma} \int_0^\alpha \exp\{-(x-f)^2/2\sigma^2\} dx \quad (7.17)$$

$$F_{\text{total}} = \frac{1}{\sqrt{2\pi}\sigma} \int_0^\infty \exp\{-(x-f)^2/2\sigma^2\} dx. \quad (7.18)$$

Where f is the ratio of the observed number of events to the SSM prediction before and after the statistical subtraction of spallation events. σ is the total error of the ratio. The

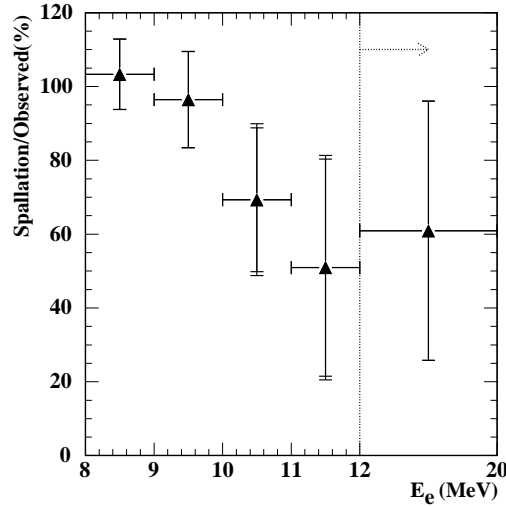


Figure 7.12: Spallation contamination in each energy bins. The horizontal axis shows the total energy and the vertical axis shows the ratio of spallation events to observed events. The inner error bar shows only the statistical error and the outer error bar shows the statistical and systematic combined error.

blue lines in Figure 7.15 show 90% C.L. limits on the $\bar{\nu}_e$ flux before the subtraction. The red lines show the limits after the subtraction (only for $E \geq 8$ MeV). By combining the statistics for $8 \text{ MeV} \leq E \leq 20 \text{ MeV}$, a global upper limit of 0.8% to the SSM neutrino flux is obtained.

7.4.3 Angular distribution analysis

Some authors have indicated that the positron angular distribution may be useful for the search for $\bar{\nu}_e$ in the SK data [72, 73] especially in the lower energy region [74]. The $\cos \theta_{\text{sun}}$ direction can be formulated as $f(\cos \theta_{\text{sun}}) = 0.5 \times (1 + \alpha \times \cos \theta_{\text{sun}})$, where α is monotonically increasing coefficient with neutrino energy (except near the reaction threshold), and α turns over from negative to positive at $E_\nu \sim 13$ MeV [56]. The angular information is useful for the $\bar{\nu}_e$ search at the lowest neutrino energies where $f(\cos \theta_{\text{sun}})$ has a significant slope and the event statistics are large. The expected $\cos \theta_{\text{sun}}$ distribution of $\bar{\nu}_e$ events are obtained by a detector simulation using the formula as shown in Figure 7.16.

Solar neutrino elastic scattering is also a background in this analysis. Almost all elastic scattering events have $\cos \theta_{\text{sun}} > 0.5$, and events with $\cos \theta_{\text{sun}} \leq 0.5$ are used. We also subtract the small amount of elastic scattering events spilled into $\cos \theta_{\text{sun}} \leq 0.5$ using a Monte Carlo simulation ($\sim 5\%$ for 5-20 MeV). Another background is $^{18}\text{O}(\nu_e; e)^{18}\text{F}$ [75, 76]. There is only a small number of events from this (0.03% \sim 2%, depending on energy),

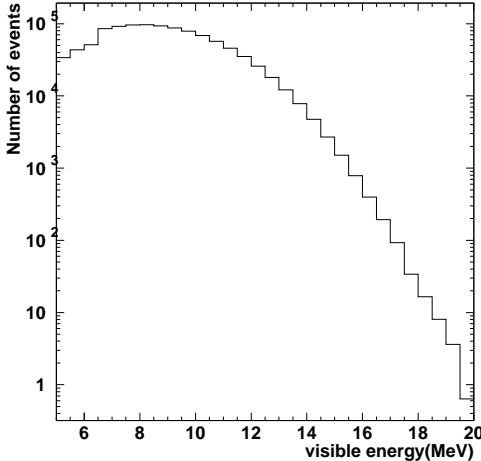


Figure 7.13: The expected energy spectrum of $\bar{\nu}_e$ events after all reductions obtained by a M.C. simulation. The dip around ~ 6 MeV is caused by the live time difference of the LE and the SLE ($\lesssim 6.5$ MeV) trigger data.

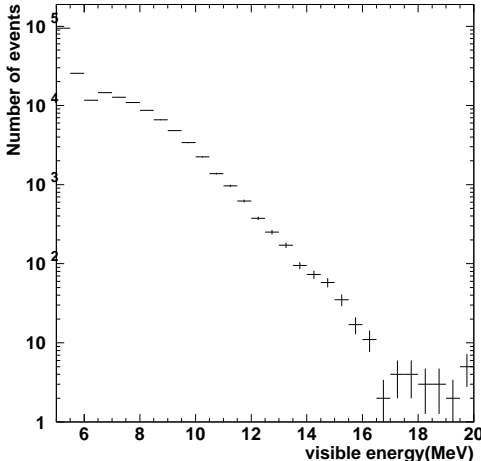


Figure 7.14: Energy spectrum of the observed data after all reductions.

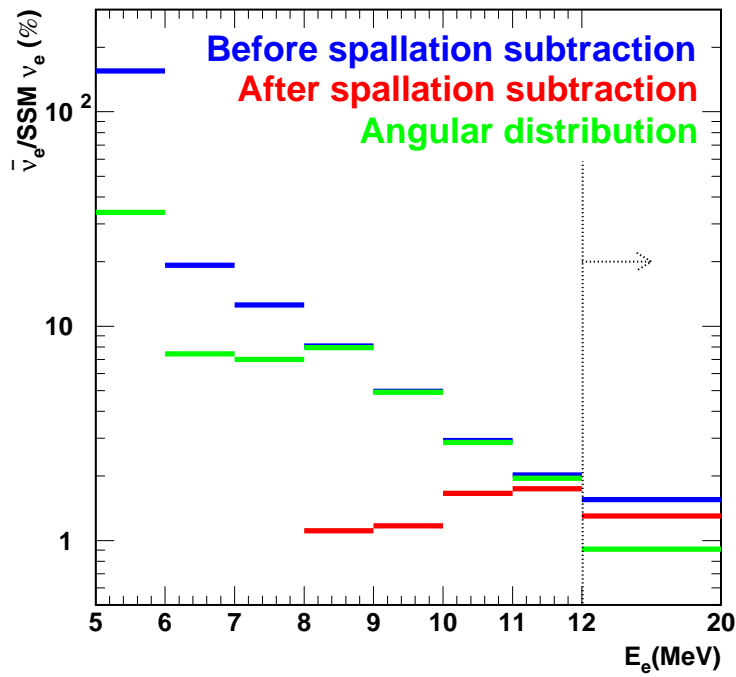


Figure 7.15: Summary of $\bar{\nu}_e$ limits that assuming ${}^8\text{B}$ spectrum is kept. The horizontal axis shows visible energy ($\sim E_{\bar{\nu}_e} - 1.3$ MeV) and the vertical axis shows the 90% C.L. $\bar{\nu}_e$ rate normalized to the SSM ν_e rate. The blue and red lines show the 90% C.L. upper limit of the ratio before and after the statistical subtraction of the spallation background, respectively. The green lines show the limit from the angular distribution analysis.

but electrons from this process have a negative slope in their angular distribution and look like the low-energy $\bar{\nu}_e$. Their contributions are subtracted from the data using the ν_e flux measured by the charged current reaction in SNO, 1.76×10^6 /cm²/sec [77]. A $\bar{\nu}_e$ flux upper limit is obtained using a χ^2 test of the slope on the $\cos \theta_{\text{sun}}$ distribution. The χ^2 is defined for each energy as follows:

$$\chi^2 = \sum_{i=1}^{N_{\text{cos}}} \left\{ \frac{N_i^{\text{data}} - N_i^{\text{el}} - N_i^{18\text{O}} - \delta N_i^{\bar{\nu}_e} - \beta N_i^{\text{BG}} (1 + \gamma \cos \theta_{\text{sun}})}{\sigma_i^{\text{stat.}}} \right\}^2 + \left(\frac{\gamma}{\sigma^{\text{syst.}}} \right)^2 \quad (7.19)$$

i is the index for the $\cos \theta_{\text{sun}}$ bin ($\cos \theta_{\text{sun}} \leq 0.5$, $N_{\text{cos}} = 30$), N_i^{data} the number of observed events, $\sigma_i^{\text{stat.}}$ the statistical error, N_i^{el} the expected number of elastic scattering events, $N_i^{18\text{O}}$ the expected number of events from the $^{18}\text{O}(\nu_e; e)^{18}\text{F}$ reaction, $N_i^{\bar{\nu}_e}$ the number of $\bar{\nu}_e$ events, N_i^{BG} the number of all the other backgrounds almost uncorrelated in direction with the Sun (flat distribution). N_i^{el} and $N_i^{18\text{O}}$ are both $\lesssim 2\%$ of N_i^{data} , and the systematic errors of these terms are negligible. $\sigma^{\text{syst.}}$ ($= 0.5\%$) is the systematic error of the shape of the background and γ is the parameter that takes this into account. β parameterizes the amount of such background events. We divided the parameter space for δ into a grid, and minimized χ^2 with respect to β and γ at each grid point. The resulting γ and χ_{min}^2 indicated good fits to the data. χ^2 as a function of δ obtained in this way is an input to a probability function,

$$\text{Probability} = e^{-(\chi^2 - \chi_{\text{min}}^2)/2}. \quad (7.20)$$

The typical Probability distribution is shown in Figure 7.17. From this analysis, we set a 90% C.L. upper limit for each energy bin. The green lines in Fig. 7.15 show the results. It should be noted that the spallation background subtraction is not applied in this analysis for two reasons. First, at $E < 8$ MeV, spallation events are a small minority of the total background. Second, at $E > 8$ MeV, there are insufficient statistics to perform the spallation subtraction for various angular bins.

7.4.4 ^8B spectrum independent limit

The analysis described so far assumes that the $\bar{\nu}_e$ originates from ^8B solar neutrinos. We also generalized our search by assuming a monochromatic $\bar{\nu}_e$ source at various energies and set conservative $\bar{\nu}_e$ flux upper limits. $\bar{\nu}_e$ upper limits are obtained by the following method.

1. The positron energy is approximately, related to the neutrino energy

$$E_{e^+} \sim E_{\bar{\nu}_e} + M_p - M_n = E_{\bar{\nu}_e} - 1.293 \text{ MeV}. \quad (7.21)$$

Where M_p is the proton mass, M_n is the neutron mass. But, looking in detail, some energy is carried by the recoil neutron and the positron energy is scattering angle

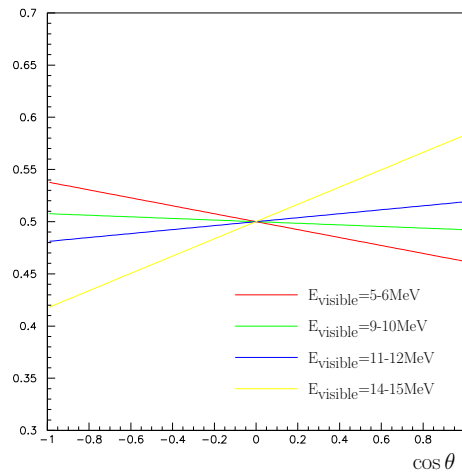


Figure 7.16: Positron angular distributions to the $\bar{\nu}_e$ incident angle for each visible energy

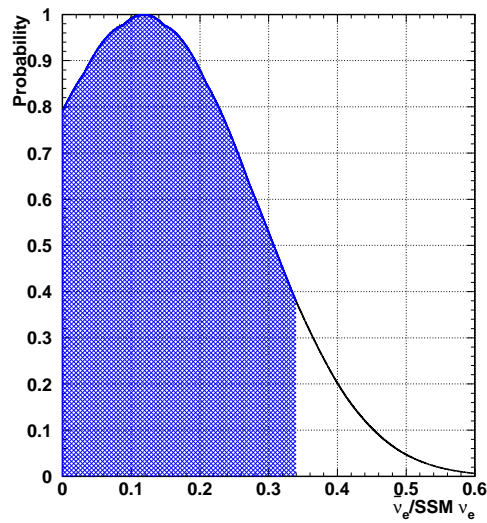


Figure 7.17: Typical Probability distribution of the shape analysis for visible energy 5 - 6 MeV.

dependent. The angular distribution and this angular dependence are considered in the M.C. simulation for each monochromatic neutrino energy.

2. The same reductions used for the real data, and $\cos \theta_{sun} \leq 0.5$ cut are applied.
3. We then obtain the positron visible energy distribution for each $\bar{\nu}_e$ energy. The obtained positron spectrum is well described by a Gaussian.
4. The peak value and 1σ range of the spectrum are obtained by a Gaussian fit as shown in Figure 7.18.
5. Finally, we calculated the $\bar{\nu}_e$ flux upper limit by comparing the observed number of events and M.C. events within this energy region. The procedure of the limit calculation is same as that for the ^8B spectrum dependent analysis.
6. We also apply the statistical subtraction of the spallation backgrounds for more strict limits.

This upper limit is very conservative because we do not take into account of the large spill-over from lower energy bins that is implied by the sharply falling spectrum seen in the data. The 90% C.L. limits are shown in Figure 7.19.

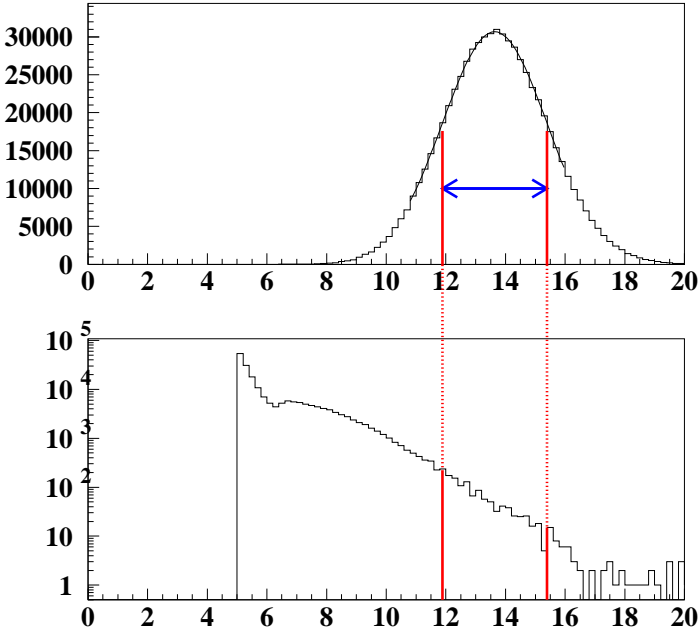


Figure 7.18: Energy spectra of observed and M.C. data. The upper figure shows the M.C. energy spectrum for the case $E_{\bar{\nu}_e} = 15$ MeV. The lower figure shows the energy spectrum of the observed data. The red line shows 1σ range from gaussian fitting.

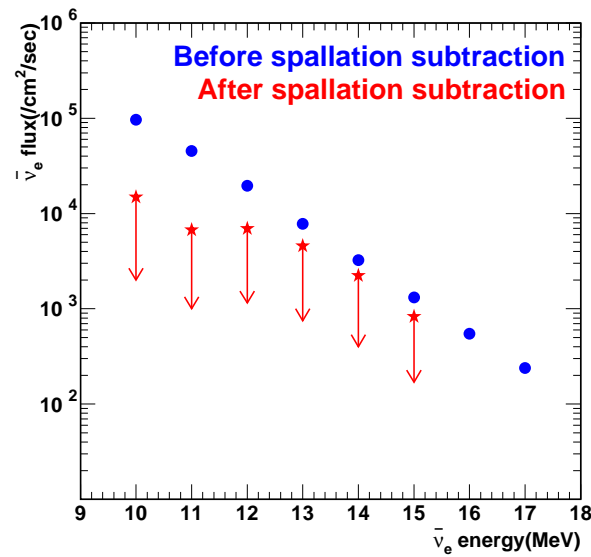


Figure 7.19: 90% C.L. upper limits of the $\bar{\nu}_e$ flux for each monochromatic $\bar{\nu}_e$ energy. The horizontal axis shows neutrino energy and the vertical axis shows the flux limit. The circles show the limits before the spallation subtraction while the stars show the limits after the subtraction. The two highest-energy bins have an insufficient number of events for the statistical subtraction.

Chapter 8

Discussions

In this chapter, physics interpretations of the results presented in Chapter.7 based on 1496 days of the Super-Kamiokande data. In section.8.1, a global analysis with the other solar neutrino results and the KamLAND results is discussed in the context of the most succeeded neutrino oscillation hypothesis. In section.8.2, constraints on the neutrino magnetic moment and magnetic field in the sun are discussed and the impacts on the global neutrino oscillation analysis are described.

8.1 Oscillation study

As described in Chapter.2, all the solar neutrino experiments except the SNO NC measurement have claimed deficit of solar neutrinos. Under the two flavor neutrino oscillation hypothesis, a global analysis of all these results together with the SNO NC is performed.

In order to treat correlations of the results properly a χ^2 method with a correlation matrix is used. The definition of χ^2 is as follows,

$$\begin{aligned}\chi^2 &= \sum_{i,j=1}^{N_{exp}} (R_i^{exp} - R_i^{osc}) V_{ij}^{-1} (R_j^{exp} - R_j^{osc}) \\ &+ \sum_{i=1}^{N_{zenith}} \sum_{j=1}^{N_{ene}} \frac{\{R_{ij}^{data} - (\alpha \cdot R_{ij}^{osc}(^8B) + \beta \cdot R_{ij}^{osc}(hep)) / f_i^{corr}(\epsilon_s, \epsilon_r, \epsilon_b)\}^2}{\sigma_i^2} \\ &+ \epsilon_s^2 + \epsilon_r^2 + \epsilon_b^2.\end{aligned}\tag{8.1}$$

Where each parameters in this χ^2 are the following,

- N_{exp}
The number of flux measurements, which is 5 in this analysis (combined Ga rate, Cl rate, SK rate, SNO CC rate, SNO NC rate ; see Chapter.2).

- R_i^{exp}
The ratio of the observed flux to the SSM BPB2001 prediction for each measurements.
- R_i^{osc}
The ratio of the expected neutrino flux with neutrino oscillations to the SSM prediction for each measurements.
- V_{ij}
The error matrix made of the following elements,
 $V_{ij} = (\sigma_{ij}^{cs})^2 + (\sigma_{ij}^{SSM})^2 + (\sigma_{ij}^{exp})^2$, where σ_{ij}^{cs} is the error of the effective cross section, σ_{ij}^{SSM} is the error of the SSM rate prediction, σ_{ij}^{exp} is the error for each flux experiments [78]. In the σ_{ij}^{SSM} , following error correlations are considered ; radiative opacities in the sun, luminosity and age of the sun, metallicity(Z/A), heavy element and helium diffusion in the sun, nuclear S-factors S_{11} , S_{33} , S_{34} , S_{17} , $S_{1,14}$.
- N_{zenith}
The number of SK zenith angle bins, which is 7 in this analysis.
- N_{ene}
The number of SK energy bins (=6 for the energy range from 5.5 MeV to 16.0 MeV).
- R_{ij}^{data}
The observed SK flux ratio to the SSM prediction in each energy bins.
- $R_{ij}^{osc}(^8B)$, $R_{ij}^{osc}(hep)$
The ratio of expected 8B and hep neutrino fluxes with neutrino oscillations to the SSM prediction in each energy bins.
- α , β
Free flux normalization parameters for the shape analysis. These are varied freely to minimize the χ^2 .
- f_i^{corr}
The correlated error function consists of the following components(see Sec.7.3.1), $f_i^{corr} = (1 + s_i \cdot \epsilon_s)(1 + r_i \cdot \epsilon_r)(1 + b_i \cdot \epsilon_b)$, where s_i, r_i, b_i are the spectrum distortion from the uncertainties of the energy scale, the energy resolution, the 8B neutrino spectrum, respectively. And $\epsilon_s, \epsilon_r, \epsilon_b$ denote the amplitude of the deformation. These are varied to minimize the χ^2 but give penalty terms in the formula.
- σ_i
Square of the quadratic sum of statistical errors and uncorrelated errors for each energy bins.

The first term in this χ^2 represents flux constraints of the 5 measurements. The second and third terms are the relative shape analysis of the SK zenith angle spectra, and the third term constraints the shape deformation from various uncertainties. The Super-Kamiokande is a real time observation and both the time and the energy information are available. Figure 8.1 shows the observed zenith angle spectra and the expected spectra of recoil electrons with neutrino oscillations for two typical oscillation parameters.

The minimum χ^2 (χ_{min}^2) is 42.82 with 45 degrees of freedom at $\sin^2 \theta = 0.82$ and $\Delta m^2 = 6.9 \times 10^{-5} \text{eV}^2$. Figure 8.2 shows the calculated allowed region with the KamLAND allowed region, where 68.3%, 95%, 99%, 99.73% C.L. allowed region are defined as $\chi^2 < \chi_{min}^2 + 2.30, 5.991, 9.21, 11.8$, respectively. And, when we combine the solar neutrino results with KamLAND result under an assumption of the CPT invariance, we obtain the allowed region as shown in Figure 8.3. The LMA2 region is not favored at 99% C.L. any more, and only the LMA1 region remains at the confidence level.

8.2 RSFP+MSW study

If neutrino has a finite magnetic moment, magnetic field in the sun may change the solar neutrino spectrum. The oscillation analysis done in the previous section is the special case of more general RSFP+MSW hypothesis. If we chose the magnetic moment to be zero, the RSFP+MSW hypothesis becomes the simple neutrino oscillation hypothesis. Once RSFP and neutrino oscillations are considered simultaneously, there is a possibility to create anti-electron-neutrinos in the sun. In this section, constraints on the magnetic moment are discussed using the $\bar{\nu}_e$ flux limit in Chapter.7.

8.2.1 Magnetic field in the sun

As described in Sec. 2.3.4, The neutrino propagation is expressed by equation 2.61 in case that neutrino has magnetic moment and is a Majorana particle. The term μB in equation 2.61 is relevant for magnetic spin flip of neutrinos. The transition magnetic moment always appears as the combination with the magnetic field, μB_{sun} . Therefore only $\mu_{\nu} \times B_{\text{sun}}$ is the measurable parameter in the study of RSFP. Even unfortunately, there are only a few references on the magnetic field in the sun as follows :

- From helioseismology, $R/R_{\text{sun}} > \sim 0.7$ region is the convection zone and $R/R_{\text{sun}} < \sim 0.7$ is the radiation zone [79].
- An upper limit of the magnetic field is 300 k Gauss near the base of the convection zone and 20 k Gauss at the radiation zone [80, 81].
- An upper limit of magnetic field in the convection zone is less than 7 M Gauss [82].

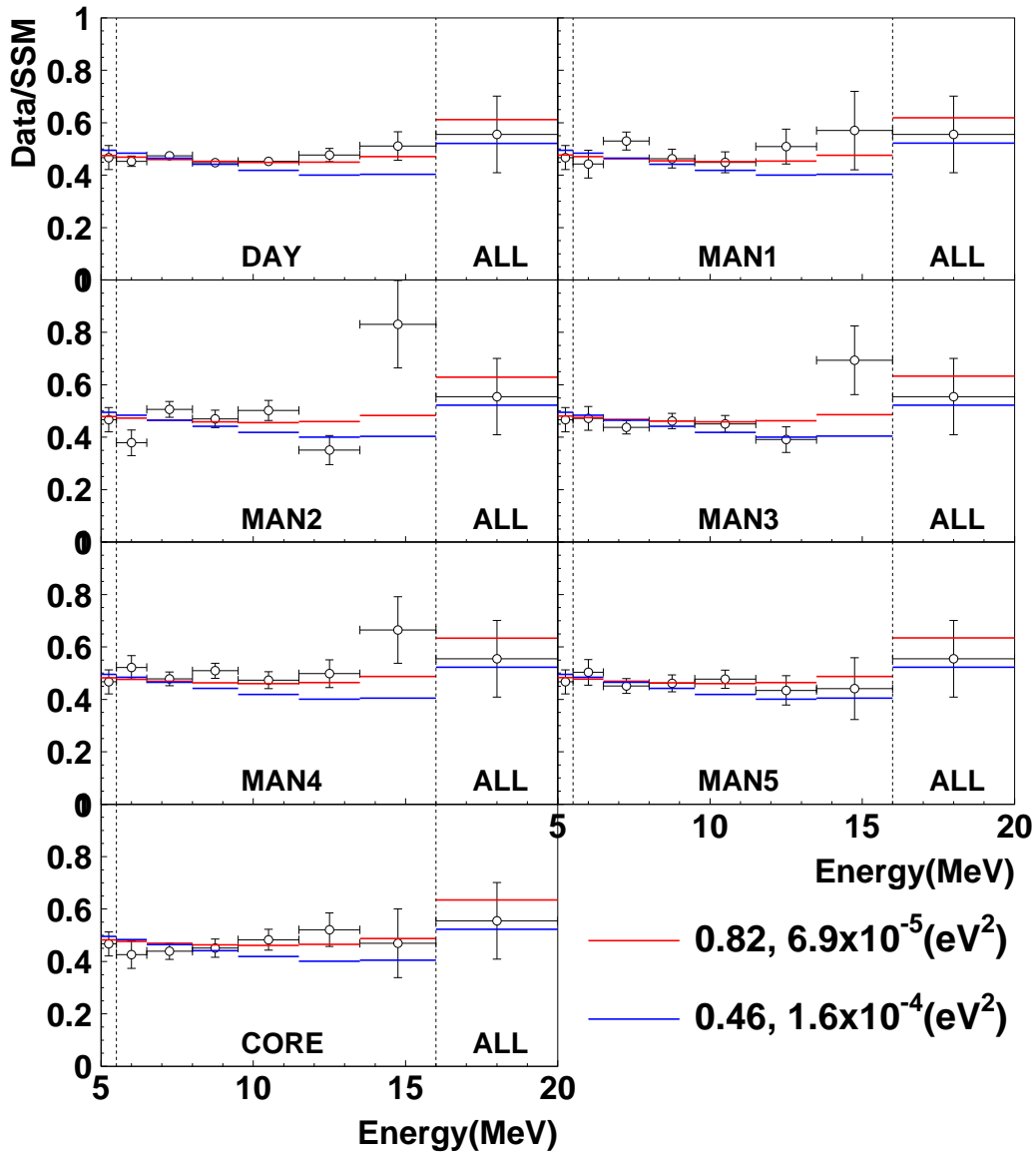


Figure 8.1: The zenith angle spectra with the expected spectra in the cases of $(\sin^2 2\theta, \Delta m^2) = (0.82, 6.9 \times 10^{-5} \text{eV}^2), (0.46, 1.6 \times 10^{-4} \text{eV}^2)$

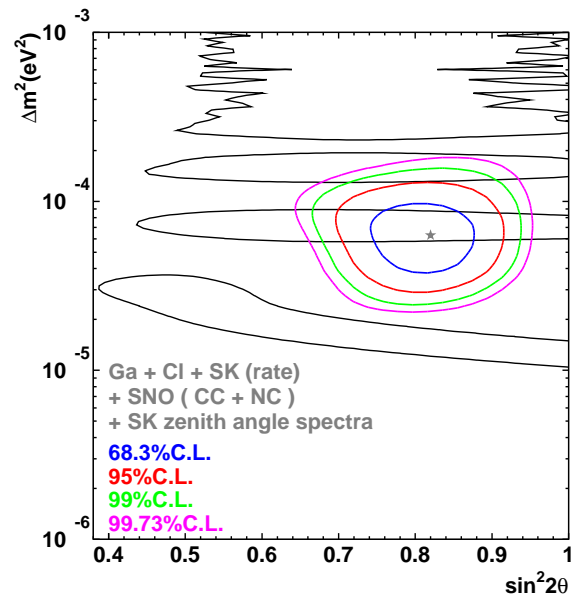


Figure 8.2: The allowed region of Δm^2 and $\sin^2 2\theta$ from a global analysis of the solar neutrino results. The KamLAND 95% C.L. allowed regions are also shown.

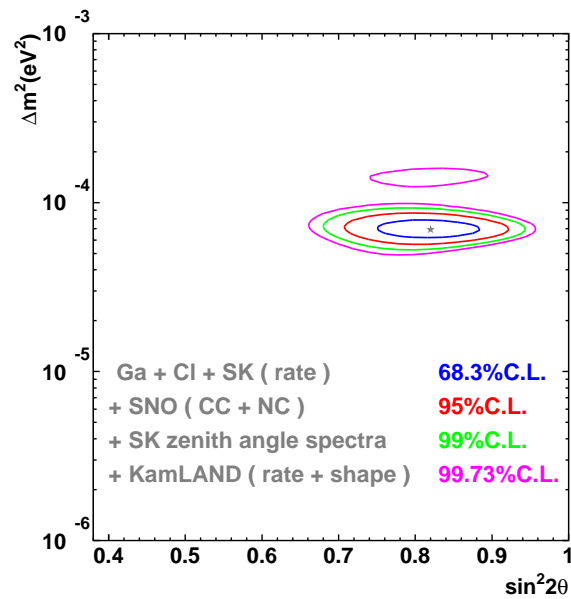


Figure 8.3: The allowed region of Δm^2 and $\sin^2 2\theta$ from a global analysis of all solar neutrino results and KamLAND result

We fixed the μ_ν at the current upper limit $1.0 \times 10^{-10} \mu_B$ in the analysis. But instead, we varied the magnetic field from 100 Gauss to 10 MGauss. Therefore the range of $\mu_\nu \times B_{\text{sun}}$ we used is $1 \times 10^{-8} \sim 1 \times 10^{-3} \mu_B \text{ Gauss}$.

For a numerical calculation, we need a profile of the magnetic field. There is no reliable theory on the profile. And we used the following three simple models for the magnetic field in the sun [83] :

- Profile1 :

$$B = 0 \quad (x < x_R) \quad (8.2)$$

$$B = B_{\text{MAX}} \cdot \frac{x - x_R}{x_C - x_R} \quad (x_R \leq x < x_C) \quad (8.3)$$

$$B = B_{\text{MAX}} \cdot \left(1 - \frac{x - x_C}{1 - x_C}\right) \quad (x_C \leq x < 1) \quad (8.4)$$

where B_{MAX} is the maximum magnetic field in the sun, s is a radial position in unit of the solar radius, x_R and x_C are parameters and equal to 0.7, 0.85, respectively.

- Profile2 :

$$B = 0 \quad (x < x_R) \quad (8.5)$$

$$B = B_{\text{MAX}} \cdot \frac{x - x_R}{x_C - x_R} \quad (x_R \leq x < x_C) \quad (8.6)$$

$$B = B_{\text{MAX}} \cdot \left[1 - \left(\frac{x - 0.7}{0.3}\right)^2\right] \quad (x_C \leq x < 1) \quad (8.7)$$

where $x_R = 0.65$ and $x_C = 0.75$.

- Profile3 :

$$B = 2.16 \times 10^3 \quad (x < x_C) \quad (8.8)$$

$$B = \frac{B_{\text{MAX}}}{0.998} \cdot \left[1 - \left(\frac{x - 0.75}{0.04}\right)^2\right] \quad (x_R \leq x < x_C) \quad (8.9)$$

$$B = \frac{B_{\text{MAX}}}{\cosh 30(x - x_C)} \quad (x_C \leq x < 1) \quad (8.10)$$

where $x_R = 0.7105$ and $x_C = 0.7483$.

Figure 8.4 shows magnetic field profiles in case that the maximum magnetic field is 300 k Gauss. B_{MAX} is written as B_{sun} later on.

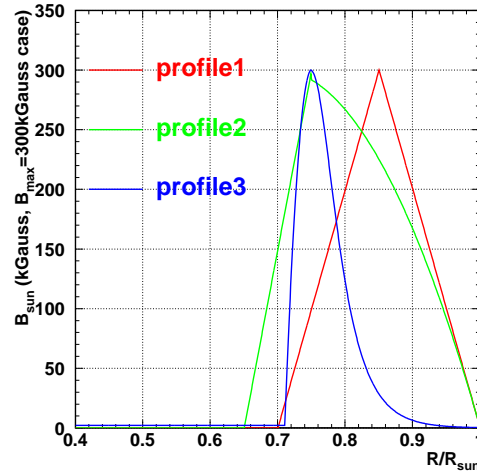


Figure 8.4: The assumed magnetic field profiles in the sun as a function of radius. The maximum magnetic field is fixed to 300 kGauss in this figure.

8.2.2 Constraints on neutrino magnetic moment from flux measurements and zenith angle spectra

A numerical calculation of neutrino propagation in the sun is performed. It supposes that neutrino is Majorana type and has a finite magnetic moment. The propagation matrix is the Hamiltonian of the RSFP+MSW hybrid model defined in Sec. 2.3.4. In the matrix, four neutrino states (two flavors and their anti-particles) are considered. A electron neutrino created at the center is traced following the propagation equation and probabilities to be four neutrino states are obtained as shown in Figure 8.5. In the example ν_e is generated at $R/R_{sun} = 0.05$ and propagates outward. $\nu_{\mu,\tau}$ appear in the radiative zone by a flavor oscillation. And at the convective zone, $\bar{\nu}_e$ and $\bar{\nu}_{\mu,\tau}$ appear by the following conversions,

$$\nu_e \xrightarrow{\text{RSFP}} \bar{\nu}_{\mu,\tau} \xrightarrow{\text{MSW}} \bar{\nu}_e, \quad (8.11)$$

$$\nu_e \xrightarrow{\text{MSW}} \nu_{\mu,\tau} \xrightarrow{\text{RSFP}} \bar{\nu}_e. \quad (8.12)$$

Figure 8.6 shows the neutrino conversion probabilities as a function of neutrino energy for each parameters and profiles. The magnetic field in the earth is small enough, and only the following neutrino oscillations are considered for the propagation in the earth,

$$\nu_e \longleftrightarrow \nu_{\mu,\tau}, \quad (8.13)$$

$$\bar{\nu}_e \longleftrightarrow \bar{\nu}_{\mu,\tau}. \quad (8.14)$$

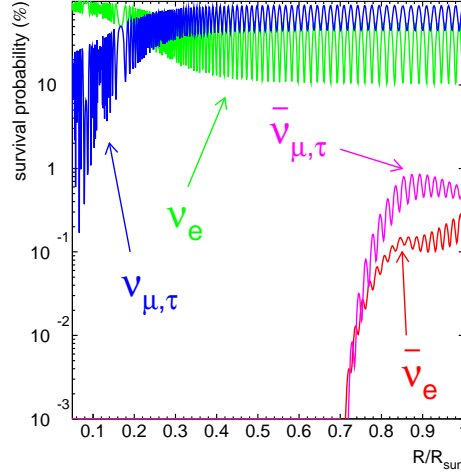


Figure 8.5: Probabilities to be each neutrino states as a function of radial position. Used parameters are $\sin^2 2\theta = 0.84$, $\Delta m^2 = 6.9 \times 10^5 \text{ eV}^2$, $\mu_\nu B_{\text{sun}} = 3 \times 10^{-5}$ for profile1.

When we fit to the observed zenith angle spectra and flux from solar neutrino measurements, we must consider interactions of additional neutrino types. In the SK case, all types of neutrinos (ν_e , $\nu_{\mu,\tau}$, $\bar{\nu}_e$, $\bar{\nu}_{\mu,\tau}$) interact with electrons.

Radiochemical experiments are insensitive to neutrinos other than ν_e and the treatment of them are the same as the neutrino oscillation study. And the SNO observes only ν_e as CC events or all neutrino types equivalent as NC event.

A global analysis of the solar neutrino results for the hybrid model is done with the χ^2 similar to the one for the oscillation analysis.

$$\begin{aligned}
\chi^2 &= \sum_{i,j=1}^{N_{exp}} (R_i^{exp} - R_i^{combine}) V_{ij}^{-1} (R_j^{exp} - R_j^{combine}) \\
&+ \sum_{i=1}^{N_{zenith}} \sum_{j=1}^{N_{ene}} \frac{\{R_{ij}^{data} - (\alpha \cdot R_{ij}^{combine}(^8B) + \beta \cdot R_{ij}^{combine}(hep)) / f_i^{corr}(\epsilon_s, \epsilon_r, \epsilon_b)\}^2}{\sigma_i^2} \\
&+ \epsilon_s^2 + \epsilon_r^2 + \epsilon_b^2.
\end{aligned} \tag{8.15}$$

An allowed region is defined in the three dimensional parameter space ($\sin^2 2\theta$, Δm^2 , $\mu_\nu B_{\text{sun}}$) for each magnetic profile models. Thus the definition of the 95%C.L. allowed region is $\chi^2 < \chi_{min}^2 + 7.82$, and the 90%C.L. allowed region is $\chi^2 < \chi_{min}^2 + 6.25$. Figure 8.7~8.9 shows the allowed regions for each $\mu_\nu B_{\text{sun}}$ and magnetic field profiles.

The minimum χ^2 s are 42.76, 42.28, 42.75 at $(\sin^2 2\theta, \Delta m^2, \mu_\nu B_{\text{sun}}) = (0.82, 6.3 \times 10^{-5} \text{ eV}^2, 3 \times 10^{-5} \mu_B \text{ Gauss})$, $(0.88, 7.9 \times 10^{-5} \text{ eV}^2, 1 \times 10^{-4} \mu_B \text{ Gauss})$, $(0.82, 6.3 \times 10^{-5} \text{ eV}^2, 3 \times 10^{-5} \mu_B \text{ Gauss})$,

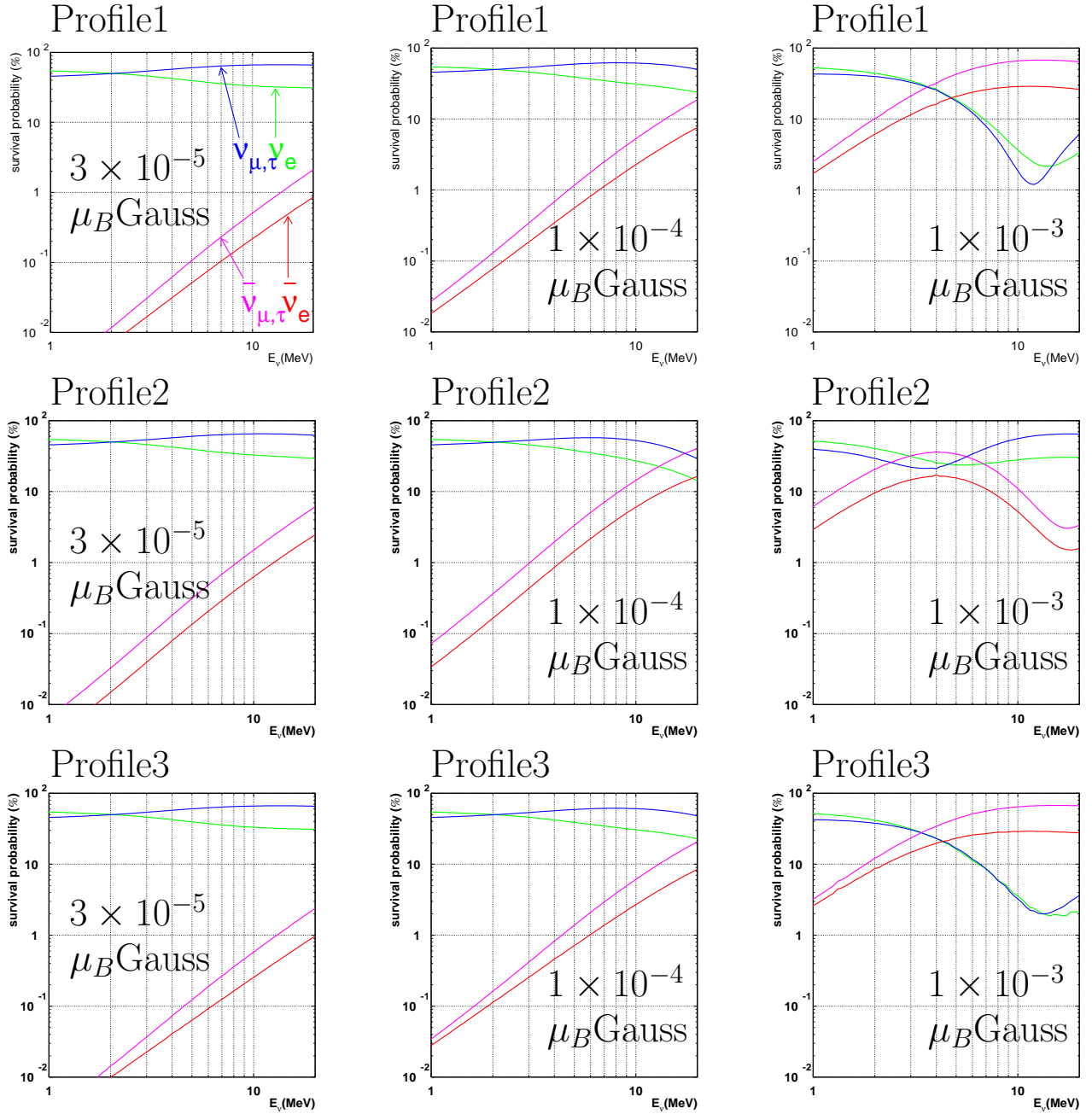


Figure 8.6: Neutrino spectra for each magnetic field profiles and each $\mu_\nu B_{\text{sun}}$. Used oscillation parameters are $\sin^2(2\theta) = 0.84$, $\Delta m^2 = 6.92 \times 10^{-5} \text{eV}^2$.

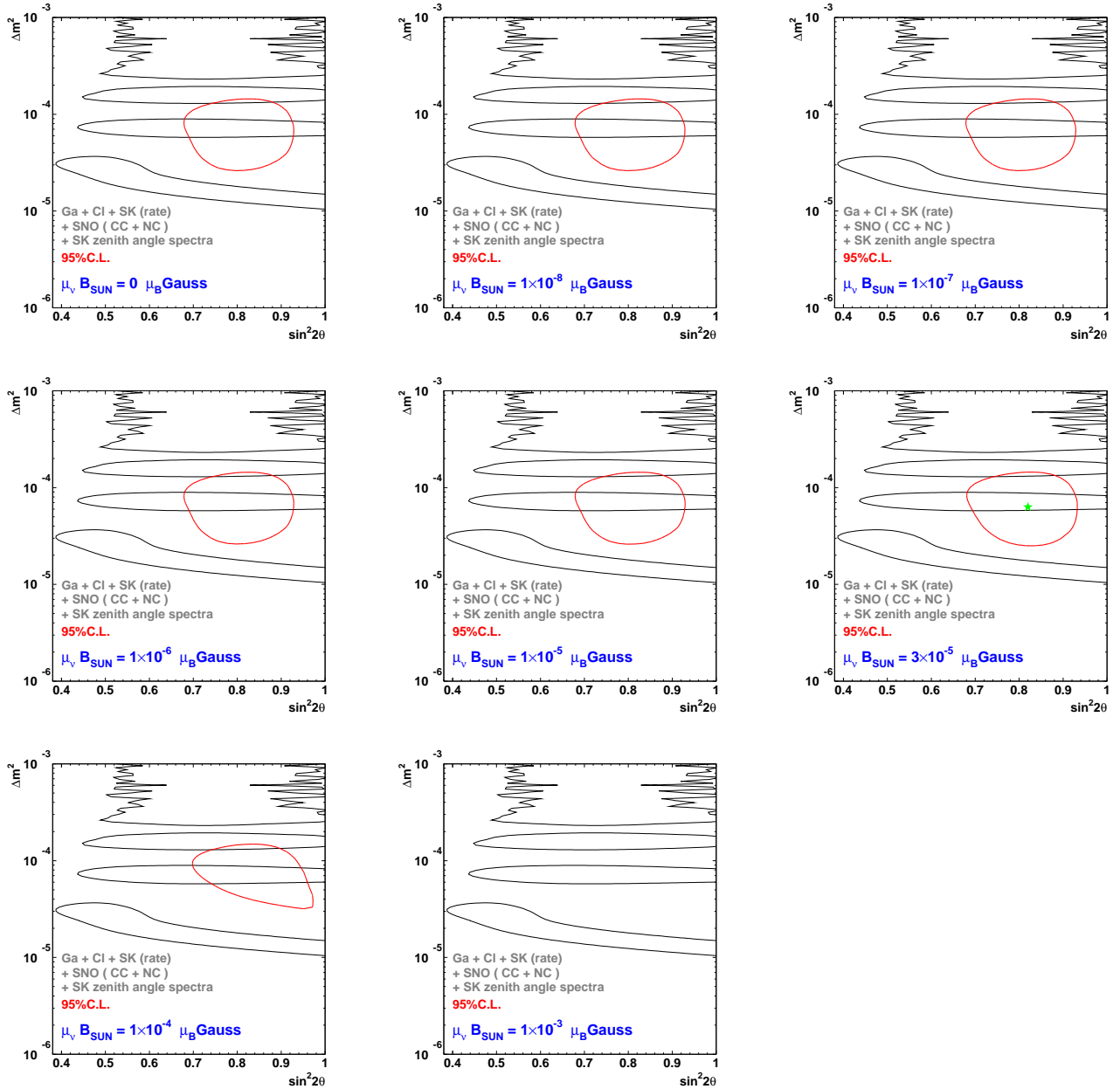


Figure 8.7: 95% C.L. allowed region for each $\mu_\nu B_{\text{sun}}$ in a case of profile1

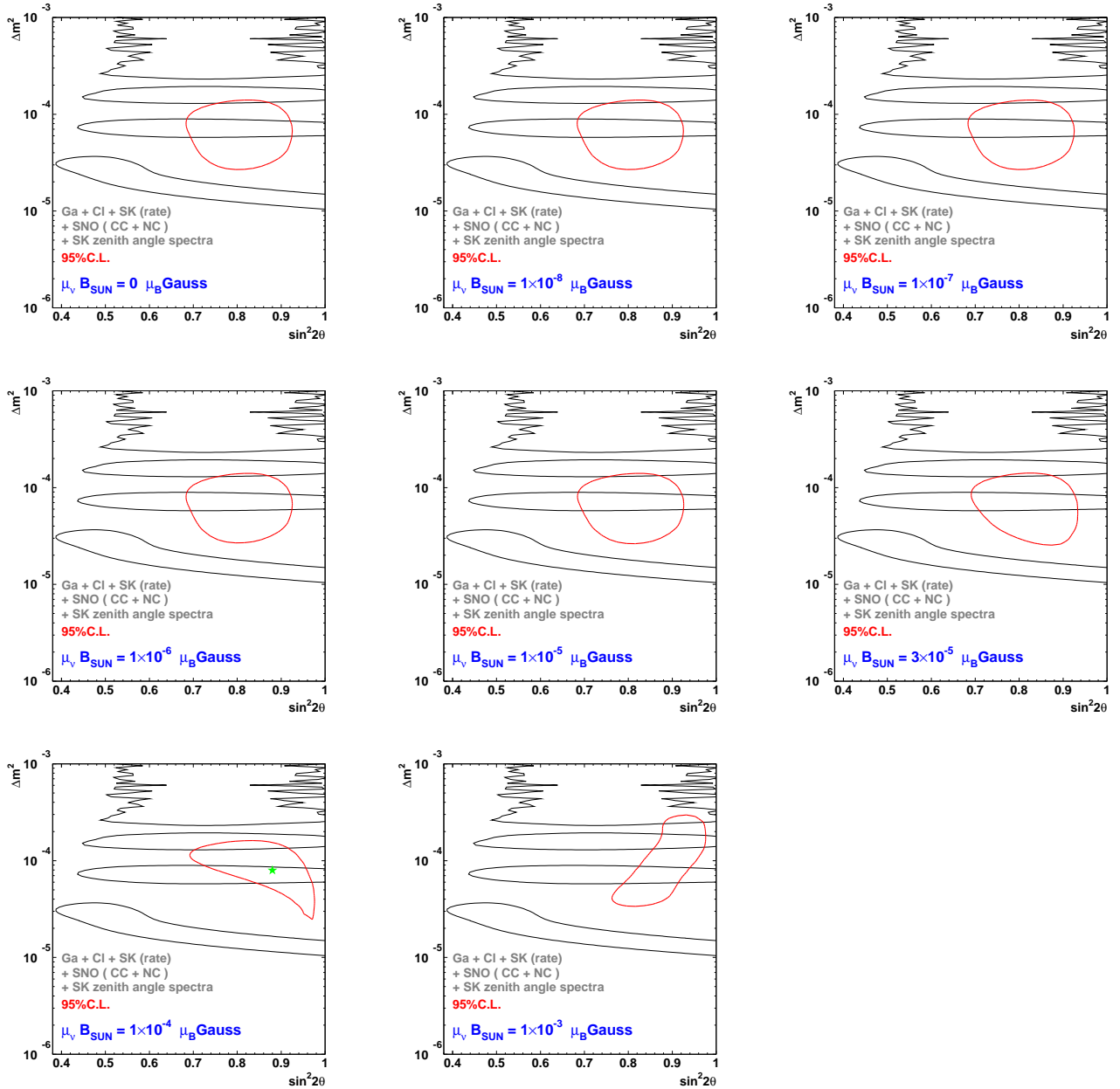


Figure 8.8: 95% C.L. allowed region for each $\mu_\nu B_{\text{sun}}$ in a case of profile2

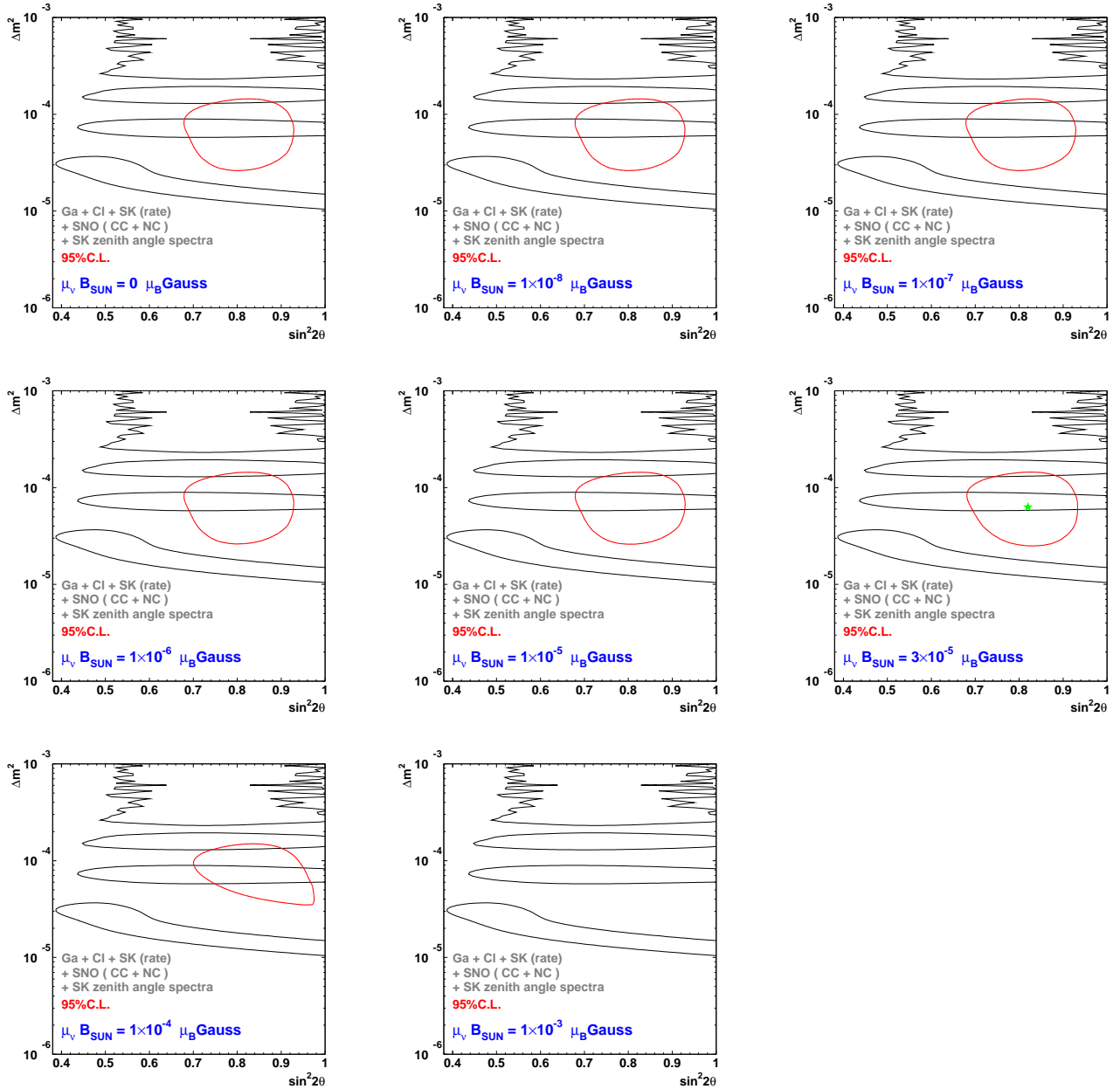


Figure 8.9: 95% C.L. allowed region for each $\mu_\nu B_{\text{sun}}$ in a case of profile3

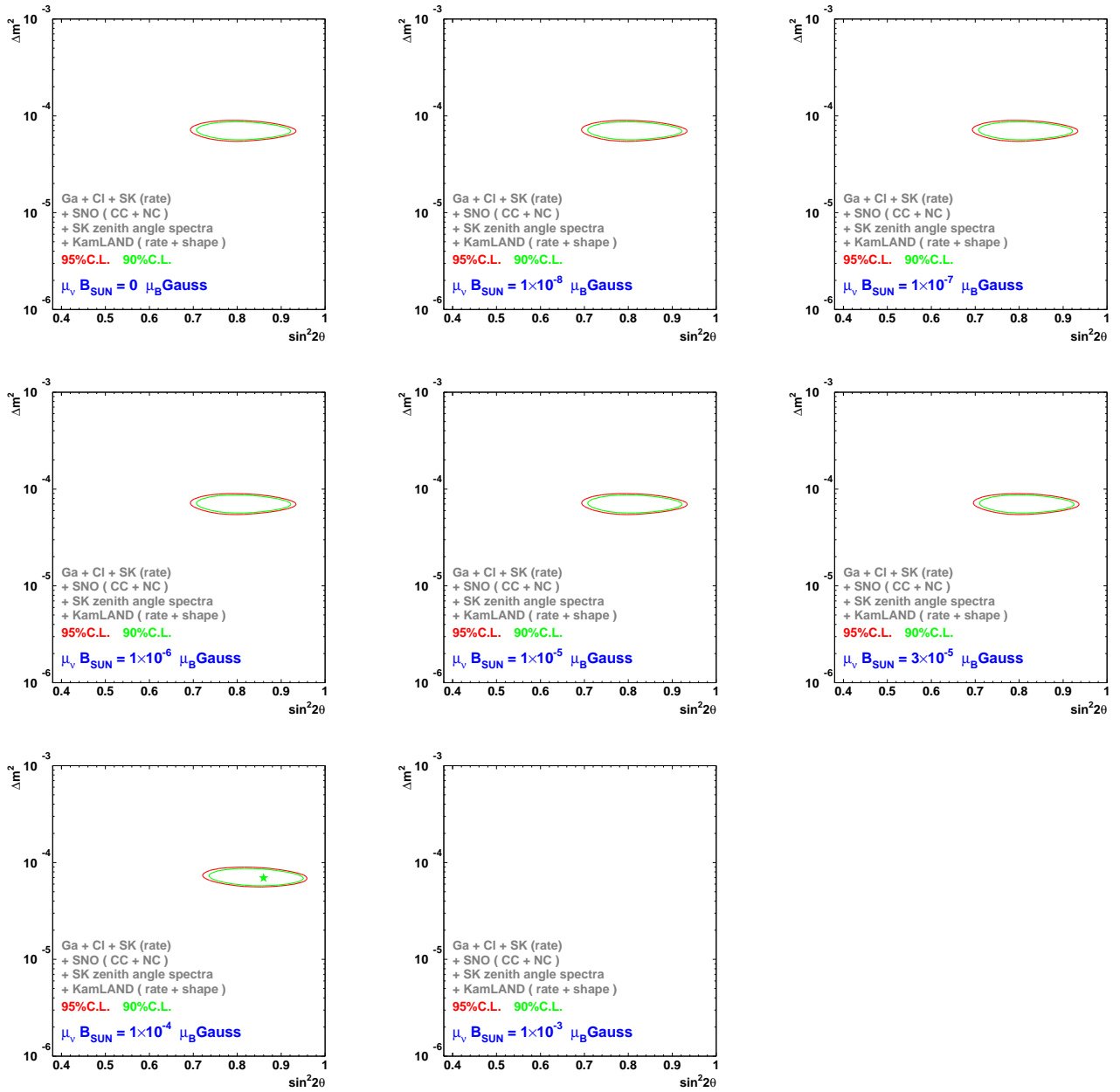


Figure 8.10: 95% C.L. solar global + KamLAND allowed region for each $\mu_\nu B_{\text{SUN}}$ in case of profile

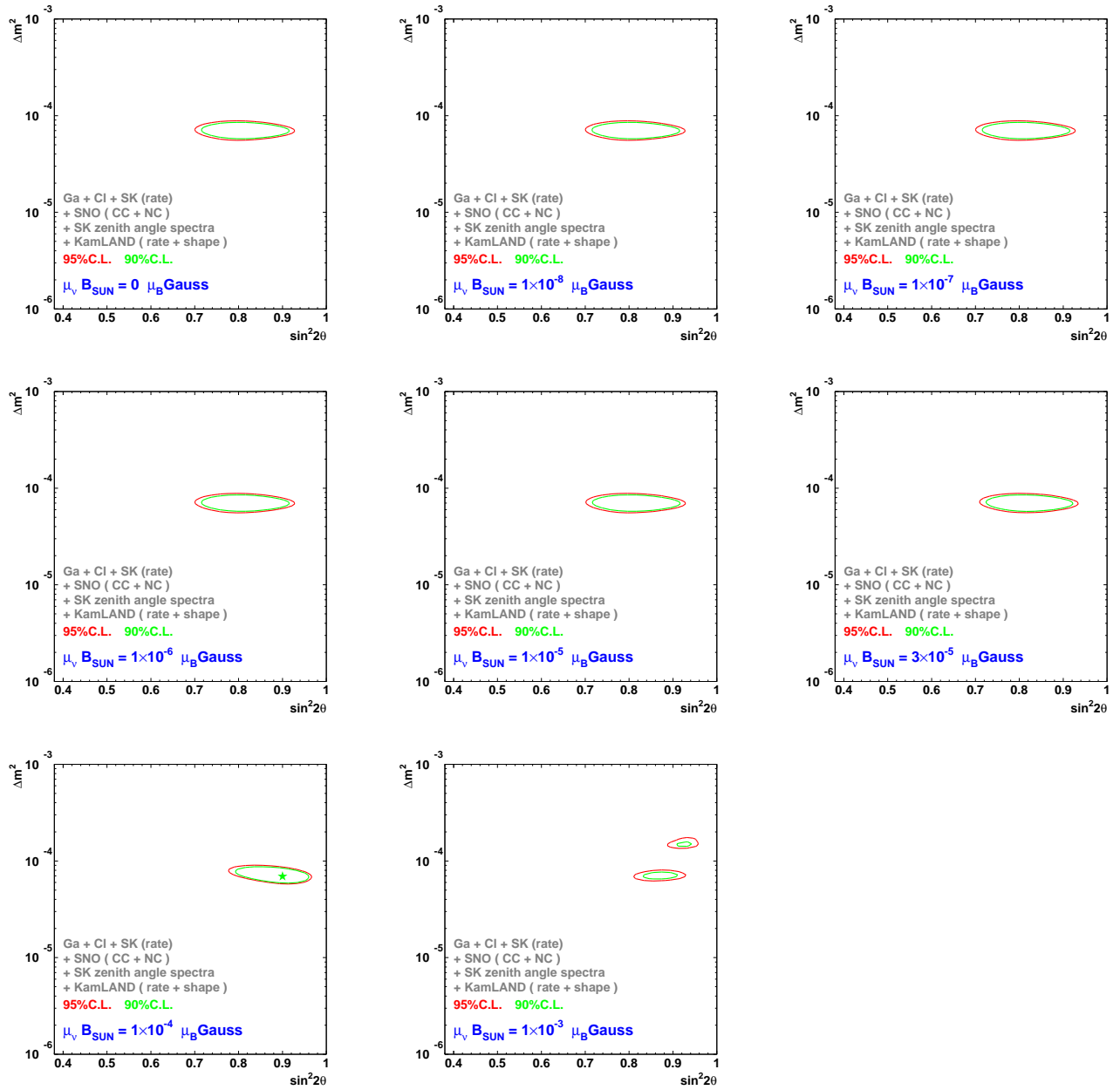


Figure 8.11: 95% C.L. solar global + KamLAND allowed region for each $\mu_\nu B_{\text{SUN}}$ in case of profile2

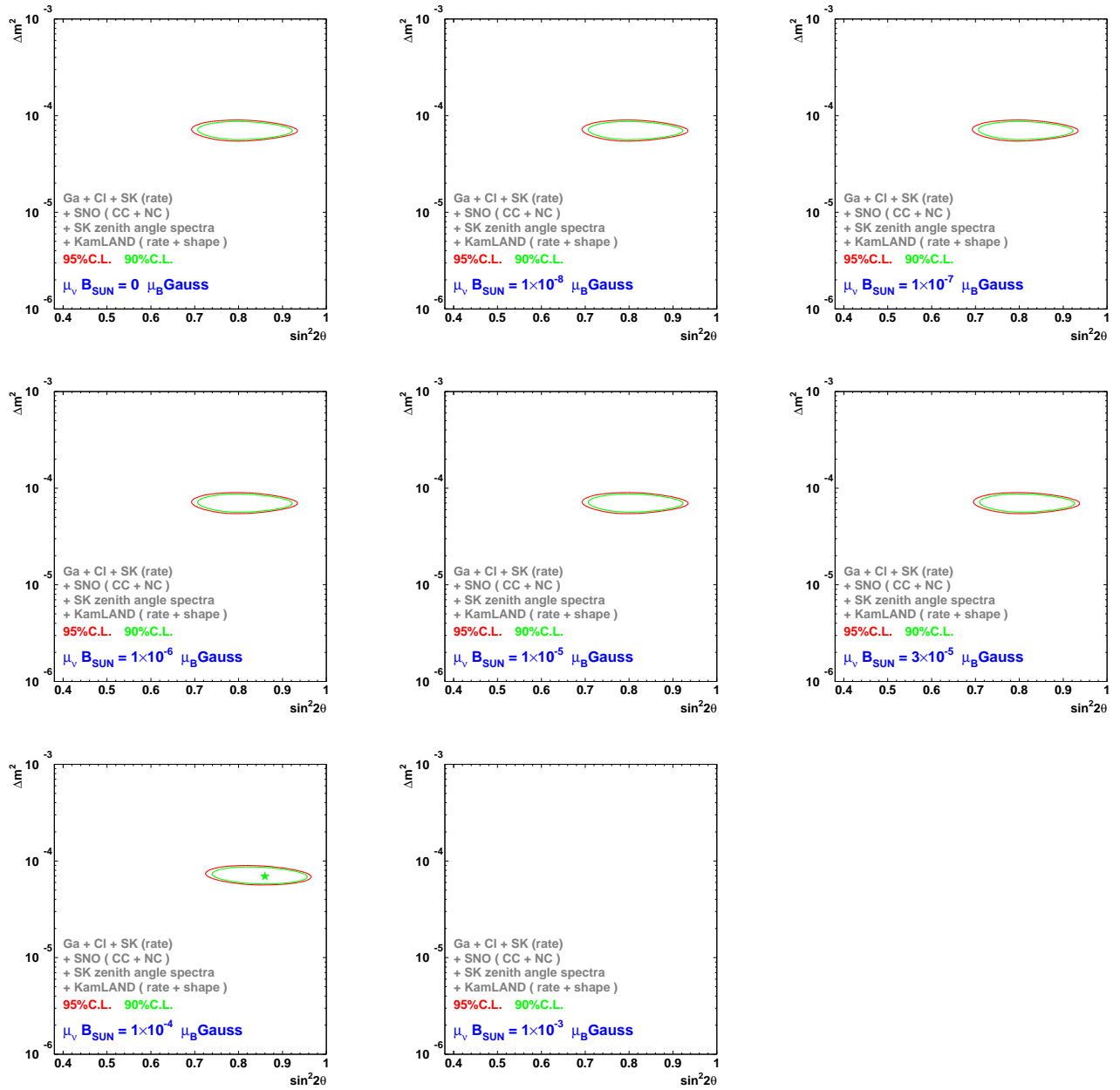


Figure 8.12: 95% C.L. solar global + KamLAND allowed region for each $\mu_\nu B_{\text{SUN}}$ in case of profile3

for profile1, profile2, profile3, respectively. The KamLAND result doesn't change with a finite neutrino magnetic moment. In the case profile1 case, it keeps the shape up to $\mu_\nu B_{\text{sun}} = 3 \times 10^{-5} \mu_B \text{Gauss}$. Effects of the RSFP start to appear at $\mu_\nu B_{\text{sun}} = 1 \times 10^{-4} \mu_B \text{Gauss}$ and finally the allowed region disappears at $\mu_\nu B_{\text{sun}} = 1 \times 10^{-3} \mu_B \text{Gauss}$. Profile3 has similar behavior with the profile1 case. And in the profile2 case, distortion of the allowed region appears at $\mu_\nu B_{\text{sun}} \geq 3 \times 10^{-5} \mu_B \text{Gauss}$ but the allowed region still remains even at $\mu_\nu B_{\text{sun}} = 1 \times 10^{-3} \mu_B \text{Gauss}$. From these contours, we can summarize this analysis as follows :

- Only RSFP doesn't explain KamLAND results but it can be a subdominant process and $\mu_\nu B_{\text{sun}}$ can be as large as $\sim 3 \times 10^{-5} \mu_B \text{Gauss}$ with the magnetic profiles we've tested.
- The RSFP effect becomes significant over $1 \times 10^{-4} \mu_B \text{Gauss}$ but still has an allowed region and is still tolerable.
- When $\mu_\nu B_{\text{sun}}$ exceeds $1 \times 10^{-3} \mu_B \text{Gauss}$, effects of RSFP are so strong and there is no allowed region anymore in some cases.

Figure 8.10~8.12 shows the allowed regions from solar global with KamLAND for each $\mu_\nu B_{\text{sun}}$ and magnetic field profiles. The tendency is the same as that of the above.

8.2.3 Constraint on neutrino magnetic moment from the $\bar{\nu}_e$ flux limit

We discussed about constraints on magnetic moment and magnetic fields in the sun by using a spectrum distortion in the previous section. But now we have one more information, which is the $\bar{\nu}_e$ flux limit. For example the $\bar{\nu}_e$ flux upper limit at SK is 0.8% of the SSM neutrino flux at 90% C.L. in the visible energy region 8~20 MeV supposing energy independent conversion. In order to investigate constraints on the hybrid model from the $\bar{\nu}_e$ flux limit, we define $\bar{\nu}_e/\text{SSM}$ as number of expected $\bar{\nu}_e$ events from the hybrid model over number of expected $\bar{\nu}_e$ events when all solar neutrinos are converted to $\bar{\nu}_e$ in the visible energy region 8 - 20 MeV. Figure 8.13 shows expected $\bar{\nu}_e/\text{SSM}$ as a function of $\mu_\nu B_{\text{sun}}$ for typical oscillation parameters in each profiles.

The expected $\bar{\nu}_e/\text{SSM}$ is calculated for each oscillation parameters and $\mu_\nu B_{\text{sun}}$, and $\bar{\nu}_e/\text{SSM} \geq 0.8\%$ region is surveyed as shown in Figure 8.14.

Combining the $\bar{\nu}_e$ flux limit with the solar global fit obtained in Figure 8.10, 8.11, 8.12, we can obtain more strict upper limit of $\mu_\nu B_{\text{sun}}$. In Figure 8.15, 8.16, 8.17, the 90% C.L. allowed region of the solar+KamLAND global fit and the 90% C.L. excluded region from the $\bar{\nu}_e$ upper limit are overlaid. In all profiles, all the allowed regions are excluded by the $\bar{\nu}_e$ flux limit at 90% C.L. when $\mu_\nu B_{\text{sun}} \geq 1 \times 10^{-4} \mu_B \text{Gauss}$. In order to have a solution in the hybrid model, $\mu_\nu B_{\text{sun}}$ has to be less than $1 \times 10^{-4} \mu_B \text{Gauss}$.

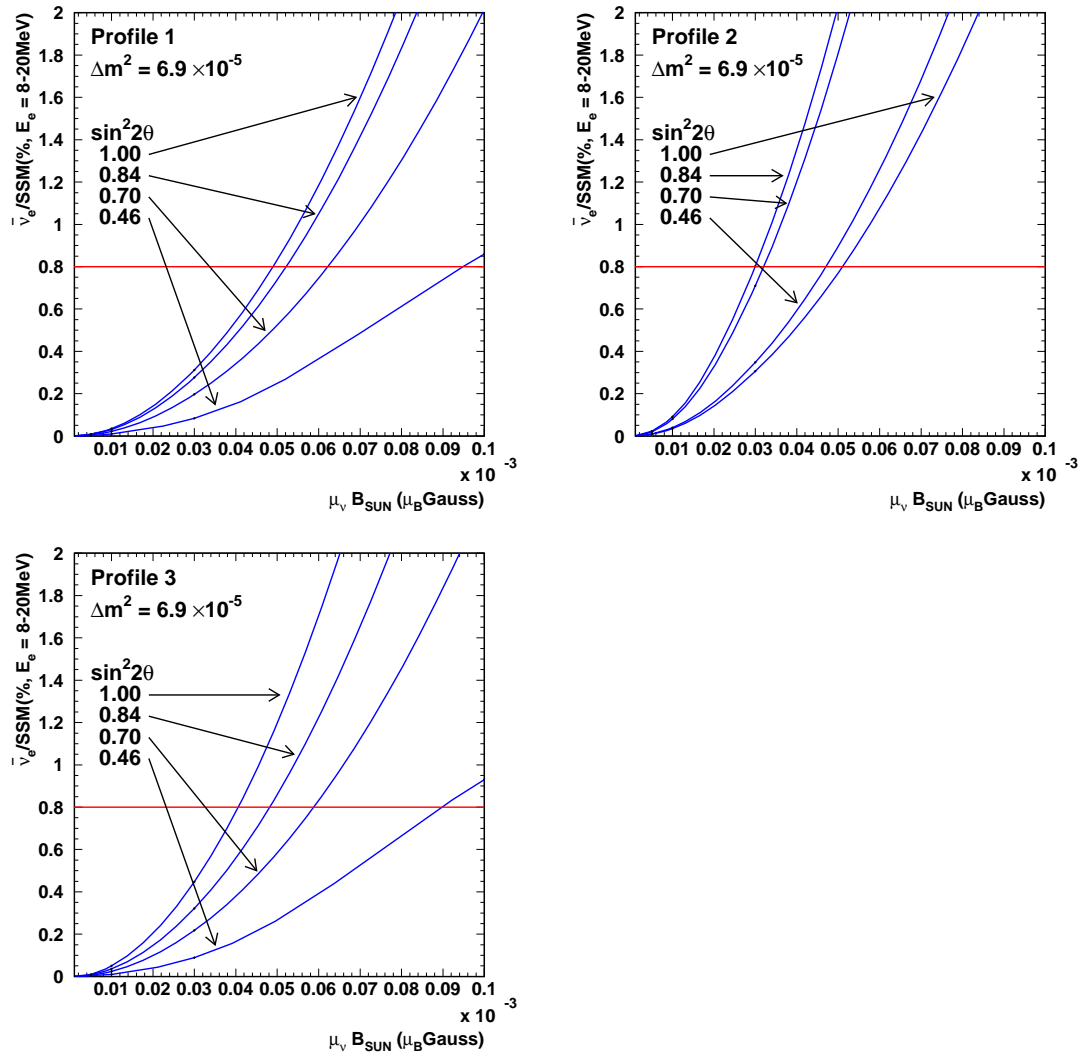


Figure 8.13: Expected $\bar{\nu}_e/SSM$ as a function of $\mu_\nu B_{sun}$ for each parameters and each profiles.

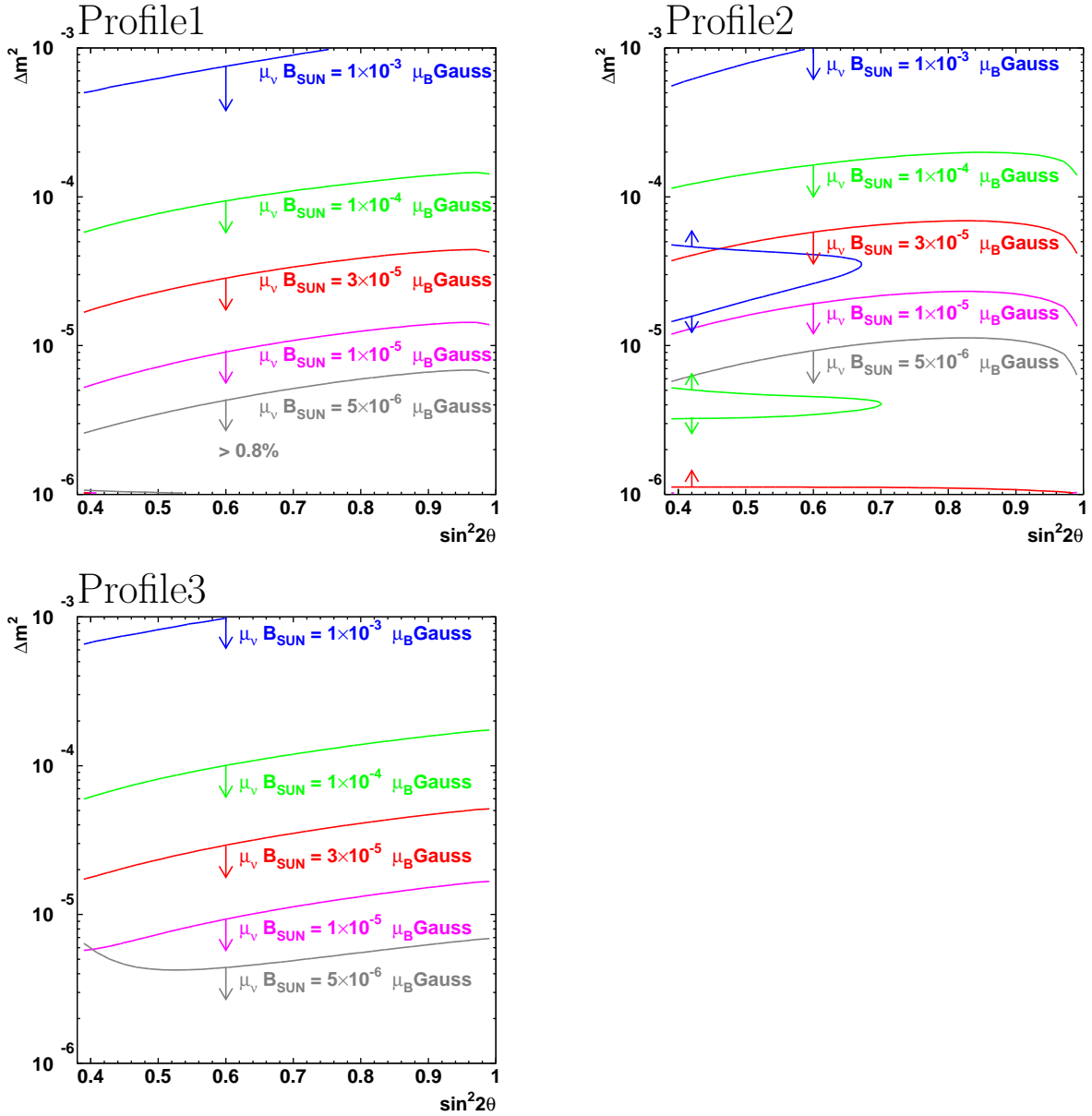


Figure 8.14: Excluded region of oscillation parameters from the $\bar{\nu}_e$ flux limit for each $\mu_\nu B_{\text{sun}}$ and magnetic field profiles. Each lines shows for each $\mu_\nu B_{\text{sun}}$ and arrows show regions where $\bar{\nu}_e / \text{SSM} \geq 0.8\%$.

Considering the upper limit of B_{sun} to be 300 kGauss in the convection zone, we can obtain an upper limit of Majorana transition magnetic moment as $3.3 \times 10^{-10} \mu_B$.

8.2.4 Flux bias and spectrum distortion from RSFP

We also study how much subdominant effects of RSFP on the ${}^8\text{B}$ neutrino flux and spectrum distortions are allowed.

Figure 8.18 shows the expected energy spectra of ${}^8\text{B}$ neutrino events in SK at the following typical parameters in the allowed regions as described in the previous section, $(\sin^2 2\theta, \Delta m^2, \mu_\nu B_{\text{sun}}) = (0.82, 4.2 \times 10^{-5} \text{eV}^2, 3 \times 10^{-5} \mu_B \text{Gauss}), (0.88, 7.9 \times 10^{-5} \text{eV}^2, 3 \times 10^{-5} \mu_B \text{Gauss}), (0.82, 5.0 \times 10^{-5} \text{eV}^2, 3 \times 10^{-5} \mu_B \text{Gauss})$, for profile1, profile2, profile3, respectively. The maximum deviations from the oscillation only case ($\mu_B B_{\text{sun}} = 0$) are only 2~3% at the maximum allowed value ($\mu_B B_{\text{sun}} = 3 \times 10^{-5} \mu_B \text{Gauss}$).

Shape distortions from RSFP is weaker in lower energy region, and the effect on the number of elastic scattering events is smaller as shown in Figure 8.19. In $\mu_\nu B_{\text{sun}} = 3 \times 10^{-5} \mu_B \text{Gauss}$ case, the flux differences from the oscillation-only case is within 1 % at the allowed region from the solar global fit described in Sec 8.2.3.

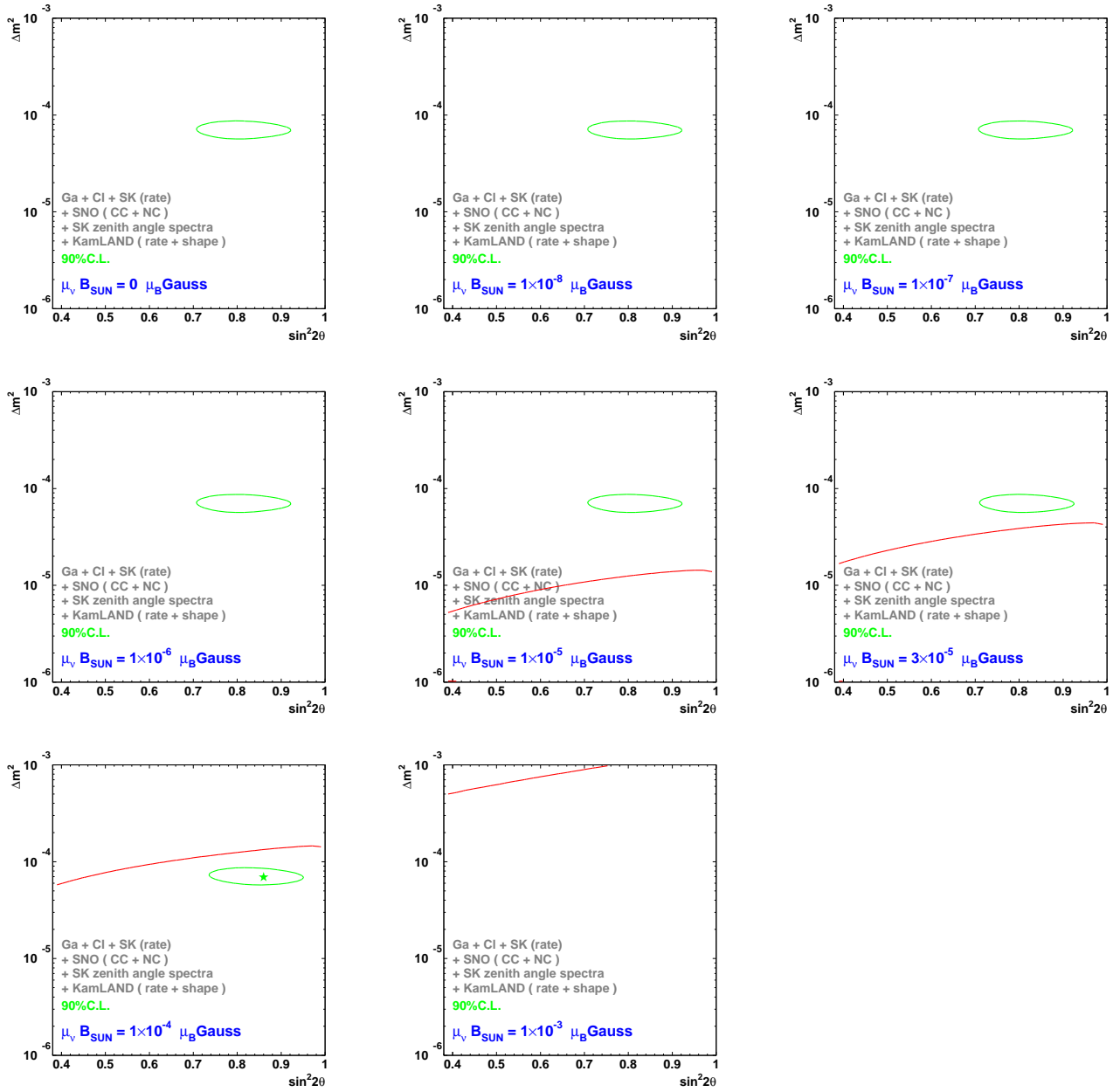


Figure 8.15: 90% C.L. allowed region from the solar + KamLAND global fit (green line) and 90% C.L. excluded region from the $\bar{\nu}_e$ limit (red line) for profile1

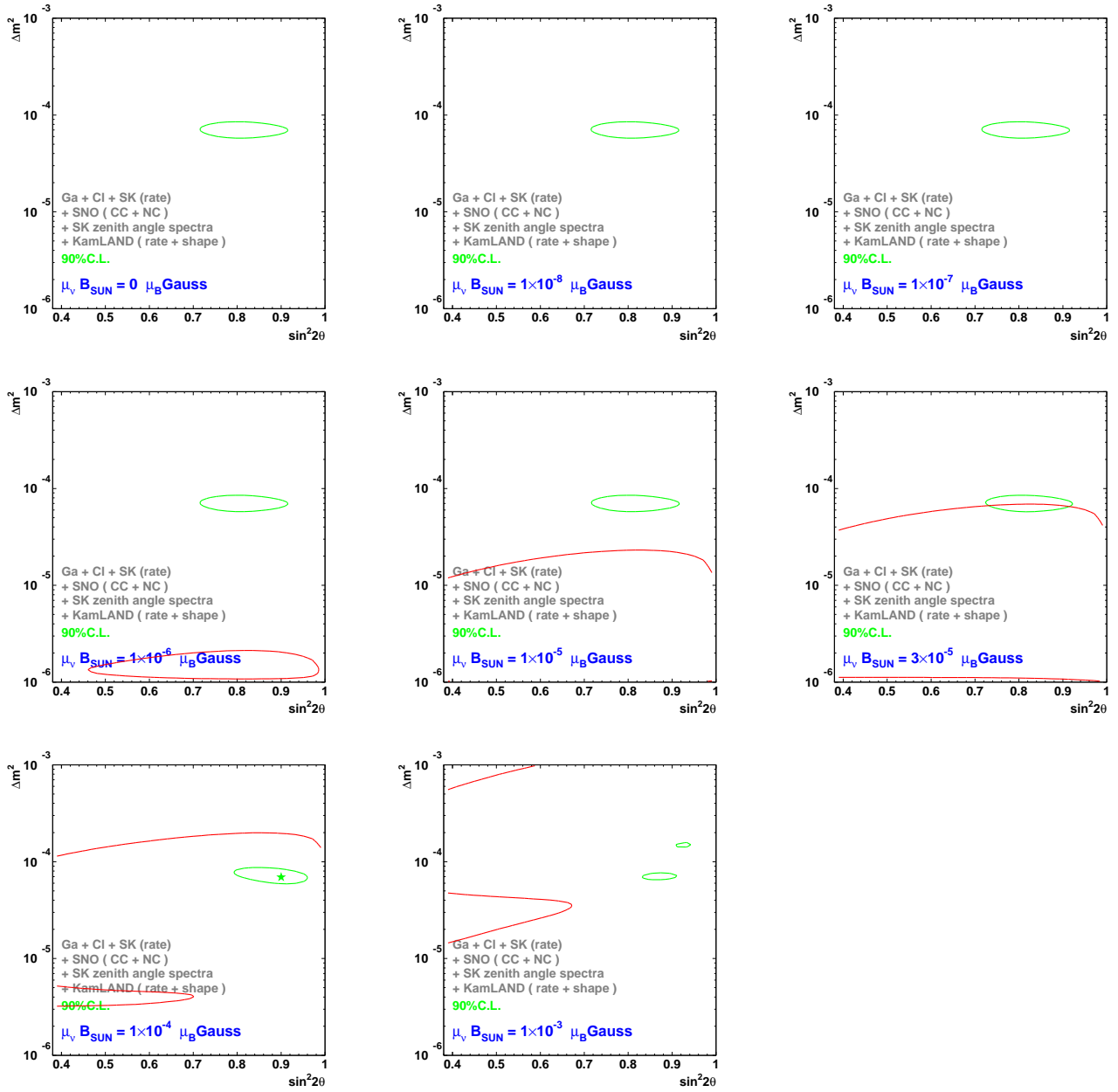


Figure 8.16: 90% C.L. allowed region from the solar + KamLAND global fit (green line) and 90% C.L. excluded region from the $\bar{\nu}_e$ limit (red line) for profile2

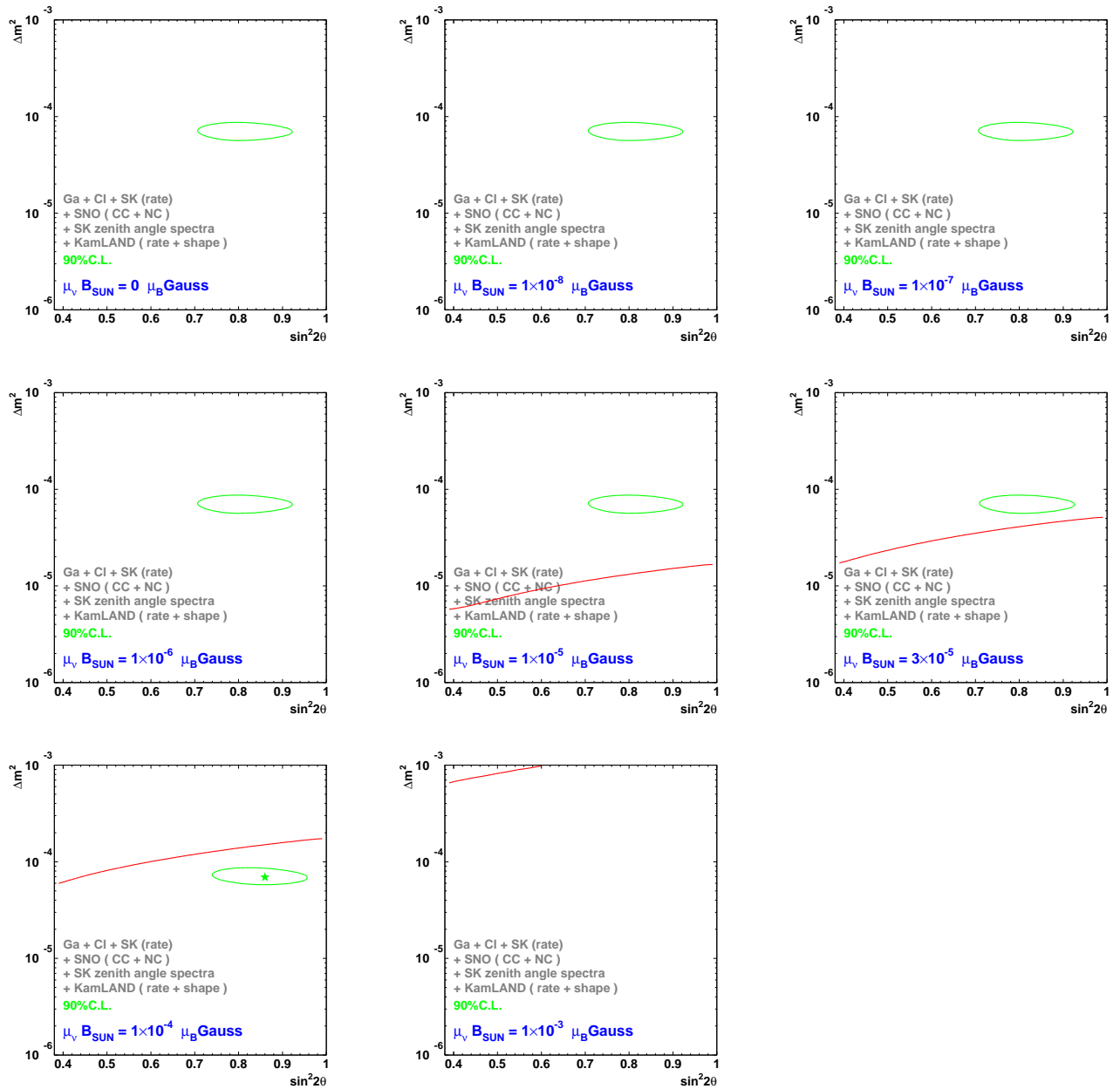


Figure 8.17: 90% C.L. allowed region from the solar + KamLAND global fit (green line) and 90% C.L. excluded region from the $\bar{\nu}_e$ limit (red line) for profile2

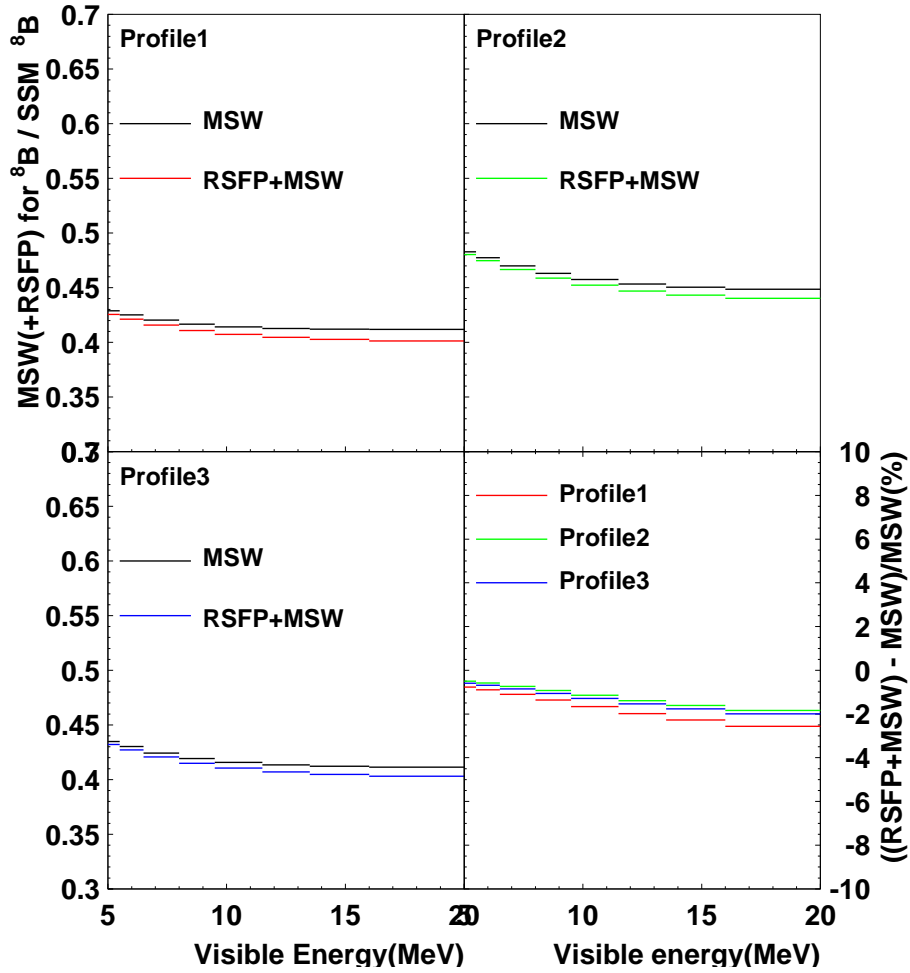


Figure 8.18: Spectrum distortions from only MSW effect and MSW with RSFP. Upper figures and left lower figure show expected energy spectra from ${}^8\text{B}$ neutrinos at SK for only MSW case and RSFP with MSW case. Selected parameters are (magnetic field, $\sin^2 2\theta$, Δm^2 , $\mu_\nu B_{\text{sun}}$) = (Profile1, 0.82, $4.2 \times 10^{-5} \text{eV}^2$, $3 \times 10^{-5} \mu_B \text{Gauss}$), (Profile2, 0.88, $7.9 \times 10^{-5} \text{eV}^2$, $3 \times 10^{-5} \mu_B \text{Gauss}$) and (Profile3, 0.82, $5.0 \times 10^{-5} \text{eV}^2$, $3 \times 10^{-5} \mu_B \text{Gauss}$). Lower right figure shows deviations of RSFP+MSW spectra from the MSW-only spectrum.

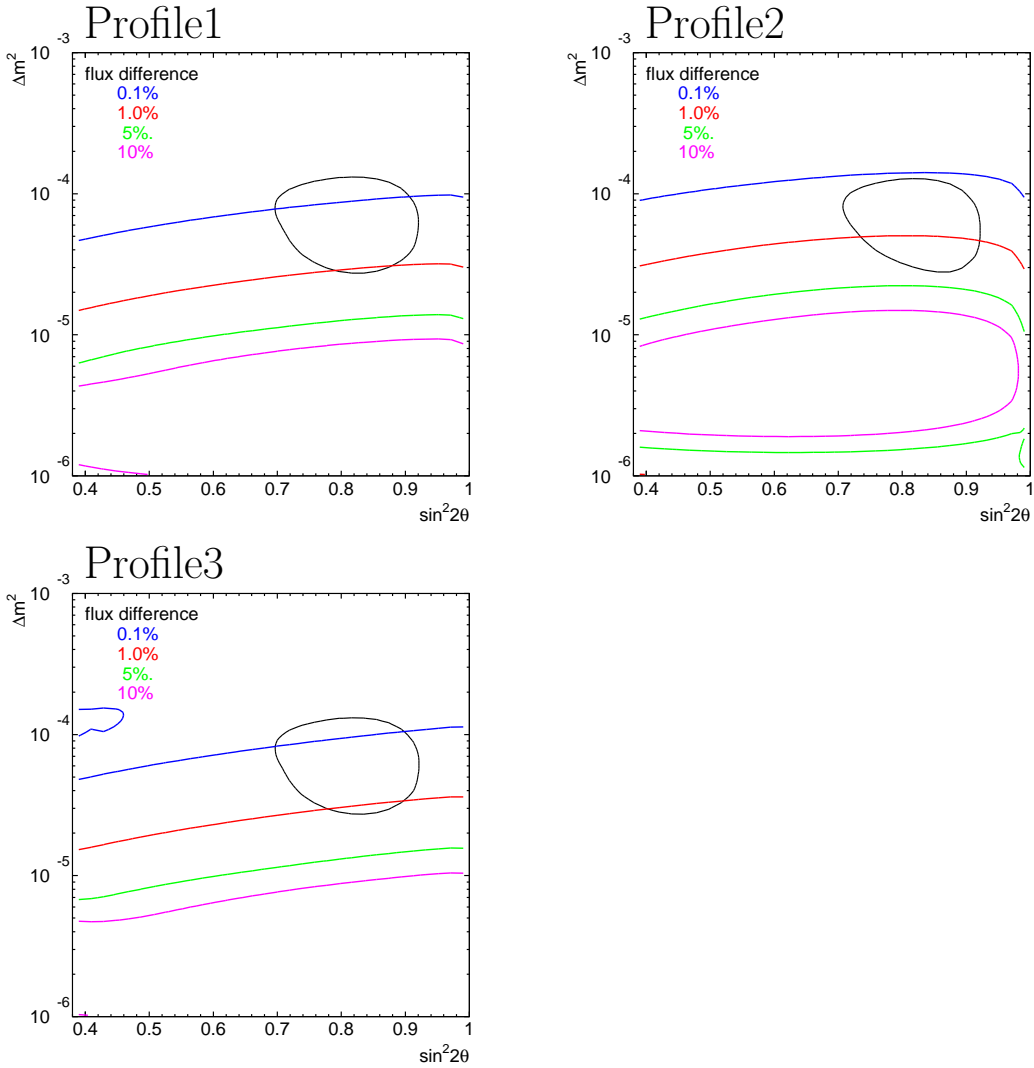


Figure 8.19: Differences of number of elastic scattering events between MSW and MSW with RSFP at SK, $N_{\text{exp}}(\text{MSW}) - N_{\text{exp}}(\text{RSFP} + \text{MSW})$. For the MSW with RSFP case, $\mu_B B_{\text{sun}} = 3 \times 10^{-5} \mu_B \text{Gauss}$ is used.

Chapter 9

Conclusion

A measurement of ^8B neutrinos from the sun and a search for anti-electron-neutrinos from the sun have been done based on 1496 live days of Super-Kamiokande-I data taken from May 31 1996 to July 2001.

The ^8B solar neutrino flux measured by elastic scattering is,

$$\Phi_\nu/\Phi_{SSM\nu_e} = 0.465 \pm 0.005(\text{stat.})_{-0.015}^{+0.016}(\text{sys.}).$$

From a global oscillation analysis using all solar flux measurements, SK zenith angle spectra and KamLAND results, only the LMA1 oscillation parameter region is favored at the 99% confidence level.

No significant excess of $\bar{\nu}_e$ events have been observed and we set an upper limit on the conversion probability to $\bar{\nu}_e$ of the ^8B solar neutrino as

$$\Phi_{\bar{\nu}_e}/\Phi_{SSM\nu_e} \leq 0.8\% \text{ (90\% C.L.)}$$

for visible energy 8 MeV - 20 MeV.

We also set a flux limit for monochromatic $\bar{\nu}_e$ for $E_{\bar{\nu}_e} = 10 \text{ MeV} - 17 \text{ MeV}$.

A global analysis for the RSFP+MSW hybrid model has been also performed and it turned out that only $\mu_\nu B_{\text{sun}} < 1 \times 10^{-4} \mu_B \text{ Gauss}$ is allowed at 90% C.L. This limit corresponding to $\mu_\nu = 3.3 \times 10^{-10} \mu_B$ for B_{sun} is 300 k Gauss

Finally it is pointed out that the RSFP is possible as subdominant process only up to a few % level.

Appendix A

Definition of spallation likelihood

The spallation likelihood functions consist of the following parameters,

- ΔL : Distance from the low-energy event to the preceding muon track.
- ΔT : Time difference between the muon and the low-energy event.
- Q_{res} : Residual charge of the muon event ($= Q_{total} - Q_{unit} \times L_{\mu}$).

where Q_{total} is the total charge, Q_{unit} is the charge per unit length and L_{μ} is the reconstructed muon track length. Two sets of likelihood function are prepared according to a quality of the muon track reconstruction. When the reconstruction is successful, we use the likelihood function :

$$L_{spa}(\Delta L, \Delta T, Q_{res}) = L_{spa}^{\Delta L}(\Delta L, Q_{res}) \times L_{spa}^{\Delta T}(\Delta T) \times L_{spa}^{Q_{res}}(Q_{res}). \quad (\text{A.1})$$

And when it failed, we avoid to use ΔL and the following likelihood function is employed,

$$L_{spa}(\Delta T, Q_{total}) = L_{spa}^{\Delta T}(\Delta T) \times L_{spa}^{Q_{res}}(Q_{total}). \quad (\text{A.2})$$

Where $L_{spa}^{\Delta L}(\Delta L, Q_{res})$, $L_{spa}^{\Delta T}(\Delta T)$, $L_{spa}^{Q_{res}}(Q_{res})$ and $L_{spa}^{Q_{res}}(Q_{total})$ are likelihood functions for ΔL , ΔT , Q_{res} and Q_{total} . Each functions is explained in the following sections.

A.1 Likelihood for ΔL

Figure A.1 shows the ΔL distribution from spallation candidate events for six Q_{res} ranges ($L_{spa-cand}^i(\Delta L)$). Selection criteria of the spallation candidates are $\Delta T < 0.1$ sec and $N_{eff} \geq 50$. Each Q_{res} region is denoted by serial number i in Table A.1. The peak around $0 \sim 100$ cm is caused by spallation events and that around 1500 cm is caused by non-spallation events distributing uniformly along in phase space. In order to obtain the ΔL distribution of the non-spallation events ($L_{non-spa}^i(\Delta L)$, $i = 1, 6$), uniformly distributing

| i | $Q_{res}(\text{pC})$ | A_i | B_i | C_i | ΔL |
|-----|------------------------------------|--------|--------|-------|-----------------------------------|
| 1 | $< 5 \times 10^4$ | 0.353 | 2.107 | 5.594 | |
| 2 | $5 \times 10^4 \sim 1 \times 10^5$ | 1.850 | 2.081 | 7.176 | |
| 3 | $1 \times 10^5 \sim 2 \times 10^5$ | 3.697 | 1.850 | 7.608 | $\Delta L < 250.2 \text{ cm}$ |
| | | | 0.836 | 5.071 | $\Delta L \geq 250.2 \text{ cm}$ |
| 4 | $2 \times 10^5 \sim 1 \times 10^6$ | 15.14 | 1.301 | 8.175 | $\Delta L < 363.57 \text{ cm}$ |
| | | | 0.622 | 5.706 | $\Delta L \geq 363.57 \text{ cm}$ |
| 5 | $1 \times 10^6 \sim 2 \times 10^6$ | 92.98 | 0.9020 | 9.187 | $\Delta L < 520.1 \text{ cm}$ |
| | | | 0.5369 | 7.288 | $\Delta L \geq 520.1 \text{ cm}$ |
| 6 | $\geq 2 \times 10^6$ | 352.88 | 0.7128 | 9.843 | $\Delta L < 547.02 \text{ cm}$ |
| | | | 0.3417 | 7.813 | $\Delta L \geq 547.02 \text{ cm}$ |

Table A.1: The six ranges of Q_{res} and the parameters for the likelihood function $L_{spa}^{\Delta L}(\Delta L, Q_{res})$ for Q_{res}

vertex positions are chosen randomly in the fiducial volume. Then, a prototype of the spallation likelihood distribution $L_{spa}^{\Delta L'}(\Delta L, Q_{res})$ is defined as follows,

$$L_{spa}^{\Delta L'}(\Delta L, Q_{res}) = \frac{L_{spa-cand}^i(\Delta L) - L_{non-spa}^i(\Delta L)}{L_{non-spa}^i(\Delta L)} \text{ for } i\text{-th } Q_{res} \text{ region.} \quad (\text{A.3})$$

The $L_{spa}(\Delta L, Q_{res})$ is modeled by the following function,

$$L_{spa}^{\Delta L, fit}(\Delta L, Q_{res}) = \frac{\exp(B_i - C_i \Delta L)}{A_i}, \quad (\text{A.4})$$

and fitted $L_{spa}^{\Delta L'}(\Delta L, Q_{res})$. Each coefficient A_i, B_i, C_i is summarized in Table A.1. Then, the likelihood function for ΔL is obtained as follows,

$$L_{spa}^{\Delta L}(\Delta L, Q_{res}) = L_{spa}^{\Delta L, fit}(\Delta L, Q_{res}). \quad (\text{A.5})$$

The distributions of $L_{spa}^{\Delta L'}(\Delta L, Q_{res})$ and likelihood function $L_{spa}^{\Delta L}(\Delta L, Q_{res})$ are shown in Figure A.2.

A.2 Likelihood for ΔT

Figure A.3 shows the ΔT distributions from the spallation candidate events for each time range. Spallation candidates are selected by $\Delta L < 300\text{cm}$, $N_{eff} \geq 50$ and $Q_{res} < 10^6$. These distributions are fitted with an hypothetical function,

$$L_{spa}^{\Delta T, fit}(\Delta T) = \sum_{i=1}^7 A_i \left(\frac{1}{2}\right)^{-\frac{\Delta T}{\tau_{1/2}^i}}. \quad (\text{A.6})$$

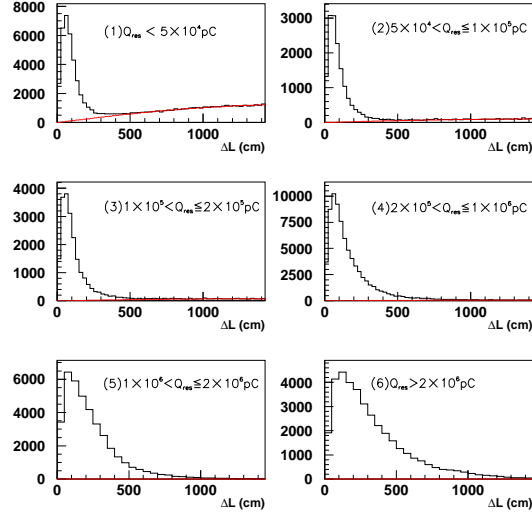


Figure A.1: ΔL distribution for each Q_{res} range

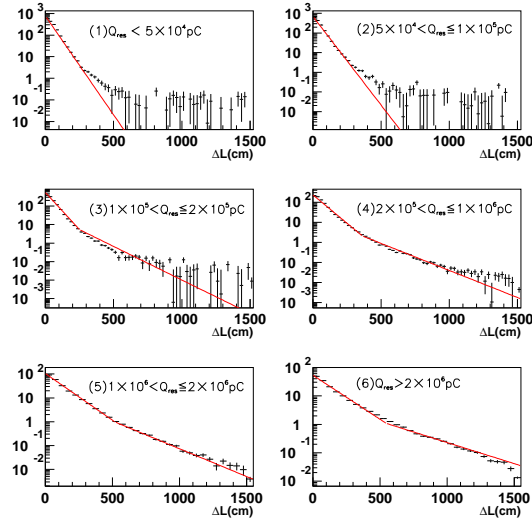


Figure A.2: The distribution of the likelihood function for ΔL . Cross marks are the $L_{spa}^{\Delta L'}(\Delta L, Q_{res})$ and lines are the likelihood function $L_{spa}^{\Delta L}(\Delta L, Q_{res})$ for 6 Q_{res} regions

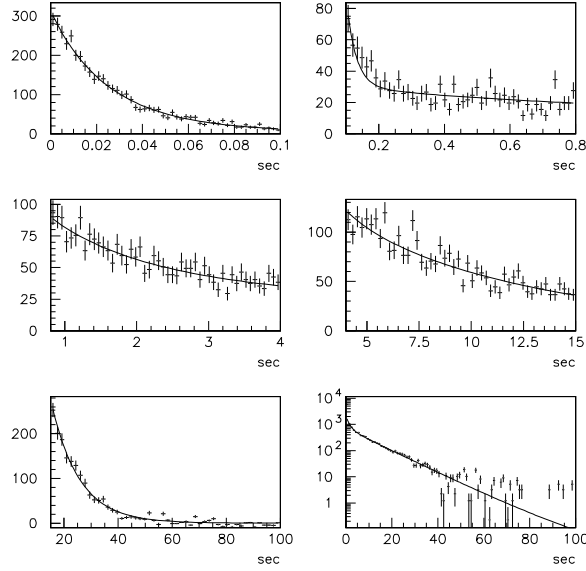


Figure A.3: ΔT distribution for each time bins. Cross marks are ΔT and lines are fitted likelihood function $L_{spa}^{\Delta T}(\Delta T)$

Where $\tau_{1/2}^i$ is a half life time of typical radioactive spallation products. The used half life times and corresponding radioactivities are summarized in Table A.2. The likelihood function for ΔT is obtained as follows,

$$L_{spa}^{\Delta T}(\Delta T) = L_{spa}^{\Delta T, fit}(\Delta T). \quad (\text{A.7})$$

A.3 Likelihood for Q_{res}

In order to obtain the likelihood function for residual charge $L_{spa}^{Q_{res}}(Q_{res})$, time correlated events with low energy events ($\Delta T < 0.1$, $N_{eff} \geq 50$) and non-correlated events are selected. Figure A.4 shows the Q_{res} distribution for spallation candidates ($Q_{spa}^{Q_{res}}(Q_{res})$) and non-spallation candidates ($Q_{non-spa}^{Q_{res}}(Q_{res})$). By using these two distributions, prototype likelihood distribution $L_{spa}'^{Q_{res}}(Q_{res})$ is obtained as follows,

$$L_{spa}'^{Q_{res}}(Q_{res}) = \frac{Q_{spa}^{Q_{res}}(Q_{res}) - Q_{non-spa}^{Q_{res}}(Q_{res})}{Q_{non-spa}^{Q_{res}}(Q_{res})}. \quad (\text{A.8})$$

To obtain the Q_{res} likelihood function, the prototype distribution is fitted by following polynomial functions,

| i | radioactivity | $\tau_{1/2}^i$ | A_i |
|-----|----------------------|----------------|--------|
| 1 | ${}^{12}_5\text{B}$ | 0.02023 | 120100 |
| 2 | ${}^{12}_7\text{N}$ | 0.0110 | 33900 |
| 3 | ${}^9_3\text{Li}$ | 0.178 | 338.6 |
| 4 | ${}^8_3\text{Li}$ | 0.84 | 1254 |
| 5 | ${}^{15}_6\text{C}$ | 2.449 | 134.7 |
| 6 | ${}^{16}_7\text{N}$ | 7.134 | 676.1 |
| 7 | ${}^{11}_4\text{Be}$ | 13.83 | 7.791 |

Table A.2: The parameters of the likelihood $L_{spa}^{\Delta T}(\Delta T)$

For $Q_{res} \leq 5.0 \times 10^5$,

$$L_{spa}^{Q_{res},fit}(Q_{res}) = \sum_{i=0}^4 A_i (Q_{res})^i. \quad (\text{A.9})$$

For $Q_{res} > 5.0 \times 10^5$,

$$L_{spa}^{Q_{res},fit}(Q_{res}) = \sum_{i=0}^2 A_i (Q_{res})^i. \quad (\text{A.10})$$

The Concrete likelihood functions for Q_{res} are obtained as follows,
For $Q_{res} < 0$ pC,

$$L_{spa}^{Q_{res}}(Q_{res}) = 1.5071 \times 10^{-4}. \quad (\text{A.11})$$

For $0 < Q_{res} \leq 5.0 \times 10^5$ pC,

$$\begin{aligned} L_{spa}^{Q_{res}}(Q_{res}) &= 1.5071 \times 10^{-4} + 7.138 \times 10^{-9} Q_{res} \\ &+ 9.987 \times 10^{-14} Q_{res}^2 - 1.307 \times 10^{-19} Q_{res}^3 \\ &+ 6.407 \times 10^{-26} Q_{res}^4. \end{aligned} \quad (\text{A.12})$$

For $Q_{res} > 5.0 \times 10^5$,

$$L_{spa}^{Q_{res}}(Q_{res}) = -2.644 \times 10^{-2} + 7.086 \times 10^{-8} Q_{res} - 3.661 \times 10^{-15} Q_{res}^2. \quad (\text{A.13})$$

Figure A.5 shows the prototype likelihood distribution $L_{spa}^{Q'_{res}}(Q_{res})$ and the fit result $L_{spa}^{Q_{res}}(Q_{res})$.

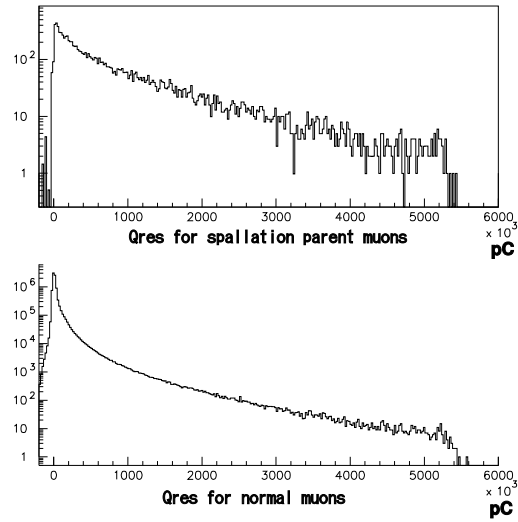


Figure A.4: Q_{res} distribution for the spallation candidate event (upper) and the non-candidate event (lower).

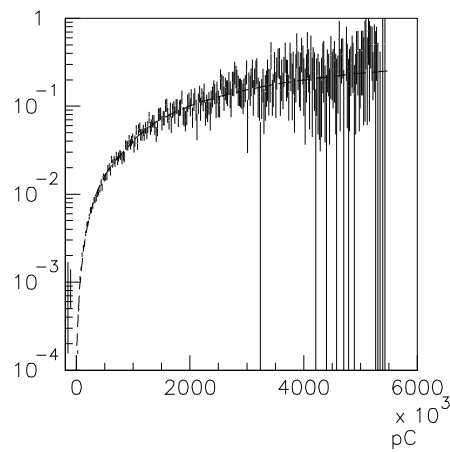


Figure A.5: The distribution of the likelihood function for Q_{res} . Cross marks are the $L_{spa}^{Q_{res}}(Q_{res})$ and lines are the likelihood function $L_{spa}^{Q_{res}}(Q_{res})$.

Appendix B

Numerical calculation of neutrino propagation

In order to obtain the survival probabilities of neutrinos, neutrino propagation in the sun and in the earth is numerically calculated. The generation points of each neutrinos are shown in Figure 2.7, and the initial wave function of neutrinos are defined as follows,

$$\phi_\nu = \begin{pmatrix} \nu_e \\ \nu_x \\ \bar{\nu}_e \\ \bar{\nu}_x \end{pmatrix} = \begin{pmatrix} 1 \\ 0 \\ 0 \\ 0 \end{pmatrix}. \quad (\text{B.1})$$

The neutrino propagation in matter for the two flavor Majorana neutrino case is expressed by the time development differential equation (2.61). Thus we must integrate the Hamiltonian along the path from production points to the surface of the sun (and from the incident point in the earth to SK detector, as shown in Figure B.1). To solve the equation, the orthogonalized matrix is used at each step instead of the flavor basis matrix. When we propagate the neutrinos, we suppose that the Hamiltonian $H(t)$ can be regarded as constant in a short time step Δt ($H(t) \simeq H(t+\Delta t) = H_0$), then the propagation equation $i\frac{d}{dt}\phi(t) = H_0\phi(t)$ can be easily solved as,

$$\phi'(t + \Delta t) = \phi'(t)e^{-iH_0'\Delta t} \quad (\text{B.2})$$

where $H_0' = VH_0V^{-1}$ is an orthogonal matrix, V the rotation matrix and $\phi'(t) = V\phi(t)$ shows the eigen-vector. The wave function at $t' = t + \Delta t$ is obtained as follows,

$$\phi(t + \Delta t) = V^{-1}(V\phi(t)e^{-iH_0'\Delta t}). \quad (\text{B.3})$$

The neutrinos are traced to the direction of the earth in the sun as shown in the left figure on B.1. The step size of calculation is $1/5000 \times R_{\text{sun}}$ (R_{sun} is the solar radius), and

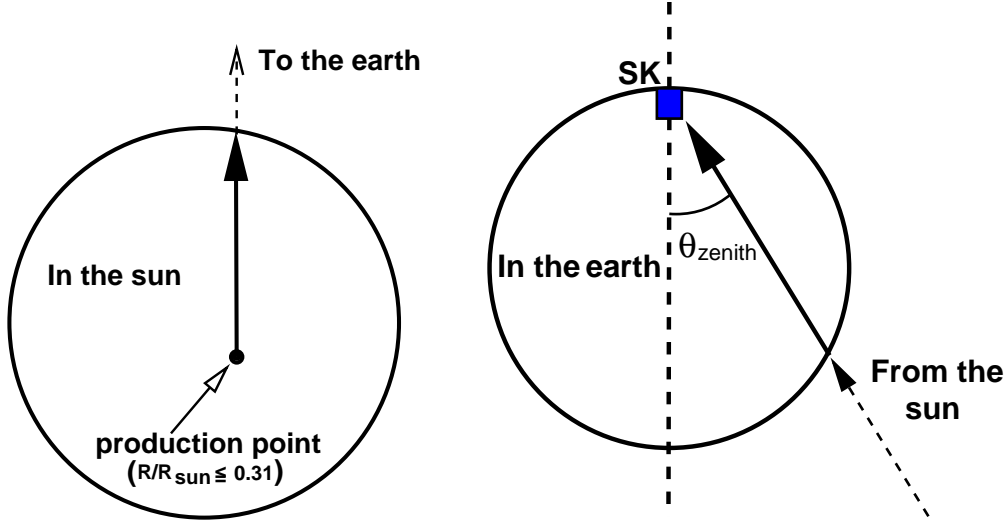


Figure B.1: Direction of the neutrino propagation

| parameter types | number of parameters |
|--|---|
| generation points in the sun | 176 points (θ : 11, radius : 16) |
| propagation width in the sun | $R_{\text{sun}} / 5000$ |
| oscillation parameters | $\sin^2 2\theta$: 32, Δm^2 : 250 |
| neutrino types | 8 |
| propagation width in the earth | 1000m ($\sim R_{\text{earth}} / 5000$) |
| zenith angle ($\cos \theta_{\text{zenith}}$) | 100 |
| magnetic field profile | 3 types |
| magnetic moment \times magnetic field | 12 |
| solar neutrino measurements | 5 |

Table B.1: Parameters and step sizes for MSW+RSFP study

this size is sufficiently small to calculate the change of propagation matrix. Table B.1 shows the step size of neutrino propagation and other parameters.

At night, neutrinos penetrate the earth and the matter effect needs to be considered. We use the electron density shown in Figure B.2 in the earth [84] where the electron density was calculated with Z/A (charge to mass ratio) of 0.468 for the core and 0.497 for the mantle [84, 85]. In this calculation, we neglect the magnetic field effect because the magnetic field in the earth is 3~5 orders of magnitude lower than that in the sun and propagation length is two orders of magnitude shorter. So the neutrino flavor transition happens only between $\nu_e \leftrightarrow \nu_\mu$ and $\bar{\nu}_e \leftrightarrow \bar{\nu}_\mu$ by an oscillation. Electron density profile along neutrino path changes according to the incident angle to the SK (θ_{zenith}) as shown in Figure B.1. To estimate the matter effects, we divided the $\cos \theta_{\text{zenith}}$ to 100 bins and traced the neutrinos in the earth.

Assuming neutrino incoherence at the earth, flavor transition in the sun and neutrino oscillation in the earth can be calculated separately. Thus survival probabilities for each zenith angle bin at SK are obtained by following equations,

$$P_{\nu_e}(\text{zenith}) = P_1 P_{1e,\text{zenith}} + P_2 P_{2e,\text{zenith}} = P_1(1 - P_{2e,\text{zenith}}) + P_2 P_{2e,\text{zenith}}, \quad (\text{B.4})$$

$$P_{\nu_\mu}(\text{zenith}) = P_1 P_{1\mu,\text{zenith}} + P_2 P_{2\mu,\text{zenith}} = P_1(1 - P_{2\mu,\text{zenith}}) + P_2 P_{2\mu,\text{zenith}}, \quad (\text{B.5})$$

$$P_{\bar{\nu}_e}(\text{zenith}) = P_1 P_{1\bar{e},\text{zenith}} + P_2 P_{2\bar{e},\text{zenith}} = P_1(1 - P_{2\bar{e},\text{zenith}}) + P_2 P_{2\bar{e},\text{zenith}}, \quad (\text{B.6})$$

$$P_{\bar{\nu}_\mu}(\text{zenith}) = P_1 P_{1\bar{\mu},\text{zenith}} + P_2 P_{2\bar{\mu},\text{zenith}} = P_1(1 - P_{2\bar{\mu},\text{zenith}}) + P_2 P_{2\bar{\mu},\text{zenith}}, \quad (\text{B.7})$$

where P_1, P_2, P_1^-, P_2^- are the probabilities to be mass eigenstates $\nu_1, \nu_2, \bar{\nu}_1, \bar{\nu}_2$ at the surface of the sun. $P_{1e,\text{zenith}}, P_{2e,\text{zenith}}$ are the probabilities to be detected as ν_e if the neutrinos arrive at the earth as ν_1, ν_2 , taking into account the matter effect in the earth. $P_{1\bar{e},\text{zenith}}, P_{2\bar{e},\text{zenith}}$ are the anti-particle part for $\bar{\nu}_e$ and $\bar{\nu}_1, \bar{\nu}_2$. And $P_{1\mu,\text{zenith}}, P_{2\mu,\text{zenith}}, P_{1\bar{\mu},\text{zenith}}, P_{2\bar{\mu},\text{zenith}}$ are similarly defined. Finally, integrating the zenith angle bins with a weight of detector livetime, we obtained survival probabilities for each neutrinos.

For the other solar neutrino experiments, we also consider the matter effect in the earth but we don't know the live time weight. Thus we estimated the time weight for each zenith angle bins only using the latitude. Because livetime for zenith angle bins are different from the latitude of the detector location (Gallex/GNO : $42^\circ 05'$, SAGE : $43^\circ 42'$, Homestake : $44^\circ 21'$, SNO : $46^\circ 28'$). Considering these effect, expected neutrino survival probabilities for each solar neutrino experiments are calculated.

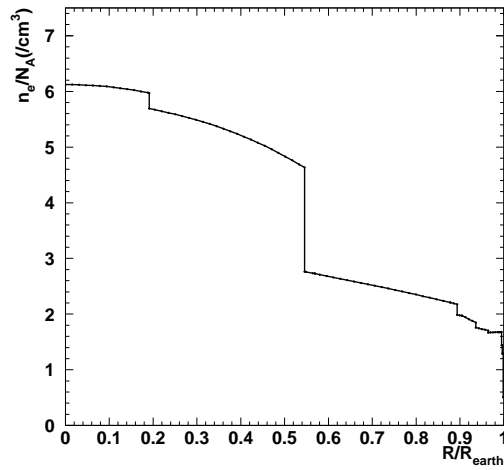


Figure B.2: The electron density distribution as a function of the radius of the earth. where N_A the Avogadro constant.

Appendix C

Spectrum distortion from neutrino magnetic moment

When neutrinos have magnetic moment (where, magnetic moment is not only transition magnetic moment but also magnetic dipole moment for Dirac neutrinos), electromagnetic interaction can take place between neutrinos and electrons with the following cross section,

$$\left(\frac{d\sigma}{dT}\right)_{EM} = \mu_\nu^2 \frac{\pi\alpha^2}{m_e^2} \left(\frac{1}{T} - \frac{1}{E_\nu}\right),$$

where T is the kinetic energy of electron ; $E_e - m_e$ and E_ν is the neutrino energy. Thus, cross section of total neutrino-elastic scattering will be larger than that of standard considering the weak interaction, especially at lower energy region.

In this thesis, we have not included the electro-magnetic effect in neutrino-electron elastic scattering. Because in RSFP+MSW analysis, we treated neutrino magnetic moment \times magnetic field as one parameter, and we could not fix the magnetic field in the sun. Thus when we write $\mu_\nu B_{\text{sun}} = 3.0 \times 10^{-5} \mu_B \text{Gauss}$, there are various combinations such as (magnetic moment, magnetic field) = $(3.0 \times 10^{-10} \mu_B, 1.0 \times 10^5 \text{Gauss})$, $(1.0 \times 10^{-10} \mu_B, 3.0 \times 10^5 \text{Gauss})$, $(3.0 \times 10^{-11} \mu_B, 1.0 \times 10^6 \text{Gauss})$.

However, as one of results in this thesis, RSFP effect on spectrum distortion turned out to be negligible. On the other hand, electro-magnetic effect becomes larger as energy goes lower. Thus we have a statistical advantage to use this effect for neutrino magnetic moment search in lower energy region. Figure C.1 shows observed energy spectrum of recoil electron with expected energy spectra. In this figure, we assume $\mu_\nu = 1.0 \times 10^{-10} \mu_B$. By comparing red lines with blue line, we may be able to set an upper limit on magnetic moment independent of Majorana or Dirac type.

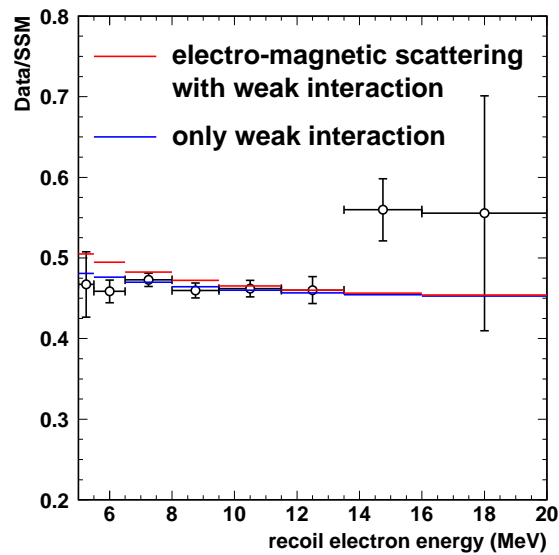


Figure C.1: Expected energy spectrum of recoil electrons with and without electro-magnetic interaction. Blank circles show observed data, blue lines show expected spectrum from only weak interaction in RSFP+MSW analysis with $\mu_\nu B = 3 \times 10^5 \mu_B \text{Gauss}$, and red lines show expected spectrum from weak + electro-magnetic scattering with $\mu_\nu B = 3 \times 10^5 \mu_B \text{Gauss}$ and $\mu_\nu = 1.0 \times 10^{-10} \mu_B$. In this figure, we consider only ^8B neutrinos.

Bibliography

- [1] R. Davis, Jr., *et al.*, Phys. Rev. Lett. **20** (1968) 1205
- [2] S. Fukuda, *et al.*, Phys. Lett. B **539** (2002) 179
- [3] Q. R. Ahmad, *et al.*, Phys. Rev. Lett. **87** (2001) 071301
- [4] K. Eguchi, *et al.*, Phys.Rev.Lett. **90** (2003) 021802
- [5] W. Pauli. Letter to L. Meitner and her colleagues (letter open to the participants of the conference in Tubingen) (1930)
- [6] E. Fermi, Z. physik. **88** (1934) 161
- [7] F. Reines and C. L. Cown, Jr., Phys. Rev. **92** (1953) 830
- [8] G. Danby, *et al.*, Phys. Rev. Lett. **9** (1962) 36
- [9] K. Kodara, *et al.*, Phys. Lett. B **504** (2001) 218
- [10] The LEP collaborations, the LEP Electroweak Working Group and the SLD Heavy Flavour Group, hep-ex/0212036
- [11] V. M. Lobashev, *et al.*, Phys. Lett. B **460** (1999) 227
- [12] K. Assamagan,*et al.*, Phys. Rev. D **53** (1996) 6065
- [13] R. Barete, *et al.*, Euro. Phys. J. C **2** (1998) 395
- [14] D. N. Sperge, *et al.*, Astrophys. J. Suppl. **148** (2003) 175
- [15] K. Fujikawa and R. E. Shrock, Phys. Rev. Lett. **45** (1980) 963
- [16] B. Kayser Phys. Rev. D **30** (1984) 1023
- [17] J. E. Kim, Phys. Rev. D **14** (1976) 3000 ;
M. A. Beg, W. J. Marciano and M. Ruderman, Phys. Rev. D **17** (1978) 1395

- [18] M. Fukugita and T. Yanagida, Phys. Rev. Lett. **58** (1988) 1807
- [19] J. F. Beacom and P. Vogel, Phys. Rev. Lett. **83** (1999) 5222
- [20] Z. Daraktchieva, *et al.*, Phys. Lett. B **564** (2003) 190
- [21] D. A. Krakauer, *et al.*, Phys. Lett. B **252** (1990) 177
- [22] L. B. Auerback, *et al.*, Phys. Rev. D **63** (2001) 112001
- [23] R. Schwienhorst, *et al.*, Phys. Lett. B **513** (2001) 23
- [24] G. G. Raffelt, Phys. Rev. Lett. **64** (1990) 2856
- [25] J. N. Bahcall, *et al.*, Phys. Rev. Lett. **90** (2003) 131301
- [26] J. N. Bahcall, *et al.*, Astrophys. J. **555** (2001) 990
- [27] C. E. Ortiz, *et al.*, Phys. Rev. Lett. **85** (2000) 2909
- [28] B. T. Cleveland, *et al.*, Astrophys. J. **496** (1998) 505
- [29] P. Anselmann, *et al.*, Phys. Lett. B **285** (1992) 376
M. Altmann, *et al.*, Phys. Lett. B **490** (2000) 16
- [30] E. Bellotti, talk in TAUP 2003
- [31] J. N. Abdurashitov, *et al.*, Phys. Lett. B **328** (1994) 234
- [32] V. N. Gavrin, talk in TAUP 2003
- [33] S. N. Ahmed, *et al.*, nucl-ex/0309004
- [34] R. Davis, *et al.*, Prog. Part. Nucl. Phys. **32** (1994) 13
- [35] A. Cisneros, Astrophys. Space. Sci **10** (1971) 87
- [36] L. B. Okun, M. B. Volosin and M. I. Vysotsky, Sov. J. Nucl. Phys. **44** (1986) 440
- [37] C. S. Lim and W. J. Marciano, Phys. Rev. D **37** (1988) 1368
- [38] E. Kh. Akhmedov, Phys. Lett. B **213** (1988) 64
- [39] Y. Fukuda, *et al.*, Phys. Rev. Lett. **77** (1996) 1683
- [40] J. Pulido and E. Kh. Akhmedov, Astropart. Phys. **13** (2000) 227
- [41] C. S. Lim, *et al.*, Phys. Lett. B **243** (1990) 389

- [42] R. S. Raghavan, *et al.*, Phys. Rev. D **66** (2002) 113008
- [43] E. Kh. Akhmedov and J. Pulido, Phys. Lett. B **553** (2003) 7
- [44] L. Wolfenstein, Phys. Rev. D **17** (1978) 2369, D **20** (1979) 2634,
- [45] S. P. Mikheyev, A. Yu. Smirnov, Sov. J. Nucl. Phys. **42** (1985) 913
- [46] H. Murayama, <http://hitoshi.berkeley.edu/neutrino/>
- [47] K. Eguchi, *et al.*, hep-ex/0310047
- [48] A. Milsztajn, hep-ph/0301252
- [49] D.O. Caldwell and P.A. Sturrock, hep-ph/0305303
- [50] The Super-Kamiokande collaboration
<http://www-sk.icrr.u-tokyo.ac.jp/sk/lowe/index.html>
- [51] J.Yoo, *et al.*, Phys.Rev. D **68** (2003) 092002
- [52] S. Fukuda, *et al.*, Nucl. Inst. Meth., A **501** (2003) 418
- [53] W.C.Haxton, Nucl. Inst. Meth., A **264** (1988) 37
- [54] J. N. Bahcall, *et al.*, Phys. Rev. D **51** 6146 (1995)
- [55] M. Fukuita, A. Suzuki , Physics and Astrophysics of Neutrinos (1994)
- [56] P. Vogel and J. F. Beacom, Phys. Rev. D **60** (1999) 053003
- [57] H. Kume, *et al.*, Nucl. Inst. Meth., **205** (1983) 443
- [58] A. Suzuki, *et al.*, Nucl. Inst. Meth., A **329** (1993) 299
- [59] Y. Takeuchi, *et al.*, Phys. Lett. **452** (1999) 418
- [60] C. Mitsuda, master thesis, University of Niigata (2001)
- [61] M. Nemoto, master thesis, University of Tokai (1998)
- [62] H. Ikeda, *et al.*, Nucl. Inst. Meth., A **320** (1992) 310
- [63] GEANT Detector Description and Simulaion Tool, CERN Program Library (1993)
- [64] T. Araki, private communication.
This expected histogram is consisted by the information of thickness of the Mt.Ikenoyama and neighboring mountains with MUSIC [65].

- [65] P. Antonioli *et al.*, *Astropart. Phys.* **7** (1997) 357
- [66] A. Morel, *et al.*, *Limnology and Oceanography* **22** (1977) 709
- [67] H. A. Maclead, *Thin-Film Optical Filters* (1986)
- [68] H. Tsushima, master thesis, University of Tohoku (1998)
- [69] H. Ishino, "Measurement of the solar neutrino energy spectrum at Super-Kamiokande" Ph.D thesis, University of Tokyo (1998)
- [70] M. Nakahata, *et al.*, *Nucl. Inst. Meth., A* **421** (1999) 113
- [71] E. Blaufuss, *et al.*, *Nucl. Inst. Meth., A* **458** (2001) 638
- [72] G. Fiorentini, *et al.*, *Phys. Lett. B* **413** (1997) 378
- [73] E. Torrente-Lujan, *Phys. Lett. B* **494** (2000) 255
- [74] J. F. Beacom, private communication
- [75] W.C. Haxton and R. G. H. Robertson, *Phys. Rev. C* **59** (1999) 515
- [76] J. Yoo, private communication
- [77] Q. R. Ahmad, *et al.*, *Phys. Rev. Lett.* **89** (2002) 011301
- [78] G. L. Fogli and E. Lisi, *Astropart. Phys.* **3** (1995) 185
- [79] J. Christensen-Dalsgaard, *et al.*, *Astrophys. J.* **378** (1991) 413
- [80] E.N.Parker, in "The Structure of the Sun", proc. of the VI Canary Islands School, Cambridge University Press (1996) 299
- [81] H. M. Anita, *et al.*, *Astro. & Astro.* **360** (2000) 335
- [82] A. Friedland, *Astro-ph/0211377*
- [83] J. Pulido, *hep-ph/0106201*
- [84] D. L. Anderson, "Theory of the Earth", Blackwell scientific publications (1989)
- [85] J. N. Bahcall and P. I. Krastev, *Phys. Rev. C* **56** (1997) 2839